

Technische Universität München
Institut für Energietechnik

Lehrstuhl für Thermodynamik

Flame Flashback in Premixed Hydrogen-Air Combustion Systems

Georg Martin Baumgartner

Vollständiger Abdruck der von der Fakultät für Maschinenwesen der
Technischen Universität München zur Erlangung des akademischen Grades
eines

DOKTOR – INGENIEURS

genehmigten Dissertation.

Vorsitzender:

Univ.-Prof. Dr. Julien Provost

Prüfer der Dissertation:

1. Univ.-Prof. Dr.-Ing. Thomas Sattelmayer

2. Prof. Dr. Jens Klingmann

Univ. Lund, Schweden

Die Dissertation wurde am 08.09.2014 bei der Technischen Universität München eingereicht
und durch die Fakultät für Maschinenwesen am 25.11.2014 angenommen.

A bisserl was geht immer.

Franz Münchinger alias Monaco Franze
(aus der gleichnamigen Serie des
Deutschen Fernsehens, 1983)

Preface / Vorwort

This work was conducted at the Lehrstuhl für Thermodynamik of the Technische Universität München (TUM) from February 2010 to June 2014. It forms a part of the BIGCCS project, performed under the Norwegian research program "Centres for Environment-friendly Energy Research (FME)". The author acknowledges the following partners for their contributions: Aker Solutions, ConocoPhillips, Det Norske Veritas AS, Gassco AS, Hydro Aluminium AS, Shell Technology AS, Statkraft Development AS, Statoil Petroleum AS, TOTAL E&P Norge AS, and the Research Council of Norway (193816/S60).

This work would not have been possible without the support of many people. First and foremost, I offer my sincerest gratitude to my supervisor, Professor Dr.-Ing. Thomas Sattelmayer, whose guidance and support from the initial to the final level enabled me to develop a deep understanding of the subject whilst providing me with the scientific freedom needed to work in my own way. Furthermore, I am thankful for the opportunity to lead the "Reactive Flows" research group at the institute and the chance to participate in a short-term research exchange at the University of California in Irvine (UCI). Here I would also like to thank Professor Vincent McDonell for the welcoming atmosphere at the UCI and my lab mate, Zhixuan Duan, for the fruitful collaboration and for making my stay in California very pleasant.

Special thanks to Professor Jens Klingmann from Lund University, Sweden, for reviewing this thesis and for being the second examiner as well as to Professor Dr. Julien Provost for organizing the doctoral examination and being the chairman during the oral exam.

I am also grateful to Professor Truls Gundersen from the NTNU in Trondheim, Norway, who kindly organized regular researcher meetings and get-togethers in Norway, which effectively fostered scientific and personal exchange within the BIGCCS group.

Weiterhin bedanke ich mich bei allen aktuellen und ehemaligen Mitarbeitern des Lehrstuhls für Thermodynamik, insbesondere auch bei den Mitarbeitern des Sekretariats und der Werkstätten, für die stets kollegiale Zusammenarbeit, die gegenseitige Hilfsbereitschaft und die vielen unterhaltsamen Stunden am Lehrstuhl. Mein besonderer Dank gilt dabei meinem Vorgänger, Dr.-Ing. Christian Eichler, für die gründliche Einführung in die Thematik des Flammenrückschlags und für das Teilen seiner Erfahrungen hinsichtlich der Umsetzung von Rückschlagsexperimenten. Lorenz Böck danke ich für seine Hilfe bei der Anwendung des LIF-Systems und meiner Nachfolgerin, Vera Hoferichter, danke ich für die fruchtbringenden Diskussionen und die reibungslose Übergabe des Forschungsprojekts.

Nicht unerwähnt lassen möchte ich meinen langjährigen Bürokollegen, Leonhardt Hörth, der stets für eine angenehme Büroatmosphäre und für das intensive Pflegen der bayrischen Sprache sorgte. In diesem Zusammenhang gebührt auch Michael Hertweck als dem mutmaßlichen Gründer der lehrstuhlinterne Weißwurstgruppe großer Dank für diese Pflege des bayrischen Brauchtums sowie sämtlichen Mitgliedern dieser erlauchten Runde für die kurzweiligen Stunden.

Stellvertretend für viele andere möchte ich mich – genderkonform und in alphabetischer Reihenfolge – bei Balbina Hampel, Marcus Grochowina, Josef Haßberger, Christoph Jörg, Dr.-Ing. Stephan Parzinger, Matthias Utschick und Michael Wagner für ihre Freundschaft und die zahlreichen gemeinsamen Unternehmungen bedanken.

Zahlreiche Studenten und Praktikanten haben mit großer Einsatzbereitschaft und durch ihre tatkräftige Unterstützung maßgeblich zum Erfolg dieser Arbeit beigetragen, wofür ich allen sehr herzlich danke.

Mein größter Dank gebührt meiner Familie, insbesondere meinen Eltern, die mich auf meinem Weg stets unterstützt und gefördert haben. Mein abschließender Dank gilt Jasmine für ihren erfrischenden Humor und die mir entgegengebrachte Unterstützung in der finalen Phase dieser Arbeit.

München, im Dezember 2014

Georg Baumgartner

Teile dieser Arbeit wurden vom Autor bereits vorab als Konferenz- und Zeitschriftenbeiträge veröffentlicht [5–7, 26, 31]. Alle Vorveröffentlichungen sind entsprechend der gültigen Promotionsordnung ordnungsgemäß gemeldet. Sie sind deshalb nicht zwangsläufig im Detail einzeln referenziert. Vielmehr wurde bei der Referenzierung eigener Vorveröffentlichungen Wert auf Verständlichkeit und inhaltlichen Bezug gelegt.

Parts of this Ph.D. thesis were published by the author beforehand in conference proceedings and journal papers [5–8, 26, 31]. All of these prior printed publications are registered according to the valid doctoral regulations. Therefore, they are not necessarily quoted explicitly in the text. Whether they were referenced, depended on maintaining comprehensibility and providing all necessary context.

Abstract / Kurzfassung

The potential occurrence of flame flashback is a critical safety hazard in pre-mixed combustion systems as it can lead to severe hardware damage. This applies in particular to highly reactive fuels, such as hydrogen-rich synthesis gases or pure hydrogen, and to low-velocity flow regions, such as wall boundary layers. In this work, flashback was investigated both on a macroscopic and on a microscopic scale for turbulent hydrogen-air flames using advanced optical measurement techniques. The flashback behavior was determined for various burner geometries and operating conditions, and the decisive influential parameters on flashback propensity were identified. In addition, an improved theoretical model describing the flashback process of unconfined flames was developed, which eliminates the shortcomings of the existing model.

Das potentielle Auftreten von Flammenrückschlägen in vorgemischten Verbrennungssystemen stellt ein großes Sicherheitsrisiko dar, weil diese zu massiver Beschädigung von Bauteilen führen können. Dies trifft in besonderem Maße dann zu, wenn hochreaktive Brennstoffe, wie zum Beispiel wasserstoffreiche Synthesegase oder reiner Wasserstoff, verwendet werden oder wenn die Strömungsgeschwindigkeiten niedrig sind, wie zum Beispiel in Wandgrenzschichten. In dieser Arbeit wurde das Rückschlagsverhalten von turbulenten Wasserstoff-Luft-Flammen sowohl auf makroskopischer als auch auf mikroskopischer Ebene mit Hilfe moderner optischer Messtechnik untersucht. Dabei wurden eine Vielzahl von verschiedenen Brennergeometrien und Betriebsbedingungen berücksichtigt und die entscheidenden Einflussparameter auf die Rückschlagsneigung identifiziert. Zusätzlich wurde ein verbessertes theoretisches Modell zur Beschreibung des Rückschlagsverhaltens von frei brennenden Flammen entwickelt, in welchem die Unzulänglichkeiten des existierenden Modells beseitigt wurden.

Contents

1	Introduction	1
1.1	Current Knowledge	2
1.1.1	Boundary Layer Flashback of Unconfined Flames	3
1.1.2	Recent Findings on Boundary Layer Flashback of Confined Flames	8
1.2	Scope of the Project and Structure of the Thesis	10
2	Basics of Isothermal and Reactive Flows	13
2.1	Fluid Flow	13
2.1.1	Boundary Layer Flow	17
2.1.2	Boundary Layer Separation	21
2.1.3	Swirl Flows	25
2.2	Premixed Combustion	27
2.2.1	Laminar Flame Characteristics	27
2.2.2	Turbulence-Flame Interaction	29
2.2.3	Near-Wall Flame Quenching	31
2.2.4	Flame Backpressure	32
3	Experimental Setup and Measurement Techniques	33
3.1	Tube Burner Setups	33
3.1.1	TUM Burner	33
3.1.2	BaCaTeC Burner	36
3.2	Channel Burner Setup	37
3.3	Experimental Procedure	40
3.3.1	Tube Burners	41
3.3.2	Channel Burner	42
3.4	Measurement Techniques	42
3.4.1	Chemiluminescence	43
3.4.2	Mie Scattering	45

3.4.3	Particle Image Velocimetry (PIV)	46
3.4.3.1	Basic Principle	46
3.4.3.2	Simultaneous PIV and Chemiluminescence . . .	47
3.4.4	Planar Laser-Induced Fluorescence (PLIF)	50
3.4.4.1	Basic Principle	50
3.4.4.2	Simultaneous PLIF and Chemiluminescence . .	53
4	Isothermal Flow Fields	55
4.1	Tube Burner	55
4.2	Channel Burner	59
5	Macroscopic Flashback Studies - Various Burner Configurations	61
5.1	General Considerations and Terminology	61
5.2	Effect of Flame Enclosure on Flashback Propensity	64
5.2.1	Confined Flame Holding	64
5.2.2	Open Flame Holding	66
5.2.3	Influence of Enclosure Size	67
5.3	Influence of Burner Material on Flashback Behavior	69
5.3.1	Flashback Limits	71
5.3.2	Theoretical Heat Transfer Analysis	73
5.4	Summary of the Findings for Different Burner Types and Preliminary Conclusions	74
6	Macroscopic Flashback Studies - Variation of Operating Conditions	77
6.1	Flashback Limits for Preheated Mixtures	77
6.2	Influence of Swirl on Flashback	81
6.2.1	Experimental Approach and Isothermal Flow Field	83
6.2.1.1	Tube Burner Setup	83
6.2.1.2	Isothermal Flow Field	83
6.2.2	Measurement Approach	87
6.2.2.1	High-Speed Mie Scattering	87
6.2.2.2	Simultaneous High-Speed OH*-Photography from Two Perspectives	88
6.2.3	Results and Discussion	89
6.2.3.1	Flashback Limits	89
6.2.3.2	Flame Propagation	91
6.2.4	Summary and Conclusions	94
6.3	Influence of Boundary Layer Injection on Flashback Behavior . .	98

6.3.1	Experimental Approach and Isothermal Flow Field	99
6.3.1.1	Design of the Boundary Layer Injection Devices	99
6.3.1.2	Isothermal Flow Field in the Burner Tube	101
6.3.1.3	Experimental Procedure and Flame Holding . . .	103
6.3.2	Results and Discussion	104
6.3.2.1	Boundary Layer Injection: $a=113$ mm	105
6.3.2.2	Boundary Layer Injection: $a=213$ mm and $a=313$ mm	113
6.3.3	Summary and Conclusions	114
7	Microscopic Investigation of the Onset of Flashback	121
7.1	Velocity Field for Isothermal Flow and Stable Combustion	122
7.2	Velocity Field during Flame Flashback	124
8	Theoretical Analysis of the Flashback Process	133
8.1	Theoretical Analysis of Confined Flame Flashback	133
8.1.1	Qualitative Analysis	133
8.1.2	Quantitative Analysis	136
8.2	Theoretical Analysis of Unconfined Flame Flashback	141
8.2.1	Transition from Stable Unconfined Flame to Flashback .	141
8.2.2	Improved Flashback Model for Unconfined Flames	142
8.2.3	Implications of the Improved Model for the Flashback Be- havior of Unconfined Flames	150
9	Summary and Conclusions	153
A	Isothermal Flow Field in the Plenum of the TUM Burner	157
B	Long-Distance Microscopes	159
B.1	Micro-PIV Measurements	159
B.2	Micro-PLIF Measurements	159
	Bibliography	171

Nomenclature

Latin Symbols

a	Thermal diffusivity	$[\text{m}^2/\text{s}]$
a	Distance	$[\text{m}]$
A	Area	$[\text{m}^2]$
A_{21}	Constant rate of spontaneous emission	$[\text{1/s}]$
b	Velocity coefficient	$[-]$
B	Constant for law-of-the-wall	$[-]$
B_{12}	Einstein coefficient for stimulated emission	$[\text{m}^2/\text{J s}]$
B_{21}	Einstein coefficient for induced absorption	$[\text{m}^2/\text{J s}]$
c	Thermal capacity	$[\text{J/kg K}]$
C_p	Non-dimensional pressure coefficient	$[-]$
d	Diameter	$[\text{m}]$
d	Normal distance	$[\text{m}]$
D	Mass diffusivity	$[\text{m}^2/\text{s}]$
d_f	Flashback distance	$[\text{m}]$
\dot{D}	Axial flux of angular momentum	$[\text{Nm}]$
f	Focal distance	$[\text{mm}]$
g	Velocity gradient	$[\text{1/s}]$
h	Channel height	$[\text{m}]$
\dot{I}	Axial flux of axial momentum	$[\text{Nm}]$
k	Coefficient	$[-]$
k	Turbulent kinetic energy	$[\text{m}^2/\text{s}^2]$
l_t	Integral length scale	$[\text{m}]$
l_η	Kolmogorov length scale	$[\text{m}]$
L	(Characteristic) length	$[\text{m}]$
\dot{m}	Mass flow rate	$[\text{kg/s}]$

NOMENCLATURE

M	Molar mass	[kg/kmol]
n	Exponent	[-]
n	Number	[-]
p	Pressure	[Pa]
p_0	Reference pressure	[Pa]
\dot{q}	Heat flux	[W/m ³]
Q_{21}	Total quenching rate	[1/s]
r	Radius, radial position	[m]
s	Streamwise distance	[m]
s_f	Burner rim distance at flashback onset	[m]
S	Flame speed	[m/s]
S	Swirl number	[-]
t	Time	[s]
T	Temperature	[K]
Tu	Turbulence intensity	[-]
u	Velocity component in x-direction	[m/s]
\bar{u}	Bulk flow velocity	[m/s]
u_τ	Shear stress velocity	[m/s]
V	Volume	[m ³]
v	Velocity component in y-direction	[m/s]
w	Velocity component in z-direction	[m/s]
x	Axial coordinate	[m]
X	Molar fraction	[-]
y	Wall-normal coordinate	[m]
y_f	Wall-normal distance of flashback streamline	[m]
z	Lateral coordinate	[m]
z	Axial cylinder coordinate	[m]

Greek Symbols

α	Angle	[°]
β	Angle	[°]
β	Coefficient	[-]
γ	Ratio of specific heats	[-]
δ	Boundary layer thickness	[m]
δ_b	Balancing distance	[m]

δ_f	Flame thickness	[m]
δ_i	Thickness of inner reaction layer	[m]
δ_{ij}	Kronecker delta	[-]
δ_q	Quenching distance	[m]
δ_r	Maximum backflow height	[m]
Δ	Difference	[-]
ϵ	Turbulent dissipation rate	[m ² /s ³]
κ	Von Karman constant	[-]
μ	Dynamic viscosity	[kg/m s]
λ	Air excess ratio	[-]
λ	Wavelength of light	[m]
λ	Thermal conductivity	[W/m K]
ν	Kinematic viscosity	[m ² /s]
ϕ_{12}	Constant	[-]
ϕ_{21}	Constant	[-]
Φ	Equivalence ratio	[-]
ρ	Density	[kg/m ³]
σ	Standard deviation	
τ	Shear stress	[Pa]
ω	Turbulent frequency	[1/s]
ω_ϕ	Azimuthal vorticity	[1/s]
ω_r	Radial vorticity	[1/s]
ω_z	Axial vorticity	[1/s]
$\vec{\omega}$	Vorticity vector	[1/s]

Superscripts

-	Averaged quantity
*	Electronically excited state
'	Fluctuation

Subscripts

ad	Adiabatic
c	Critical condition
f	Flame
f	Flashback

l	Laminar
max	Maximal
min	Minimal
pred	Prediction
ref	Reference state
sep	Separation
t	Turbulent
W	Wall
∞	Freestream

Nondimensional Numbers

Da	Damköhler number
Le	Lewis number
Ma	Mach number
Pe	Peclet number
Re	Reynolds number
Sc	Schmidt number

Acronyms

AFT	Adiabatic flame temperature
BaCaTeC	Bavaria California Technology Center
BLF	Boundary Layer Flashback
CCS	Carbon Capture and Storage
CFD	Computational Fluid Dynamics
CIVB	Combustion Induced Vortex Breakdown
DBD	Dielectric Barrier Discharge
DNS	Direct Numerical Simulation
fps	Frames per second
IA	Interrogation Area
ICCD	Intensified Charge-Coupled Device
IR	Infrared
LES	Large Eddy Simulation
LIF	Laser-Induced Fluorescence
LNG	Liquified Natural Gas
NSE	Navier-Stokes Equations

Nd:YLF	Neodymium-doped Yttrium Lithium Fluoride
Nd:YVO ₄	Neodymium-doped Yttrium Orthovanadate
PIV	Particle Image Velocimetry
PLIF	Planar Laser-Induced Fluorescence
RANS	Reynolds-Averaged Navier-Stokes
rms	Root mean square
RSM	Reynolds Stress Model
SST	Shear Stress Transport
TUM	Technische Universität München, Germany
UCI	University of California in Irvine, USA
URANS	Unsteady Reynolds Averaged Navier Stokes
USA	United States of America
UV	Ultraviolet
vol.	Volume
vs.	Versus
2D	Two-dimensional
3D	Three-dimensional

Mathematical Operators

∂	Partial derivative
∇	Nabla operator
\times	Vector product
\cdot	Scalar product
$\langle \dots \rangle$	Time average

1 Introduction

Sustainable power generation from the remaining fossil fuel resources on our planet is one of the key challenges to satisfy the world's energy demand while simultaneously minimizing the negative impacts on the environment. Regarding the reduction of carbon dioxide (CO_2) emissions, Carbon Capture and Storage (CCS) technologies are a promising concept. They are aimed at capturing CO_2 either before or after the actual power generation process and storing the greenhouse gas underground. In the pre-combustion CO_2 capture route, natural gas reforming or coal gasification processes are deployed to produce gases with very high hydrogen content, which can then be used as carbon-free energy sources in industrial applications, e.g. for firing a gas turbine.

In the gas turbine industry, the development trend is toward lean premixed combustion because of the low achievable level of nitrogen oxide (NO_x) emissions through controlling the peak combustion temperature by the amount of excess air. However, premixed combustion of hydrogen-rich gases in an undiluted manner remains a very challenging issue. Compared to hydrocarbon fuels, the reactivity of hydrogen is much higher due to its entirely different thermo-physical properties (wider flammability limits, smaller quenching distances, higher diffusivity, and higher flame speed) [82]. Therefore, the risk of flame flashback into regions upstream of the desired flame position is significantly higher than for hydrocarbon applications. This applies in particular to regions where the flow velocity is low, for instance, in wall boundary layers or wake regions. Flame flashback in a technical application can lead to combustion instabilities and hardware damage due to overheating of machine components that are not designed for high temperatures, which in turn can even result in catastrophic failure of the whole machine [15, 81]. Therefore, a comprehensive understanding of flashback is crucial for the safety and reliability of premixed combustion systems.

1.1 Current Knowledge

Generally spoken, flame flashback from the desired flame position into upstream flow regions is initiated when the local flame speed exceeds the local flow velocity at a certain position. Flashback can be assigned to one of the following four mechanisms [29, 71, 85]:

1. **Core Flow Flashback:** The local flame speed exceeds the bulk flow velocity, leading to flashback in the core flow. In turbulent flows, velocity fluctuations can provoke this situation.
2. **Flashback due to Combustion Instabilities:** The interaction of acoustic modes, flow fluctuations and associated heat release fluctuations can cause periodically occurring flashbacks.
3. **Flashback due to Combustion Induced Vortex Breakdown (CIVB):** In swirl-stabilized burners, a recirculation zone is created on the burner axis at the cross-sectional jump from the burner duct into the combustion chamber, which stabilizes the flame during regular operation. Under certain conditions, the interaction of heat release in the combustion chamber with vortical and turbulent structures in the burner duct can lead to upstream propagation of the recirculation zone and the flame, leading to flashback (cf. Sec. 2.1.3).
4. **Boundary Layer Flashback (BLF):** Due to the no-slip condition flow velocities decrease monotonously toward solid walls. If the flame speed at a certain distance from the wall is higher than the local flow velocity, the flame starts to propagate upstream along the wall boundary layer.

The substitution of hydrocarbon fuels for highly reactive hydrogen-rich fuels increases the hazard of flame flashback, in particular, regarding the first and the last two mechanisms listed above. Flashback in the core flow can be effectively counteracted by high bulk flow velocities in gas turbines as was shown in studies carried out by Karim et al. [60, 61] and Wierzba et al. [129, 130], which involved hydrogen-containing fuels. Information about flashback due to combustion instabilities can be obtained from the literature, e.g. [40, 63, 92, 117]. Regarding flashback due to CIVB, this topic has been extensively researched at the Lehrstuhl für Thermodynamik of the Technische

Universität München (TUM). Considerable progress has been made in this area [17,39,65,69,71,90,108], whereas only two projects addressed BLF [29,90]. As BLF is a safety-critical issue with regard to the development of reliable burners fired with hydrogen-rich fuels, it is important to extend the knowledge on this topic.

In the following sections a short summary of early and more recent findings concerning BLF is given in order to define the state of knowledge in this research area. At the end of this chapter, the scope of the research project as well as the structure of the thesis are presented.

1.1.1 Boundary Layer Flashback of Unconfined Flames

Lewis and von Elbe [84] conducted systematic flashback tests with perfectly premixed, laminar methane-air flames at atmospheric pressure and temperature. The fresh gas mixture was sent through 1 m long Pyrex glass tubes with inner diameters between 3 and 16 mm in order to achieve fully developed laminar flow at the tube exit, where the flame was burning in the free atmosphere. Based on these experiments they developed a model to correlate the flashback tendencies of laminar flames. Due to its great importance and its extensive application in flashback research the model is described here in detail. On the left side of Fig. 1.1 the undisturbed, laminar velocity profile $u(y)$ of the incoming mixture flow above a flat plate is sketched along with the velocity gradient g at the wall. T_0 and p_0 denote the temperature and the pressure of the approaching flow, respectively, and T_W is the temperature of the wall. On the right side, the shape of the flame during BLF is shown. The arrows represent the flame speed $S_f(y)$, which is always perpendicular to the flame surface. At each position in the flow the curvature of the flame adjusts such that there is a balance between the magnitude of the flame speed and the component of the flow velocity normal to the flame surface. Similar to the flow velocity, the flame speed also decreases toward the wall because of heat losses to the cold wall and radical recombination processes. Eventually, inside of the quenching distance δ_q , the chemical reactions are entirely quenched and the flame speed vanishes. According to this model, BLF is initiated when the flame speed S_f at a certain *balancing distance* δ_b from the wall outbalances the corresponding axial velocity u at this position. δ_b is also often referred to as *penetration distance* in the literature. Assuming a linear shape of the velocity profile between

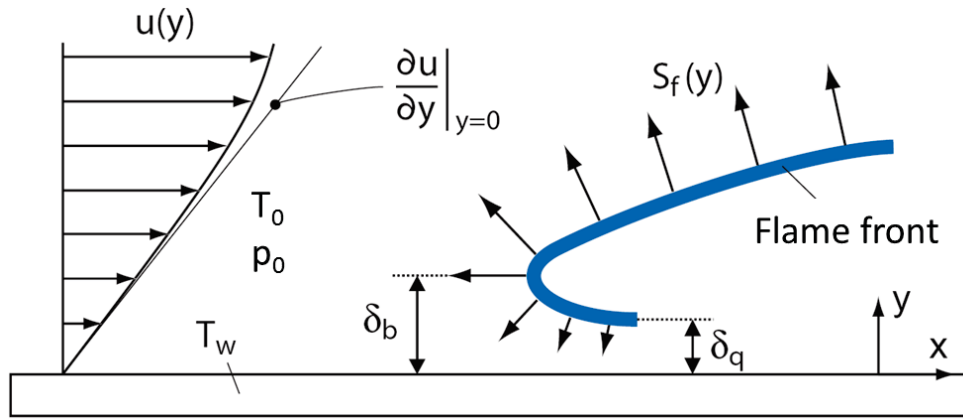


Figure 1.1: Critical velocity gradient model for laminar boundary layer flashback [29, 84]

wall and δ_b , Lewis and von Elbe expressed the flashback condition in terms of a critical velocity gradient g_c as is shown in Eq. (1.1).

$$g = \frac{\partial u}{\partial y} \Big|_{y=0} = \frac{|\tau_w|}{\mu_0} = g_c = \frac{S_f(\delta_b)}{\delta_b} \quad (1.1)$$

In Eq. (1.1), τ_w is the wall shear stress and μ_0 is the dynamic viscosity of the fresh gas mixture. The critical gradient concept implies that flashback occurs when the velocity gradient in the approaching flow falls below a certain critical value g_c . It is apparent that the critical gradient concept does not take into account any mutual interaction of flame and flow. The validity of this assumption will be discussed later. Furthermore, it must be pointed out that Eq. (1.1) is not capable of predicting g_c , because $S_f(y)$ is influenced to an unknown extent by heat exchange with the wall and by flame stretch effects. Thus, the critical gradients must be determined experimentally for different fuels, mixture compositions, temperatures, pressures, etc., because all of these variables affect $S_f(y)$ and δ_b .

Although the critical gradient concept was originally developed for laminar flames, it is also generally applied to turbulent flames. The model was extended by Wohl et al. [132] who performed detailed work on the flame structure and derived expressions for quenching and penetration distances. Putnam et al. [102] proposed a non-dimensional form of the critical gradient model by introducing a correlation between the Peclet number Pe of the flow and that of the flame. Nevertheless, due to its simplicity and convenient applicability the original form of the gradient model remained the classical way

to correlate flashback data and has been used in the majority of all flashback investigations in the literature. A study of France [38] qualitatively confirmed the validity of the model. He investigated the influence of flow development on flashback resistance for different fuels by varying the length-to-diameter ratio L/d of the burner tubes within $L/d=0.1-100$. The experiments revealed that the flashback resistance decreases with increasing L/d for a given flow rate, because the wall friction τ_w decreases as long as the flow profile develops toward its fully developed shape.

Extensive research has been dedicated to determine the critical velocity gradients for a variety of different fuels, burner geometries and operating conditions. Grumer et al. [45–51], van Krevelen et al. [70], Caffo et al. [18], Ball et al. [3] and Putnam et al. [103] conducted several tube burner studies to evaluate the flashback propensity of various hydrocarbon fuels and fuel mixtures, which partly contained hydrogen. Davu et al. [25] specifically investigated syngas (blends of hydrogen and carbon oxides) flames with varying hydrogen content and found that the Lewis number Le^1 of the fuel plays an important role in the determination of the critical gradients. Other alternative fuels, such as biomass gasification products, were examined by Fox et al. [37]. In the course of fuel flexibility and interchangeability these studies are of high relevance to the gas turbine industry [98].

Bollinger et al. [14] investigated the effect of burner tip temperature on flashback of turbulent hydrogen-oxygen flames using tubes with different diameters, materials and wall thicknesses. They observed a qualitative relationship between these variables and the flashback propensity, which was concluded to be a result of varying tip temperatures. Similar conclusions were drawn by Sogo et al. [114], who were one of the few groups that used optical measurement techniques to study flashback. They examined lean methane-air flames with Particle Image Velocimetry (PIV) and showed that the tip temperature influences flame stretch rates and heat flux to the burner and thus affects the flashback stability. In a recent study, Shaffer et al. [111] confirmed the relationship between flashback propensity and the thermal conditions near the burner rim. They showed that the tip temperature measured at flashback onset of various fuel compositions is strongly correlated with the critical velocity gradient. In addition, numerical work performed by Lee et al. [80] and Kur-

¹The Lewis number $Le = a/D$ is the ratio of the thermal diffusivity a to the mass diffusivity D .

dyumov et al. [74–76] revealed the significant role of the flame-wall heat transfer interaction on boundary layer flashback. These are important findings as they demonstrate that controlling the burner tip temperature during flashback tests is essential for obtaining reproducible results.

A more detailed and comprehensive summary of the literature on laminar and turbulent flashback, including numerical studies, is given in [29]. In summary, most of the studies involved hydrocarbon fuels and mixtures of hydrocarbons with hydrogen. The present work focuses on pure hydrogen-air flames, whose thermo-physical and chemical properties make flashback prevention particularly challenging. Therefore, flashback data from literature for laminar [33] and turbulent [35, 64] H₂-air flames at atmospheric pressure and ambient temperature are summarized in Fig. 1.2. All data were collected with tube burners of different size and the flames were stabilized in the free atmosphere at the tube exit, i.e. the stable flames were unconfined. The following observations can be made along with first conclusions based on the critical velocity gradient concept:

- Both for laminar and for turbulent conditions the peak values for g_c are shifted toward slightly rich conditions, around $\Phi=1.5$. This can be explained by Eq. (1.1) when taking into account that the laminar flame speed has a maximum around $\Phi=1.5$, whereas the quenching distance δ_q and the flame thickness δ_f are minimal [119].
- Up to $\Phi \approx 1.5$ the flashback propensity of turbulent flames in terms of g_c is approximately three times higher than that of laminar flames. This can be qualitatively explained by the higher flame speed of turbulent flames. Moreover, turbulence enhances species and heat transport processes near the wall such that δ_q and probably also δ_b decrease. Additionally, so-called low-speed streaks (cf. Sec. 2.1.1) near the wall may facilitate flashback in turbulent flow.
- The turbulent flashback data for different tube diameters collapse very well, except for near-stoichiometric mixtures, where the scatter of the flashback limits is relatively large. Smaller tube diameters seem to implicate higher critical gradients. However, the data base is rather small. The influence of the tube diameter is further discussed in Ch. 5.

Fine investigated the influence of mixture preheating [36] and pressure [34,35]

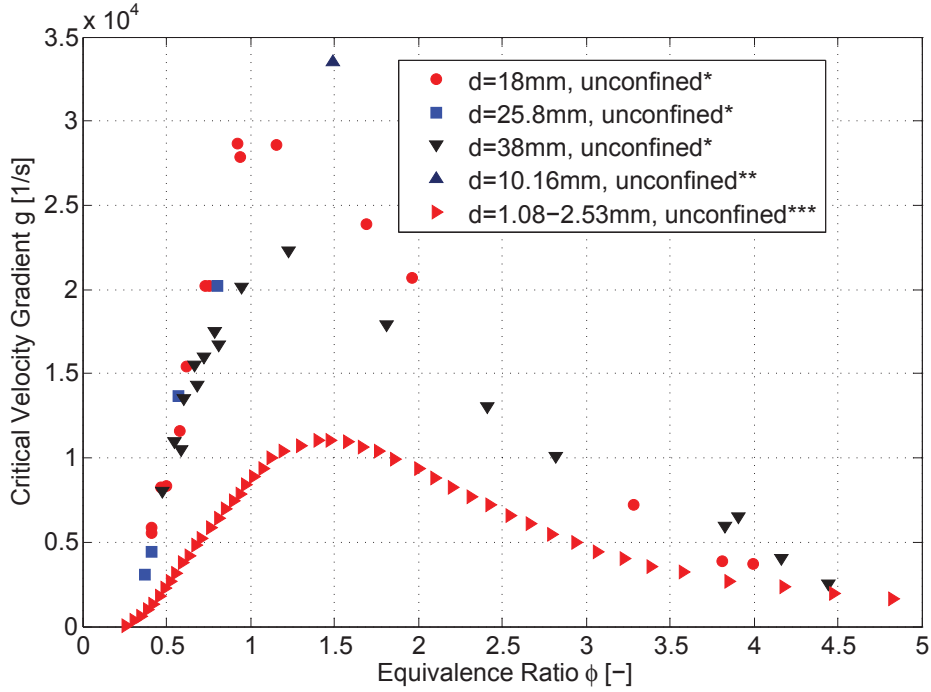


Figure 1.2: Critical velocity gradients for unconfined laminar and turbulent hydrogen-air flames, [64]*, [35]**, [33]***

on the flashback limits for laminar and turbulent H_2 -air combustion. The pressure influence was investigated from sub-atmospheric pressures up to atmospheric pressure. Equations (1.2) and (1.3) demonstrate how the critical velocity gradients scale with the preheating temperature and the pressure, respectively.

$$g_{c,H_2-air} \propto T^{1.5} \quad (1.2)$$

$$g_{c,H_2-air} \propto p^{1.35} \quad (1.3)$$

The power exponents in the equations are approximately the same for both laminar and turbulent flow. Furthermore, it turned out in the investigations that pressure and preheating temperature affect the flashback limits independently of each other. However, it should be noted that Eq. (1.2) has been devised only from experiments with H_2 -air mixtures at an equivalence ratio of $\Phi=1.5$ and Eq. (1.3) becomes inaccurate for Φ considerably smaller than unity. As a result, the validity of the correlations in the lean combustion regime is questionable.

In summary, the critical gradient concept as derived from the flame-flow situation depicted in Fig. 1.1 has been used extensively in the literature. Although the model is very useful in terms of correlating flashback tendencies for various fuels and operating conditions, a particular weakness of the model has already been detected in the early stages of flashback research. Dugger et al. [28] measured balancing distances δ_b for laminar propane-air flames and found that they are much smaller than the respective quenching distances δ_q . Similar observations were made by Berlad et al. [9] for various fuels and by Schäfer et al. [109] for kerosene-air flames. Since this would imply that the flame propagates upstream within the quenching distance above the wall, where a flame cannot be sustained, Dugger et al. commented that the backpressure of the flame (cf. Ch. 2.2.4) might alter the velocity gradient, i.e. the velocity profile, of the approaching flow. It will be elaborated on this potential interaction of the flame with the flow in the next section.

1.1.2 Recent Findings on Boundary Layer Flashback of Confined Flames

In a previous Ph.D. project at the Lehrstuhl für Thermodynamik, Eichler [29] conducted flashback experiments with laminar and turbulent flames using a channel burner setup. The premixing duct had a rectangular cross-section with high aspect ratio. Contrary to all the flashback studies presented in Sec. 1.1.1 the flame was not burning in the free atmosphere at the duct exit, but it was stabilized inside the duct by means of a hot ceramic tile that was mounted flush with the surrounding wall. That is, the flame was already confined inside the channel duct in stable mode. Applying advanced optical measurement techniques Eichler found that there is a distinct interaction between the stable flame and the approaching flow, which leads to flow separation and the associated formation of backflow regions directly upstream of the flame. This in turn has a huge negative impact on the flashback stability. He could confirm this observation for a confined, laminar H_2 -air flame burning in a flat plate boundary layer by means of a Direct Numerical Simulation (DNS). Recently, Gruber et al. [44] performed a computationally very expensive DNS of the flashback process of a turbulent, confined channel flame and they also observed flow stagnation and backflow regions. This is a very important finding because real burner applications must be flashback-safe even if a flame accidentally enters the fuel supply duct, for instance, due to an intermittent

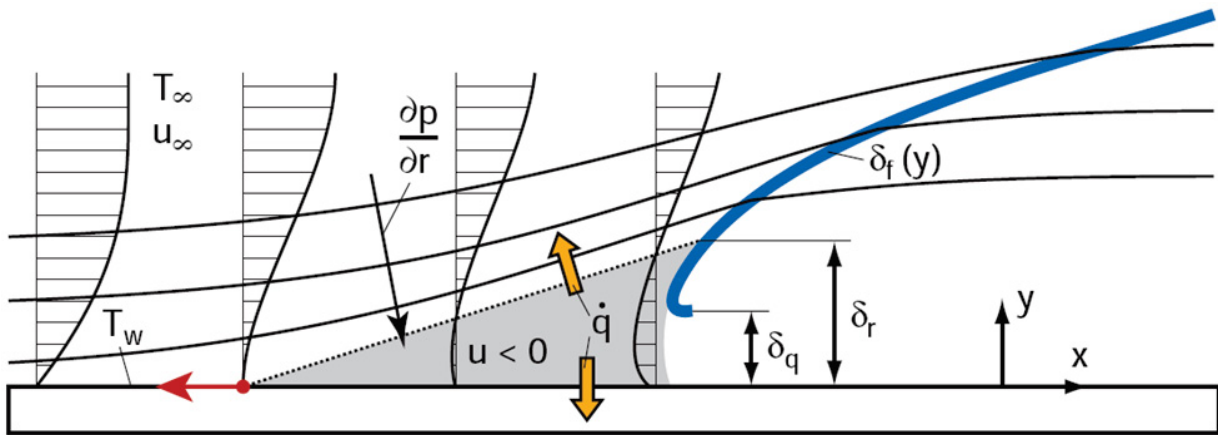


Figure 1.3: Boundary layer flashback model for confined flames [29]

velocity drop or due to self-ignition. In these cases it must be ensured that the flame is washed out instead of propagating further upstream.

Based on this finding, Eichler developed a new flashback model for confined flames, because the critical gradient model - in spite of reflecting a situation that coincides exactly with that of a confined flame rather than with that of a freely burning flame - does not account for the observed flame-flow interaction. The new model is shown in Fig. 1.3. Similar to Fig. 1.1 the flame with thickness δ_f and the quenching distance δ_q are depicted on the right. The development of the flow profile as it approaches the flame is depicted to the left of it. As a result of the flame backpressure the streamlines are deflected away from the wall (in positive y -direction) and a backflow region with maximum height δ_r is formed. In the latter, heat \dot{q} is transferred to the wall and to the external streamlines. According to Eichler, the flame can only propagate upstream if it is anchored inside the backflow and if δ_r is greater than δ_q , i.e. a backflow region must exist. This is a somewhat misleading conclusion, because on the one hand, backflow might indeed exist without the flame flashing back, for instance when δ_r is considerably smaller than δ_q . On the other hand, due to its consumption speed the flame might already be able to propagate upstream upon sufficient retardation of the approaching flow without backflow regions existing, i.e. without flow separation taking place. This situation is discussed in detail in Chs. 7 and 8.

Furthermore, Eichler studied confined flames in diverging channel ducts, i.e. the approaching flow experienced an adverse pressure gradient in streamwise direction. He found that this further increases the flashback propensity, which

is in agreement with the proposed model, because adverse pressure gradients facilitate boundary layer separation. It is again emphasized that the critical gradient model shown in Fig. 1.1 does not account for such a different pressure boundary condition in any way.

1.2 Scope of the Project and Structure of the Thesis

As became obvious in the literature review, the critical gradient model developed by Lewis and von Elbe does not correctly represent the conditions during flashback of a confined flame. The same applies to flashback of an initially unconfined flame, because the position of the flame relative to the approaching flow in Fig. 1.1 is entirely different. In real combustion systems, e.g. in gas turbines, the flame is usually stabilized at the transition between the combustion chamber and the fuel(-air) injector. The latter is also referred to as *burner* or *premixing duct* in the rest of the thesis. Consequently, the flame is unconfined in its stable position. A flashback model correctly capturing the transition from stable, unconfined flame mode to flashback is missing. From a practical point of view the following unresolved issues require additional research as they have not been adequately addressed in the past:

- Influence of the burner exit design, i.e. the flame holding mechanism, on flashback.
- Influence of low to moderate swirl on boundary layer flashback.
- Flashback propensity of preheated hydrogen-air flames in the lean combustion regime.
- Methodologies to increase the flashback stability, i.e. to increase the safe operating range of premixed combustion systems.

Based on these points, the scope of the present project was to study flashback in rotationally symmetric applications for a variety of different operating conditions. More specifically, the influence of flame holding configuration, burner material, swirl intensity, and mixture preheating on the flashback propensity of hydrogen-air flames was investigated. Furthermore, the effect of boundary layer air injection on flashback initiation and upstream flame propagation was examined. In addition, microscopic measurements were performed

to reveal the mechanisms involved during the transition from stable flame to flashback. Based on the outcome of this research the existing flashback model was revised. Special effort was made toward conducting all the experiments under well-defined boundary conditions in order to be able to assess the exclusive effect of only one parameter at a time. The latter mainly involved precise temperature control of burner components during operation as well as characterizing the isothermal flow fields (see Ch. 4).

The outline of the thesis is as follows:

Chapter 2 covers the basics of isothermal and reactive flows that are important for the understanding and the analysis of the experimental results. In Ch. 3 the experimental infrastructure and flashback test procedure along with the measurement techniques employed are described. Chapter 4 deals with the isothermal flow fields in the different test setups. The macroscopic flashback behavior of turbulent hydrogen-air flames is investigated for a number of different burner and flame holding configurations in Ch. 5 and for different operating conditions in Ch. 6. A detailed, microscopic study on the onset of flashback for an unconfined flame is presented in Ch. 7, followed by a theoretical analysis of the flashback behavior of unconfined and confined flames in Ch. 8, where also an improved flashback model for unconfined flames is introduced. In the last chapter, the main aspects of the thesis are summarized along with conclusions and guidelines for flashback-safe design of practical burners.

2 Basics of Isothermal and Reactive Flows

This chapter deals with the basics of isothermal and reactive flows, which are crucial for the analysis and interpretation of the subsequent flashback experiments.

2.1 Fluid Flow

Both computational flow simulations and experimental flows will be treated later in this thesis. Therefore, this section provides the necessary background knowledge, starting with general three-dimensional flows toward two-dimensional boundary layer flows and how the different flows can be described numerically, e.g. by means of turbulence models. Unless otherwise stated, the following content is based on the works of Munson et al. [94], Schlichting [110], and White [128].

Generally, any type of fluid flow can be fully described mathematically by a system of interdependent, inhomogeneous, non-linear, partial differential equations. These equations are the results of a differential balance of mass, momentum, and energy acting on a locally fixed, infinitesimal flow control volume. Using Stoke's approach for the shear stress tensor and neglecting body forces yields the Navier-Stokes equations (NSE). The following derivations are performed for incompressible Newtonian fluids under steady-state conditions. These are reasonable simplifications regarding the simulations of the isothermal burner flow upstream of the reaction zone in the later chapters, because the flow velocities are relatively low ($Ma \ll 0.3$) and transient behavior is not considered. The resulting expressions for mass and momentum conservation are shown in Eqs. (2.1)-(2.4).

$$\frac{\partial u}{\partial x} + \frac{\partial v}{\partial y} + \frac{\partial w}{\partial z} = 0 \quad (2.1)$$

$$u \frac{\partial u}{\partial x} + v \frac{\partial u}{\partial y} + w \frac{\partial u}{\partial z} = -\frac{1}{\rho} \frac{\partial p}{\partial x} + \nu \left[\frac{\partial^2 u}{\partial x^2} + \frac{\partial^2 u}{\partial y^2} + \frac{\partial^2 u}{\partial z^2} \right] \quad (2.2)$$

$$u \frac{\partial v}{\partial x} + v \frac{\partial v}{\partial y} + w \frac{\partial v}{\partial z} = -\frac{1}{\rho} \frac{\partial p}{\partial y} + \nu \left[\frac{\partial^2 v}{\partial x^2} + \frac{\partial^2 v}{\partial y^2} + \frac{\partial^2 v}{\partial z^2} \right] \quad (2.3)$$

$$u \frac{\partial w}{\partial x} + v \frac{\partial w}{\partial y} + w \frac{\partial w}{\partial z} = -\frac{1}{\rho} \frac{\partial p}{\partial z} + \nu \left[\frac{\partial^2 w}{\partial x^2} + \frac{\partial^2 w}{\partial y^2} + \frac{\partial^2 w}{\partial z^2} \right] \quad (2.4)$$

In Eqs. (2.1)-(2.4), u , v and w are the velocity components in x-, y- and z-direction, respectively, ρ is the fluid density, ν the kinematic viscosity, and p the pressure. For a detailed derivation of the NSE and their treatment for different flows the reader is referred to the literature, e.g. [94, 110, 128].

The focus in this work is on turbulent flows, which are characterized by high Reynolds numbers Re . The latter are a measure for the ratio of inertial to viscous forces acting on a fluid.

$$Re = \frac{uL}{\nu} \quad (2.5)$$

In Eq. (2.5), u is the streamwise velocity and L is a characteristic dimension of the flow geometry. For instance, the critical Reynolds number for both tube flow and channel flow is $Re_c \approx 2300$, with the characteristic length being the tube diameter d and the channel height h , respectively. The inherent character of turbulent flow is that the local velocity vector $\vec{u}(\vec{x}, t)$ stochastically fluctuates over time. Solving the NSE for technical flows, which are mostly characterized by complicated flow geometries and high turbulence intensities, requires extreme computational effort and usually exceeds the resources available. Therefore, it is common practice to apply a statistical approach, where the velocity vector is divided into a time-averaged term $\langle u \rangle$ and a fluctuating term u' as is shown in Einstein notation in Eq. (2.6).

$$u_i(\vec{x}, t) = \langle u_i \rangle(\vec{x}, t) + u'_i(\vec{x}, t) \quad (2.6)$$

Per definition, the following expressions apply to Eq. 2.6:

$$\lim_{\Delta t \rightarrow \infty} \left(\frac{1}{\Delta t} \int_{t_0}^{t_0 + \Delta t} u_i dt \right) = \langle u_i \rangle \quad \text{and} \quad \langle u'_i \rangle = 0 \quad (2.7)$$

This approach is referred to as *Reynolds decomposition*. The dimensionless turbulence intensity Tu is defined as

$$Tu = \frac{1}{\langle u \rangle} \sqrt{\frac{1}{3} (\langle u'^2 \rangle + \langle v'^2 \rangle + \langle w'^2 \rangle)}. \quad (2.8)$$

Characteristic for turbulent flow is the formation of eddies, whose sizes cover a wide range of length scales. The size of the largest eddies corresponds to the characteristic length L of the geometry. They are described by the integral length scale l_t . These eddies are unstable and successively break up into smaller ones until they reach their minimum size, which is characterized by the Kolmogorov length scale l_η . In this way the turbulent kinetic energy k of the large eddies is successively transferred to smaller eddies until it is dissipated by molecular viscosity in the Kolmogorov eddies.

Inserting Eq. (2.6) into Eqs. (2.1)-(2.4) yields the Reynolds-Averaged Navier-Stokes (RANS) Equations, which are shown in Eqs. (2.9) and (2.10).

$$\frac{\partial \langle u_i \rangle}{\partial x_i} = 0 \quad (2.9)$$

$$\langle u_j \rangle \frac{\partial \langle u_i \rangle}{\partial x_j} = -\frac{1}{\rho} \frac{\partial \langle p \rangle}{\partial x_i} + \nu \frac{\partial^2 \langle u_i \rangle}{\partial x_j^2} - \frac{\partial \langle u'_i u'_j \rangle}{\partial x_j} \quad (2.10)$$

As can be seen, apart from the appearance of the term $\langle u'_i u'_j \rangle$ in the momentum equation, the NSE have not changed significantly. This term is referred to as Reynolds-Stress tensor. Since the fluctuating velocity has been replaced by its time-averaged value in Eq. (2.10), the Reynolds-stress tensor can be seen as an additional term that accounts for the influence of turbulence on the flow. This additional term leads to the well-known RANS closure problem, because the number of unknowns (three velocity components, pressure, and stress tensor) exceeds the number of available equations (one for mass conservation and three for momentum conservation). In order to close this system of equations, the Reynolds-Stress Tensor needs to be adequately modeled. The most common and verified modelling approach is based on the eddy viscosity hypothesis, where a proportionality between the Reynolds stresses and the derivatives of the mean flow variables is assumed.

$$-\langle u'_i u'_j \rangle = \nu_t \left(\frac{\partial \langle u_i \rangle}{\partial x_j} + \frac{\partial \langle u_j \rangle}{\partial x_i} \right) - \frac{2}{3} \delta_{ij} k \quad (2.11)$$

In Eq. (2.11), δ_{ij} is the Kronecker delta, ν_t the turbulent viscosity, and k the turbulent kinetic energy. Inserting Eq. (2.11) into Eq. (2.10) results in the following expression:

$$\langle u_j \rangle \frac{\partial \langle u_i \rangle}{\partial x_j} = -\frac{1}{\rho} \frac{\partial \langle p \rangle}{\partial x_i} + \nu \frac{\partial^2 \langle u_i \rangle}{\partial x_j^2} + \nu_t \left(\frac{\partial^2 \langle u_i \rangle}{\partial x_j^2} + \frac{\partial^2 \langle u_j \rangle}{\partial x_i \partial x_j} \right) - \frac{2}{3} \delta_{ij} \frac{\partial k}{\partial x_j} \quad (2.12)$$

It must be noted that ν_t is not a physical viscosity, but an artificial quantity that needs to be modeled again. For this purpose, a number of different eddy viscosity models have been developed. The most common turbulence models, which are also relevant for the current work, are briefly described below. All of them are so-called two-equation models where two coupled transport equations are solved, which describe the turbulence by means of characteristic velocity and length scales. A comprehensive overview of turbulence models is provided in [131].

- The k - ϵ model relates the turbulent viscosity ν_t to the turbulent kinetic energy k and the turbulent dissipation rate ϵ (rate of dissipation of the turbulent kinetic energy). The resulting transport equations for k and ϵ contain a number of constants that have been determined through data fitting for a wide range of turbulent flows. The underlying assumption of this model is isotropic turbulence, which makes it ideal for non-swirling shear-free flows.
- The k - ω model relates the turbulent viscosity to the turbulent kinetic energy k and the turbulent frequency ω (characteristic frequency of the energy-dissipating eddies). The constants in the resulting equations are determined in a similar manner as in the k - ϵ model. The k - ω model is superior in flows with anisotropic turbulence, e.g. in boundary layer flows.
- In technical flows there are often both regions with isotropic turbulence and regions with anisotropic turbulence, for instance in tube flow. The Shear-Stress-Transport (SST) model combines the advantages of the k - ω

and the k - ϵ model. Depending on the flow region it switches between the two models using appropriate blending functions.

2.1.1 Boundary Layer Flow

Boundary Layer flows are particularly relevant for the current work, because flashback took place in the low-velocity region close to the wall in the majority of the experiments presented later. To gain better insight into these flows, Prandtl [101] non-dimensionalized the NSE and performed order of magnitude estimations with the remaining terms. Given that the boundary layer thickness δ is small compared to the characteristic dimensions of the geometry, the following simplifications can be made for $Re \gg 1$ (z-direction is neglected):

$$u \gg v \quad (2.13)$$

$$\frac{\partial u}{\partial y} \gg \frac{\partial u}{\partial x} \quad (2.14)$$

$$\frac{\partial v}{\partial y} \gg \frac{\partial v}{\partial x} \quad (2.15)$$

In Eqs. (2.13)-(2.15) x is the wall-parallel, streamwise coordinate, and y is the wall-normal coordinate. Applying these simplifications to the NSE (Eqs. (2.1)-(2.4)) and neglecting low-order terms yields

$$\frac{\partial p}{\partial y} = 0 \quad (2.16)$$

for the momentum equation in y -direction. Consequently, the pressure does not vary across the boundary layer thickness and is therefore determined by the freestream. Based on this, the momentum equation in x -direction can be written as

$$u \frac{\partial u}{\partial x} + v \frac{\partial u}{\partial y} = -\frac{1}{\rho} \frac{dp}{dx} + \nu \frac{\partial^2 u}{\partial y^2}. \quad (2.17)$$

Compared to the full NSE, Prandtl's boundary layer equations are considerably simpler to solve. For laminar flow without pressure gradients, Blasius [10] provides an exact analytic solution, which is not shown here. He found that the velocity profile in the laminar boundary layer is linear directly at the

wall within approx. 30 % of the boundary layer thickness. For turbulent flows, Reynold's decomposition of the velocity vector (cf. Eq. (2.6)) can again be applied to the NSE in order to derive the boundary layer equations. Using the assumptions in Eqs. (2.13)-(2.15) the resulting expressions for mass and momentum conservation are as follows:

$$\frac{\partial \langle u \rangle}{\partial x} + \frac{\partial \langle v \rangle}{\partial y} = 0 \quad (2.18)$$

$$\langle u \rangle \frac{\partial \langle u \rangle}{\partial x} + \langle v \rangle \frac{\partial \langle u \rangle}{\partial y} = -\frac{1}{\rho} \frac{\partial p_\infty}{\partial x} + \nu \frac{\partial^2 \langle u \rangle}{\partial y^2} - \frac{\partial \langle u'v' \rangle}{\partial y} \quad (2.19)$$

$$0 = -\frac{1}{\rho} \frac{\partial p_\infty}{\partial y} - \frac{\partial \langle v'^2 \rangle}{\partial y} \quad (2.20)$$

Integration of Eq. (2.20) over the boundary layer thickness δ yields:

$$\langle p(y) \rangle + \rho \langle v'^2 \rangle = p_\infty \quad (2.21)$$

Since $\langle v'^2 \rangle$ vanishes at the wall and in the non-turbulent freestream, the mean pressure at the wall and in the freestream are identical. However, in between, the pressure can vary and is thus a function of y within the boundary layer thickness. Solutions can be obtained from RANS, where the turbulent shear terms in the momentum equations need to be modeled. Only for very simple cases, approximate analytic solutions can be obtained [110].

In the literature turbulent boundary layers are usually divided into three regions - the inner region directly next to the wall, the overlap layer, and the outer region. In these regions, the velocity profile is correlated by the non-dimensional, wall-parallel velocity u^+ and by the non-dimensional wall coordinate y^+ .

$$u^+ = \frac{u}{u_\tau}, \quad y^+ = \frac{y}{\nu} u_\tau \quad (2.22)$$

The shear stress velocity u_τ can be calculated through Eq. (2.23).

$$u_\tau = \sqrt{\frac{\tau_W}{\rho}} \quad (2.23)$$

- In the **inner region**, viscous shear is dominating. It is further divided into the laminar sublayer ($y^+ \leq 5$), where

$$u^+ = y^+, \quad (2.24)$$

and the buffer layer ($5 < y^+ < 30$), where the linear relation between u^+ and y^+ merges with the subsequent logarithmic region.

- In the **overlap layer** ($30 \leq y^+ \leq 350$), both viscous and turbulent shear are important. The so-called logarithmic *law-of-the-wall* applies, which is widely used in the literature and in CFD codes.

$$u^+ = \frac{1}{\kappa} \ln y^+ + B \quad (2.25)$$

The empirically determined constants $\kappa=0.41$ and $B=5.0$ are also adopted in the present work.

- In the **outer region** ($y^+ > 350$) turbulent shear dominates and the velocity profile depends on the pressure gradient in the freestream (U_∞), as is indicated in the so-called *velocity defect law*:

$$\frac{U_\infty - u}{u_\tau} = f(p) \quad (2.26)$$

It is important to note that these regions describe the time-averaged behavior of a turbulent boundary layer, whereas the time-resolved structure is characterized by the existence of small-scale and large-scale coherent structures. For instance, characteristic elongated zones continuously form and disappear next to the wall, in which the fluid velocity is below or above the time-mean velocity. Those are often referred to as low-speed streaks and high-speed streaks, respectively [113]. For a comprehensive treatment of the time-resolved phenomena in turbulent flow the reader is referred to the literature [105, 106].

For practical purposes, the boundary layer thickness δ is usually defined as the distance from the wall where the axial velocity u has reached 99% of its freestream value U_∞ (cf. Fig. 2.1).

$$\delta = y \Big|_{u=0.99U_\infty} \quad (2.27)$$

The shape of the boundary layer profile can be characterized by three other parameters:

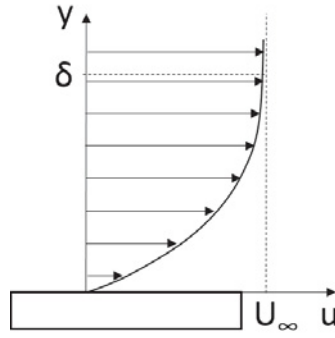


Figure 2.1: Boundary layer flow over a solid wall

1. The **displacement thickness** δ_1 is a measure for how far the streamlines are deflected away from the solid surface in boundary layer flow (compared to inviscid potential flow for the same configuration).

$$\delta_1 = \int_0^\infty \left(1 - \frac{u}{U_\infty}\right) dy \approx \int_0^\delta \left(1 - \frac{u}{U_\infty}\right) dy \quad (2.28)$$

2. The **momentum thickness** δ_2 is a measure for the momentum loss through friction in boundary layer flow (compared to inviscid potential flow for the same configuration).

$$\delta_2 = \int_0^\infty \frac{u}{U_\infty} \left(1 - \frac{u}{U_\infty}\right) dy \approx \int_0^\delta \frac{u}{U_\infty} \left(1 - \frac{u}{U_\infty}\right) dy \quad (2.29)$$

3. The **kinetic energy thickness** δ_3 is a measure for the kinetic energy loss in boundary layer flow (compared to inviscid potential flow for the same configuration).

$$\delta_3 = \int_0^\infty \frac{u}{U_\infty} \left(1 - \left(\frac{u}{U_\infty}\right)^2\right) dy \approx \int_0^\delta \frac{u}{U_\infty} \left(1 - \left(\frac{u}{U_\infty}\right)^2\right) dy \quad (2.30)$$

Based on these three parameters, the so-called shape factors H_{12} and H_{32} can be calculated, which are indicators for the nature of the boundary layer.

$$H_{12} = \frac{\delta_1}{\delta_2} \quad (2.31)$$

$$H_{32} = \frac{\delta_3}{\delta_2} \quad (2.32)$$

In laminar boundary layer flow without pressure gradient (*laminar Blasius boundary layer*), $H_{12}=2.59$ and $H_{32}=1.57$. In turbulent boundary layers without pressure gradient, $H_{12} \approx 1.3-1.5$ and $H_{32} \approx 1.7-2.0$. The shape factors can also be used to judge whether flow separation is imminent. The corresponding values for laminar flow are $H_{12}>4$ and $H_{32}<1.515$ [110]. For turbulent flow the limits are approximately $H_{12}>1.8-2.4$ and $H_{32}<1.46$ [20], with the exact position of separation onset being a little more vague (cf. Sec. 2.1.2).

2.1.2 Boundary Layer Separation

The low-velocity, low-momentum fluid in boundary layers is particularly susceptible to the influence of adverse pressure gradients. That is, flow reversal can occur when a certain adverse pressure gradient is exceeded. This is referred to as *flow separation*. As illustrated in Fig. 2.2, the boundary layer thickness δ quickly increases upon separation. The instantaneous separation point is defined as the location where the wall shear stress τ_w vanishes. Taking into consideration that $\partial v/\partial x \ll \partial u/\partial y$ yields:

$$\tau_w = \left. \frac{\partial u}{\partial y} \right|_{y=0} = 0 \quad (2.33)$$

It is worth noting that compared to laminar flow, separation in turbulent flow is not a sudden event, but rather a gradual process of temporary separation and reattachment, until complete separation occurs at a certain position [112]. Thus, turbulent boundary layer separation is difficult to predict, which also explains the variation in the critical shape factors H_{12} and H_{32} (cf. Sec. 2.1.1).

Stratford [115] developed a relatively simple criterion to predict the position of flow separation. He divided the turbulent boundary layer, which is subjected to an adverse pressure gradient, into two regions. His main assumptions were that the shear forces in the outer region are small compared to the inertia forces or the pressure gradient. Therefore, the pressure rise only causes a lowering of the dynamic head profile, whereas the shape of the profile stays approximately unchanged (cf. Fig. 2.3). In the inner region, the inertia forces are considered small such that the pressure gradient is balanced by the gradient of the shear stress. Along with a joining condition that assures a smooth

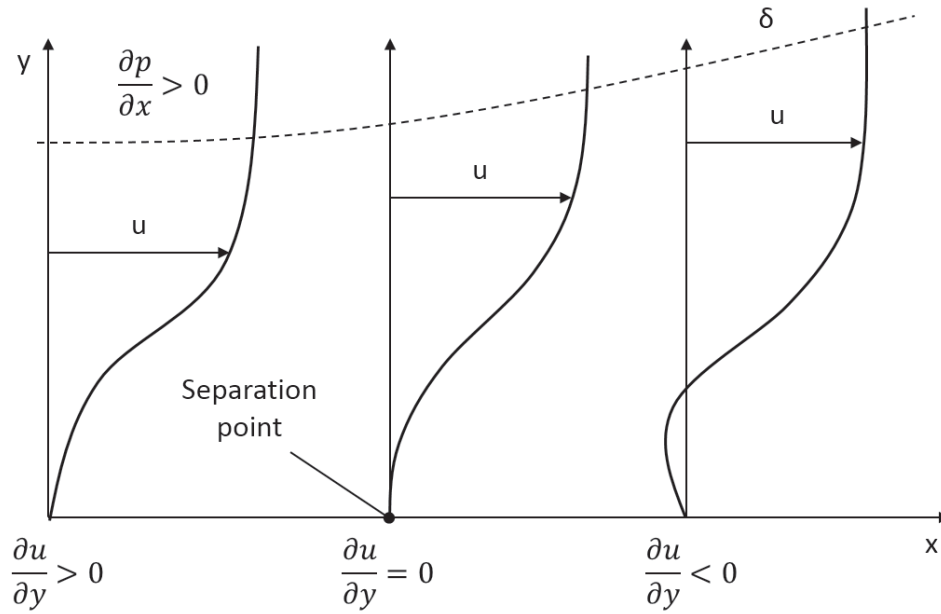


Figure 2.2: Boundary layer separation due to an adverse pressure gradient

transition of u and $\partial u/\partial y$ between inner and outer region, he derived the following criterion for flow separation in turbulent boundary layers:

$$(2C_p)^{0.25(n-2)} \left(x \frac{dC_p}{dx} \right)^{0.5} = 1.06\beta (10^{-6} Re)^{0.1} \quad (2.34)$$

The empirically determined factor β in Eq. (2.34) slightly depends on the second derivative of the pressure, with $\beta=0.66$ for $d^2p/dx^2 < 0$ and $\beta=0.73$ for $d^2p/dx^2 \geq 0$. The exponent n slightly varies with the Reynolds number at the separation point, but usually assumes values between $n=6$ ($Re \leq 10^6$) and $n=8$ ($Re > 10^8$). The non-dimensional pressure coefficient C_p and the local Reynolds number Re in the equation are calculated as follows (with p_0 being the pressure before the adverse pressure gradient starts, cf. Fig. 2.4):

$$C_p(x) = \frac{p(x) - p_0}{\frac{1}{2}\rho U_\infty^2} \leq \frac{4}{7}, \quad Re(x) = \frac{U_\infty x}{\nu} \quad (2.35)$$

The limitation $C_p \leq 4/7$ formally results from the joining condition at the transition between inner and outer region. As can be seen from Eq. (2.34), the separation propensity is determined by the integral adverse pressure distribution $C_p(x)$, the local pressure gradient dC_p/dx and the cumulated distance x over

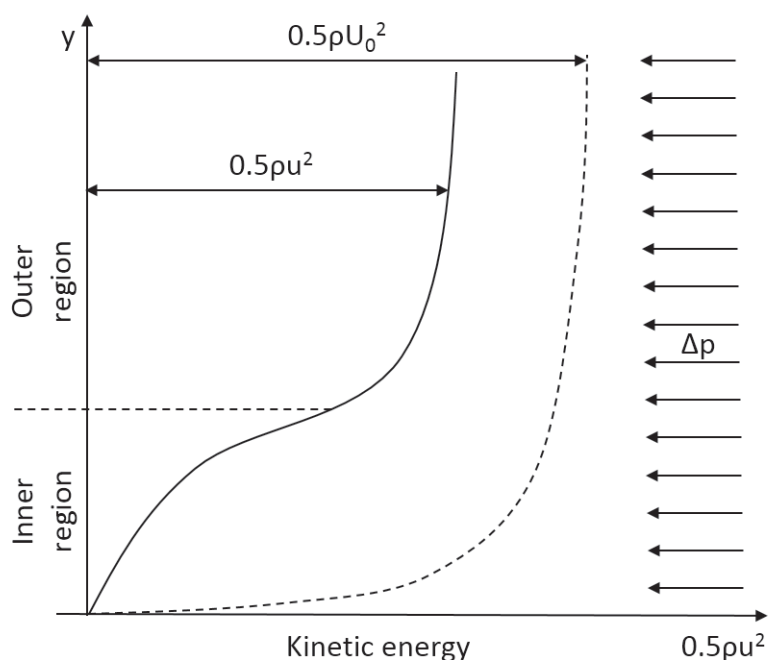


Figure 2.3: Influence of an adverse pressure gradient on boundary layer flow according to Stratford [115]

which the adverse pressure gradient acts. The equation is valid for fully developed turbulent flow with the pressure rise starting at the position $x=0$. If there is a region of laminar flow, or flow with a favorable pressure gradient, x must be replaced by $(x - x')$ in Eqs. (2.34) and (2.35), i.e. a 'false origin' x' of the pressure rise is assumed in the calculations. Details on the determination of x' can be found in [20]. The Stratford criterion assumes that the pressure continuously increases in streamwise direction, such that the coordinate x that fulfills Eq. (2.34) is the separation position x_{sep} . If the pressure stagnates or decreases before the criterion is fulfilled, the flow does not separate.

Cebeci et al. [20] compared the Stratford criterion with three other methods for the prediction of separation in turbulent boundary layers – Head's method [54], Goldschmied's method [41], and the Cebeci-Smith method [19]. These three methods are very briefly described below:

- **Goldschmied's separation criterion** is based on a certain value for C_p , above which separation is predicted. Thus, this criterion does not take into account any details of the pressure rise, for instance, the shape of the pressure distribution.

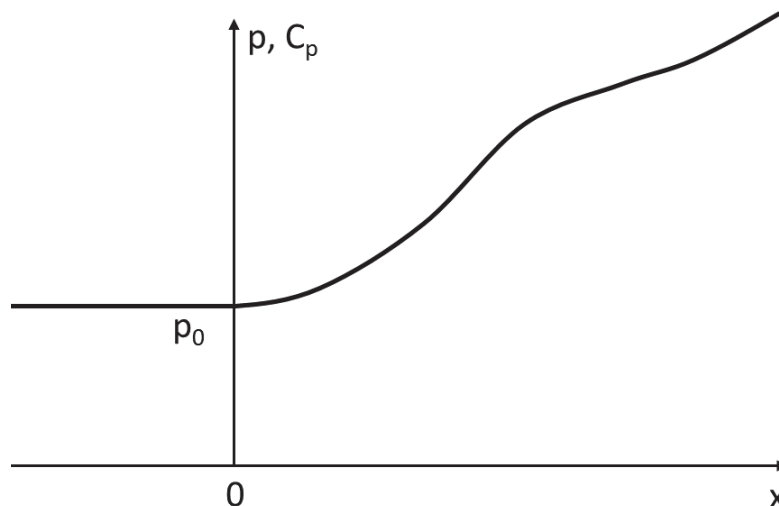


Figure 2.4: Schematic of the qualitative pressure distribution assumed in the Stratford model

- **Head's method** is an integral method that takes full account of the shape of the pressure rise. It uses a momentum integral equation with approximations for the calculation of wall friction (Ludwig-Tillman expression) and expressions for the boundary layer shape factor H (cf. Sec. 2.1.1). Separation is predicted when the shape factor H exceeds a certain value. Separation is assumed to exist when H is between 1.8 and 2.4.
- The **Cebeci-Smith method** is a differential method, which takes full account of the shape of the pressure distribution. It directly uses the zero-wall-shear-stress condition as the separation parameter.

Cebeci et al. applied all four criteria to different test flows and concluded that all methods except Goldschmied's method are suitable for the prediction of turbulent boundary layer separation, with Stratford's method being slightly conservative, i.e. separation is mostly predicted somewhat too early. Stratford himself stated that the separation point is likely to be predicted between 0 and 10% too early. However, compared to Head's method and the Cebeci-Smith method, the Stratford criterion is considerably more convenient to apply in calculations, because it does not require detailed boundary layer calculations. Therefore, the Stratford criterion is very useful for practical purposes, because it does not require detailed knowledge about the boundary layer, while still giving satisfactory results.

2.1.3 Swirl Flows

In this section, a very brief introduction to swirl flows is given, because in some of the experiments in Ch. 6 flashback due to Combustion Induced Vortex Breakdown (CIVB) plays a role. For the description of swirl flows in cylinder coordinates (with the z -axis being the cylinder axis), the identity

$$\vec{\omega} = \begin{pmatrix} \omega_r \\ \omega_\phi \\ \omega_z \end{pmatrix} \equiv \nabla \times \vec{u} = \begin{pmatrix} \frac{1}{r} \frac{\partial u_z}{\partial \phi} - \frac{\partial u_\phi}{\partial z} \\ \frac{\partial u_r}{\partial z} - \frac{\partial u_z}{\partial r} \\ \frac{1}{r} \left(\frac{\partial(r \cdot u_\phi)}{\partial r} - \frac{\partial u_r}{\partial \phi} \right) \end{pmatrix} \quad (2.36)$$

is usually used to derive the incompressible vorticity transport equation from the Navier-Stokes equations (cf. Sec. 2.1).

$$\begin{aligned} \frac{\partial \vec{\omega}}{\partial t} = & - \underbrace{(\vec{u} \cdot \nabla) \vec{\omega}}_{\text{convection}} - \underbrace{\vec{\omega} (\nabla \cdot \vec{u})}_{\text{dilatation}} + \underbrace{(\vec{\omega} \cdot \nabla) \vec{u}}_{\text{stretching/tilting}} + \underbrace{\frac{1}{\rho^2} (\nabla \rho \times \nabla p)}_{\text{baroclinic torque}} \\ & + \underbrace{\nu (\nabla^2 \omega) + (\nabla \nu) \times \nabla^2 \vec{u}}_{\text{diffusion/dissipation}} \end{aligned} \quad (2.37)$$

Burmberger [17] discussed the terms in Eq. (2.37) in detail, which is beyond the scope of this work. For the discussion of CIVB the baroclinic torque in Eq. (2.37) plays a decisive role. CIVB implies that there is a zone of negative axial velocity u_z on the cylinder axis, in which the flame propagates against the main flow direction. The production of negative azimuthal vorticity ω_ϕ is a necessary condition for the occurrence of vortex breakdown, because this is the only mechanism that can induce negative axial velocities on the symmetry axis according to the Biot-Savart law [16, 17]. Vortex breakdown and the associated creation of a recirculation zone is utilized in swirl burners to anchor the stable flame in the combustion chamber. Several of the terms in Eq. (2.37) can contribute to the production of negative azimuthal vorticity. In flow without pressure or density gradients, or when the pressure and the density gradient are aligned, the baroclinic torque vanishes (cf. Fig. 2.5(a)). As a result, the baroclinic torque normally does not contribute to the production of negative azimuthal vorticity in isothermal flow. By contrast, in reactive flow the radial pressure gradient due to the swirling fluid motion is perpendicular to the strong axial density gradient due to combustion. Thus, the baroclinic torque

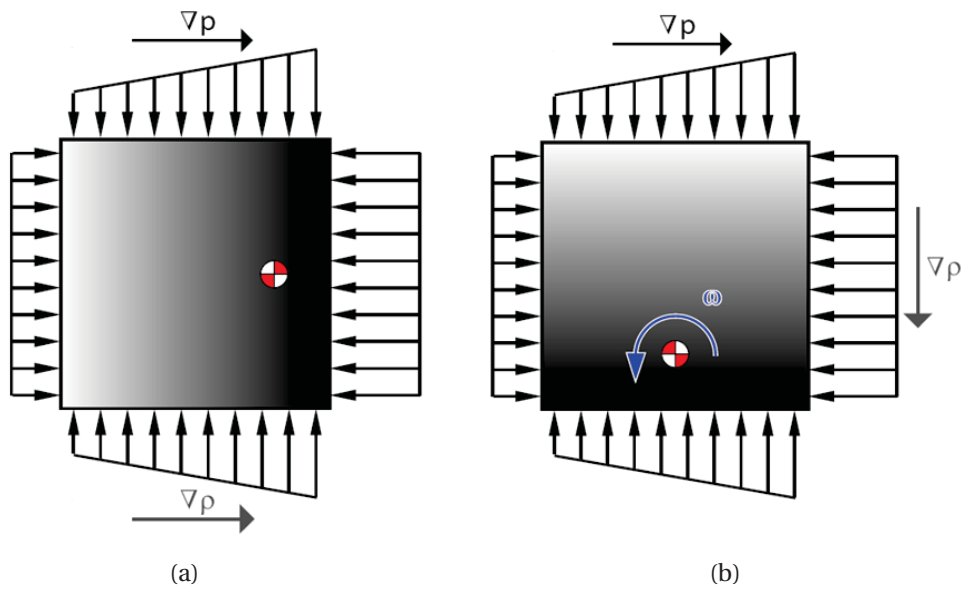


Figure 2.5: Baroclinic torque on a fluid element according to [17] with pressure and density gradient parallel (a) and perpendicular (b)

contributes to the production of negative azimuthal vorticity, which – upon exceeding a certain strength – displaces the recirculation zone and the flame in upstream direction, leading to flashback due to CIVB (cf. Fig. 2.5(b)). It is noted that the reaction at the same time produces positive azimuthal vorticity due to the associated volume expansion (cf. Eq. (2.37)). Thus, the occurrence of flashback is determined by the dominating one of these two influences.

In technical systems, the dimensionless swirl number S is mostly used to characterize swirl flows. The latter is defined as the ratio of the axial flux of angular momentum \dot{D} to the axial flux of axial momentum \dot{I} divided by the burner exit radius r :

$$S = \frac{\dot{D}}{\dot{I}r} \quad (2.38)$$

Although swirl flows cannot be fully described by this single parameter [42], the CIVB flashback propensity is often expressed in terms of critical swirl numbers S_c , above which flashback due to CIVB might occur. For a comprehensive treatment of swirl flows and CIVB the reader is referred to the literature, e.g. [17].

2.2 Premixed Combustion

Combustion can be described as a rapid exothermal oxidation process generating heat, or both light and heat [83, 119]. Generally, it can be differentiated between diffusion flames, where fuel-oxidizer-mixing and combustion take place quasi-simultaneously, and premixed flames, where fuel and oxidizer are perfectly mixed prior to combustion. The focus in this work is on premixed flames. Unless otherwise stated, the following content is based on the works of Peters [99], Law [78], and Turns [119].

2.2.1 Laminar Flame Characteristics

Three parameters that are of particular importance in the context of premixed combustion are the fuel-oxidizer equivalence ratio Φ , the laminar flame thickness δ_f , and the laminar flame speed S_l .

The fuel-air equivalence ratio Φ is a dimensionless number, which is commonly used to differentiate between fuel-lean, stoichiometric, and fuel-rich combustion regimes. In the scientific community, the air-fuel ratio λ , which is the inverse of the equivalence ratio, is also frequently used for this characterization. For a given fuel-oxidizer system, Φ is defined as the actual fuel-to-oxidizer ratio in the mixture divided by the stoichiometric fuel-to-oxidizer ratio.

$$\Phi = \frac{1}{\lambda} = \frac{(\dot{m}_{fuel}/\dot{m}_{ox.})_{real}}{(\dot{m}_{fuel}/\dot{m}_{ox.})_{stoich.}} \quad (2.39)$$

Thus, Φ equal to unity represents a stoichiometric mixture, whereas Φ smaller than unity indicates a lean combustion regime and Φ greater than unity a rich combustion regime, respectively.

In premixed combustion, the reactants and the products are separated by a flame front of thickness δ_f . Employing a one-dimensional approach, the flame can be divided into three zones – the preheat zone, the reaction zone and the equilibrium zone [99]. The qualitative trend of the temperature and the heat release rate across a flame front is shown in Fig. 2.6.

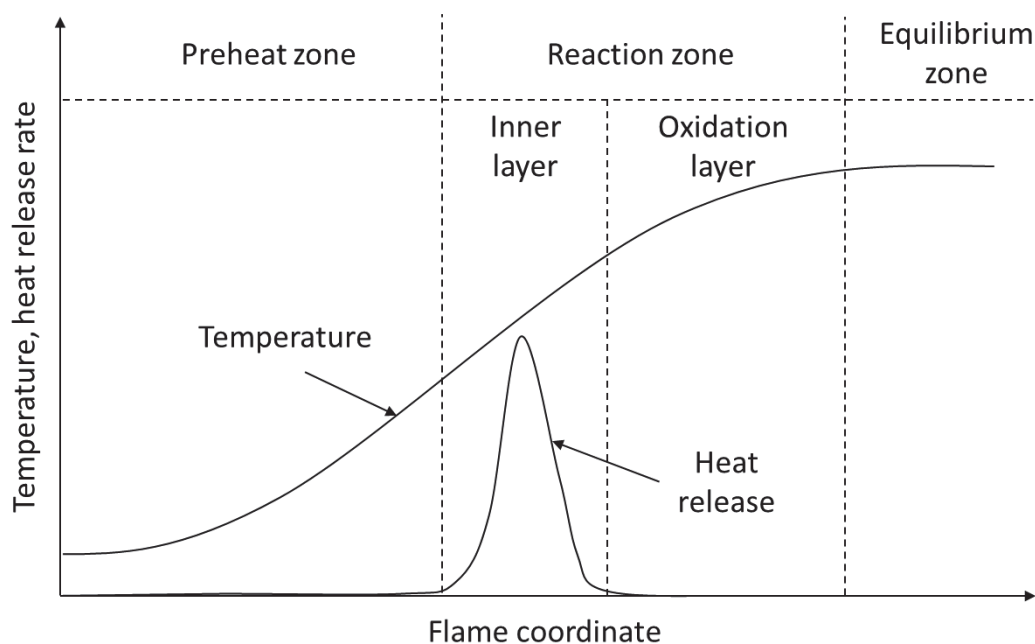


Figure 2.6: Structure of a premixed flame front according to [99]

- In the **preheat zone**, the reactants are heated to the ignition temperature through heat transfer from the burnt products. This process is chemically inert and no heat is released in this zone.
- The **reaction zone** can be further divided into two layers. In the inner layer, chain-branching reactions are initiated, which form combustion radicals that keep the reaction running. All the fuel is consumed in this layer and most of the heat is released. In the oxidation layer, the species are oxidized to form the end product and the maximum temperature is reached.
- In the **equilibrium zone**, all species reach their equilibrium states without further heat being released.

Turns [119] assumes equal thicknesses for the preheat and the reaction zone along with a linear temperature increase from the reactants' temperature T_0 to the adiabatic flame temperature¹ T_{ad} within the flame thickness δ_f . Based on this, he derived the following expression for δ_f :

¹ The adiabatic flame temperature is the highest possible temperature in a flame assuming adiabatic conditions, i.e. without considering any heat losses

$$\delta_f = \frac{2a}{S_l} \quad (2.40)$$

It is noted that the thickness of the reaction zone is often assumed to be much smaller than that of the preheat zone [99] and is therefore neglected in the derivation of δ_f . As a result, the factor 2 in Eq. (2.40) drops out. In the equation, a is the thermal diffusivity of the unburnt mixture and S_l is the laminar flame speed. The latter is the speed at which a one-dimensional laminar flame front propagates into the fresh gas mixture. It can be accurately determined for a given mixture at a certain temperature and pressure, for instance by measuring the clearly defined angle of the flame cone relative to the direction of the incoming flow in tube burner experiments.

2.2.2 Turbulence-Flame Interaction

While the laminar flame speed solely depends on the chemical and thermal properties of the mixture, the turbulent flame speed is greatly affected by the character of the flow. According to Peters [99], this flame-turbulence interaction can be categorized as five different flame regimes. These are shown in Fig. 2.7, where the ratio of the integral length scale l_t to the laminar flame thickness δ_f is plotted versus the root mean square (rms) value of the velocity fluctuations u'_{rms} over the laminar flame speed S_l . In the figure, Re_t is the turbulent Reynolds number, which is composed of u'_{rms} and l_t according to Eq. (2.41).

$$Re_t = \frac{u'_{rms} l_t}{\nu} \quad (2.41)$$

- In the **laminar flames** regime, $Re_t < 1$ applies, indicating that the turbulent fluctuations are too small to affect the combustion processes, i.e. the flame behavior is entirely laminar.
- In the **wrinkled flamelets** regime the velocity fluctuations are smaller than the laminar flame speed. Consequently, the flame front is weakly wrinkled but the laminar flame speed remains the dominating parameter.

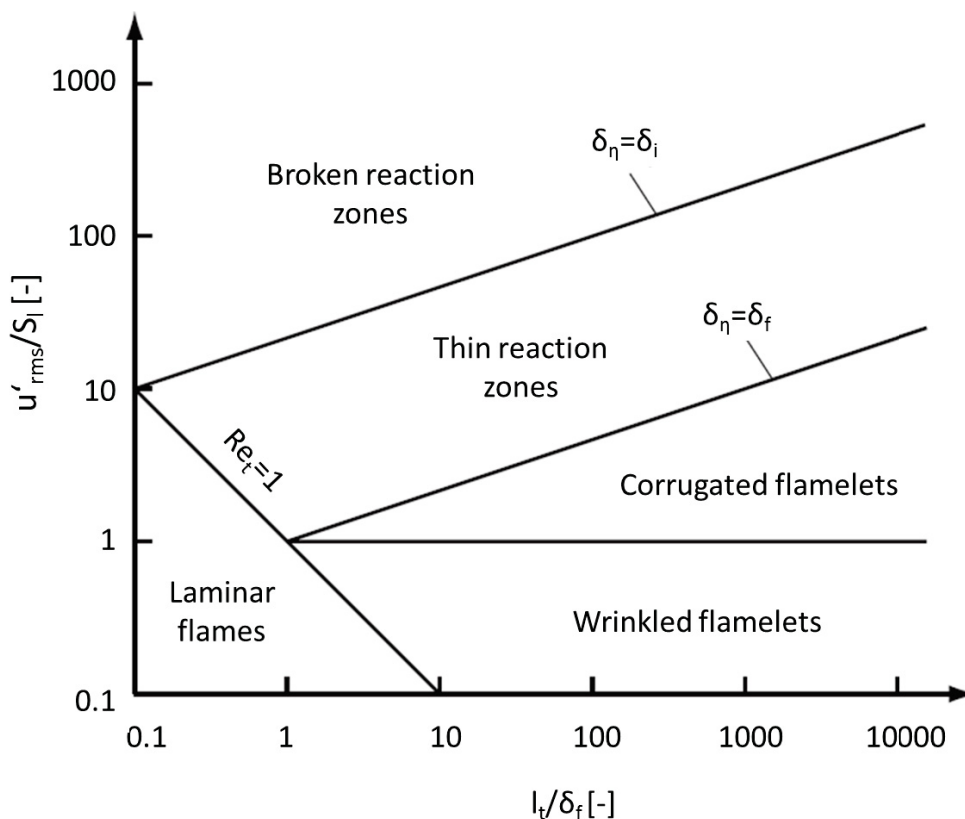


Figure 2.7: Turbulent combustion regimes according to Peters [99]

- The **corrugated flamelets** regime is characterized by strongly wrinkled flame fronts due to turbulence, which significantly increases the reacting surface and therefore leads to higher consumption speeds. However, the size of the Kolmogorov eddies δ_η is still larger than the laminar flame thickness δ_f . Therefore, the eddies do not influence the processes inside the flame.
- In the **thin reaction zones** regime the Kolmogorov eddies are able to penetrate into the flames's preheat zone, which enhances mixing and heat transfer between the inner reaction layer and the preheat zone. Since the smallest eddies are larger than the thickness δ_i of the inner layer, the chemical reactions are not influenced by turbulence.
- In the **broken reaction zones** regime, the Kolmogorov eddies are small enough to enter the inner reaction zone. This causes local flame extinction due to excessive heat losses to the preheat zone.

The regimes of wrinkled flames, corrugated flames and thin reaction zones are often summarized as the *flamelet regime*. This implies that the flame can be considered as locally laminar with a one-dimensional structure.

It is obvious that these different modes of interaction between flame and flow complicate the determination of turbulent flame speeds. In addition, multi-dimensional effects impact both the laminar and the turbulent flame speed, for instance hydrodynamic and flame stretch effects, nonequidiffusion effects, etc. A review on this topic can be found in [79].

2.2.3 Near-Wall Flame Quenching

Flame quenching in the vicinity of a cold wall is an important phenomenon regarding boundary layer flashback. Since the wall-parallel flow velocity continuously decreases toward the wall due to the no-slip condition, flame quenching is the only mechanism that can prevent upstream flame propagation along the wall. The chemical reactions cannot sustain within a certain distance from the wall, which is referred to as quenching distance δ_q . Quenching is caused by heat losses from the flame to the wall and third body recombination reactions of combustion radicals (cf. reaction of hydrogen with oxygen in Sec. 3.4.1). Additionally, non-inert walls can catalyze or inhibit the chemical reactions. As a result, the quenching distance is influenced by various parameters, such as fuel and oxidizer, mixture temperature and pressure, equivalence ratio, wall material, wall temperature, and near-wall velocity field. Moreover, δ_q is sensitive to the motion of the flame relative to the wall, i.e. whether the flame moves toward the wall (head-on quenching) or alongside the wall (side-wall quenching). Due to this complexity, δ_q is usually evaluated in experiments or numerical simulations. In the literature, the quenching distance is often expressed as a multiple of the laminar flame thickness δ_f , with the proportionality constant being the Peclet number at quenching conditions Pe_q .

$$Pe_q = \frac{\delta_q}{\delta_f} \quad (2.42)$$

2.2.4 Flame Backpressure

The so-called backpressure of a premixed flame is a result of momentum conservation across the flame front. A laminar, one-dimensional flame front can be treated as a planar, combustion wave that propagates into the fresh mixture with a speed much smaller than the sonic speed ($M \ll 1 \rightarrow$ slow deflagration). Assuming steady, adiabatic conditions and neglecting potential energy, the expressions for mass and momentum conservation across the flame front can be written as follows in a coordinate system that moves with the flame [83]:

$$\rho_1 u_1 = \rho_2 u_2 \quad (2.43)$$

$$\rho_1 u_1^2 + p_1 = \rho_2 u_2^2 + p_2 \quad (2.44)$$

Eqs. (2.43) and (2.44) are referred to as *Rankine-Hugoniot conditions*, where indices '1' apply to the reactants and indices '2' to the products. Combining the two equations yields a simplified formula for the calculation of the laminar, one-dimensional flame backpressure Δp_f .

$$\Delta p_f = p_1 - p_2 = \rho_1 u_1^2 \left(\frac{\rho_1}{\rho_2} - 1 \right) \quad (2.45)$$

Through application of the ideal gas law the density ratio in Eq. (2.45) can be substituted for the temperature ratio, assuming $p_1 \approx p_2$, which is reasonable, because $(p_1 - p_2)/p_1 \ll 1$. Replacing u_1 by the laminar flame speed S_l and T_2 by the adiabatic flame temperature T_{ad} gives:

$$\Delta p_f \approx \rho_1 S_l^2 \left(\frac{T_{ad}}{T_1} - 1 \right) \quad (2.46)$$

The laminar flame backpressure Δp_f is typically below approx. 100 Pa. Nevertheless, it is an important parameter in conjunction with boundary layer flows. As was described in Sec. 1.1.2, it can potentially cause flow separation in these low-velocity regions.

3 Experimental Setup and Measurement Techniques

In this chapter, the experimental infrastructure for the flashback tests as well as the measurement techniques employed are described. Three different setups were used - two tube burner configurations and a channel burner.

3.1 Tube Burner Setups

Since practical burner applications usually feature rotationally symmetric geometries, the purpose of using tube burners was to study the flashback behavior of hydrogen flames in setups resembling practical geometries. Part of these experiments were conducted in collaboration with the University of California in Irvine (UCI), USA, with financial support from the Bavaria California Technology Center (BaCaTeC). The tube burners employed at the Technische Universität München (TUM Burner) and the UCI (BaCaTeC Burner), respectively, are described in the following sections.

3.1.1 TUM Burner

A schematic of the basic setup of the tube burner test rig used at TUM is shown in Fig. 3.1. Hydrogen and air were perfectly premixed far upstream of the burner section using a static flow mixer (Sulzer Chemtech AG SMV DN40). The mixture entered the large-volume plenum from the bottom through a porous sintered metal plate, which homogenized the flow by introducing a high pressure loss. The flow settled in the plenum and was then accelerated into a quartz glass tube by means of a nozzle, from where the velocity profile developed toward the tube exit. The inner diameter of the tube was constant at $d=40$ mm and the total length was $L=400$ mm. Some tests were conducted with a smaller tube ($d=20$ mm, $L=400$ mm). Nozzle and pilot burner

(cf. Fig. 3.1) were adapted accordingly. At the tube exit, the main flame was stabilized in the free atmosphere by a water-cooled, concentric pilot burner, which is shown in Fig. 3.2.

Pure pilot hydrogen was injected into the main flow under an angle of 45° through an annular slot of 1 mm axial width. It was initially ignited by an external methane-air burner (not shown in the figure). The axial extension of the pilot burner arrangement was only 13 mm in order to provide for maximum optical access during the onset of flashback. All parts of the pilot burner were made from stainless steel and the water-cooling was found to keep the temperature of the burner rim below 60°C during all flashback tests. According to [84] and in-house experience on flashback testing [31], these burner tip temperatures can be considered sufficiently low to assume negligible influence on the flashback limits. A second, very similar pilot burner, which was made from brass (CuZn30), was used in some experiments in order to study the effect of burner material on flashback behavior (cf. Sec. 5.2 and 5.3). The corresponding tests are clearly marked in the respective results sections.

The test rig was operated at atmospheric pressure and the filtered combustion air could be preheated up to approximately $T=450^\circ\text{C}$ in an electrical heater with a maximum power input of 32 kW. All mass flow rates — except for the pilot mass flow — were controlled by Bronkhorst thermal mass flow controllers with maximum mass flow deviations of $\pm 1\%$. The amount of pilot hydrogen was measured by an ABB variable-area flow meter with an accuracy of $\pm 10\%$. It was set to less than 4 vol.-% of the main hydrogen mass flow during all tests. The pilot gas was shut off well before flashback occurred, because the main flame was then self-stabilizing at the burner rim. In this way, any influence of the pilot flame on the flashback process could be eliminated.

The plenum was equipped with a type K thermocouple that detected the sudden temperature increase during a flashback and commenced the shutdown procedure. This comprised shutdown of all fuel supply lines and purging of the test section with 500 standard liters per minute air. Additionally, the sintered metal plate at the bottom of the plenum prevented the upstream propagating flame from entering the fuel supply duct, because the flame was quenched inside the small $30\ \mu\text{m}$ pores. Optical access to the combustion zone from the bottom was provided by a quartz glass plate in the center of the sintered metal plate.

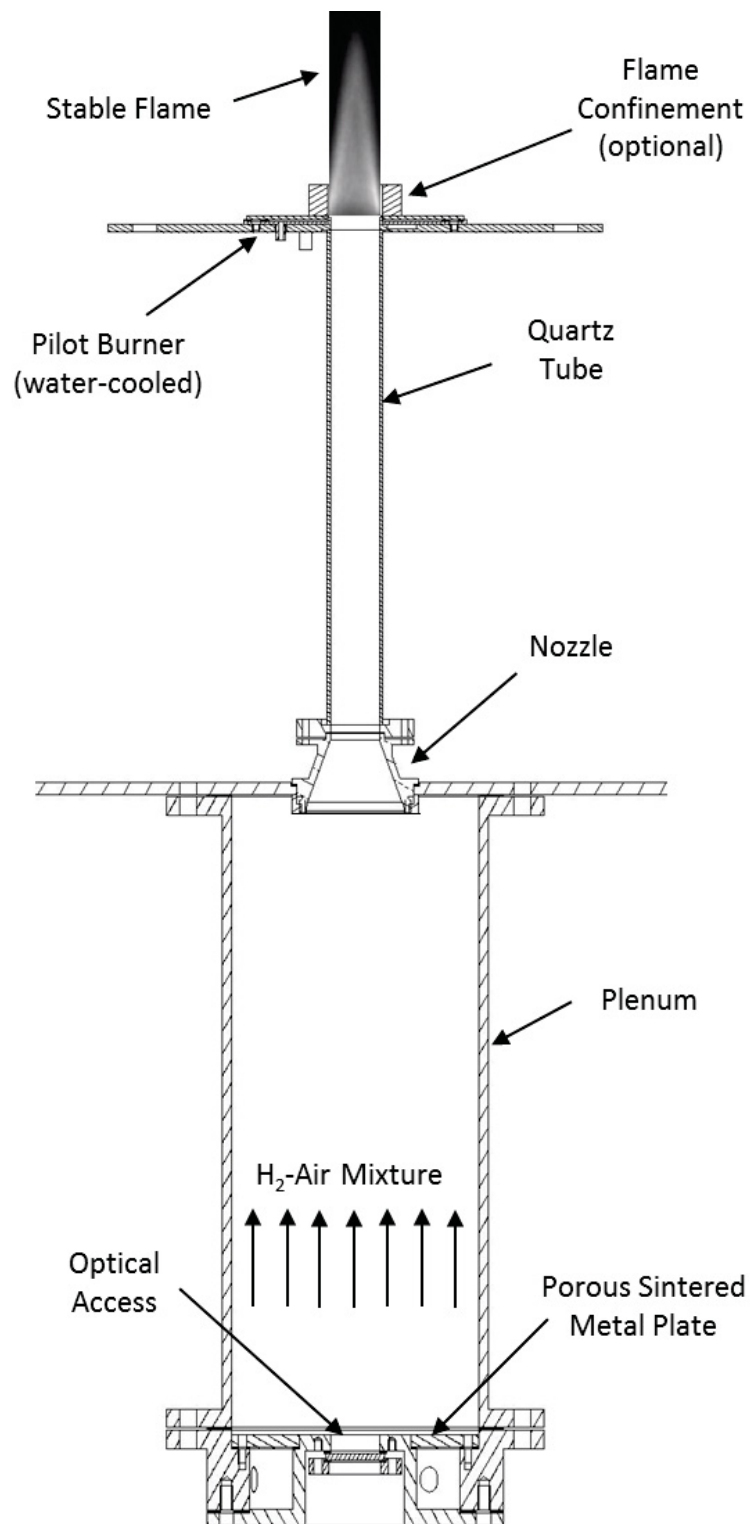


Figure 3.1: Basic design of the TUM tube burner test rig

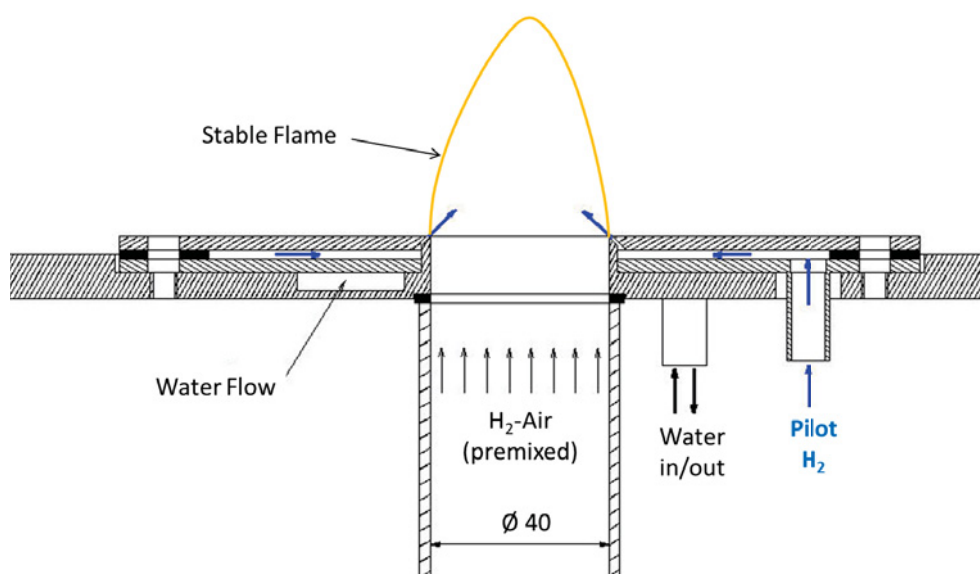


Figure 3.2: Details of pilot burner

Optional add-ons to the basic setup, such as flame confinement, boundary layer injection devices, and swirl generator, will be described in the respective results sections. The isothermal flow field in this burner setup is presented in Ch. 4.1.

3.1.2 BaCaTeC Burner

As mentioned above, part of the data presented in this thesis were collected within a university collaboration between the TUM and the UCI in the framework of BaCaTeC. The main goals were as follows:

- Share knowledge about flashback among the universities
- Find out whether flashback data from different test rigs can be collapsed (interlaboratory comparison)
- Extend the existing flashback data base

All these experiments were conducted at the UCI using the so-called BaCaTeC setup. In the latter, some hardware from the TUM burner was installed at the UCI test cell. More specifically, the nozzle, the 40 mm quartz tube and the pilot burner were used, as shown in Ch. 3.1.1. All the other components (plenum,

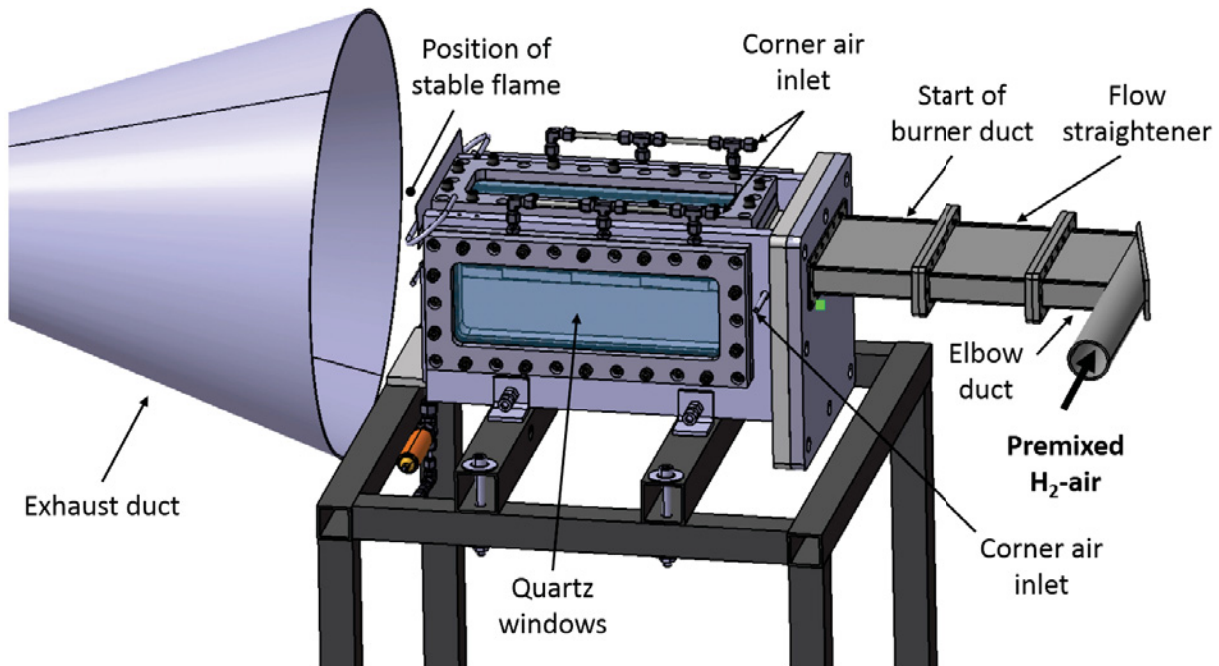


Figure 3.3: Channel burner test rig

fuel-air premixing, flashback and test rig control) were from the UCI. As a result, the setup resembled that of the TUM burner and was therefore suited for interlaboratory comparison. Further details on the experimental infrastructure at the UCI can be obtained in [26, 27, 111]. The BaCaTeC studies involved a number of different burner/flame configurations, which are described in detail in Ch. 5.

3.2 Channel Burner Setup

Drawbacks of rotationally symmetric burners are their limited optical access due to curved walls and the fact that the position of the onset of flashback is random. In order to overcome these problems, a rectangular channel burner was designed. Its plain side walls facilitated detailed optical measurements and, due to the characteristic flow profile inside the channel, the position of the onset of flashback could be predicted more easily. The setup of the channel burner rig is shown in Fig. 3.3.

The fundamental design of the test rig resembled the one used in a previous Ph.D. project [29]. Most parts of the experimental infrastructure, such as

gas supply and control, flow premixing, air preheating, and boundary layer treatment, have been kept the same. Changes were made to the exhaust duct and to the burner section, which is optically accessible from three sides through quartz glass windows. The latter were manufactured very accurately and mounted flush with the surrounding stainless steel walls in order to avoid flow perturbations at the transitions. In the setup used in this project, the downstream end of the burner was no longer attached to a combustion chamber. Instead, the flame was burning into the free environment and the exhaust gases were sucked off by an exhaust duct, which was offset approximately 150 mm in the axial direction.

The working principle of the test rig was as follows: Flow rates of pressurized, filtered air and fuel (natural gas or hydrogen) were controlled by thermal mass flow controllers (Bronkhorst) with maximum flow deviations of approximately $\pm 1\%$. The air passed through a 65 kW preheater, which was capable of increasing the air temperature up to approx. 450°C. Fuel and air were then perfectly premixed in a static flow mixer (Sulzer Chemtech CompaX DN40). Thereafter, the mixture passed through the 90° elbow duct, from where it entered the rectangular duct. The flow was then homogenized in the flow conditioning section and proceeded downstream into the optically accessible burner duct. At the end of the burner duct, the reactive fuel-air mixture was ignited by two small pilot flames, which helped stabilize the main flame in the free atmosphere. The exhaust gases were sucked into the exhaust duct and were blown out of the laboratory. More details on the flow components upstream of the burner section can be found in [29].

The two pilot burners were mounted with sufficient vertical offset from the edges of the lower and the upper wall, respectively, to avoid any influence on the flow and flame behavior (cf. Fig. 3.5). The pilot flames were burning in diffusive mode and they were fed with pure hydrogen coming out of a row of small holes that were drilled into each of the two horizontally arranged feed pipes. The upper pilot feed pipe was interrupted in the lateral center of the burner duct to allow for inserting a laser light sheet from the top (for measurements).

The burner section is illustrated in more detail in Figs. 3.4 and 3.5. The length of the rectangular duct amounted to 590 mm at a height of 17.5 mm and a lateral width of 158 mm. The axial extension of the lower wall could be var-

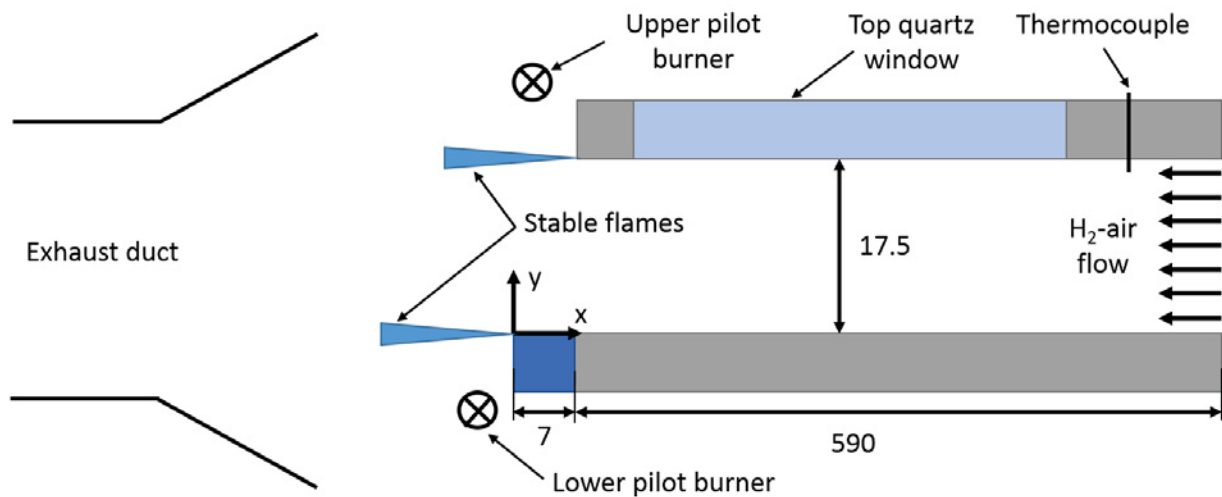


Figure 3.4: Schematic of the channel burner test section

ied in discrete steps by attaching additional plates of variable thicknesses. In this way, the flashback behavior could be influenced such that the flashback tended to occur on the lower wall (cf. Sec. 5.2.2). This was beneficial with respect to the detailed investigation of the onset of flashback with very small fields-of-view, because all the measurement equipment could be aligned for measurements at the lower wall. Furthermore, the offset of the lower wall allowed for optical access to the location of flashback onset from the top and from both sides. In the present work, the offset between upper wall and lower wall was kept at 7 mm during all tests. To check whether this offset influences the flashback limits in an appreciable way, some experiments were also conducted with equally long walls for comparison (cf. Sec. 5.2.2).

In order to provide for well-defined temperature boundary conditions, the two side walls and the top wall of the burner section were convectively cooled by blowing cooling air onto them from the outside. Since the structure supporting the lower burner wall was hollow, it could also be cooled convectively with air from below. The temperatures of the upper and the lower wall were monitored by type K thermocouples (two on the upper wall and three along the lower wall).

A peculiarity of the rectangular flow ducts is that in the four corners the boundary layers from two adjacent perpendicular walls merge, leading to particularly thick boundary layers in the corners. In order to avoid flashback along the corners, air was blown into each of them. The total amount of blow-

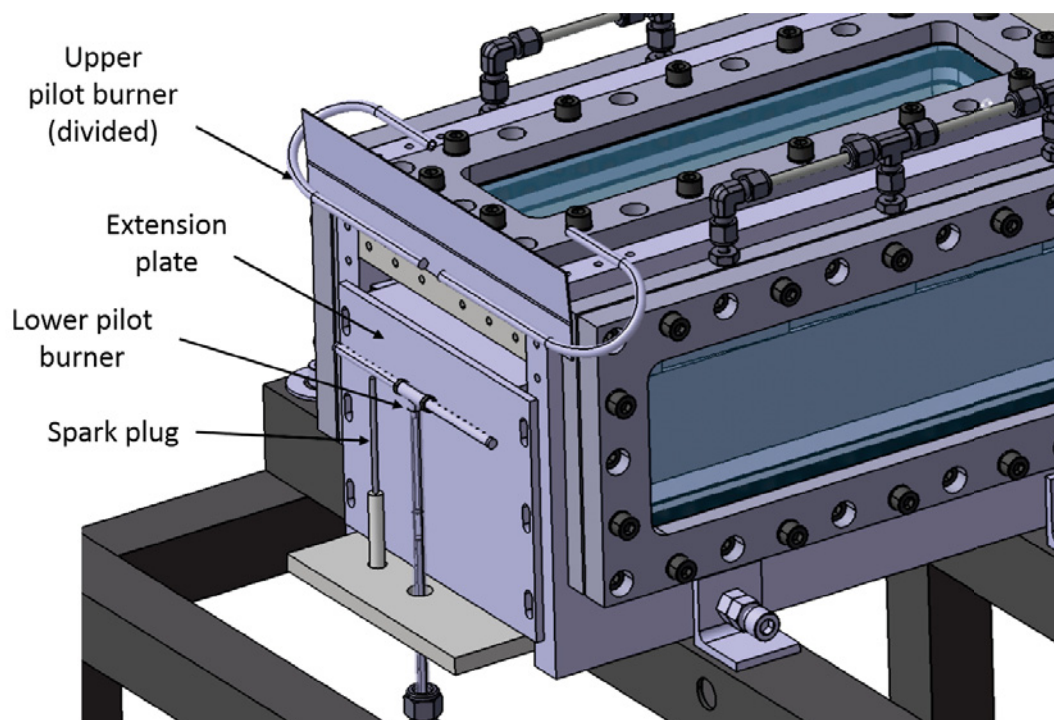


Figure 3.5: Detailed view of the channel burner exit

ing air was kept below 4 % of the main air mass flow during all tests. It has been verified by means of CFD simulations that this small amount of blowing air did not appreciably change the gas composition and the velocity profile in the center region of the flow duct, where the flashback process was investigated. More detailed information on the boundary layer treatment in the corners can be obtained from [29] and [30].

During the event of a flashback the flame inside the burner was detected by a type K thermocouple, which slightly extended into the flow duct in the center of the upper wall just upstream of the top window (cf. Fig. 3.4). As soon as the temperature measured exceeded a certain threshold value, which was dependent on the air preheating temperature, the fuel supply was shut off and the test section was flushed with an air mass flow of $\dot{m}=120$ g/s.

3.3 Experimental Procedure

The macroscopic flashback tests at the two tube burner test rigs and at the channel burner test rig are conducted in a similar fashion. The detailed procedures are described in the following two sections.

3.3.1 Tube Burners

Both the TUM burner and the BaCaTeC burner were operated in the same manner. First, the total air mass flow rate through the tube was adjusted to a specific value. Thereafter, the pilot gas was turned on and ignited by an external (methane-air) flame. As soon as the pilot flame was burning, the external flame was shut off and the hydrogen for the main flame was turned on. While the total air mass flow rate was kept constant, the amount of hydrogen was increased in little steps. After each stepwise increase it has been waited until mass flow oscillations had leveled off. The pilot flame was turned off as soon as the main flame was self-stabilizing at the tube exit, which always occurred well before the flashback event. This eliminated any influence of the pilot flame on the flashback process. On further increase of the hydrogen mass flow rate, the flame eventually flashed back into the tube. The advantage of this experimental procedure was that only the settings of one mass flow controller were changed during the approach toward flashback, namely those of the hydrogen mass flow controller. In this way, oscillations of the desired equivalence ratio could be kept small.

To check whether the experimental procedure has an influence on the flashback behavior, some tests were executed according to different test protocols. These are:

- TUM burner: After a stable flame has been established, the flashback event was initiated by a stepwise reduction of the bulk flow velocity at a fixed equivalence ratio.
- BaCaTeC burner: After a stable flame has been established, the flashback event was initiated by a stepwise reduction of the bulk flow velocity at a fixed adiabatic flame temperature (AFT).

The results showed that varying the test procedure did not influence the flashback behavior.

In the present investigation the flashback event was defined as the (global) equivalence ratio when the flame propagated upstream into the burner duct for the first time, i.e. when the flame started to show unstable behavior. This is important to note, because during some tests with very lean mixtures ($\Phi < 0.35$)

flashback was no sudden event, instead the flame started to flicker back and forth, repeatedly entering the burner for a short time, being washed out again, and so forth, before it eventually entirely flashed back into the plenum (without any further change of mass flow rates).

3.3.2 Channel Burner

Flashback experiments with the channel burner were done in a very similar fashion as with the tube burners. First, a fixed flow rate for the corner blowing air was set, which was less than 4 % of the main combustion air flow rate during all experiments. Thereafter, a low air flow rate through the burner was adjusted, the pilot gas (hydrogen) was turned on, and the lower pilot flame was ignited by means of a spark plug. This in turn ignited the upper pilot flame. Then, the final air mass flow rate was set and the fuel flow was turned on and successively increased. The pilot flames were switched off, when the main flame self-stabilized at the burner exit, such that they did not influence the flashback process in any way. While keeping the air mass flow rate constant, the fuel mass flow rate was increased until flashback occurred. The definition of flashback was the same as for the tube burners.

3.4 Measurement Techniques

In this section the optical measurement techniques used for studying flashback phenomena are described. In contrast to the *conventional* measurement equipment used in this work, for instance, thermocouples and mass flow controllers, the optical techniques usually require more expensive equipment and high maintenance effort as well as optical access to the measuring zone. Nevertheless, in combustion research the advantages prevail, in particular when highly transient phenomena need to be investigated. The reasons are that optical techniques are non-intrusive to a large degree and thus do not perturb the measured flow. Additionally, they allow for very high temporal and spatial resolution as well as for planar (two-dimensional) measurement fields. Unless otherwise stated, the content in this section is based on the works of Nitsche et al. [96] and Goulard [43].

3.4.1 Chemiluminescence

Chemiluminescence measurement is a relatively simple standard technique in combustion research for characterizing flames. The reaction zone is visualized through capturing the light that is emitted by the flame with a camera. The light emission is caused by the relaxation of electronically excited species in the flame, for instance OH^* , CH^* , CO_2^* and C_2^* . These excited molecules are directly formed in the reaction zone as intermediate species. They have very short residence times between 10^{-8} s and 10^{-5} s [108] before they return to the electronic ground state. Thus, they can be cited as evidence for the existence of combustion. During the relaxation process the molecules emit light within a characteristic wavelength band. For some of the molecules the emission intensity peaks at certain (known) wavelengths, which facilitates their detection. In hydrogen applications the hydroxyl-radical (OH^*) is mostly utilized as a marker of the combustion zone because of the absence of carbon (C) atoms. The OH^* molecule exhibits an emission intensity peak at $\lambda=306.4$ nm, which requires optical equipment that is transmissive in the UV range as well as an image-intensified camera for detection. The processes behind the formation of the OH -radical are now described on the basis of the reaction of hydrogen with atmospheric oxygen. The formation and consumption of the species HO_2 and H_2O_2 are neglected in the following derivation.

As indicated in Eq. (3.1), the two reactants (H_2 and O_2) do not directly form the product H_2O . Instead, a chain reaction consisting of 19 reversible elementary reactions is taking place [62, 97].



During ignition the particle with the weakest chemical bond (here: H_2) is split into two reactive radicals with unpaired electrons (indicated by " \cdot "). This reaction is referred to as *initiation* (Eq. (3.2)).



Afterwards, the H_2/O_2 *chain branching* reactions shown in Eqs. (3.3)-(3.6) and the H_2/O_2 *dissociation/recombination* reactions shown in Eqs. (3.7)-(3.10) take place, which involve the species H_2 , O_2 , H , O , OH and the third body M .



It becomes obvious that the reactions above aid one another, so that the number of highly reactive radicals (OH , O , H) dramatically increases once combustion is initiated. The end product water (H_2O) is formed by reactions (3.5) and (3.10), and the chain reaction (usually) stops when all the fuel is burnt [125].

The reaction equations also show that the presence of OH -radicals is crucial for the existence of combustion and, thus, they can be used to determine the locations where combustion takes place. A proportion of the OH -molecules is directly formed in an electronically excited state as a result of the exothermic elementary reactions. These excited molecules emit characteristic light when they return to the electronic ground state, as was mentioned in the beginning of this section. In combination with a high-speed camera and proper optical equipment (UV lenses, bandpass filter), the combustion zones can be visualized with very high temporal and spatial resolution in this way. A drawback of this relatively simple measurement method is that the signal detected by the camera is line-of-sight integrated. This problem can be overcome by employing planar laser-induced fluorescence (cf. Sec. 3.4.4).

In this project the following image-intensified cameras were used for chemiluminescence measurements: Hamamatsu C4336-02 (30 fps, continuous mode) and Photron FASTCAM-ultima APX-I² (up to 120,000 fps).

3.4.2 Mie Scattering

In flow investigations it is often advantageous to visualize the flow in order to study the overall flow field or certain effects, such as flow separation, recirculation zones, flow mixing, etc. [96]. Flow visualization can be achieved by seeding of the flow with appropriate tracer particles, which are assumed to faithfully follow the flow dynamics, while the test area is well illuminated against the background. The light reflected by the tracer particles, which is referred to as Mie scattering¹, is then detected by a camera. Through tracking of single particles or the particle distribution over time, the flow pattern, including the velocity vectors, can be visualized. This procedure, however, involves a number of difficulties in the practical application and makes high demands on the tracer particles deployed. Some of them are listed below [91]:

- The particles must match the fluid properties (i.e. density, temperature) of the main flow reasonably well in order to follow the flow satisfactorily → Particle diameter as small as possible.
- The particles must be inherently reflective, so that as much of the incident light as possible is reflected and scattered toward the camera. Furthermore, the reflection intensity should be the same in all spatial directions, so that the percentage of incident light that is scattered toward the camera does not vary across the particles. → Particle diameter as big as possible, geometry of the particles should not implicate a preferred direction of reflection.
- The measuring section should be illuminated well and uniformly.
- The melting point of the tracer particles must be sufficiently high if they are used in high temperature flow → They must not change their diameter or reflexion properties under heat generation.
- The particles should be chemically inert in case of investigating reactive flows.

The two last named requirements particularly apply to the environment in a combustion zone (high temperature, reactive flow). Typical tracer materials

¹The scattering of electromagnetic radiation by a sphere is referred to as *Mie scattering*. It is described by the Mie solution to Maxwell's equations [12]

for these applications are TiO_2 , Al_2O_3 , SiC and ZrO_2 -powder, all of which feature the disadvantage of high mass density. As a result, their diameters must be kept very low (typically a few micrometers) in order the particles being able to follow the flow dynamics. However, this has a negative effect on the amount of reflected light that can be detected by the camera. Thus, a compromise between a small and a big particle diameter has to be reached.

The test area is usually illuminated by a laser source and the laser beam is converted to a sheet of light by a cylindrical lens [4]. The associated velocity measuring method is referred to as Particle Image Velocimetry (PIV) (cf. Sec. 3.4.3).

Tracer techniques have in common that they are non-intrusive to a large degree. The distortion of the fluid flow through the added tracers is generally negligible if they are properly chosen. In the present investigation TiO_2 seeding particles ($\rho=3800 \text{ kg/m}^3$) with a mean diameter of $0.1\text{-}1 \mu\text{m}$ were used for all Mie scattering and PIV measurements. Their ability to properly follow the dynamics in highly turbulent flows as well as their reflection characteristics has been demonstrated in several former Ph.D. projects at the Lehrstuhl für Thermodynamik, e.g. in [29, 67, 124].

3.4.3 Particle Image Velocimetry (PIV)

The Particle Image Velocimetry (PIV) technique has also been extensively elaborated in several former Ph.D. thesis at the Lehrstuhl für Thermodynamik, e.g. in [29, 67, 90, 108, 124]. Therefore, only the basic principle and the practical application within the current project is described in this section.

3.4.3.1 Basic Principle

As mentioned in the section above, PIV is based upon Mie scattering images. The velocity components in the laser-illuminated x-y-plane are derived from the particle motion between two consecutively taken Mie scattering images (\mathbf{I}_1 and \mathbf{I}_2) that are separated by a short time offset Δt (cf. Eq. (3.11) and synchronization scheme for laser and camera in Fig. 3.7) [104].

$$u = \frac{\Delta x}{\Delta t}, \quad v = \frac{\Delta y}{\Delta t} \quad (3.11)$$

For statistical evaluation of Eq. (3.11), the measuring field is subdivided into so-called *interrogation areas* within which the particle displacement is computed through spatial cross-correlation. This procedure yields one mean velocity vector per interrogation area. The time offset between I_1 and I_2 is adjusted based on the anticipated velocity, the interrogation area (IA) size, the camera resolution, and the overall size of the measuring field. The derivation of the velocity field can be improved by adaptive cross-correlation starting with a large IA size to get an initial guess of the velocity vectors and subsequently reducing the IA size step-by-step to the desired size. Modern PIV software automatically deforms and shifts the positions of the IAs between I_1 and I_2 depending on the mean velocity vector calculated in the preceding correlation loop, which considerably increases the number of correlated particles. Additionally, the determination of the position of the correlation peak within an IA, i.e. the mean particle displacement, can be improved through sub-pixel interpolation using a statistical model, for instance a Gaussian peak.

3.4.3.2 Simultaneous PIV and Chemiluminescence

The practical implementation in the present study is explained on the basis of high-speed (μ -)PIV measurements in the channel burner rig (cf. Sec. 3.2). The corresponding results will be presented in Ch. 7. The term μ -PIV implies that the spatial resolution of the correlated velocity field is between 10^{-4} and 10^{-7} m [2]. Some of the PIV measurements presented in this thesis were performed with lower velocity resolution as well as with a low-speed laser system. Nevertheless, the general approach was similar to that for the high-speed μ -measurements.

The laser system used for the (μ -)PIV measurements was comprised of a pulsed, frequency-doubled Nd:YLF laser (Litron LDY 304 PIV) with two cavities emitting radiation at an output wavelength of 527 nm in Q-switch mode. The pulse duration was 150 ns and the two cavities could be separately triggered at repetition rates up to 20 kHz. In the present study, both cavities were operated at 3 kHz, which yielded a PIV double image frequency of 3 kHz accordingly. The pulse separations were between $\Delta t=3\mu s$ and $\Delta t=8\mu s$, depending

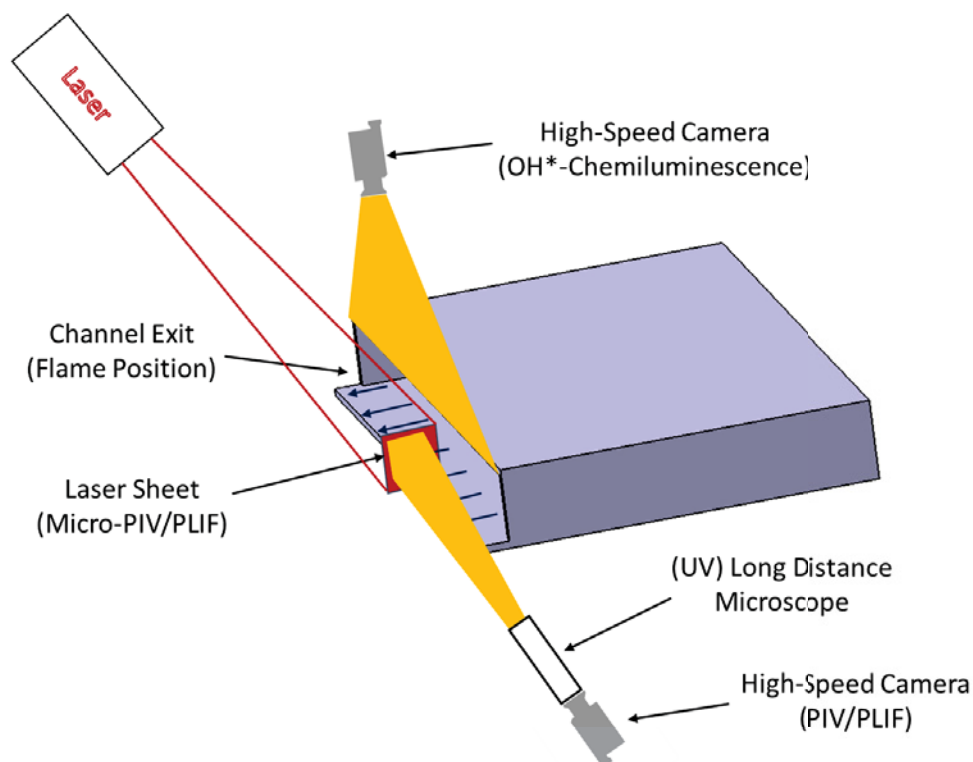


Figure 3.6: Setup for simultaneous PIV/PLIF and chemiluminescence

on bulk flow velocity. A laser sheet with an approximate thickness of 0.3 mm was inserted in the lateral center of the burner channel outlet as is illustrated in Fig. 3.6. Black paint was applied at the position where the laser light hit the lower channel wall. Moreover, the laser sheet was not inserted from vertically above the lower wall, but it was inclined from the vertical axis by approximately 30° in flow direction, i.e. rotated around the z -axis defined in Fig. 3.4. As a result, the reflections of the laser light in the Mie-scattering images were confined to a thin layer above the wall with an approximate thickness of only 0.2 mm (cf. Ch. 7)

Upstream of the elbow duct in Fig. 3.3, the mixture flow was homogeneously seeded with TiO_2 particles, which could sustain the high temperatures during combustion. For image recording, a high-speed camera (Photron FASTCAM SA-X) was combined with a long distance microscope (Infinity K2/S with CF-3 lens, specifications in Appendix B.1). The general applicability of long distance microscopes for μ -PIV measurements has been demonstrated by Kähler et al. [58, 59]. Moreover, concerning the microscope used in the present study, Eichler et al. [32] investigated potential velocity bias due to out-of-plane

particle motion as well as the presence of velocity gradients in the flow, and they found the microscope is very suitable for PIV measurements in boundary layers. For measurements with combustion, the high-speed camera was equipped with a bandpass filter (transmission range: 527 ± 10 nm) to reduce luminescence light from the flame.

PIV data analysis was done with the MATLAB-based software PIVlab [118]. It uses a cross-correlation algorithm with adaptive window deformation and sub-pixel shifting through B-spline interpolation. Apart from linear contrast stretch, the recorded Mie scattering images were not manipulated in any way. The adaptive cross-correlation process started with interrogation windows of size 48×48 pixel and ended with size 24×24 pixel after a second iteration step. Given a 50 % overlap of the interrogation windows, a camera field of view of 4.15×4.15 mm² and a camera resolution of 1024×1024 pixel, this resulted in a spatial resolution of $50 \mu\text{m}$ for the velocity field.

The velocity data was processed as follows: Outliers were removed by means of a median filter of size 3×3 vectors with a tolerance of two times the local standard deviation. Additionally, a window filter was applied, where plausible values for maximum and minimum flow velocities in x- and y-direction were specified, for instance, only negative values for velocity u in the isothermal case (please note definition of x-axis in Fig. 3.4). For interpolation of the removed vectors from their neighbors a kernel size of 3×3 vectors was used. The percentage of interpolated vectors was as high as 20 % in some tests. However, this can be traced back to the orientation of the PIV camera. As mentioned above, the extension of the PIV field of view in the experiments was 4.15×4.15 mm². The left-hand boundary was located 2.15 mm to the left of the downstream edge of the lower channel wall ($x = -2.15$ mm), and the lower boundary was at $y = -1.25$ mm below this edge (cf. Fig. 3.4). Thus, there were almost no seeding particles visible in the recorded images in the wake downstream of the lower channel wall (cf. Fig. 7.1), which explains the high percentage of interpolated vectors. Taking this into account, the percentage of invalid vectors in the areas with seeding particles was always less than 10 %.

In the experiments it was important to assess whether the propagation of the leading flame tip during flashback happened in the PIV measurement plane or not. Therefore, an image-intensified high-speed camera (Photron FASTCAM-ultima APX-I²) combined with a UV lens ($f = 45$ mm) and a bandpass

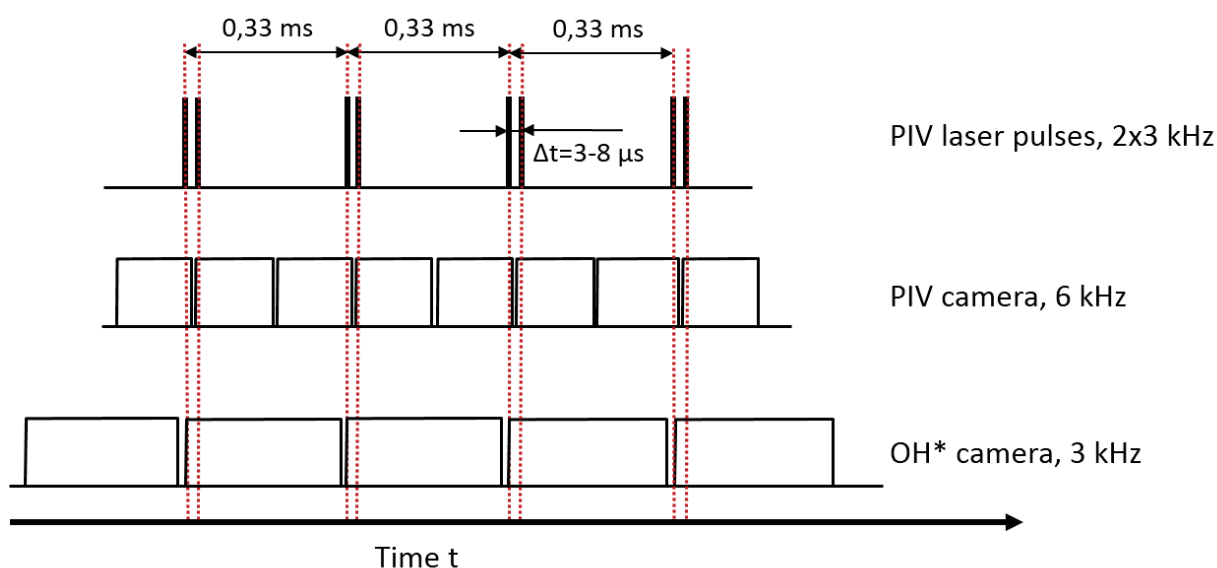


Figure 3.7: Synchronization scheme for simultaneous application of PIV and chemiluminescence

filter (transmission range: 307 ± 5 nm) was used to simultaneously record the flame's OH* chemiluminescence from the top at a frame rate of 3 kHz. The two PIV laser cavities and the two high-speed cameras were synchronized by a digital delay generator (Quantum Composers 9314E) according to the synchronization scheme depicted in Fig. 3.7.

3.4.4 Planar Laser-Induced Fluorescence (PLIF)

Planar laser-induced fluorescence (PLIF) is a two-dimensional spectroscopy technique. It is particularly suitable for the detection of so-called minority species in combustion zones, such as OH, CH, NO, CO, NH, CN and C₂. Minority species implies that the concentration of the respective species is ranging from less than 0.1 % down to a few parts per million (ppm) or even less.

3.4.4.1 Basic Principle

PLIF is based on the absorption and emission of photons and works as follows: The measurement section is illuminated by a laser, which is usually pulsed in order to obtain high peak power and is tunable in wavelength. The laser beam is converted to a very thin (two-dimensional) sheet of light by the combina-

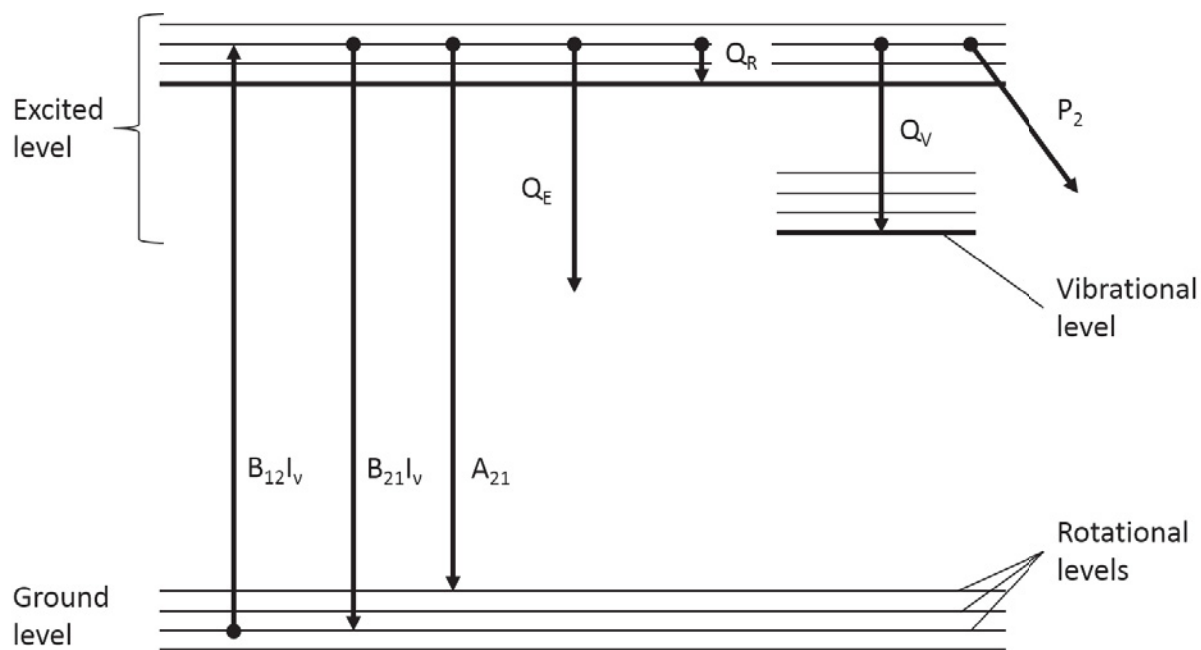


Figure 3.8: Simplified scheme of laser-induced fluorescence and relaxation processes in a multi-level system [55]

tion of a cylindrical lens and a plano-convex lens. The wavelength of the laser is tuned to a value that corresponds to the energy difference between two particular energy levels of the species to be detected. The exact energetic state of the valence electrons of a molecule can be characterized by the energy level, which is further divided into a number of rotational and vibrational levels. A fraction of the ground state molecules absorbs the incident laser light and is excited to a higher electronic energy state (excited state). This procedure is indicated by the vertical upwards pointing arrow in Fig. 3.8, where B_{12} is the Einstein coefficient for induced absorption and I_v is the spectral intensity of the laser light. After a very short residence time between 10^{-8} and 10^{-5} s a number of different relaxation processes are possible for the molecules, which are also schematically depicted in Fig. 3.8 [55, 77].

- Stimulated emission: The electron returns to the exact same energetic level from where it has been excited (ground state) through laser-stimulated emission of a photon with the same wavelength as the laser light $\rightarrow B_{21} \cdot I_v$
- Fluorescence: The electron returns to an energetically higher or equally high quantum state of the ground level by spontaneous emission of fluo-

Transition (Nomenclature)	Wavelength [nm]	Transition probability [-]
$X^2\Pi(v'' = 0) \rightarrow A^2\Sigma^+(v' = 0)$	≈ 308	$1.073 \cdot 10^{-2}$
$X^2\Pi(v'' = 0) \rightarrow A^2\Sigma^+(v' = 1)$	≈ 283	$2.636 \cdot 10^{-3}$
$X^2\Pi(v'' = 0) \rightarrow A^2\Sigma^+(v' = 2)$	≈ 262	$4.161 \cdot 10^{-4}$
$X^2\Pi(v'' = 0) \rightarrow A^2\Sigma^+(v' = 3)$	≈ 248	$5.987 \cdot 10^{-5}$
$A^2\Sigma^+(v' = 1) \rightarrow X^2\Pi(v'' = 1)$	≈ 315	-

Table 3.1: Overview of vibrational transitions of the OH-radical [73]

rescent light ($\lambda_{fluor} \geq \lambda_{laser}$) $\rightarrow A_{21}$

- Quenching: The molecule returns to the ground level or another excited level through collisions with other molecules ($\rightarrow Q_E$), or a population redistribution within the excited energy level occurs, i.e. transfer of rotational or vibrational energy ($\rightarrow Q_R, Q_V$). In all three cases no radiation is emitted.
- Predissociation: The molecule dissociates into other molecules without emitting radiation $\rightarrow P_2$

The signal used in PLIF measurements is the fluorescent light originating from spontaneous emission of photons (A_{21}). The intensity of the fluorescent light of one particular electronic transition is measured by means of an ICCD (Intensified Charged-Coupled Device) camera after the light has passed through a filter, which is mainly transparent for light with the desired wavelength. As already mentioned above, the tuned, monochromatic laser beam is able to accurately excite one specific energy level of a molecule. From quantum mechanics it is known at which wavelengths an excited species can emit light. Thus, if the detection wavelength of the ICCD camera (filter) is chosen such that it is different from the wavelength of possible fluorescent light of any other molecule in the test area, the existence of a particular species can be proved. The OH-radical is taken as an example: It can be excited from the ground state by laser light at a wavelength of $\lambda \approx 283$ nm while the fluorescence is measured at $\lambda \approx 307$ nm. The wavelengths and the transition probabilities for five common transitions of the OH-radical are shown in Tab. 3.1.

PLIF systems have been used since 1984 and are meanwhile state of the art in combustion research. They allow for the localization of the flame front and the

reaction zones and can even be used for quantitative temperature and concentration measurements. However, the necessity of having a pump laser, a tunable dye laser, optical equipment and an ICCD-camera make them very expensive. Moreover, the maintenance effort is quite high because the dye of the dye laser must be changed regularly and the laser beam needs to be aligned from time to time. Nevertheless, the results that can be obtained with such a system are outperforming those of many other systems. PLIF systems allow for very high temporal resolution because of the very short laser pulses and they are therefore capable of studying highly transient processes. In combination with an ICCD camera, which is capable of detecting very low fluorescence intensities down to single photons, very high spatial resolution can be achieved. Consequently, PLIF systems are very helpful for the optimization of combustion processes [4].

3.4.4.2 Simultaneous PLIF and Chemiluminescence

In the present study, a high-speed PLIF system comprising of a pulsed, frequency doubled Nd:YVO₄ pump laser (Edgewave IS8II) and a tunable dye laser (Sirah Credo) was used to obtain time-resolved information about the flame shape during the onset of flashback. Only one of the two pump laser cavities was operated at a frequency of 20 kHz, emitting radiation at a wavelength of $\lambda=532$ nm (pulse duration: 8 ns). The required output wavelength of $\lambda=282.925$ nm for the excitation of the OH molecule was adjusted in the dye laser, with Rhodamine 6G used as dye. The PLIF system is described in further detail in [11]. For image recording, a high-speed camera (Photron FAST-CAM SA-X) was combined with an image intensifier (Hamamatsu C10880-03). By attaching a band pass filter (transmission range: 320 ± 20 nm) to the camera, the LIF signal, which appeared at a wavelength around $\lambda=307$ nm, could be separated from the excitation wavelength. Moreover, limiting of the exposure time to only 110 ns yielded negligible distortion of the PLIF signal due to line-of-sight integrated OH* chemiluminescence ($\lambda=307$ nm) coming from the flame (cf. Fig. 3.9).

PLIF measurements were conducted both with a standard UV lens ($f=105$ mm) for macroscopic measurements and with a UV long distance microscope (La Vision Questar QM1 UV, specifications in Appendix B.2) for microscopic measurements (μ -PLIF). The experimental setup was identical to that for the PIV

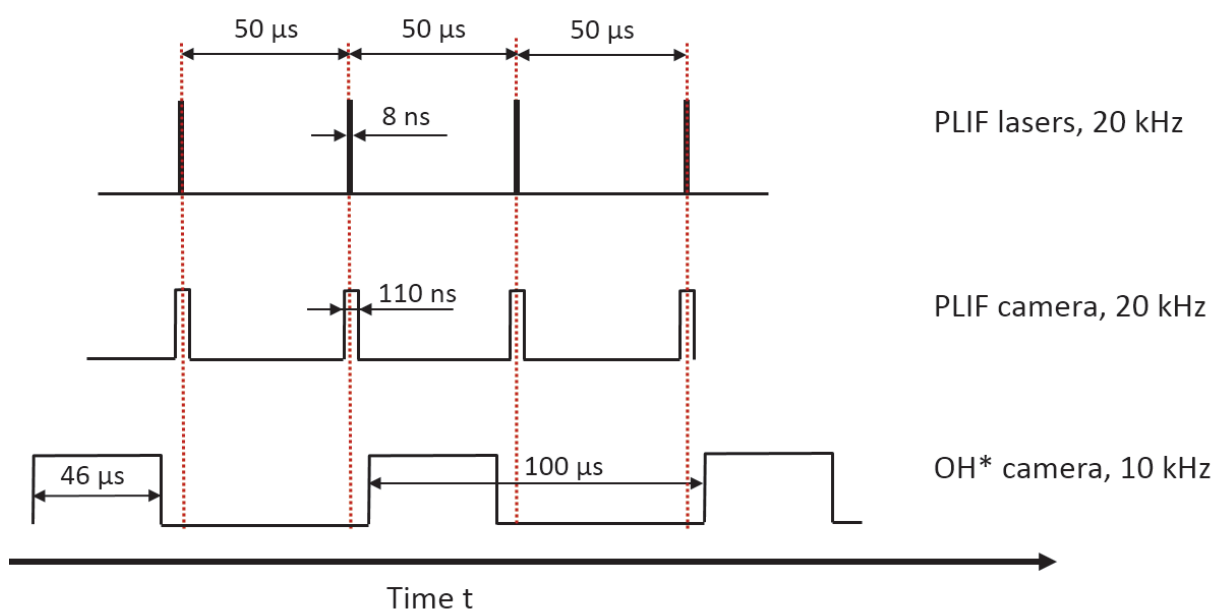


Figure 3.9: Synchronization scheme for simultaneous application of PLIF and chemiluminescence (not true to scale)

measurements described in Sec. 3.4.3.2, including the simultaneous capture of the OH^* chemiluminescence from the top at a frame rate of 10 kHz (cf. Fig. 3.6). PLIF laser, PLIF camera and image intensifier as well as the chemiluminescence high-speed camera were synchronized by means of a digital delay generator (Stanford Research DG645) according to the synchronization scheme shown in Fig. 3.9. As illustrated in the figure, the exposure time of the OH^* camera is limited to $46 \mu\text{s}$ (max. exposure time at 10 kHz: $100 \mu\text{s}$). Despite using a bandpass filter (transmission range: $307 \pm 5 \text{ nm}$), this was necessary in order to remove the intense laser pulse from the recorded frame.

4 Isothermal Flow Fields

As mentioned in Sec. 1.2, the objective of the present project was to investigate flame flashback under well-defined boundary conditions. For this purpose, the isothermal flow fields in the test setups, i.e. the flow fields without combustion, had to be characterized. This was done for both the TUM burner (cf. Sec. 3.1.1) and the channel burner (cf. Sec. 3.2). It was particularly important to accurately determine the shape of the axial velocity profile at the burner exit, i.e. at the position of the stable flame, because the flashback propensity of flames will be mostly expressed in terms of critical wall velocity gradients of the approaching flow (cf. Chs. 5 and 6). Since the BaCaTeC burner (cf. Ch. 3.1.2) and the TUM burner were identical with regard to the hardware installed directly upstream of the stable flame position, the corresponding isothermal flow fields near the burner outlet, which is the flow region that is relevant for flashback studies, could be considered similar. Therefore, the BaCaTeC burner was not investigated separately.

4.1 Tube Burner

Due to the small length-to-diameter ratio of the quartz glass tube ($L=400$ mm, $d=40$ mm), it was not known a priori whether the velocity profile at the tube outlet is fully developed. Thus, theoretical correlations for fully developed, turbulent pipe flow could not be used for the determination of the velocity gradients without verification. In order to obtain realistic velocity gradients, a combined experimental and numerical approach was chosen. First, the velocity profile above the burner exit was measured by means of particle image velocimetry (PIV). The measured profile was then compared to a Reynolds-averaged Navier–Stokes (RANS) simulation, and the quality of the match in the outer region of the boundary layer and the core flow field was assumed to be an indicator for the agreement of the wall friction between measurement and simulation.

For the PIV experiments, TiO_2 seeding particles were injected into the flow inside the plenum (cf. Fig. 3.1). The data evaluation was performed with the commercial software Dantec FlowManager [24] using interrogation areas of size 32×32 pixels and an overlap of 75 %. After cross-correlation, a window filter with plausible values for maximum und minimum flow velocities was applied, in order to remove velocity outliers. As the conditions during the measurements were stationary, it was averaged over 150 instantaneous velocity fields to obtain a representative average velocity distribution at the burner outlet.

The RANS simulations were performed in ANSYS CFX 12.0 using two different two-equation turbulence models — the $k-\omega$ model and the shear stress transport (SST) model (cf. Sec. 2.1). In both cases, the wall boundary layers were fully resolved ($y^+ < 1$, no automatic wall functions). The simulation domain comprised of the entire plenum, the nozzle and the quartz glass tube (cf. Fig. 3.1). At the inlet a constant axial velocity boundary condition (block profile) and a medium turbulence intensity of the flow of $Tu=5\%$ were prescribed. Given the high pressure loss caused by the sintered metal plate at the bottom of the plenum and the associated flow homogenization, this was a reasonable assumption. At the outlet of the domain an atmospheric pressure boundary condition was applied.

The resulting experimental and numerical velocity profiles at the tube burner exit for pure air at two different bulk flow velocities ($\bar{u}=7.5\text{ m/s}$ and $\bar{u}=10\text{ m/s}$) are exemplarily shown in Fig. 4.1 (the flow in the large-volume plenum is shown in Appendix A). Aside from minor discrepancies, the experimental results and the simulations match very well in the outer boundary layer region and the core flow. Deviations are observed in the region where the shear layer between particle-laden flow and atmosphere has started to deform the boundary layer profile in the experiment. The simulation using the SST turbulence model, which is known to combine the good near-wall behavior of the $k-\omega$ model and the excellent far-field behavior of the $k-\epsilon$ model, shows a slightly better match to the experiment and has been chosen for all following comparisons. It is concluded from Fig. 4.1 and analogous results from measurements at various bulk flow velocities that the velocity gradients at the wall are accurately represented by the RANS simulations. In a next step, the RANS velocity gradients are compared to predictions from the Blasius correlation for fully developed turbulent pipe flow [110]:

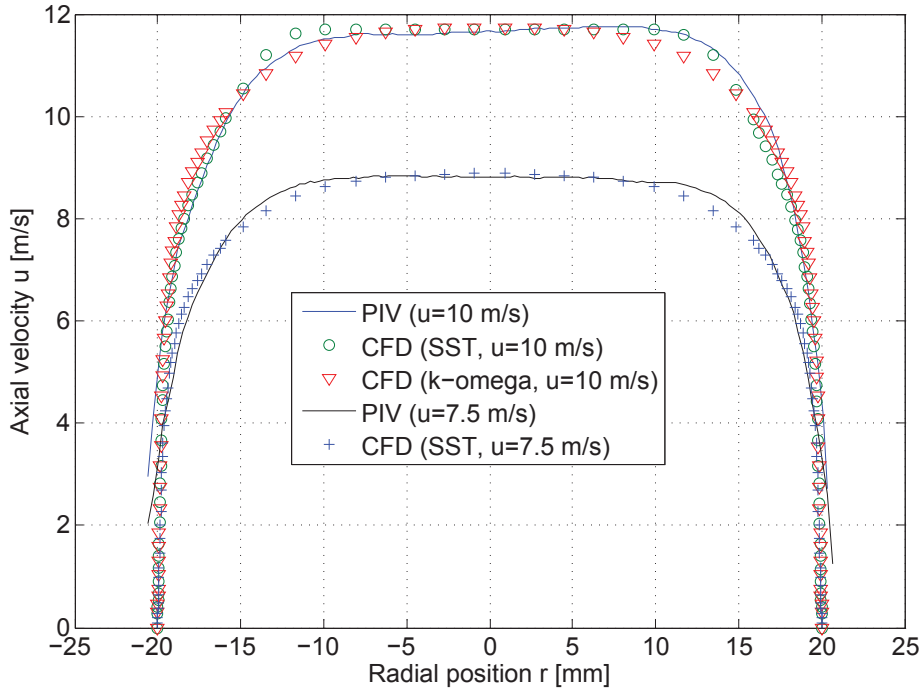


Figure 4.1: Isothermal velocity profiles at tube burner outlet

$$g = \frac{\tau_w}{\mu} = 0.03955 \bar{u}^{7/4} \nu^{-3/4} d^{-1/4} \quad (4.1)$$

In Eq. (4.1), g is the velocity gradient at the wall, τ_w the wall shear stress, μ and ν the dynamic and the kinematic viscosity of the mixture, respectively, d the tube diameter, and \bar{u} the bulk flow velocity.

Although the flow in the experimental setup was not fully developed, it turned out that this has no appreciable effect on the velocity gradients at the wall (mean errors lay within $\pm 4\%$). Thus, the latter can be calculated from the correlation of Eq. (4.1). In order to gain further insight into the nature of the flow, the boundary layer shape factors introduced in Sec. 2.1.1 were calculated. Applying Eqs. (2.28)-(2.32) to the velocity distributions in Fig. 4.1 delivers $H_{12}=1.48$ and $H_{32}=1.77$ for $\bar{u}=7.5$ m/s, and $H_{12}=1.45$ and $H_{32}=1.77$ for $\bar{u}=10$ m/s, respectively.¹ Thus, the shape factors demonstrate that the boundary layer profile can be considered perfectly turbulent.

As a result, the critical gradients in the flashback experiments were calculated

¹ For U_∞ , the maximum values of u in Fig. 4.1 were taken.

according to Eq. (4.1). The dynamic viscosity μ of the gas mixture was calculated according to Wilke's method [89] using Eqs. (4.2)-(4.4).

$$\mu_{H_2-air} = \mu_{H_2} \left(1 + \phi_{12} \frac{X_{air}}{X_{H_2}}\right)^{-1} + \mu_{air} \left(1 + \phi_{21} \frac{X_{H_2}}{X_{air}}\right)^{-1} \quad (4.2)$$

$$\phi_{12} = \frac{1}{2\sqrt{2}} \left(1 + \frac{M_{H_2}}{M_{air}}\right)^{-0.5} \left(\left(1 + \frac{\mu_{H_2}}{\mu_{air}}\right) \left(\frac{M_{air}}{M_{H_2}}\right)^{0.25} \right)^2 \quad (4.3)$$

$$\phi_{21} = \frac{1}{2\sqrt{2}} \left(1 + \frac{M_{air}}{M_{H_2}}\right)^{-0.5} \left(\left(1 + \frac{\mu_{air}}{\mu_{H_2}}\right) \left(\frac{M_{H_2}}{M_{air}}\right)^{0.25} \right)^2 \quad (4.4)$$

In Eqs. (4.2)-(4.4), M is the molar mass and X is the molar fraction of hydrogen and air, respectively. The bulk flow velocity u in Eq. (4.1) was obtained from the measured gas flow rates and the mixture density. The kinematic viscosity ν of the mixture was determined using Eq. (4.5).

$$\nu_{H_2-air} = \frac{\mu_{H_2-air}}{\rho_{H_2-air}} \quad (4.5)$$

In the case of preheated mixtures, the temperature dependence of the dynamic viscosity of the single components was taken into account by the empirical correlation given in Eq. (4.6) [121]. Here, A, B, C, D and E are constants that are tabulated in [121]. The respective values for hydrogen and air are shown in Tab. 4.1.

$$\mu(T) = A + B T + C T^2 + D T^3 + E T^4 \quad (4.6)$$

	A	B	C	D	E
H ₂	0.18024 · 10 ⁻⁵	0.27174 · 10 ⁻⁷	-0.13395 · 10 ⁻¹⁰	0.00585 · 10 ⁻¹²	-0.00104 · 10 ⁻¹⁵
Air	-0.03287 · 10 ⁻⁵	0.77996 · 10 ⁻⁷	-0.48801 · 10 ⁻¹⁰	0	0

Table 4.1: Constants for the calculation of the dynamic viscosity

4.2 Channel Burner

The channel burner test rig used in this project was a modification of a former test rig at the Lehrstuhl für Thermodynamik that was developed by Eichler [29, 30]. The modification only concerned the experimental infrastructure downstream of the burner exit (cf. Sec. 3.2). Eichler measured and simulated the flow inside the burner and found that the high aspect ratio cross-section produces a quasi-2D flow field in the lateral center region of the flow channel. Additionally, he performed μ -PIV measurements for two different air mass flow rates at three axial positions upstream of the burner exit. The latter is located at $x=0$ mm (cf. Fig. 3.4). Figure 4.2 shows a comparison of the wall shear stress obtained from μ -PIV with that predicted by Eq. (4.7) for fully developed turbulent channel flow [127].

$$\bar{u} = u_\tau \left(\frac{1}{\kappa} \ln \frac{h u_\tau}{\nu} + B - \frac{1}{\kappa} \right) \quad (4.7)$$

Equation (4.7) is derived from the law-of-the-wall in Eq. 2.25 and the shear stress velocity u_τ can be calculated by Eq. (2.23). It is obvious that the measured shear stress converges toward the correlation value in downstream direction (i.e. for decreasing x), because the flow adopts an almost fully developed channel velocity profile. Eichler concluded that the wall shear stress and the corresponding wall velocity gradient at the burner exit can be calculated from Eq. (4.7) with a conservative error estimation of $\pm 10\%$. Thus, Eq. (4.7) was used in this thesis for determining the velocity gradients. For this purpose, Eqs. (4.7) and (2.23) were solved iteratively with the software MATLAB using a Newton solver with an appropriate initial estimate of the solution. The calculation of the bulk flow velocity, the mixture density and the viscosities were carried out in the same manner as for the tube burner (cf. Sec. 4.1).

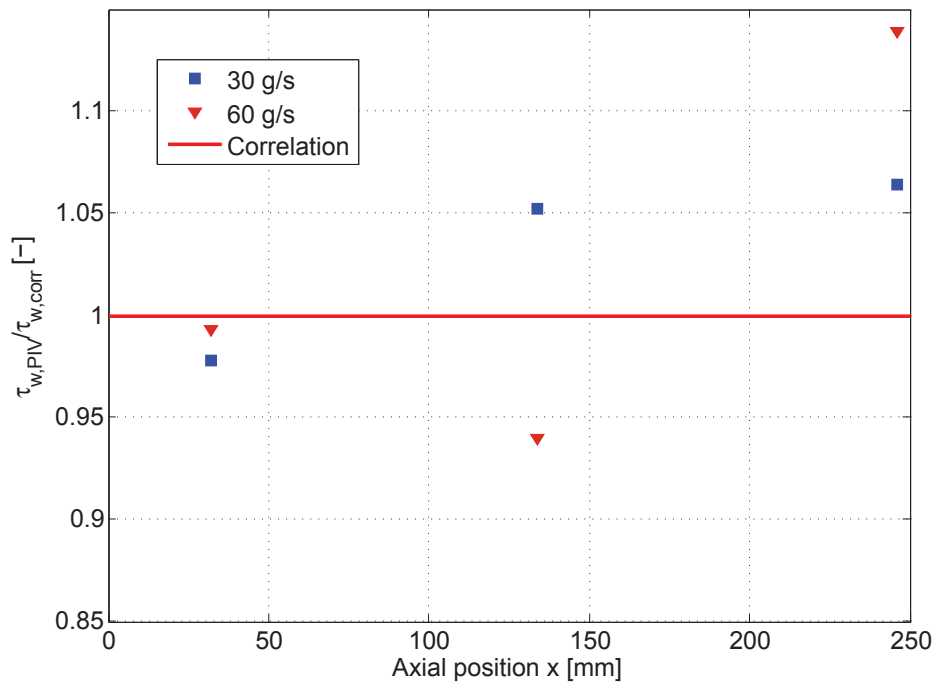


Figure 4.2: Comparison of wall shear stress from μ -PIV with theoretical correlation [29]

5 Macroscopic Flashback Studies - Various Burner Configurations

In this chapter, the macroscopic flashback behavior of hydrogen-air flames is analyzed for a wide range of geometrical burner configurations [26, 31]. The associated experiments were conducted at atmospheric pressure and all fresh gas mixtures were at room temperature prior to combustion ($T \approx 293$ K). Furthermore, only turbulent flames are considered in this chapter due to their great importance regarding practical applications.

5.1 General Considerations and Terminology

Referring to the design of the tube burner exits, the four configurations depicted in Fig. 5.1 were considered. *Bare* denotes a tube without any further equipment, *open* refers to a tube where the stable flame was burning in the free atmosphere on top of a pilot burner (brass or stainless steel) that was attached to the tube. In the *confined* configuration the stable flame was tightly surrounded by a concentric ceramic block with a diameter slightly bigger than that of the tube. In this configuration the flame was also burning on top of the pilot burner. The setup is referred to as *enclosed* when the flame on top of the pilot burner was surrounded by a large diameter quartz glass enclosure. In the open, confined and enclosed setups, cooling of the installed pilot burner could be either enabled or disabled. As for the channel burner, only results for *confined* setups from [29] and an *open* setup, respectively, are presented in this work. In both cases, the burner tip was convectively cooled with air.

During all experiments the burner tip temperature was logged using a type K thermocouple. If not explicitly stated otherwise, the test procedures described in Sec. 3.3 were employed for the flashback tests. To check the reproducibility of the results, the flashback tests were repeated at least three times for each (global) air mass flow rate. The resulting critical equivalence ratios at flash-

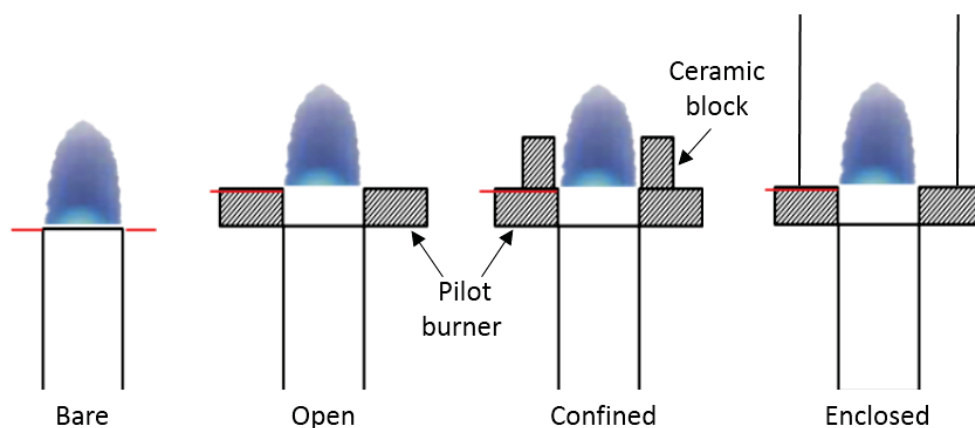


Figure 5.1: Terminology for burner configurations (cf. [26]); thermocouples in red

back were found to scatter within $\Delta\Phi = \pm 0.05$ about the average value during all tests, demonstrating good reproducibility. The flashback propensity of flames will be either expressed as critical velocity gradients or - if the latter cannot be calculated accurately - as critical bulk flow velocities. Here, the term *critical* refers to the condition at the onset of flashback. This classical approach has been adopted in almost all flashback investigations in the literature (cf. Ch. 1) and thus facilitates comparison with these data and transfer of the results to practical applications. In spite of the weaknesses of the critical gradient model (cf. Sec. 1.1.2), it will be shown in Chs. 7 and 8 that the critical velocity gradient can be used as an appropriate measure for the flashback propensity of unconfined flames.

In the majority of the flashback experiments the OH^* chemiluminescence (cf. Ch. 3.4.1) from the flame was monitored by an intensified charge-coupled device (ICCD) camera using a UV lens and a bandpass filter, which mainly transmitted light in a wavelength range of $\lambda=302\text{-}312\text{ nm}$. The camera used was a Hamamatsu C4336-02 with a resolution of 720×480 pixels, which recorded images at a frame rate of 30 Hz in continuous mode. Depending on the application, this camera was substituted for a high-speed camera, as will be mentioned in the respective locations in the text.

Prior to systematic flashback investigations the suitability of the TUM burner test rig for flashback tests was examined through comparison of the flashback limits with literature data. Khitrin et al. [64] measured critical bulk flow velocities for turbulent H_2 -air flames at atmospheric pressure and ambient temperature using tubes with different diameters. The flames were burning into

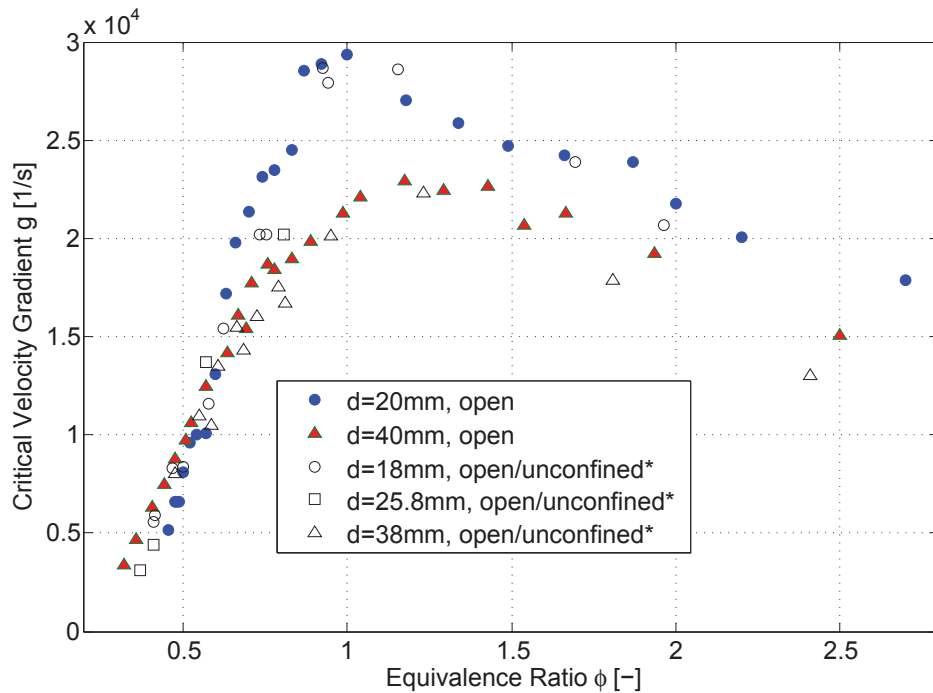


Figure 5.2: Comparison of tube burner flashback data with literature data [64]*

the free environment, but the exact design of the burner outlet regarding material and burner tip cooling is not stated in the publication. Therefore, the term *open/unconfined* is used for this configuration. Applying Eq. 4.1 to the given bulk flow velocities yields the critical velocity gradients. The latter are compared to the flashback limits measured with the *open* configuration of the TUM burner in Fig. 5.2.

It is apparent that the literature data could be reproduced very accurately with the TUM Burner setup over a wide range of equivalence ratios. The slightly higher critical gradients of the $d=18$ mm tube, in particular around stoichiometric conditions, were also reproduced. Sufficient cooling of the burner tip in the $d=20$ mm case was a little harder to achieve, because an insert with an inner diameter of $d=20$ mm was employed to adapt the $d=40$ mm pilot burner (Fig. 3.2) accordingly. Nevertheless, the tip temperatures for both the $d=20$ mm and the $d=40$ mm tube were very similar ($T_{tip} < 330$ K), which excludes the temperature as a possible explanation for the slightly different flashback propensity. Two conclusions can be drawn from the experiments:

- The TUM Burner test rig is suitable for systematic flashback tests.

- As is stated in [64], the tube diameter seems to play only a minor role with regard to flashback propensity (see also Sec. 5.4).

5.2 Effect of Flame Enclosure on Flashback Propensity

As was described in Sec. 1.1.2, Eichler [29] performed experiments with turbulent, atmospheric, *confined* H₂-air flames in quasi-2D channel flow. He found that the flashback propensity in terms of critical velocity gradients is substantially higher than for *open* tube burner flames (cf. [31]). As a reason for this, he proposed the experimentally and numerically observed interaction of the confined flame with the approaching mixture flow, causing flow separation upstream of the leading flame tip (see also [32]). However, it is unclear whether the peculiar geometry (quasi-2D channel flow versus rotationally symmetric tube flow) contributes to the observed effect. To clarify this issue, two different tests were conducted. First, a flame confinement was realized for the TUM tube burner to compare the obtained flashback limits with those of the confined channel flames. Second, the original channel burner setup was modified such that open channel flames could be studied and compared to the open tube flames.

5.2.1 Confined Flame Holding

The TUM burner with the $d=40$ mm tube was equipped with a concentric ceramic block ($d=44$ mm) downstream of the pilot burner, which tightly confined the stable flame. For these tests a previous version of the pilot burner was used, which was made from brass and was convectively cooled with air (cf. [31]). The setup yielded a backward-facing step of 2 mm and is shown in detail in Fig. 5.3.

The flame holding is illustrated in Fig. 5.4. Here, three images are superimposed – the instantaneous OH* intensities of the confined and the open flame, respectively, along with a (background) image of the pilot burner at ambient light. The OH* images were recorded at an exposure time of 1 ms and the edges of the ceramic block are marked by white lines. The following observations can be made:

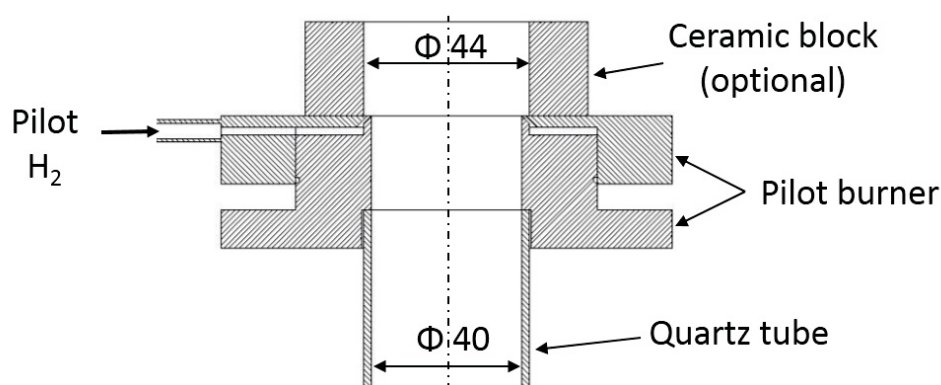


Figure 5.3: Pilot burner with flame confinement [31]

1. The line-of-sight integrated OH^* signal near the flame base is most intense in the far left and the far right side, indicating that the flame is stabilized in the shear layers above the pilot burner.
2. The flame in the confined case is not stabilized above the ceramic block as there is a rather large gap between the upper edge of the ceramic block and the OH^* signal detected at this position. By contrast, the flame cone in the confined case coincides well with the one in the unconfined case, implying that the flame is stabilized above the pilot burner in both setups. (Note: In the confined case no OH^* intensity from the flame inside the ceramic block can be captured. Due to the superposition of the confined and the open flame, the OH^* intensity above the ceramic block abruptly increases.)
3. The flame clearly flashes back along the wall boundary layer.

A scatter plot of the flashback limits for the confined tube and channel flames can be seen in Fig. 5.5. For comparison, the flashback limits from the open tube burner as well as those from [64] are also plotted (only average values from [29] are shown). Additionally, recent data of Shaffer et al. [111] for a $d=21.8$ mm tube with a $d=23.2$ mm ceramic confinement are included in the plot. The vast difference in the critical velocity gradients between confined and open flames, which reaches almost one order of magnitude for near-stoichiometric conditions, also holds for both tube burners. Interestingly, even the influence of the height of the backward-facing step is correctly

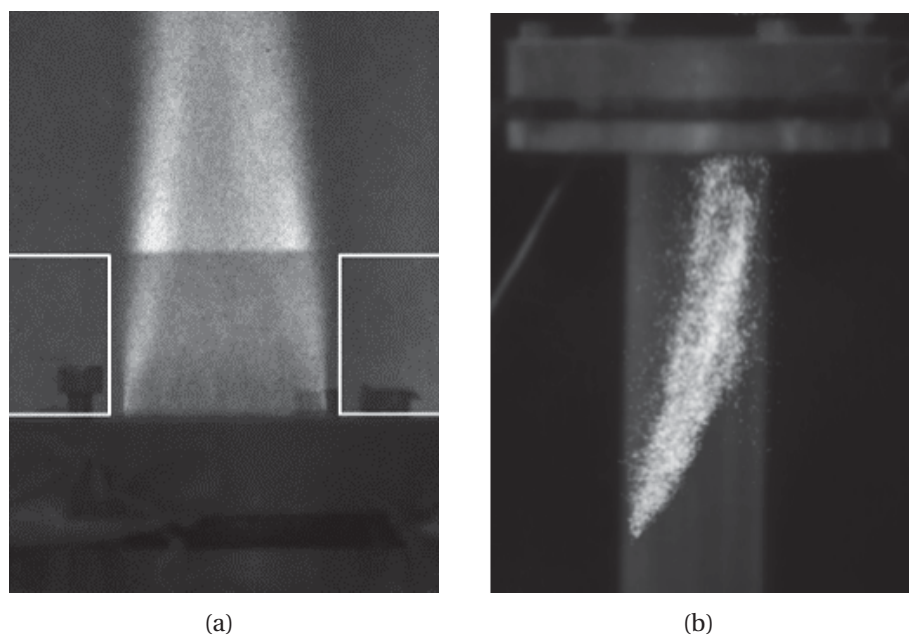


Figure 5.4: Superposition of unconfined and confined flame in stable mode (a) and flame at flashback (b). The white lines mark the edges of the ceramic block.

reflected. Step heights smaller than 2 mm could not be realized for the TUM burner, because the stable flame would not stabilize inside the confinement but downstream of it. The findings will be further discussed in Ch. 7 and theoretically analyzed in Sec. 8.1.

5.2.2 Open Flame Holding

Following up on the effect of confinement, the flashback limits for open channel flames were measured and compared to that for open tube flames ($d=20$ mm and $d=40$ mm). In this context the flashback process in the channel burner has been visualized by means of simultaneous OH^* measurements from the side and from the top. The instantaneous views shown in Fig. 5.6 demonstrate that the flame flashed back along the lower wall boundary layer in the lateral center region of the channel duct. As mentioned in Sec. 3.2, the lower wall was 7 mm longer than the upper wall during all tests. The critical velocity gradients are plotted in Fig. 5.7. It can be seen that the flashback propensity of the channel flames is slightly higher in the very lean range, but matches very well with the open tube flames with increasing equivalence ratio. This applies in particular to the tube with diameter $d=20$ mm, which is close to the height of the channel ($h=17.5$ mm). Furthermore, it has been veri-

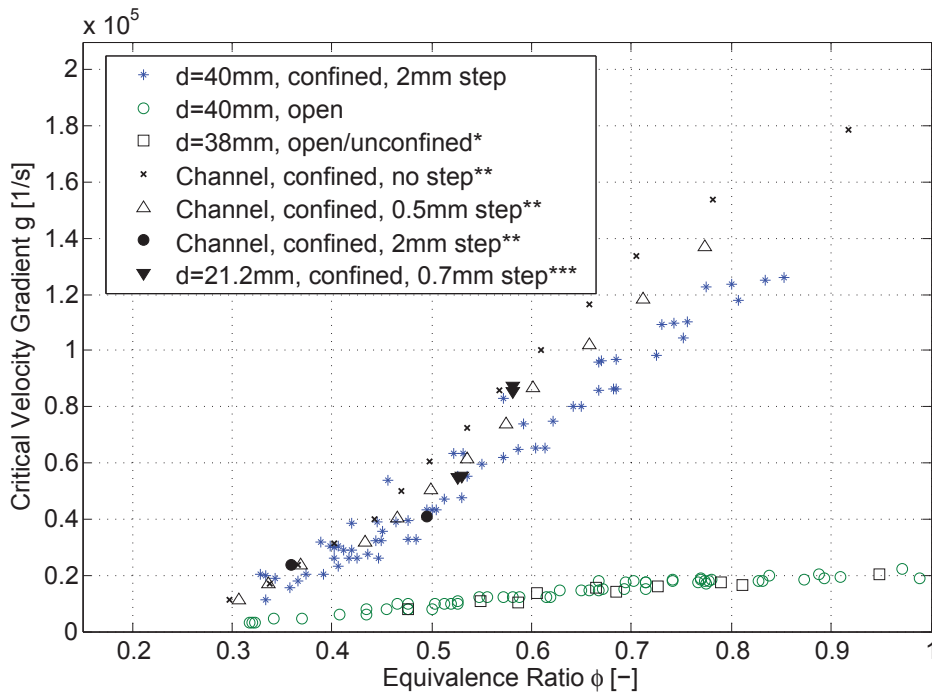


Figure 5.5: Flashback limits for confined flames, [64]*, [29]**, [111]***

fied that there is negligible influence of the 7 mm offset on the flashback limits by conducting some of the experiments with equally long burner walls.

From the results presented in Figs. 5.5 and 5.7, it can be concluded that the vast difference in flashback propensity between confined and open flames stems from the confinement, whereas the flow geometry (circular vs. rectangular) has no significant influence. In Ch. 7, the flame-flow interaction for open flame stabilization will be elaborated in detail.

5.2.3 Influence of Enclosure Size

To further investigate the influence of confinement on flashback behavior, tests with larger enclosure sizes, i.e. with a huge jump in diameter between injector and enclosure, were performed. These tests are referred to as *enclosure tests* and they were carried out with the BaCaTeC setup (cf. Sec. 3.1.2). Both a quartz tube ($d=21.9$ mm) and a stainless steel tube ($d=21.9$ mm) were considered as injectors in combination with a quartz enclosure ($d=44.9$ mm). Due to a lack of cooling capability, the tests were conducted without burner rim cooling. Some of the quartz test results were reported previously by the

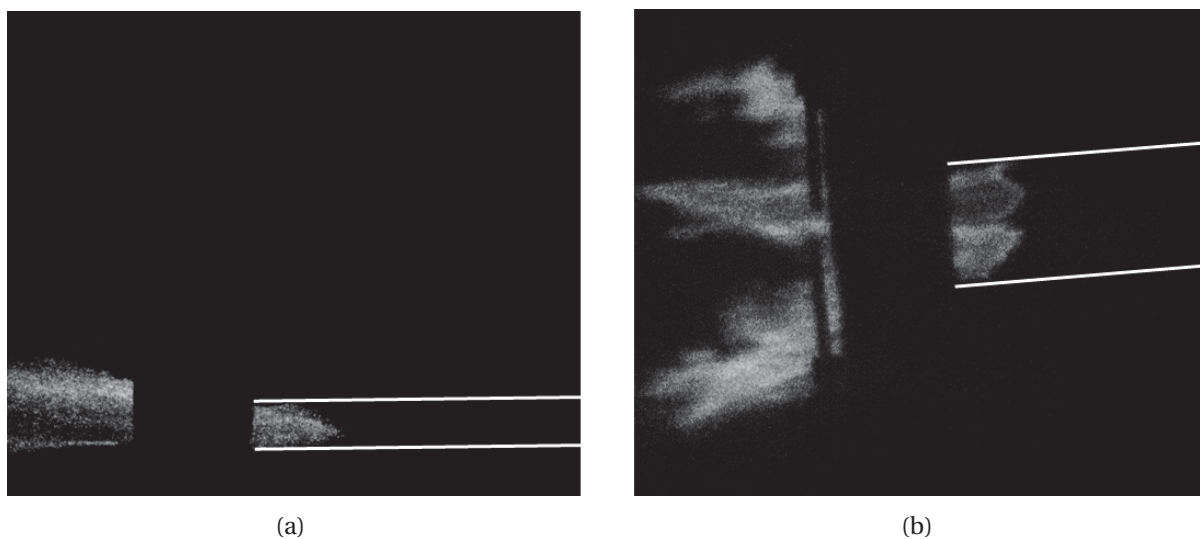


Figure 5.6: Flashback process in the channel burner: Instantaneous OH* images from the side (a) and from the top (b). In (a) the white lines mark the upper and the lower wall, respectively; in (b) they mark the lateral boundaries of the inspection window; flow direction from right to left

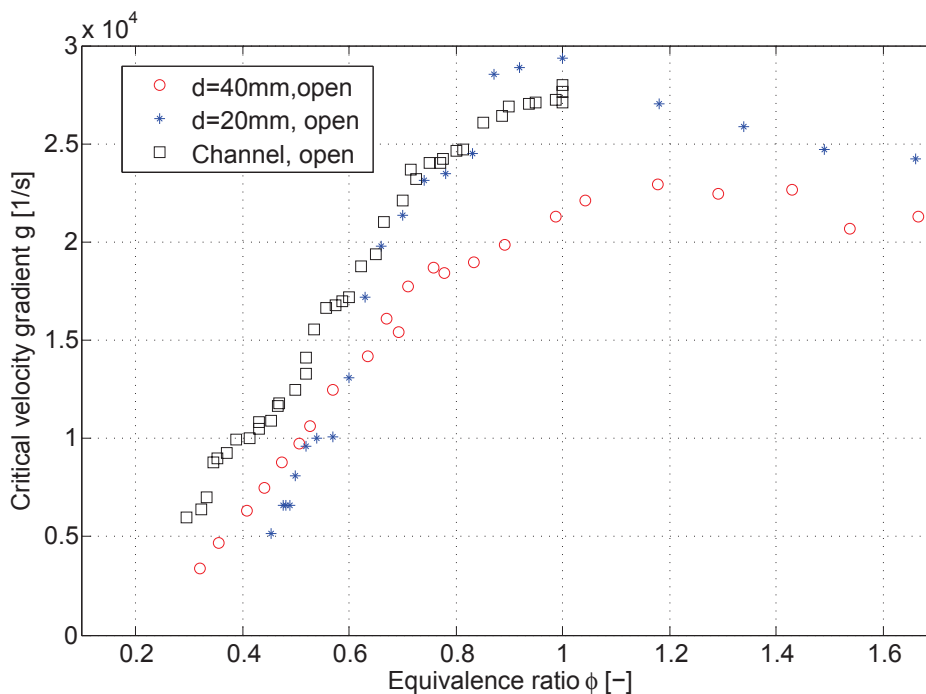


Figure 5.7: Flashback limits for open tube and channel flames

UCI [111], but additional data was added under the same conditions within the BaCaTeC cooperation between TUM and UCI (cf. Sec. 3.1).

Figure 5.8 compares the results of the enclosure tests to that of the tests without enclosure (open configuration). It can be seen that the flashback propensity for enclosed flames is generally greater than for open flames. It is also noticeable that the enclosure influence is more significant for the quartz injector. Figure 5.9 presents the tip temperature variation associated with the application of the enclosure. Only the metal tube data are included, because the tip temperatures of the quartz tubes were not measured in [111]. It can be seen that the enclosure increases the tip temperature significantly, reaching about $\Delta t=200$ K for $\Phi=0.64$. Since the thermal conductivity of quartz is lower than that of metal, it can be expected that the difference in tip temperature between the enclosed and the open quartz tube is even higher (see also Sec. 5.3).

The increase in tip temperature is likely to be responsible for the deviations in flashback propensity between open and enclosed flames. This hypothesis is corroborated by flashback experiments conducted at the UCI with a bigger enclosure size ($d=63.6$ mm) on top of the two burner tubes [111]. The authors measured the response of the flashback propensity and the associated tip temperature to the change of enclosure size. It turned out that neither the tip temperature nor the flashback limits are particularly susceptible to changes of the enclosure size. Therefore, it is concluded that the differences in flashback stability are primarily caused by the associated change in burner tip temperature, which results from the blocked entrainment of cold ambient air. This means that the flashback behavior is not very sensitive to changes in the aerodynamics caused by different enclosure sizes. It is important to note that these observations only apply to enclosures that are large compared to the burner diameter.

5.3 Influence of Burner Material on Flashback Behavior

As mentioned above, the burner material seems to play a significant role for the flashback resistance. This is an important observation since quartz is extensively employed in research to provide for optical access, whereas metal alloys are predominant in practical applications. Therefore, this material effect is discussed in more detail. The application of a quartz tube generally yielded

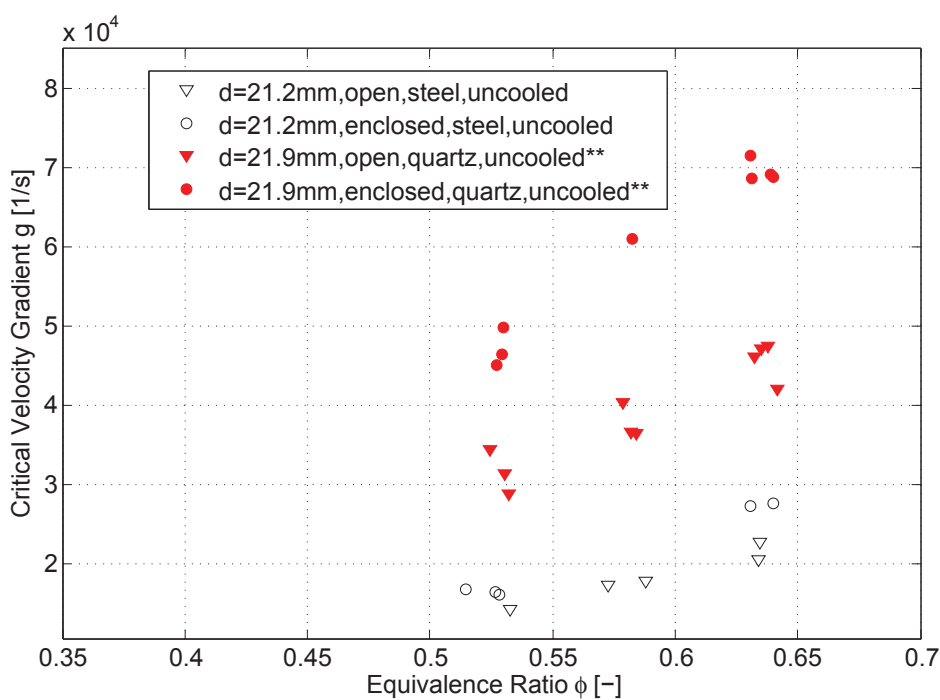


Figure 5.8: Effect of enclosure on flashback limits, [111]*

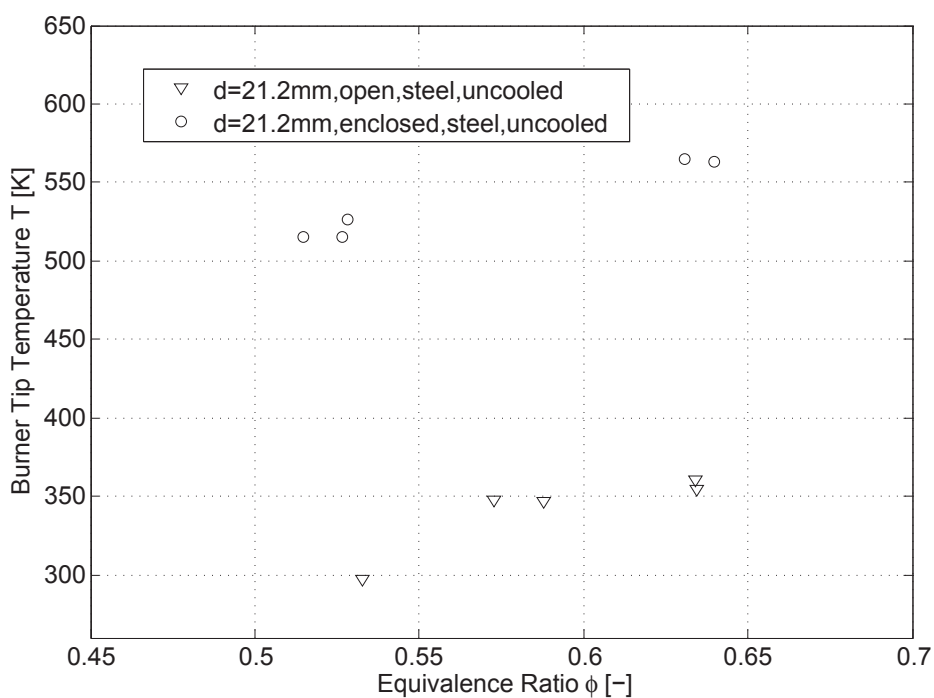


Figure 5.9: Effect of enclosure on burner tip temperature

a higher flashback propensity than that of a metal tube (Fig. 5.8). Shaffer et al. [111] reported that they could complete confinement tests only with an uncooled steel tube but not with an uncooled quartz tube due to severe experimental conditions, which again indicates that quartz reduces the resistance to flashback. However, these material effects were observed only indirectly because other parameters were varied simultaneously. This complicates the direct comparison of the materials. Therefore, a specific study on the material effect has been conducted.

5.3.1 Flashback Limits

Figure 5.10 presents the results of this study. Here, the BaCaTeC setup was simplified such that only the bare tube was left. The metal injector was made of 4130 alloy steel and two sizes of quartz injectors were tested. As shown, the tube diameter has no significant effect but the flashback propensity of the quartz tubes is larger than that of the metal tube. The discrepancy in thermal conductivity of the two materials is believed to be one of the reasons for the different flashback tendencies. Steel conducts the heat better and therefore tends to yield lower tip temperatures than the quartz tube. This is illustrated in Fig. 5.11. It is important to note that the tip temperatures for both materials were measured at the outer surface of the tube. Thus, the temperature at the inner surface of the tube is higher than indicated by the thermocouples. This applies in particular to the quartz tube. This topic is elaborated in [27], where the authors concluded that given the same heat load, quartz tubes generate a greater temperature difference between inner and outer surface than metal tubes because of their lower thermal conductivities.

Comparing the tip temperature differences plotted in Fig. 5.11 with those in Fig. 5.9, it is obvious that the difference in critical velocity gradients between quartz and steel cannot be explained by the tip temperature alone (cf. also Fig. 5.8). Instead, another effect originating from the material itself must be present. Therefore, this issue clearly requires further clarification in the future before meaningful conclusions can be drawn.

Another interesting observation was made about the flame propagation during flashback. The flame regressed completely into the mixing plenum during all of the flashback events with metal tubes. On the contrary, the flame stayed

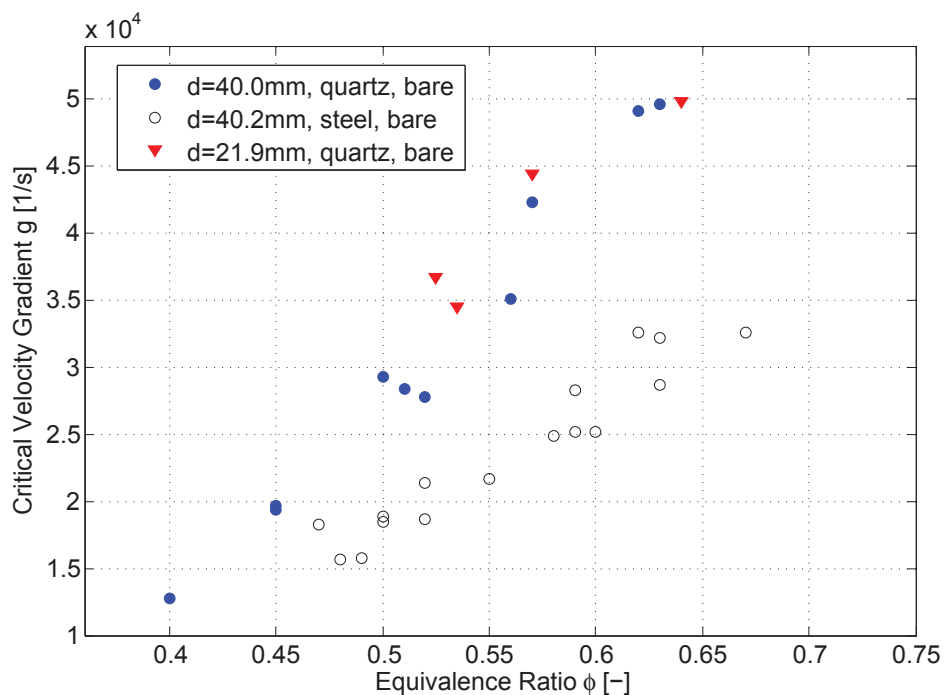


Figure 5.10: Influence of burner material on critical velocity gradients (derived from [26])

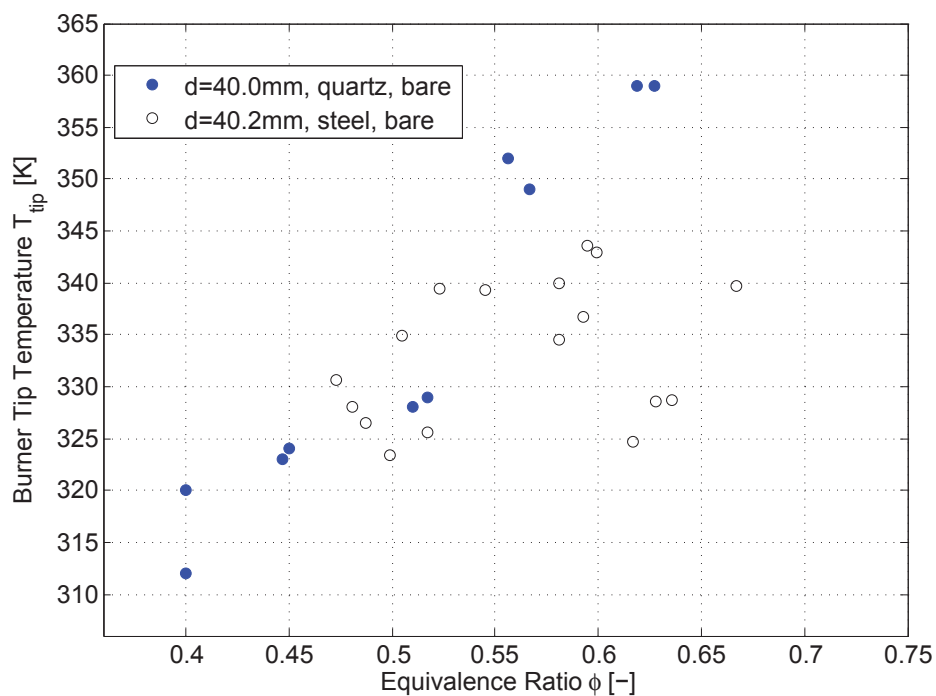


Figure 5.11: Influence of burner material on tip temperature (derived from [26])

inside the tube for a certain time during most of the tests with quartz tubes. This can again be traced back to the different thermal conductivities of the materials used. As for steel, neighboring regions are heated up more rapidly when the flame is inside the tube, which leads to very fast upstream propagation. For the quartz tube, this process is much slower, yielding slow regression speeds. This effect can potentially be utilized in a real application through applying low-conductivity burner materials or coatings, such that active control mechanisms can more easily react to incipient flashback events.

5.3.2 Theoretical Heat Transfer Analysis

In an attempt to theoretically analyze the impact of heat conduction on the upstream flame propagation a heat transfer analysis was conducted. Assuming a close connection between wall temperature and flame regression propensity, the unsteady term $\partial T/\partial t$ determines the propagation rate. The propagation of temperature gradients in the tube wall is connected with the following three terms – heat conduction, heat convection, and heat radiation. As the variation of material does not affect heat convection, this term can be omitted. As a first approximation, the radiative term is also neglected. Thus, the energy equation of the solid wall can be written as follows:

$$c\rho \frac{\partial T}{\partial t} = \lambda \frac{\partial^2 T}{\partial x^2} \quad (5.1)$$

Rearranging of the equation shows that the propagation speed is determined by the response ratio $\lambda/(c\rho)$:

$$\frac{\partial T}{\partial t} = \frac{\lambda}{c\rho} \frac{\partial^2 T}{\partial x^2} = a \frac{\partial^2 T}{\partial x^2} \quad (5.2)$$

The response ratio $\lambda/(c\rho)$ is also known as the thermal diffusivity a . Table 5.1 presents the corresponding thermophysical properties of quartz, alloy 4130, and brass. Inserting these values into Eq. (5.2), the response ratio turns out to be $a=0.42 \cdot 10^{-6} \text{ m}^2/\text{s}$ for quartz and $a=10.88 \cdot 10^{-6} \text{ m}^2/\text{s}$ for alloy 4130. It suggests that the temperature response due to flame propagation is much slower for quartz than for the steel tube. Additionally taking into account heat radiation would result in an even bigger difference in response ratio, because some

heat might be radiated through the quartz tube, whereas the metal tube is opaque. Thus, the approach above yields the minimum difference in response ratio between steel and quartz. The results of this analysis are consistent with the observed lagged flashback in [111] during tests with an uncooled, confined quartz tube.

5.4 Summary of the Findings for Different Burner Types and Preliminary Conclusions

A summary of all flashback limits measured for turbulent, atmospheric hydrogen-air jet flames at ambient temperature is given in Fig. 5.12. Data from tests with confinement and enclosure are plotted with filled symbols and red color is used for all quartz tube data. The following observations can be made:

1. A significant difference in flashback propensity between unconfined and confined flames is evident. This is true for all tube diameters and all materials as well as for different burner geometries. Explanations for this behavior will be provided in Ch. 7.
2. The effect of the burner material on flashback propensity is clearly visible, with quartz injectors being more flashback-prone than metal injectors. Small deviations can even be distinguished between brass and stainless steel. The difference in thermal conductivity of the materials has been proposed as an explanation for this behavior (cf. Sec. 8.2.3).
3. Differences in the nature of the upstream flame propagation during flashback have also been discussed for the various burner configurations. Due to the low thermal conductivity of quartz, the flame regression into

Material	Thermal capacity c [J/(kg·K)]	Thermal conductivity λ [W/(m·K)]	Density ρ [g/cm ³]	Response ratio $a = \lambda/(c\rho)$ [m ² /s]
Quartz	1,500	1.38	2.2	$0.42 \cdot 10^{-6}$
Alloy 4130	500	42.7	7.85	$10.9 \cdot 10^{-6}$
Brass (CuZn30)	398	121	8.55	$35.6 \cdot 10^{-6}$

Table 5.1: Thermophysical properties of quartz, brass and alloy

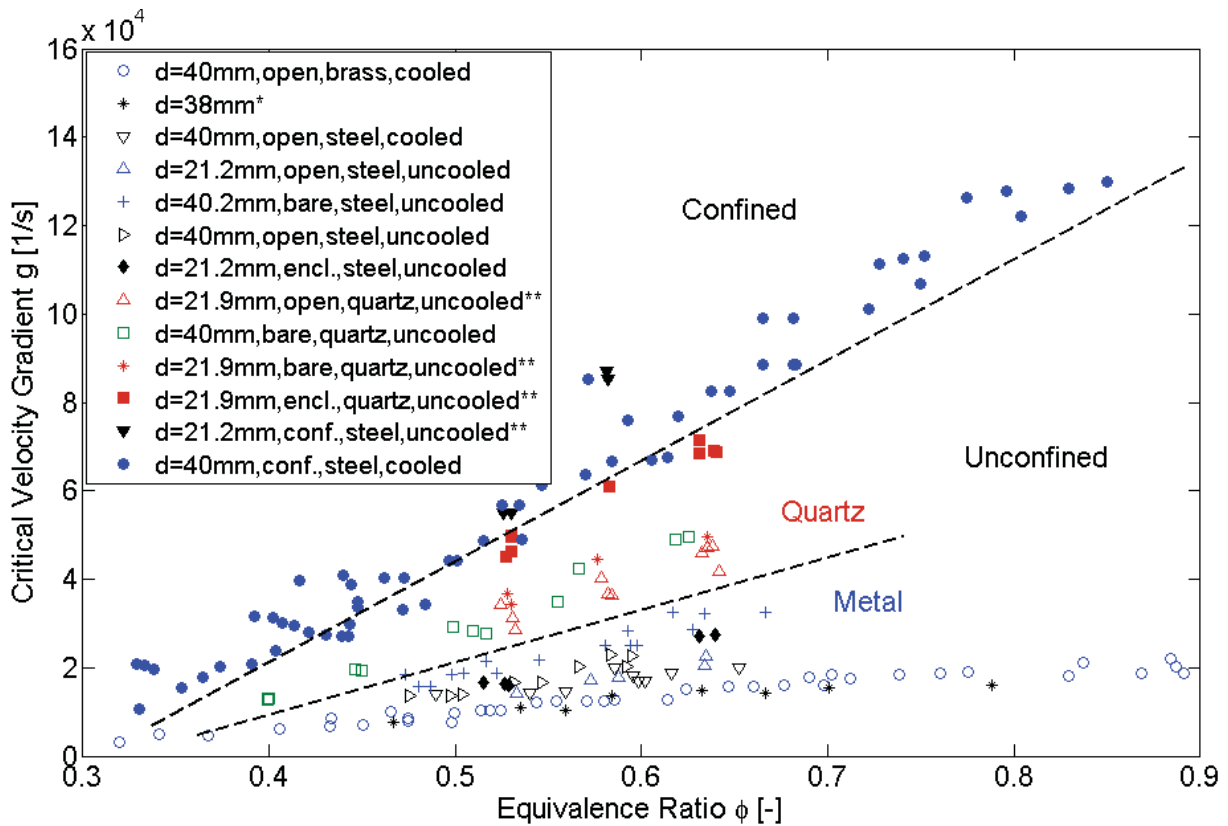


Figure 5.12: Overview of flashback limits for atmospheric H_2 -air flames, [64]*, [111]**

the premixing section is considerably slower than for a metal injector (cf. Sec. 5.3).

4. For a given material, the increase in flashback tendency due to a large-diameter flame enclosure is mainly caused by higher burner tip temperatures. The size of the enclosure was found to have only a weak influence.
5. In terms of critical velocity gradients, the burner diameter was found to have no discernible influence on the flashback limits of the turbulent hydrogen-air jet flames considered in this study. The same observation was reported by Khitritin et al. [64].

The results demonstrate that burner material, flame confinement and tip temperature have a strong effect on the flashback propensity, whereas flame enclosure diameter and burner tube diameter play a negligible role. Within the configurations tested, the lower and upper limits of flashback propensity for atmospheric hydrogen-air flames were observed for a cooled, unconfined brass injector and an uncooled, confined quartz injector, respectively. The

flashback limits for the latter configuration are not explicitly given in Fig. 5.12, because the experimental infrastructure did not allow for testing under such severe conditions (excessive heat transfer from the ceramic block to the injector, imminent burner damage, cf. [111]). The influential parameters on flashback propensity will be further discussed in Ch. 8 on the basis of a new flashback model.

6 Macroscopic Flashback Studies - Variation of Operating Conditions

In this chapter, the macroscopic flashback behavior of hydrogen-air flames is analyzed for different operating conditions [5, 6]. The associated experiments have been conducted at atmospheric pressure. Except for the tests with preheating (Sec. 6.1), all mixtures were at room temperature prior to combustion ($T \approx 293$ K) and only turbulent flames are considered in this chapter.

6.1 Flashback Limits for Preheated Mixtures

Both in stationary and mobile gas turbines the fluid is compressed before it is burned in the combustion chamber. Since this compression is accompanied by a temperature increase, it is - from a practical point of view - important to gain insight into the flashback behavior of both preheated and pressurized mixtures. With the experimental facilities described in Ch. 3 testing is only possible under atmospheric pressure. However, the electrical heater installed along the air supply line allows for assessing the effect of preheating. Two measurement campaigns with preheating temperatures up to $T=673$ K were carried out using the TUM burner and the BaCaTeC burner, respectively (cf. Sec. 3.1). Mineral wool was used in both setups to insulate the components downstream of the heater. The experiments were conducted according to the experimental procedure described in Sec. 3.3.1. During testing all burner equipment was given sufficiently long time to reach thermal equilibrium after each stepwise change in mass flow rates. For this purpose, four additional thermocouples were distributed alongside the TUM burner tube to measure its temperature from the outside. The temperature of the unburnt gas mixture was measured inside the plenum. To account for the temperature drop due to heat losses along the tube, the preheating temperature at the tube exit was determined as follows: In the first step, the temperature of the fresh mixture inside the plenum was adjusted to a value that was a little higher than

the targeted preheating temperature, and a flashback test was performed. In the second step, the flashback mass flow rates were readjusted but without combustion taking place. Thereafter, a thermocouple was immersed in the flow at the center of the tube exit to measure the temperature. In this manner, the preheating temperature could be determined very accurately without perturbing the flashback process. The resulting temperatures deviated from the targeted temperatures ($T=473$ K and $T=673$ K for the TUM burner; $T=473$ K and $T=623$ K for the BaCaTeC burner) within $\Delta T=\pm 15$ K. Air was used instead of water for cooling the pilot burner in order to match the temperature of the unburnt gas. As the preheating test procedure was very time-consuming, only a limited set of equivalence ratios was tested at two different preheating temperatures.

In Fig. 6.1 the flashback limits for the TUM burner are displayed for two preheating temperatures ($T=473$ K and $T=673$ K). Referring to the nomenclature in Fig. 5.1, an open configuration with a steel pilot burner on top of a quartz glass tube was used. It is evident that the flashback propensity increases with higher temperature for all mixture compositions. This could be expected, because the laminar flame speed of hydrogen-air mixtures increases with the preheating temperature, which leads to higher flashback propensity. In the literature, power law correlations are often proposed for the temperature dependence of the laminar, unstretched flame speed in the form of Eq. (6.1), with the exponent usually ranging between $n\approx 1.4$ [21] and $n\approx 1.7$ [100] for lean, atmospheric H_2 -air flames.

$$S_{l,H_2-air} \propto T^n \quad (6.1)$$

In an attempt to quantify the effect of preheating on the flashback limits a power-law fit is included in Fig. 6.1. Based on the results for room temperature (T_0) a proportionality exponent of $n=1.3$ (cf. Eq. 6.2) reflects the effect of preheating very precisely for both elevated temperatures over the whole range of equivalence ratios.

$$\frac{g_{c,H_2-air,T}}{g_{c,H_2-air,T_0}} = \left(\frac{T}{T_0} \right)^{1.3} \quad (6.2)$$

Thus, the critical gradients do not scale with the temperature according to

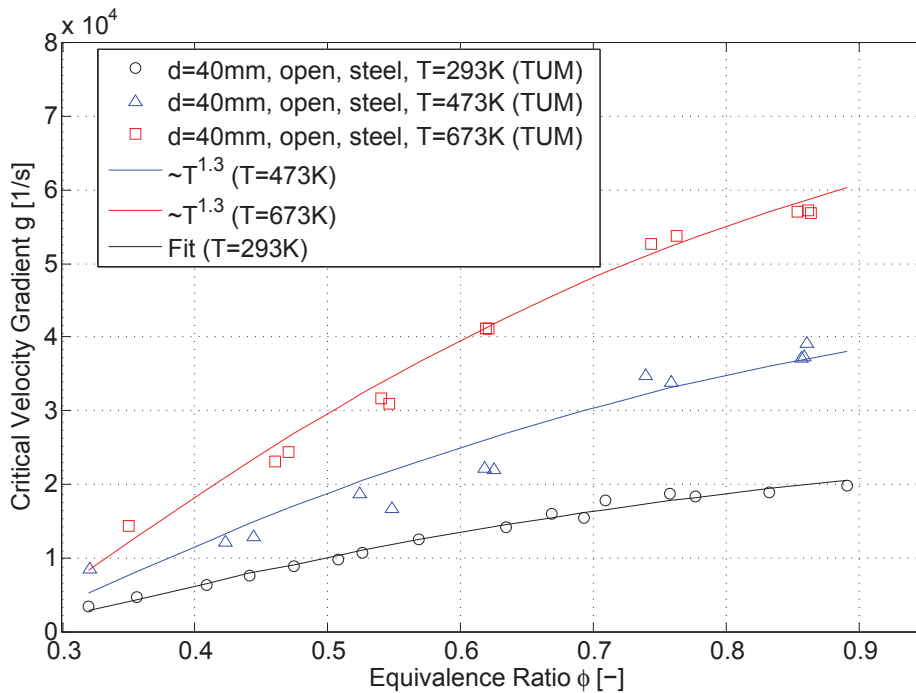


Figure 6.1: Flashback limits for preheated H₂-air flames (TUM burner)

exactly the same proportionality exponent as the unstretched, laminar flame speed. A possible explanation for this is that the actual flame speed at the position of flashback onset may be lower than predicted by Eq. 6.1 due to heat losses and radical recombination processes near the burner rim. Moreover, turbulence and flame stretch effects may impact the real flame speed.

As mentioned above, a number of tests with preheating were carried out with the BaCaTeC setup using a *bare* steel tube, i.e. the burner rim was not cooled. Only a narrow range of equivalence ratios could be covered due to capability limitations of the test rig. The results for room temperature as well as for $T=473K$ and $T=623K$ are shown in Fig. 6.2. The power-law correlation derived from the TUM burner experiments is applied to the room temperature flashback limits, which had to be extrapolated toward the leaner region for meaningful comparison. It can be seen that the flashback stability of this burner configuration is generally lower than that of the cooled TUM burner, as was elaborated in Ch. 5. Nonetheless, the correlation predicts the data for the heated mixtures reasonably well, in particular for $T=473K$. For $T=623K$, the temperature influence is slightly underpredicted. However, there is no room temperature data available in the corresponding equivalence ratio

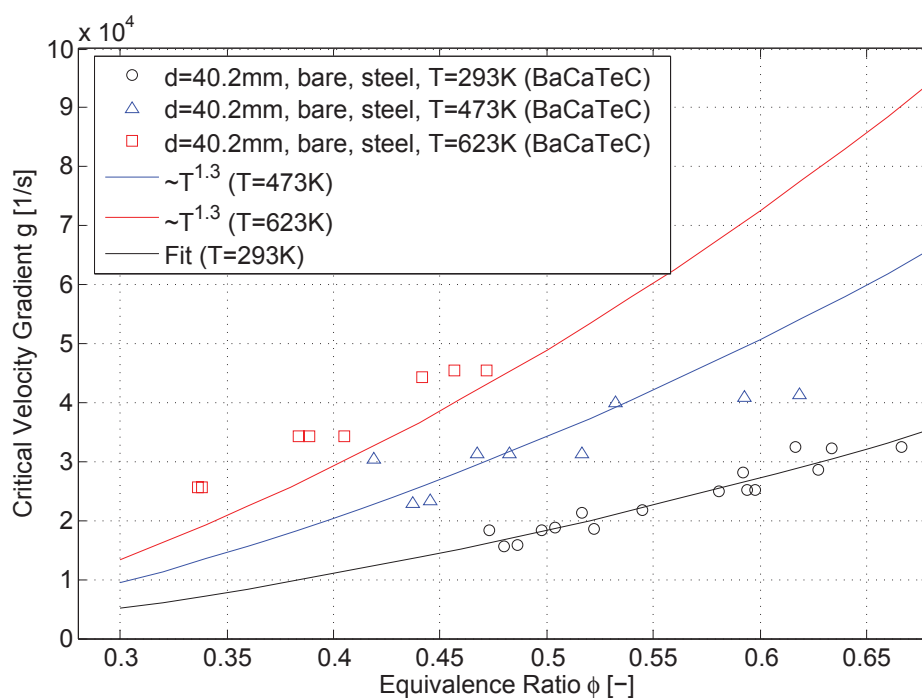


Figure 6.2: Flashback limits for preheated H_2 -air flames (BaCaTeC burner)

range. Thus, the prediction is rather uncertain, because it is solely based on extrapolated data.

In a further step, the results are compared to those obtained by Fine [36], who also conducted flashback experiments with preheated H_2 -air mixtures using an unconfined tube burner (the exact burner configuration according to the terminology defined in Fig. 5.1 is unknown, cf. Sec. 1.1.1). The respective power law correlation was shown in Eq. (1.2). Recalling that Eq. (1.2) has been devised only from experiments with H_2 -air mixtures at an equivalence ratio of $\Phi=1.5$ and at sub-atmospheric operating pressures, Fine's correlation exponent of $n=1.5$ and the one found in the present investigation for lean mixtures agree reasonably well.

Finally, the current results are compared to that obtained by Eichler [29] for preheated, *confined* channel flames. Eichler conducted experiments with lean H_2 -air mixtures at room temperature as well as for two different preheating temperatures ($T=473\text{K}$ and $T=673\text{K}$). As can be seen in Fig. 6.3 the temperature dependence of these flames is different from that for unconfined tube flames. The flashback limits are underpredicted in the very lean region and

strongly overpredicted when approaching stoichiometric conditions. Thus, the temperature dependence of these flames cannot be adequately predicted by means of the power law correlation derived for unconfined flames. This is again an indicator for the entirely different flashback behavior of unconfined and confined flames. While the flame speed essentially controls the flashback process for unconfined flames, the flame backpressure (cf. Eq. (2.46)) is the main driver for the onset of flashback in the confined case (cf. Sec. 8.1 and [32]). The role of the flame backpressure with regard to unconfined flames will be discussed in detail in Ch. 7.

In conclusion, the temperature dependence of the critical velocity gradients for *unconfined* H₂-air flames can be given as between $g_c \propto T^{1.3}$ and $g_c \propto T^{1.5}$.

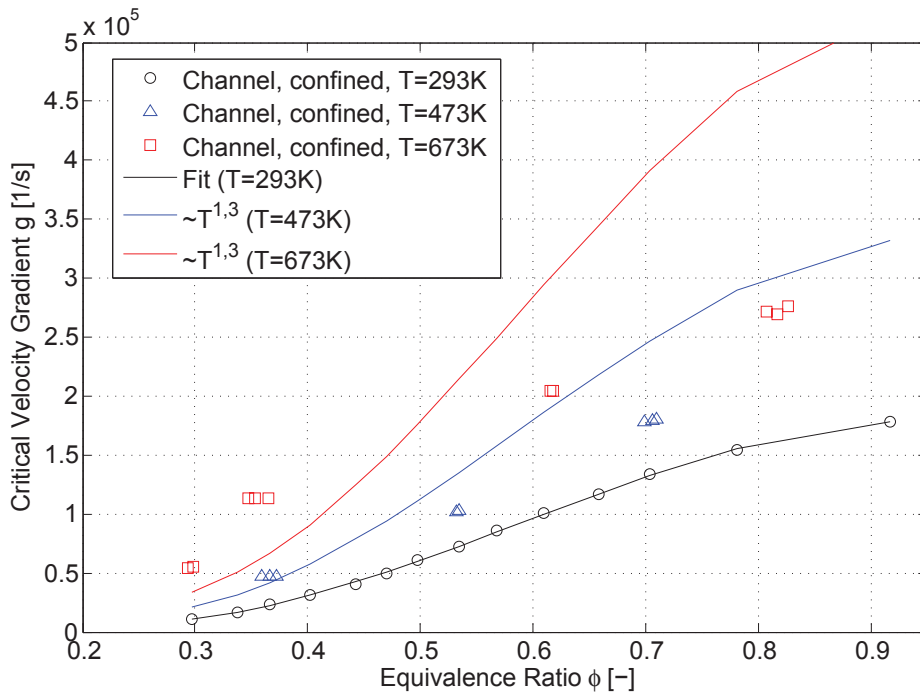


Figure 6.3: Flashback limits for preheated, confined H₂-air channel flames (derived from [29])

6.2 Influence of Swirl on Flashback

High mass flow rates and the corresponding high flow velocities in modern gas turbines require effective flame stabilization methods in order to achieve compact combustor designs, good burnout and stable combustion. For this purpose, a certain degree of swirl is imposed upon the main flow in almost all

gas turbines that are operating with premixed fuels [85]. As was described in Sec. 2.1.3, the aim is to generate a recirculation zone in the combustor close to the burner exit to anchor the flame there. However, above a certain critical swirl number S_c , this recirculation zone is able to move upstream into the burner section, leading to flashback due to Combustion Induced Vortex Breakdown (CIVB).

In the past two decades, several investigations were concerned with this phenomenon [17, 66, 68, 72, 120, 126]. The critical swirl number was found to depend upon many factors, such as geometrical features, flow field, equivalence ratio, Reynolds number, and fuel type [1, 95, 116]. The latter is becoming increasingly important because of the changeover from hydrocarbon fuels to hydrogen-rich synthesis gases in future gas turbines [85]. The limits for critical swirl numbers S_c reported in the literature, below which flashback due to CIVB does not occur, range from $S_c \approx 0.35$ [39] over $S_c \approx 0.4$ [53] to $S_c \approx 0.5$ [85]. Thus, CIVB-driven flashback should not take place in burner configurations with very weak swirl intensities, e.g. $S < 0.3$. However, most of the investigations conducted in the past were dealing with hydrocarbon fuels or synthesis gases with relatively low hydrogen content, whereas flashback prevention is particularly challenging when it comes to premixed combustion of pure hydrogen and air. For mixtures with very high burning velocities, even fairly low swirl intensities may be sufficient to stabilize the flame in the combustor. Moreover, it is shown in [86, 87] that fuel mixtures can behave very differently than the individual constituents. This has also great impact on the combustion behavior, e.g. flashback, blowout, and auto-ignition. Besides flashback due to CIVB, boundary layer flashback is a second failure mechanism often prevailing in premixed combustion systems, as was shown in the chapters before. Therefore, it is particularly important to gain insight into the combustion behavior when weak swirl is present.

In this section, the effect of weak swirl on the flashback propensity of undiluted hydrogen-air mixtures is elaborated. The swirl intensity was adjusted to a level that flashback due to CIVB was not the dominating flashback mechanism. The turbulent flashback limits were measured at ambient temperature and atmospheric pressure over a broad range of equivalence ratios. Additionally, the upstream propagation of the flame during flashback was studied in detail by means of high-speed measurement techniques.

6.2.1 Experimental Approach and Isothermal Flow Field

In the following sections, the experimental infrastructure will be described and a characterization of the flow field inside the measuring section will be given.

6.2.1.1 Tube Burner Setup

The basic setup of the TUM burner, which was described in Sec. 3.1.1, was extended by a swirl generator that was mounted upstream of the nozzle, as shown in Fig. 6.4. The generic swirl generator, which was developed at the Lehrstuhl für Thermodynamik, is depicted in detail in Fig. 6.5. The main proportion of the flow entered in circumferential direction through eight equally distributed inlet slots. The axial length of the slots was 64 mm and the width was 11.5 mm. A small fraction of the flow was going through the axial inlet orifice at the bottom of the swirl generator to provide the flow with additional axial momentum in the center region of the tube. The orifice diameter was either 12 or 15 mm in the presented experiments. The strength of the swirl that was imposed on the main flow could be varied by partly blocking the circumferential inlet slots with inserts. The shorter the remaining slot length was, the stronger the swirl was.

The goal of this study was to investigate the effect of low swirl on the flashback limits. Therefore, the swirler slots were kept entirely open in all tests. Initial tests with higher swirl intensities led to flashback due to CIVB over the whole range of equivalence ratios, which is not the focus of this thesis. Experimental and numerical investigations of the flow field generated by the swirler have shown that the swirl number for both axial inlet diameters was below $S=0.275$.

6.2.1.2 Isothermal Flow Field

The flashback propensity measured in the experiments will be expressed as critical bulk flow velocities as well as in terms of critical velocity gradients of the approaching flow. Therefore, it was important to know the shape of the velocity profile at the tube exit. The isothermal flow field for the configuration without swirl generator has already been described in Sec. 4.1.

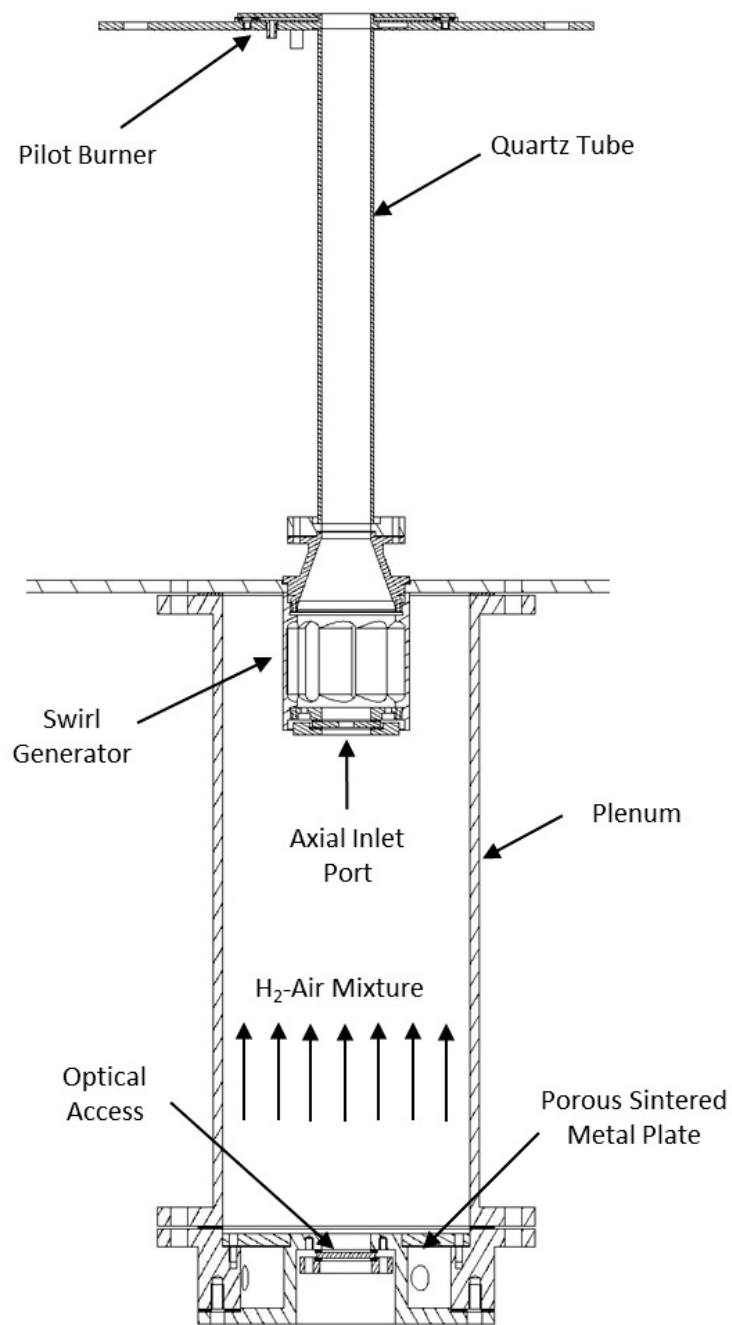


Figure 6.4: Flashback test rig with optional swirl generator

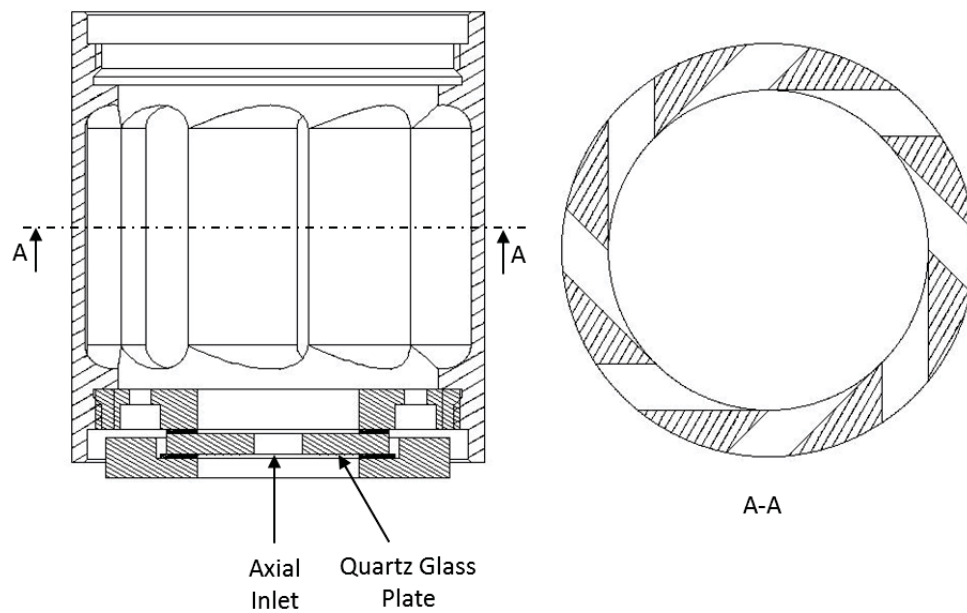


Figure 6.5: Details of the swirl generator

For the setup with swirl generator, Reynolds Averaged Navier Stokes (RANS) simulations were performed in Ansys CFX for the two different axial inlet diameters. Due to the swirling motion of the flow, the full 3D-geometry of the tube burner including the plenum was considered. Contrary to the simulations for non-swirling flow in Sec. 4.1, the wall boundary layer inside the tube was modeled by wall functions in CFX to save computing time. According to [107] a value of $y^+ \approx 30$ is ideal for using automatic wall functions. In the present simulations the value was in the range of $y^+ = 28-32$. Regarding the turbulence modeling, the Reynolds Stress Transport model (RSM) is usually favored for swirling flow due to the presence of anisotropic turbulence [57]. Nevertheless, to keep the computing time within a reasonable level, the SST turbulence model was used. Since the swirl intensity in the experiments was fairly low, the anisotropism of the turbulence can be considered low as well, such that reasonable results can be expected. Figure 6.6 compares the axial velocity profiles at the tube exit for the two swirl configurations with the one for non-swirling flow. All simulations were performed for air at atmospheric conditions and a bulk flow velocity of $\bar{u} = 12.0$ m/s. It can be seen that the two profiles for swirling flow are considerably flatter than the one for non-swirling flow. Nevertheless, the injection of the axial centerline flow yields a jet-like velocity profile even for the setups with swirling flow. Note that the boundary layer region is fully simulated in the non-swirling case, whereas wall functions were applied in the simulation with swirl. It is apparent that the 15 mm orifice

yields slightly higher axial velocities in the tube center than the 12 mm orifice, both of which are considerably lower than in non-swirling flow.

In Sec. 4.1 it was shown that the velocity profile at the tube exit for the non-swirling flow configuration was not fully developed, but the velocity gradient g at the wall could be derived from the Blasius correlation for fully developed turbulent pipe flow [110], yielding mean errors of less than $\pm 4\%$. This procedure was also adopted for swirling flow in this study, even though the real velocity gradients are likely to be slightly higher than predicted by Eq. 4.1 because of the centrifugal forces acting on the fluid, leading to higher axial velocities near the wall. The error made for these weak swirl intensities is supposed to be small, yet unknown, and therefore the flashback data will additionally be plotted as critical bulk flow velocities in Sec. 6.2.3. This allowed for testing of a broad range of flashback points without performing time-consuming simulations.

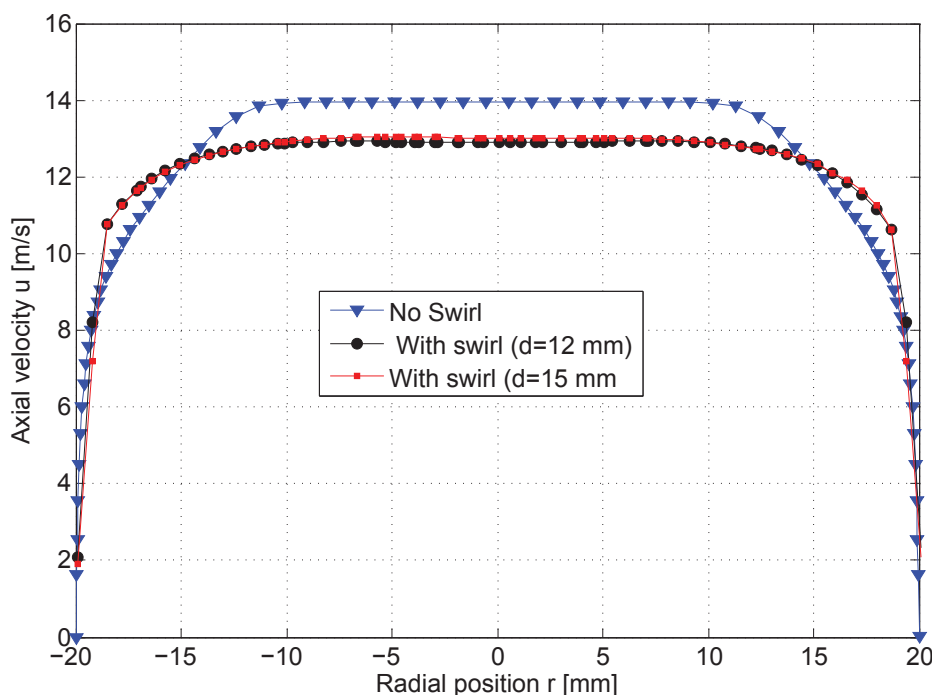


Figure 6.6: Isothermal velocity profiles for non-swirling and swirling flow at tube exit ($\bar{u}=12$ m/s)

6.2.2 Measurement Approach

The turbulent flashback limits were measured according to the procedure described in Sec. 3.3.1. During the majority of the tests the OH*-chemiluminescence from the flame was monitored by an intensified charge-coupled device (ICCD) camera (Hamamatsu C4336-02) using a UV lens and an interference filter, which mainly transmitted light in a wavelength range of 300-350 nm. The camera resolution was 720x480 pixels and the images were recorded at a frame rate of 30 Hz. More advanced measuring equipment was used to study the flashback behavior in detail, which will be described in the following sections.

6.2.2.1 High-Speed Mie Scattering

Looking at the flame from the side through the curved tube walls involves the disadvantage of image distortion in the near-wall region due to reflections. For this reason, a high-speed particle image velocimetry (PIV) system was set up to determine the exact position of the flame tip during upstream propagation in the glass tube via the density of seeding particles that travel with the flow. A schematic of the setup is depicted in Fig. 6.7. A horizontal laser sheet was inserted into the vertical tube at a certain streamwise position. The flow was seeded with TiO₂ particles and the light scattered from the illuminated particles was captured through the window at the bottom of the plenum by a high-speed camera (Photron SA 5). It is well known that the acceleration of the gas flow across a flame front causes a sudden decrease in seeding particle density. Thus, once the propagating flame reaches the laser sheet, the position of its tip within the tube cross-section is visible in the Mie scattering images. In all tests of this study, the frame rate of the high-speed camera was set to 1000 Hz and the horizontal laser sheet was inserted 22 mm upstream of the downstream pilot burner rim in order to determine the position of the flame tip shortly after flashback inception. Even though the Mie-scattering signals from the laser sheet had to pass through approximately 900 mm of seeded flow until they reached the camera, the measurement approach worked very well for non-swirling flames and reasonably well for swirling flames at low equivalence ratios. However, for swirling flames at near-stoichiometric equivalence ratios the images lacked contrast.

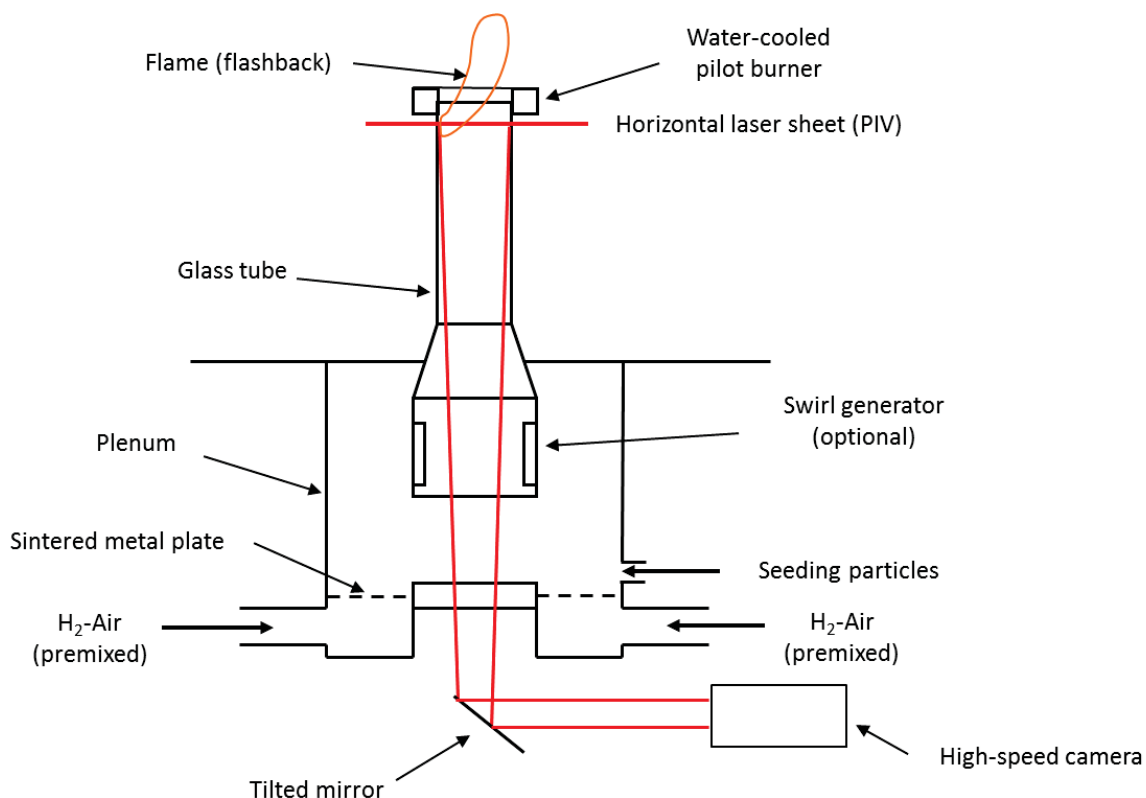


Figure 6.7: Schematic of the high-speed Mie scattering setup

6.2.2.2 Simultaneous High-Speed OH* -Photography from Two Perspectives

In order to overcome the problem of lacking image contrast and to study the detailed three-dimensional upstream motion of the flame at flashback, two identical, synchronized ICCD high-speed cameras (Photron Fastcam-ultima APX I²) were arranged around the vertical tube with an angle of 90° between them (cf. Fig. 6.8). Both cameras recorded the flame from the side. The frame rates were set to 1000 Hz and the image resolution was 1024x1024 pixels. The high-speed cameras were also equipped with UV lenses and interference filters. In this way, it was possible to track the 3D-movement of the flame tip during flashback, although the images from both cameras were line-of-sight integrated. One of the two cameras acted as the master, which gave the trigger signal to the slave (second camera). Both cameras were controlled by the Photron Fastcam Viewer software. The cameras were capable of storing 2048 images, resulting in a total recording time of approximately 2 seconds at the given frame rate. The trigger mode in the software was set to "End"-mode, i.e.

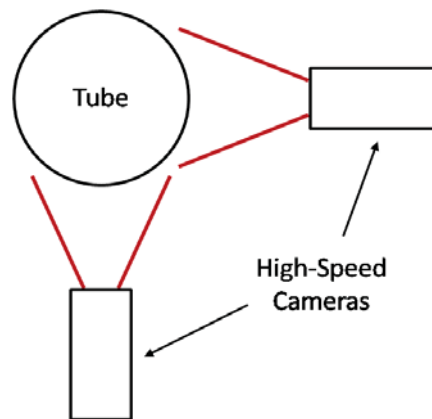


Figure 6.8: Schematic of the high-speed camera setup

the 2048 images prior to the trigger signal were stored. This left enough time to set the trigger signal manually right after a flashback had occurred.

6.2.3 Results and Discussion

In this section the experimental results concerning the turbulent flashback limits for fully premixed hydrogen-air mixtures will be presented first. Thereafter, the detailed upstream propagation of the flame during flashback will be discussed.

6.2.3.1 Flashback Limits

The flashback limits in terms of critical bulk flow velocities for the whole range of equivalence ratios tested are depicted in Fig. 6.9. The graph compares the values of the two swirling configurations with the ones for non-swirling tube flow. The following observations can be made:

1. Up to an equivalence ratio of $\Phi \approx 0.75$, the swirl slightly improves the flashback stability of the burner. This can be explained by the centrifugal forces acting on the fluid, which push the flow radially outwards, resulting in higher axial velocities near the wall when compared to the non-swirling configuration. The simulated isothermal flow fields confirm these higher axial velocities in the near-wall region, in particular up to approx. 5 mm away from the wall. As will be shown in Ch. 7, the leading flame tip propagates upstream approx. 1 mm away from the wall during

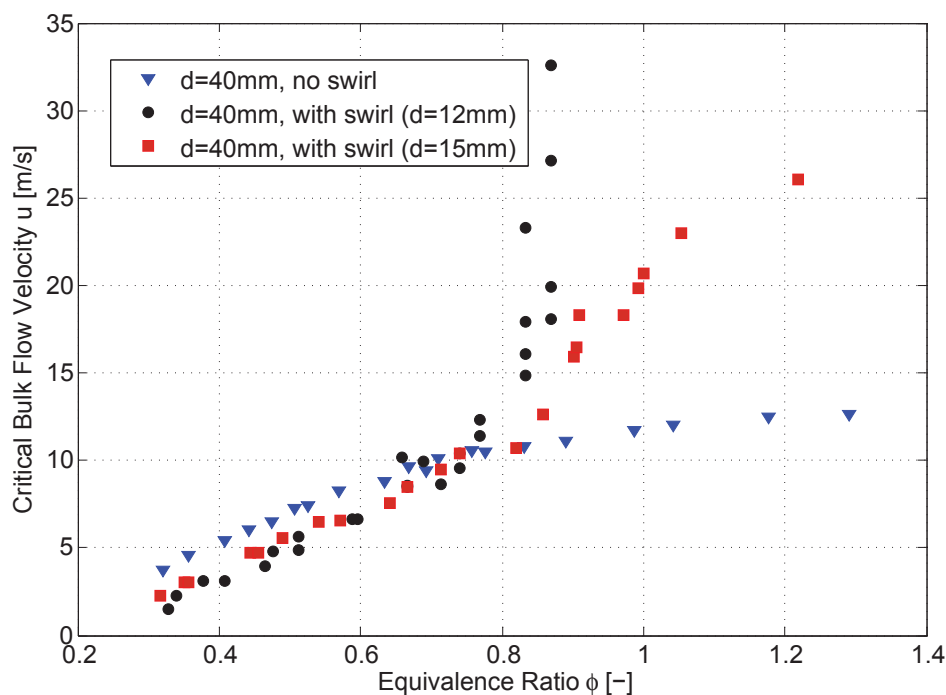


Figure 6.9: Critical bulk flow velocities for non-swirling and swirling H_2 -air flames

flashback, which explains why the swirl configurations are more resistant against boundary layer flashback. Furthermore, the radial outward motion pushes the flame base at the tube exit further out, which in turn counteracts boundary layer flashback. The positive effects on the flashback propensity are slightly weaker for the setup with the 15 mm orifice than for that with the 12 mm orifice. This is plausible because the 15 mm orifice yields higher axial velocities in the center region, which necessarily lead to comparatively lower axial velocities in the near-wall region.

2. Above an equivalence ratio of $\Phi \approx 0.75$, the flashback behavior changes dramatically. Here, the flashback propensity for swirl is substantially higher than for non-swirling flow (higher \bar{u} indicate higher flashback propensity). Contrary to the results for $\Phi < 0.75$, the swirler with the 15 mm orifice exhibits better flashback resistance than the one with the 12 mm orifice. The reasons for the steep increase and the difference in performance are discussed at the end of this section.

The flashback limits in terms of critical velocity gradients, calculated from Eq. 4.1, are shown in Fig. 6.10. The same observations as for the critical bulk

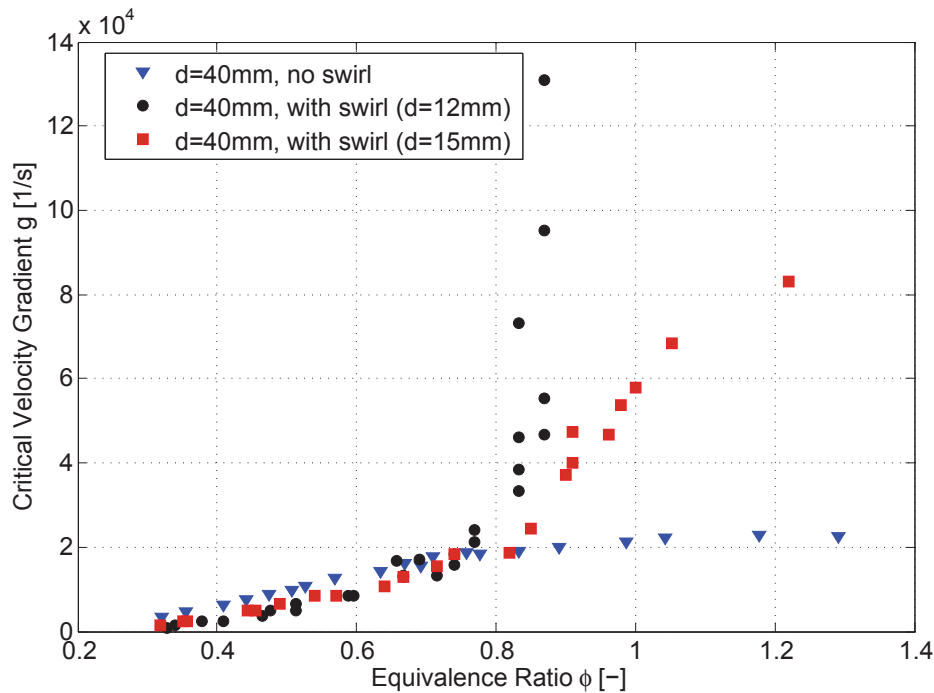


Figure 6.10: Critical velocity gradients for non-swirling and swirling H_2 -air flames

flow velocities can be made. However, it is mentioned again that the real velocity gradients for the swirling flows are likely to be slightly higher than predicted by Eq. 4.1, which would result in a better match of the three curves for $\Phi < 0.75$ in Fig. 6.10. This is also an indication for the suitability of the critical gradient concept to correlate boundary layer flashback tendencies for unconfined flames, even when low swirl is present. The situation for confined flames, though, is entirely different as will be discussed in Ch. 7.

6.2.3.2 Flame Propagation

In order to investigate the upstream flame propagation, the results of the high-speed measurement techniques described in Sec. 6.2.2 are used. Figure 6.11 shows a time series of Mie scattering images of a flashback event for a non-swirling flame at an equivalence ratio of $\Phi = 0.53$. The temporal distance between each image is $\Delta t = 2$ ms and the temporal sequence in the figure is from left to right and from top to bottom. The circular white line in the images is caused by laser light reflections at the tube wall. It can be clearly seen that the flame tip penetrates the measurement plane in the wall boundary layer region

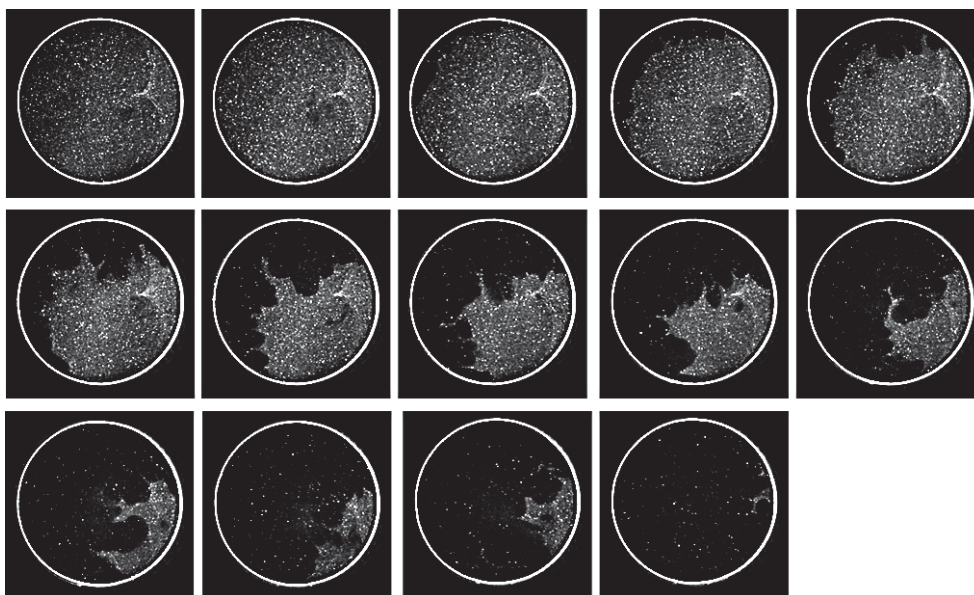


Figure 6.11: Time series of Mie scattering images for a non-swirling flame at flashback: $\Phi=0.53$, $\Delta t=2$ ms

in the upper left corner of the tube's cross section (starting at the second image). Subsequently, the rest of the flame follows the tip, first spreading out a little in circumferential direction in the boundary layer and then toward the center of the tube, until the unburned mixture in the whole cross section is consumed. Thus, the macroscopic flame motion is from the upper left toward the lower right in the images. A similar flashback behavior is observed for all non-swirling flames over the whole range of equivalence ratios. It is obvious that the boundary layer flashback mechanism applies here.

A time series of Mie scattering images for a swirling flame at a representative equivalence ratio of $\Phi=0.49$ is displayed in Fig. 6.12. The temporal distance between the images is again $\Delta t=2$ ms. Due to the rotating fluid motion, the raw images were lacking contrast. This problem could be solved by image post-processing techniques, such as linear contrast stretch, Gamma value adjustment, and some degree of unsharp masking. The rather dark spot in the center of the tube does not indicate the presence of a flame, because it is even visible in tests without flame. It is probably a result of low seeding density in this region due to centrifugal forces acting on the seeding particles. Nonetheless, from the fourth image on, it is obvious that the flame is again penetrating the measurement plane in the boundary layer, starting in the lower left corner of the cross section. In the subsequent images, the swirling motion of the flame during upstream propagation is discernible, which is imposed by the main

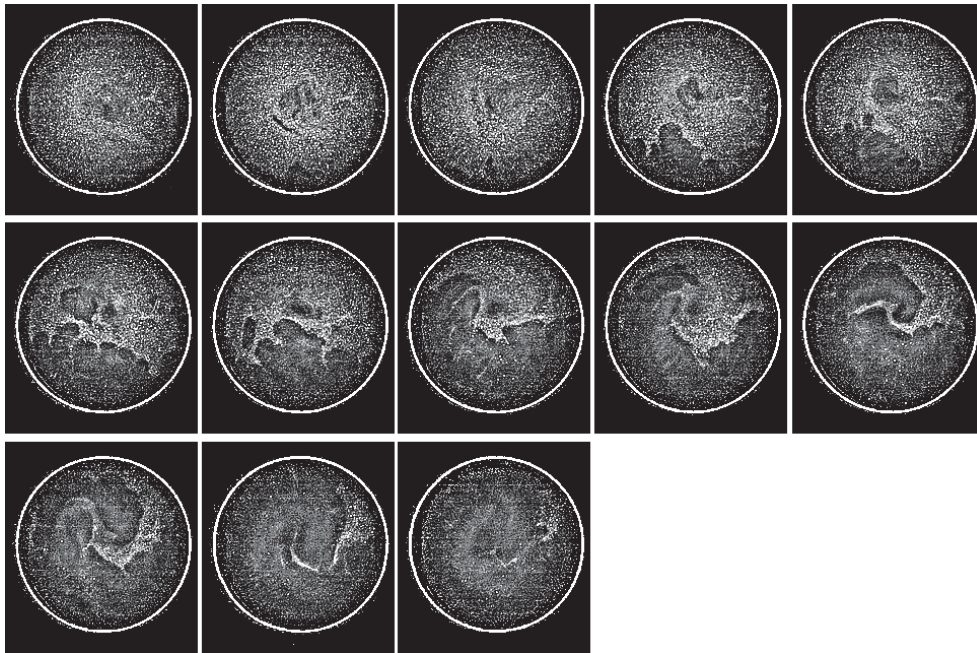


Figure 6.12: Time series of Mie scattering images for a swirling flame at flashback; $\Phi=0.49$, $\Delta t=2$ ms

flow. These high-speed recordings were conducted for a variety of equivalence ratios and the described flashback behavior was observed in the equivalence ratio range between $\Phi=0.35$ and $\Phi=0.7$. Consequently, the driving mechanism is again boundary layer flashback, because the leading tip of the flame was always propagating inside the boundary layer. As already mentioned earlier, the Mie-scattering images from the tests at higher equivalence ratios were lacking contrast, such that it was not possible to extract the position of the flame tip during flashback.

To study the upstream flame propagation also for near-stoichiometric swirling flames, the high-speed camera setup shown in Fig. 6.8 was used. A time series of flame images that were taken simultaneously from two sides are shown in Figs. 6.13 and 6.14 for a representative flashback event at an equivalence ratio of $\Phi=0.82$. The temporal distance between the image pairs is $\Delta t=2$ ms. Note that the pilot burner obstructed the view on the flame at the downstream end of the tube. The flame tip at $t=2$ ms appears in the center of the tube in both images, indicating that the initial penetration is along the tube axis. Thereafter, it propagates upstream along the centerline until $t=8$ ms, where the flame tail gets in contact with the tube walls. Between $t=12$ ms and $t=18$ ms the leading flame tip moves toward the right tube wall in the upper images,

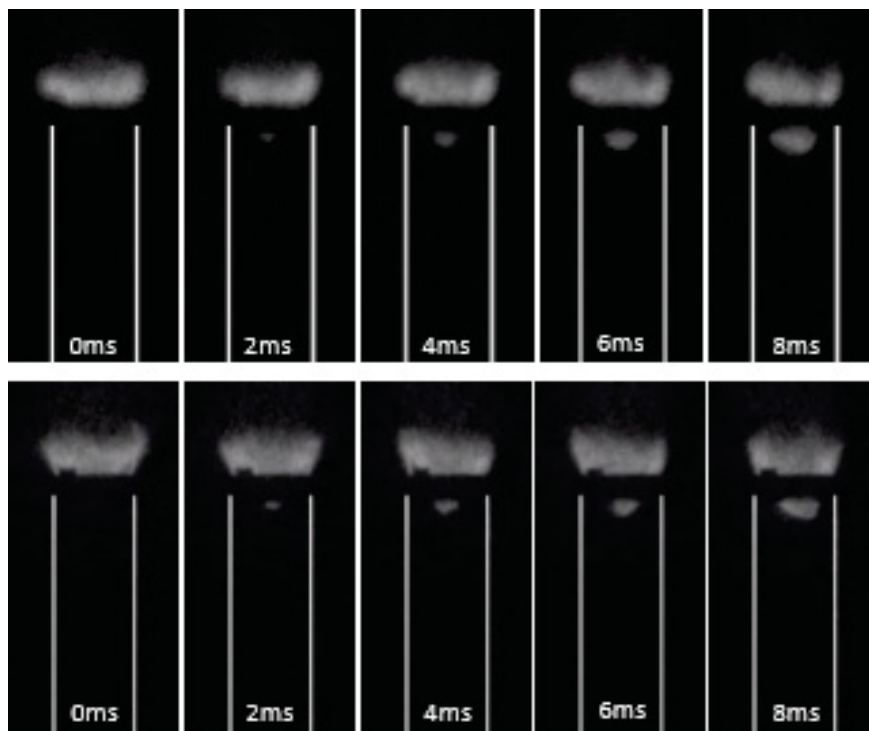
whereas it remains near the center in the lower images. That is, the flame tip reaches the boundary layer. From here, the flame propagates upstream in the very right in the upper images until $t \approx 32$ ms. In the lower images it moves also slightly to the right, indicating that the flame tip is following a helical path through the boundary layer in upstream direction. Between $t = 34$ ms and $t = 40$ ms the flame moves toward the center in the upper images, whereas it moves toward the right side in the lower images.

The macroscopic flashback behavior can be described as follows: The flame enters the tube initially in the center due to CIVB. In this situation, the streamlines in the unburnt mixture flow are bent radially outwards because of the presence of the flame in the center. Thus, boundary layer flashback seems less likely. Nevertheless, as soon as the flame tail gets in contact with the wall, the flame propagates upstream in the boundary layer, i.e. the flame tail outruns the flame tip. The latter can be explained by the fact that the flame is confined inside the tube when it touches the wall. In Sec. 5.2 it was shown that the flashback propensity for confined flames is substantially higher than for unconfined flames (see also [29, 31]). Since the flame is unconfined in its stable position at the tube exit, it does not flash back into the boundary layer in the first place. However, the increase in boundary layer flashback propensity for the afterwards confined flame is so dramatic that the flame flashes back along the boundary layer even though the near-wall flow is accelerated due to the presence of the flame tip in the center. This shows that the initial upstream flame propagation due to CIVB can lead to ultimate flashback along the wall boundary layer even for very low swirl intensities ($S < 0.3$).

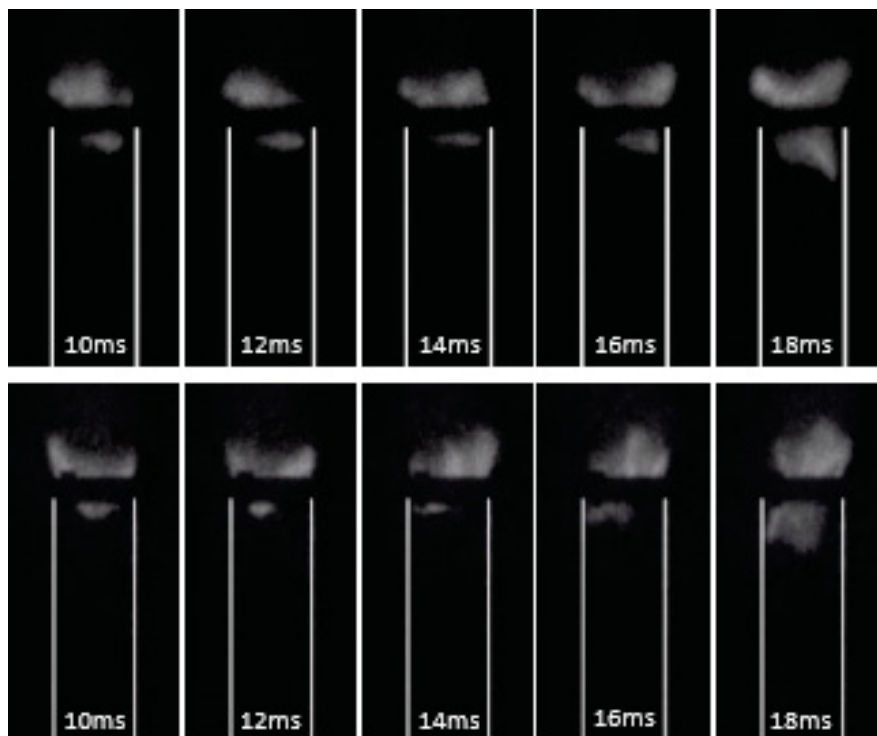
The described change in flashback mechanism is also reflected in the flashback limits plotted in Fig. 6.9. Above $\Phi \approx 0.75$, the critical bulk flow velocities increase because flashback is now initiated by CIVB. The 15 mm setup is superior in this near-stoichiometric region because of the slightly higher axial velocities in the core of the approaching flow, which deter the flame from entering the tube more effectively.

6.2.4 Summary and Conclusions

The flashback behavior of turbulent, premixed hydrogen-air flames were investigated for non-swirling as well as for weakly swirling flows. Two swirl con-

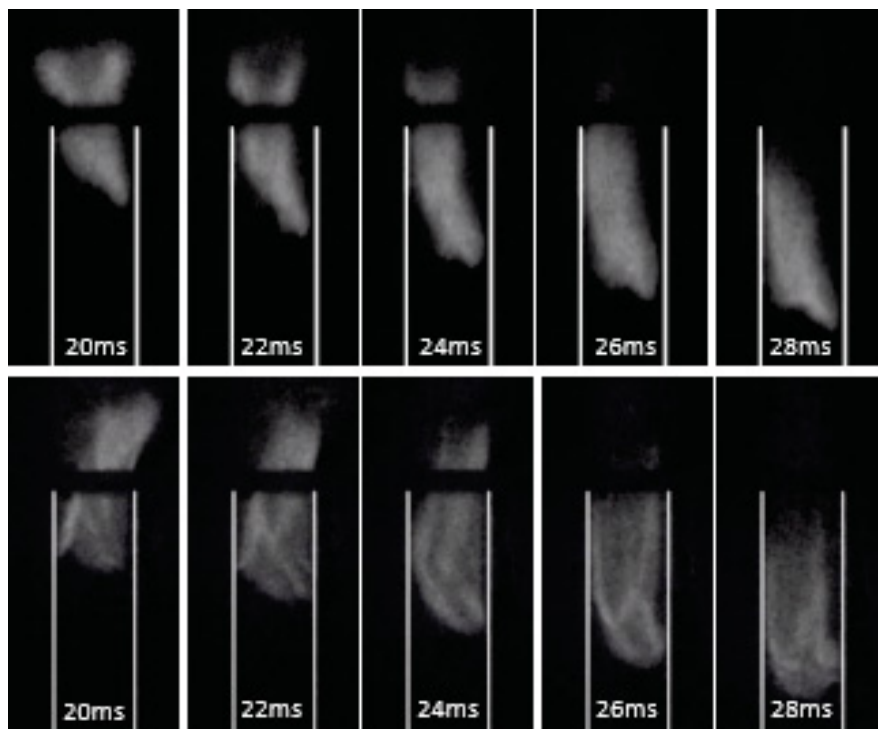


(a)

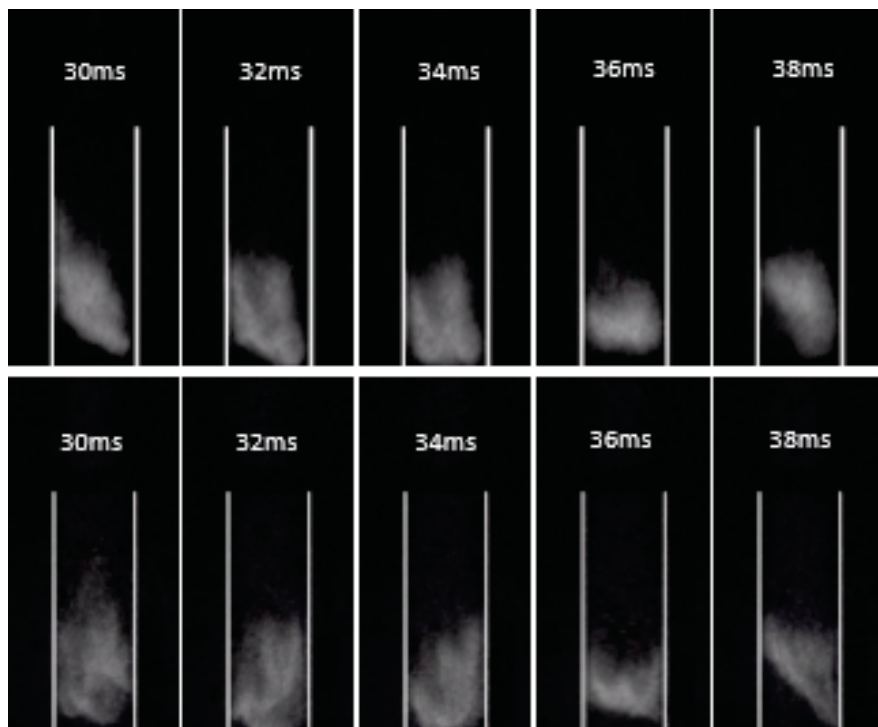


(b)

Figure 6.13: Time series of simultaneous OH*-chemiluminescence images for a swirling flame at flashback; $\Phi=0.77$, $\Delta t=2$ ms: $t=0-18$ ms



(a)



(b)

Figure 6.14: Time series of simultaneous OH*-chemiluminescence images for a swirling flame at flashback; $\Phi=0.77$, $\Delta t=2$ ms: $t=20-38$ ms

figurations with different inlet diameters for the axially injected air were considered. The flashback limits were recorded at atmospheric pressure and ambient temperature over a broad range of equivalence ratios. The detailed upstream propagation of the flame during flashback was studied by means of high-speed photography and laser diagnostic techniques.

The results showed that imposing low swirl upon the burner flow slightly reduces the flashback propensity for mixture equivalence ratios up to $\Phi \approx 0.75$. The high-speed measurements revealed that boundary layer flashback is the only driving mechanism for the upstream propagation of these flames. The same applies to non-swirling flames over the whole range of mixture ratios. The resistance to flashback is higher in swirling flow because of the radial outward motion of the fluid, which leads to higher axial velocities in the near-wall region and deters the flame from entering the tube. The setup with the smaller orifice for axial support air performed better in this operating range due to the slightly higher swirl intensity. It could be shown that the critical velocity gradient concept is suitable for correlating the boundary layer flashback limits of these unconfined, low-swirl flames.

For swirl flames above $\Phi \approx 0.75$, a strong increase in flashback propensity was observed for both swirl setups, with the configuration with higher flux of axial air being slightly more flashback resistant. In this near-stoichiometric region, flame flashback is initiated due to combustion induced vortex breakdown (CIVB). The flame first enters the tube along the tube axis until its tail gets in touch with the walls. Although the streamlines in the approaching flow are bent toward the wall in this situation, the flame eventually flashes back along the wall boundary layer. The explanation for this behavior is the huge difference in boundary layer flashback propensity between unconfined and confined flames, which was shown in Sec. 5.2.

Contrary to the current knowledge in literature, it was shown that boundary layer flame flashback can be triggered by CIVB in a hydrogen-air burner even for swirl numbers below $S=0.3$. It is important to note that the special burner configuration used in this project contributes to the occurrence of this phenomenon. The big distance between swirl generator and tube exit increases the production of negative azimuthal vorticity (cf. Sec. 2.1.3), which deteriorates the resistance against flashback due to CIVB. In technical applications this mixing length is usually much shorter. Nevertheless, the potential occur-

rence of CIVB-flashback for $S < 0.3$ must be taken into account during the design process of technical burners operating with premixed, hydrogen-rich fuels, because unfavorable aerodynamics can potentially affect the vortex core dynamics in such a way that CIVB-flashback is triggered.

6.3 Influence of Boundary Layer Injection on Flashback Behavior

The flashback results presented in the sections above demonstrated that flashback along the wall boundary layer is the dominant failure type for jet flame burners using highly reactive fuels. Thus, it is worthwhile to broaden the safe operating range of such burners by increasing their flashback resistance.

In the literature, only a few investigations have been concerned with countermeasures against flashback of highly-reactive fuels. In [23], the flashback limits for syngas-air mixtures (50 % H₂, 50 % CO) in a tube burner (d=25 mm) were measured for gas turbine like conditions. Mainly for the sake of avoiding damage to the test facility, pure nitrogen was injected into the reactive flow 150 mm upstream of the combustion chamber to stop the upstream flame propagation. It is reported that the flame anchored at the N₂-injection location during flashback, giving enough time to apply the implemented active control mechanism to flush out the flame again. However, the influence of the nitrogen injection, which amounted to 1 % of the total air flow rate during all tests, was not investigated systematically. Versailles et al. [122, 123] studied the core flow and boundary layer flashback behavior of flames fed with pure natural gas and equimolar hydrogen-natural gas mixtures, respectively. They used non-thermal Dielectric Barrier Discharge (DBD) devices, also referred to as plasma actuators, to generate ionic winds that transfer their momentum to the surrounding flow. Regarding boundary layer flashback, this technique increased the critical equivalence ratios by approx. 10-14 % for CH₄ mixtures and by approx. 3.5 % for equimolar H₂-CH₄ mixtures. However, flashback prevention is particularly challenging when it comes to premixed combustion of pure hydrogen and air. According to a comment in [85], the injection of small amounts of air into the wall boundary layer has proven to effectively prevent natural gas flashback, but it remains unclear if this also holds for highly reac-

tive fuels, such as hydrogen-rich fuels.

The main objective of the study presented in this section was to identify and assess measures to counteract boundary layer flashback in a hydrogen-air jet burner. The approach was to inject small amounts of air into the fuel-air mixture in the near-wall region at different streamwise positions upstream of the stable flame. The intention was to stop, delay or prevent flame propagation along the wall boundary layer due to dilution of the reactive mixture. In addition to that, it was investigated whether the acceleration of the near-wall fluid contributes to flashback prevention. For this purpose, both the amount of air injected and the angle of injection were varied and the flashback limits were measured for atmospheric hydrogen-air mixtures over a broad range of equivalence ratios. Air was chosen instead of any other gas, e.g. nitrogen, because it is cheap and easily available. Thus, no additional energy input is needed to produce and compress the injected gas in a practical application.

6.3.1 Experimental Approach and Isothermal Flow Field

In this section, the experimental infrastructure will be described along with a characterization of the flow field inside the measuring section. The basic setup of the TUM burner, which was described in Sec. 3.1.1, was extended by an injection device that was mounted at a certain distance upstream of the burner exit, as shown in Fig. 6.15.

6.3.1.1 Design of the Boundary Layer Injection Devices

The boundary layer injection devices could be installed at three different positions along the vertical tube ($a=113, 213$ or 313 mm) upstream of the flame. In Figs. 6.16 and 6.17 cuts of the devices for 45° -injection and radial injection, respectively, can be seen. In the left halves of both figures the flow path of the injected air is illustrated. The air was fed through two inlet ports on opposite sides of the symmetry axis and proceeded into the tube through the inclined slot and the sinter metal ring, respectively. The axial injection length of the slot amounted to approximately 0.75 mm and the one of the sinter metal ring to 9 mm. The injection into the main flow was assumed to be distributed equally around the tube's circumference. Due to the high pressure drop across

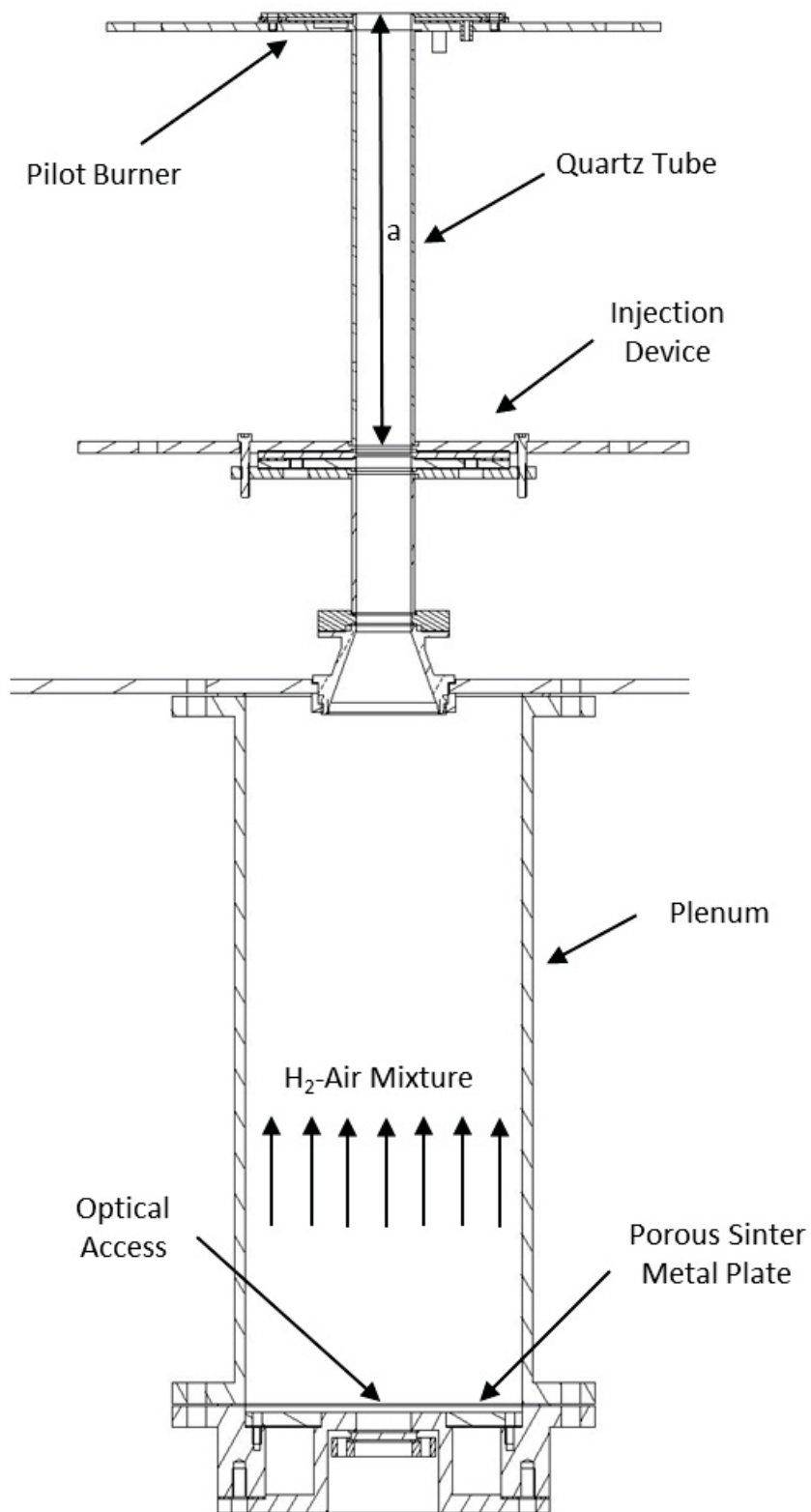


Figure 6.15: TUM tube burner with injection devices

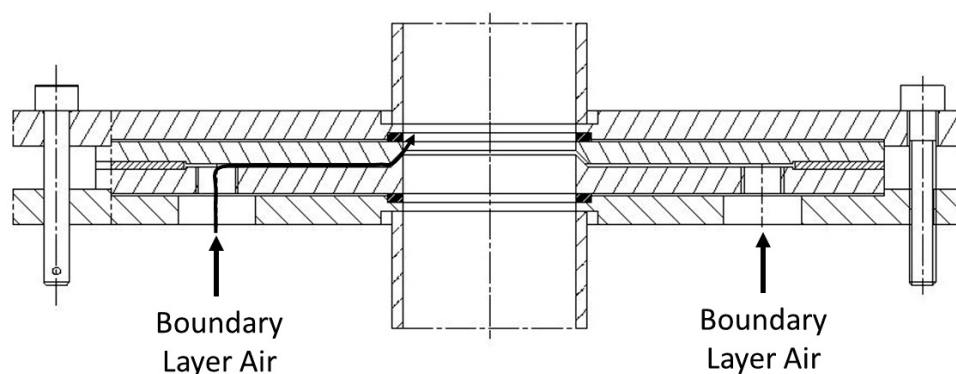


Figure 6.16: Boundary layer injection device: 45°

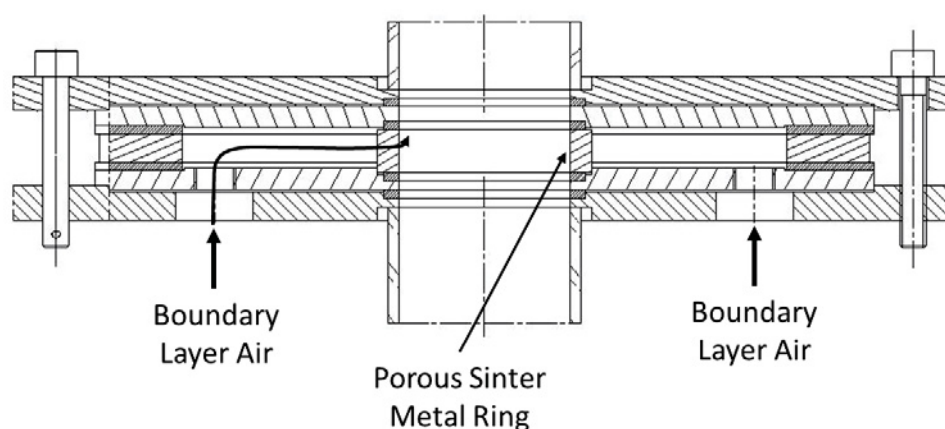


Figure 6.17: Boundary layer injection device: Radial

the sinter metal ring this assumption is likely to be valid, whereas some deviations might be present in the 45°-case (see discussion later). Except for the gaskets, all components of the injection devices were made of aluminum and the axial extensions of the assemblies of only 25-30 mm provided for good visibility of the flame during flashback. The inner diameters of the separate parts were matching the ones of the upstream and the downstream glass tube and they were positioned precisely on top of each other by means of two alignment pins in order to minimize flow disturbances at the transitions.

6.3.1.2 Isothermal Flow Field in the Burner Tube

The isothermal flow field of the basic TUM burner setup has been described in Ch. 4.1. For the setup with the injection devices Reynolds Averaged

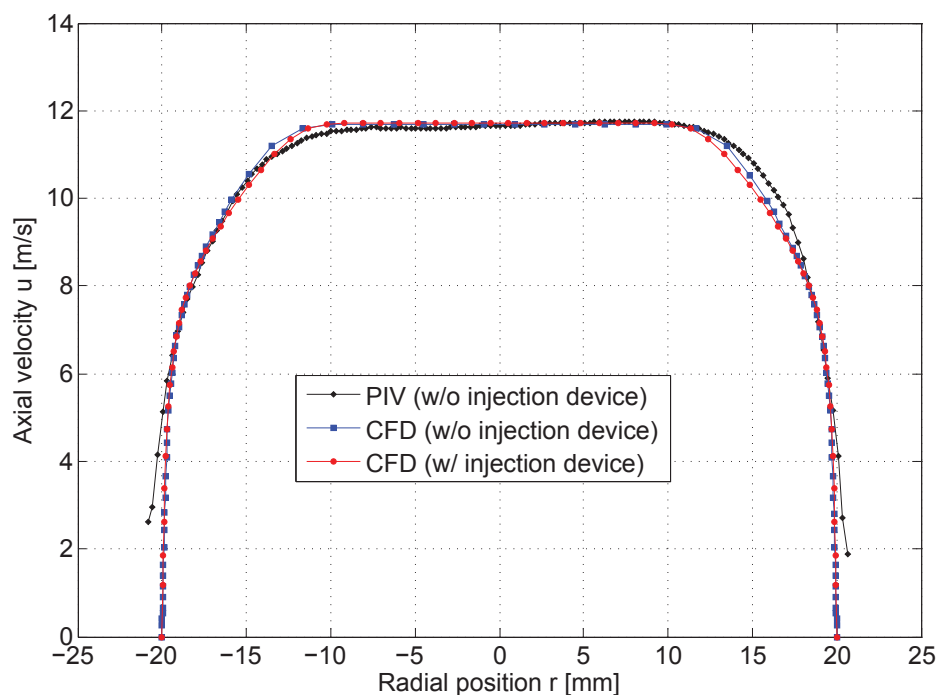


Figure 6.18: Isothermal velocity profiles at tube burner outlet with and without injection ($\bar{u}=10$ m/s)

Navier Stokes (RANS) simulations were performed in Ansys CFX for different amounts of air injected as well as for both injection angles and the different streamwise positions. In all simulations, the wall boundary layer inside the tube was well resolved ($y^+ < 1$) and the SST turbulence model was used. These simulations are also used for evaluating the distribution of the local equivalence ratio at the tube exit later on. It is well known that RANS simulations generally tend to underpredict the scalar transport in complex flows, e.g. in boundary layer flow. According to [52, 56], the turbulent Schmidt number Sc in the simulations needs to be modified accordingly in order to obtain correct quantitative results. The main purpose of the simulations in the present study was to *qualitatively* compare the equivalence ratio profiles for the different injection configurations. Therefore, and due to the lack of experimental validation data, the standard turbulent Schmidt number of $Sc=0.7$ was kept in the simulations.

Figure 6.18 compares the velocity profile of the setup without injection device to the one with injection device mounted but no air injected. The total length of the setup with injection device is slightly longer. Nevertheless, the veloc-

ity profiles are compared at the tube exit in both cases, because this is where the velocity gradient needs to be evaluated for correlating the flashback limits later. The simulations as well as the experimental measurements shown in Fig. 6.18 were performed for air at atmospheric conditions and a bulk flow velocity of $\bar{u}=10$ m/s. The fact that there are no significant deviations between the two simulated profiles and only small deviations between simulation and experiment (cf. Sec. 4.1) leads to the following conclusions:

1. The simulations are capable of delivering correct velocity results. Consequently, it can be expected that they deliver meaningful results also for the cases with boundary layer injection.
2. Although the velocity profile at the tube exit is not yet fully developed, the velocity gradient g at the wall can be derived from the Blasius correlation for fully developed turbulent pipe flow (Eq. (4.1)), such as it was done for the basic TUM burner setup (cf. Sec. 4.1).

The velocity profiles for the cases with air injected will be presented later as they will serve as a basis for discussion of the experimental results.

6.3.1.3 Experimental Procedure and Flame Holding

The flashback tests with boundary layer air injection were carried out in a similar fashion as the tests without injection. The only difference was that in the tests with injection part of the total air mass flow was taken for injection through the boundary layer devices, e.g. 5 vol.-%. Thereafter, both the main air flow and the flow rate of injected air were kept constant throughout the test and the standard test procedure described in Sec. 3.3.1 was adopted. For the definition of a flashback event, please refer to Ch. 3.3.1. To check the reproducibility of the results, the flashback tests were repeated at least three times for each global air mass flow rate. The resulting critical equivalence ratio was found to scatter within $\Delta\Phi = \pm 0.05$ about the average value.

During testing the OH*-chemiluminescence from the flame was monitored by an intensified charge-coupled device (ICCD) camera (Hamamatsu C4336-02) using a UV lens and an interference filter, which mainly transmitted light in a wavelength range of 307-312 nm. The camera resolution was 720x480 pixels and the images were recorded at a frame rate of 30 Hz.

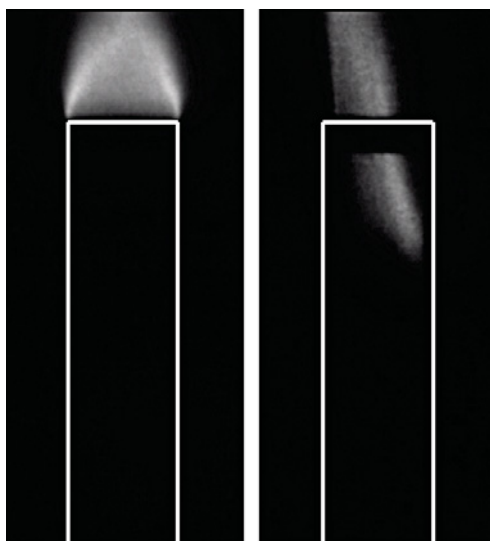


Figure 6.19: Stable flame and flame at flashback: No air injected

The flame holding prior to flashback as well as an image of the flame at flashback are depicted in Fig. 6.19. Both images were recorded at an exposure time of 33.3 ms and the tube boundaries as well as the downstream end of the pilot burner are marked by white lines. It can be clearly seen that the flame is stabilized in the shear layers above the pilot burner as the OH^* -radiation is most intense in these regions. When it comes to flashback, it is evident that the boundary layer mechanism applies here (the nontransparent area close to the tube exit is the pilot burner). Most of the experiments in the present study were conducted with low amounts of air injected, up to 5 vol.-% of the total air mass flow. With respect to the flame holding mechanism, the stable flame shape, and the flashback mechanism, the flame images shown in Fig. 6.19 are representative for these tests, too. The flame images during stable operation and flashback for higher amounts of air injected will be discussed later.

6.3.2 Results and Discussion

All flashback tests were conducted at atmospheric pressure and ambient temperature ($T=293\text{ K}$). As already mentioned earlier, the mass flow of injected air was adjusted in volume percent of the total air mass flow during all experiments. For each injection configuration (i.e. change of streamwise position or angle of injection) the flashback limits were also measured for the case without any air injected for reference. This is important, because minor changes in the flashback limits can be merely a result of small flow disturbances that

are stronger in one setup than in the other.

6.3.2.1 Boundary Layer Injection: $a=113$ mm

In Figs. 6.20 and 6.21 the flashback limits in terms of critical bulk flow velocities are shown for 45°-injection and radial injection, respectively. In addition to that, the critical velocity gradients calculated from Eq. (4.1) are presented in Figs. 6.22 and 6.23. It is important to note that the validity of Eq. (4.1) is questionable when large amounts of air are injected into the boundary layer flow. This issue will be discussed in the next section. Figures 6.20-6.23 present scatter plots of all experimental results for the respective setup. The equivalence ratios are calculated on the basis of the total air and hydrogen mass flow, i.e. including the air that is injected into the boundary layer. The visible data points do not represent the total number of tests conducted because many flashback points are lying on top of each other. In fact, each flashback point was repeated at least three times. In addition to the results obtained in this study, a few flashback points from the same burner configuration (open, stainless steel) but without any injection device mounted are included (cf. Fig. 5.12). It can be seen that the flashback limits from those experiments slightly deviate from the 0 %-results. It is likely that flow disturbances that are generated by the injection devices cause these deviations, corroborating the above-mentioned need for reference measurements.

Flashback Limits and Flame Shape:

Regarding the results with boundary layer injection, the plots demonstrate that the flashback propensity considerably decreases over the whole range of equivalence ratios for both injection methods. The curves represent different amounts of air injected. The more fluid is injected, the stronger the positive effect is, but only up to a certain limit. A few tests were conducted with 10 and 20 vol.-% injection, indicating that the resistance to flashback does no longer increase. This trend is evident from both the critical bulk velocities and the critical velocity gradients. Looking at the flame shortly before and during flashback (Fig. 6.24) reveals that the flame is adopting a different shape in these cases. When compared with the shape for little or no air injection, it changes from conical to tulip shape. The latter is usually observed in swirling flow (cf. Sec. 6.2). Moreover, the flashback images suggest that the flame is no longer

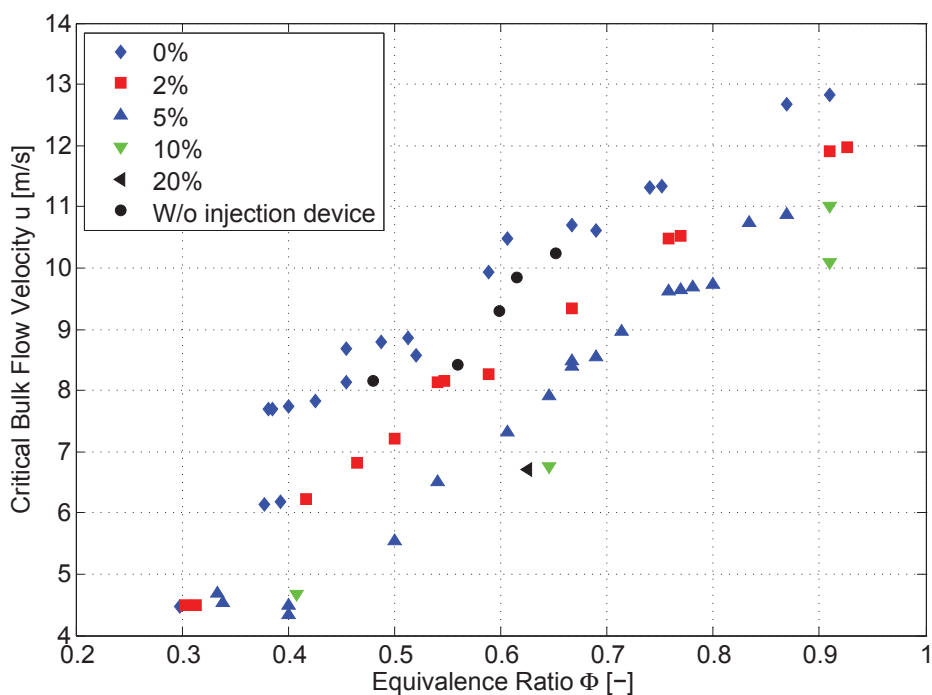


Figure 6.20: Critical bulk flow velocities, radial injection, a=113 mm

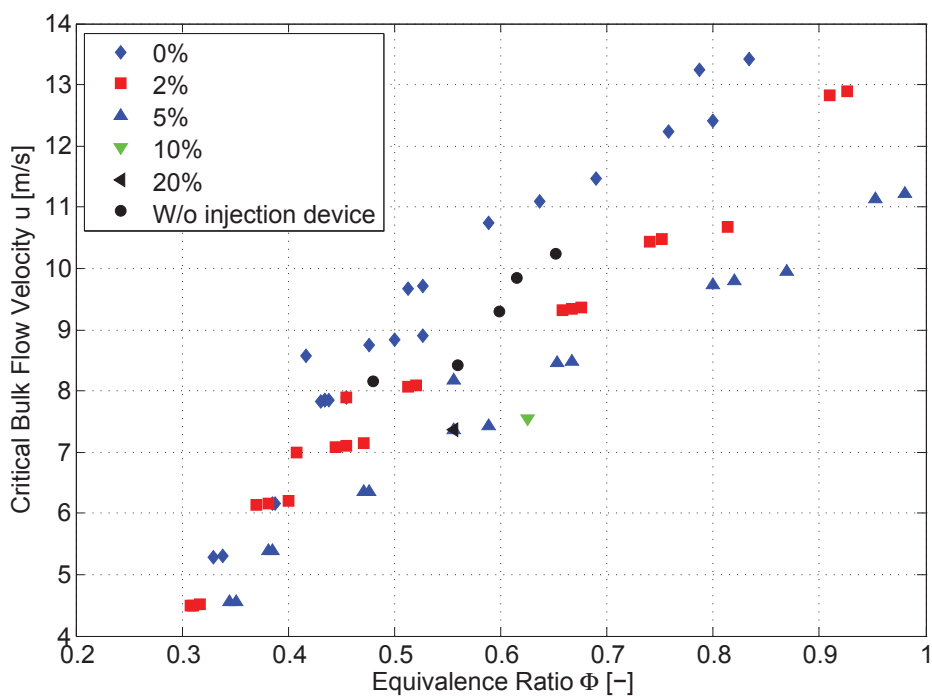


Figure 6.21: Critical bulk flow velocities, 45° injection, a=113 mm

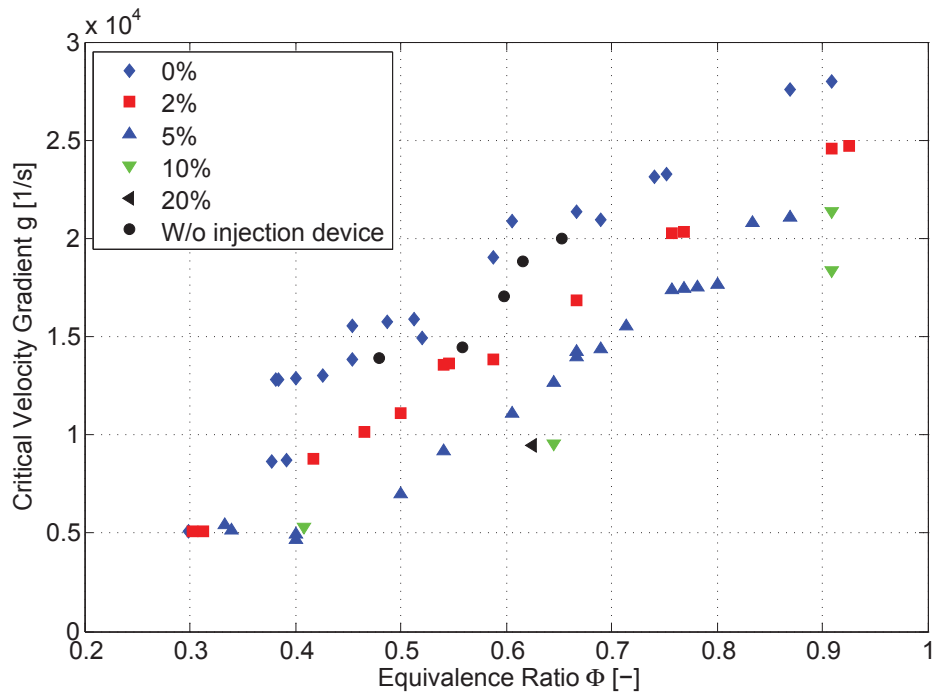


Figure 6.22: Critical velocity gradients, radial injection, $a=113$ mm

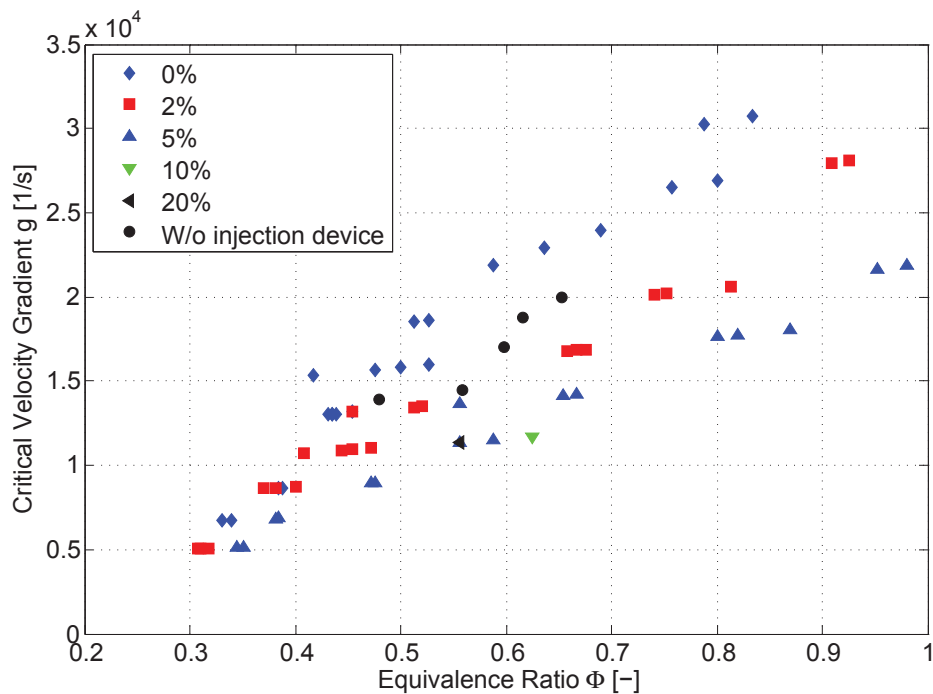


Figure 6.23: Critical velocity gradients, 45° injection, $a=113$ mm

propagating upstream in the wall boundary layer but rather in or near the center of the tube. This is plausible because for a certain global equivalence ratio Φ the injection of large amounts of air into the boundary layer results in fairly low equivalence ratios near the wall and high equivalence ratios in the center region. The massive injection also causes low axial velocities in the center, paving the way for the upstream flame propagation. Thus, it is likely that the flame does not propagate in the boundary layer but in a distance further away from the wall where the flame speed is high and the axial velocities are rather low. Nevertheless, it is emphasized that all observations discussed are based on line-of-sight integrated OH^* -chemiluminescence images recorded at a frame rate of only 30 Hz. Therefore, the detailed path of the flame during flashback cannot be determined with certainty. However, the change in flame shape from cone to tulip for the 10 %- and 20 %-injection is an indicator for a change in the velocity profile at the tube exit. As a result, the derivation of the critical velocity gradients in Figs. 6.22 and 6.23 by means of Eq. (4.1) is no longer physically meaningful. Therefore, the flashback propensity is rather assessed on the basis of the critical bulk velocities in these cases. Nonetheless, the critical velocity gradients for 10 %- and 20 %-injection are included in the plots for comparative purposes. As will be shown below, for low injection amounts (up to 5 vol.-%) the impact of the air injection on the velocity profile at the tube exit is very small.

In the 45°-case the effectiveness of the injection increases with increasing equivalence ratio, whereas a fairly constant behavior is observable for radial injection through the sinter metal ring. In this regard, it should be noted that the 0 %-injection values in the 45°-case are already higher than those in the radial case, in particular for near-stoichiometric mixtures. This can be explained by stronger flow disturbances because the flow path is interrupted by a 0.75 mm-gap at the injection location, compared to the relatively smooth transition when the sinter metal ring is mounted. This hypothesis is further confirmed by the fact that these "0 %-deviations" vanish when the injection devices are located further upstream of the tube exit (see Figs. 6.29-6.34), because the flow disturbances have more time to decay. On the other hand, the distribution of the injected air around the tube's circumference is supposed to be less uniform in the 45°-setup. It is likely that less air is passing through the sections far away from the two inlet ports and therefore the flame tends to flash back there (cf. Fig. 6.16).

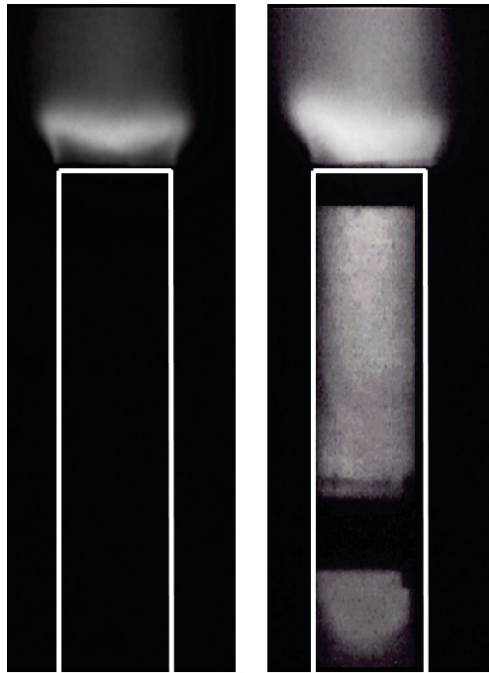


Figure 6.24: Stable flame and flame at flashback: 15% air injected

Another reason for the small differences in effectiveness of the two configurations may be the axial velocity component of the injected jet in the 45°-setup, which provides the near-wall flow with additional momentum. To investigate this influence, CFD simulations of the isothermal mixture flow were performed for a representative flashback case with a total air mass flow rate of 500 standard liters per minute, whereof 5 vol.-% were passing through the injection device. The hydrogen mass flow was set to match a global equivalence ratio of $\Phi=0.5$. The resulting axial velocity profiles at the tube exit are shown for both injection angles in Figs. 6.25 and 6.26. It can be seen that there are only very small deviations between the velocity profiles, which lead to variations in the wall velocity gradient of less than 1%. It is again noted that the critical velocity gradients plotted in Figs. 6.22 and 6.23 were calculated from Eq. (4.1), which does not account for the influence of boundary layer injection. However, the CFD simulations in Figs. 6.25 and 6.26 have shown that this approach is justified for injection amounts up to 5%, because the influence on the wall velocity gradient turned out to be marginal.

Regarding the local equivalence ratios Φ_{local} obtained from the CFD simulations (Figs. 6.27 and 6.28), it can be seen that the mixture is considerably leaner near the wall than more toward the center, with the values for 45°-injection being somewhat lower than those for radial injection. On the other

hand, the increase of the local equivalence ratio is flatter for radial injection, resulting in a larger penetration depths into the main flow. It is concluded that the positive effect of the air injection on the flashback limits stems from the dilution of the near-wall flow rather than from the marginal differences in wall velocity gradients. The small differences in performance between the two injection angles are caused by the coexistence of flow disturbances, non-uniform injection around the tube's circumference, and slightly different axial velocity profile due to the presence of a recirculation bubble in the radial setup.

To further quantify the effectiveness of the injection methods, their influence on the critical bulk flow velocity \bar{u} was calculated. Based on the bulk velocity for 0 % injection, the average reduction in critical bulk velocity for the 45°-setup amounts to $\Delta\bar{u}/\bar{u}=15.7\%$ for 2 % air injected and to $\Delta\bar{u}/\bar{u}=24.3\%$ for 5 % air injected, respectively. For the radial injection the average reduction in bulk velocity is $\Delta\bar{u}=1.4\text{ m/s}$ for 2 % injection and $\Delta\bar{u}=2.3\text{ m/s}$ for 5 % injection, respectively. When expressed in percentage of the 0 %-injection bulk velocity, the values are in the range of $\Delta\bar{u}/\bar{u}=16.6\text{-}8.8\%$ for 2 % air injected and $\Delta\bar{u}/\bar{u}=36.3\text{-}17.3\%$ for 5 % air injected, depending on the equivalence ratio Φ . Here, the lower $\Delta\bar{u}/\bar{u}$ -values correspond to higher equivalence ratios and vice versa.

Stability/Reproducibility of the Flashback Results:

To check the stability of the experimental procedure with regard to the results shown in Figs. 6.20-6.23, some of the flashback points were re-measured using a slightly different measurement procedure than that described above. Again, a fixed total air mass flow rate was adjusted, whereof 5 vol.-% were taken for the boundary layer injection. Thereafter, the hydrogen flow was turned on and a stable flame was established. The equivalence ratio was set to a fixed value that was right in between the before measured critical value for 5 %-injection and the one for 0 %-injection. Subsequently, the injection amount was decreased in 0.5 %-steps until flashback occurred. These tests were conducted for three representative flashback points of both injection configurations. The obtained critical injection amounts deviated from those shown in Figs. 6.20-6.23 by as little as $\pm 0.5\%$, which can be considered as sufficiently stable behavior.

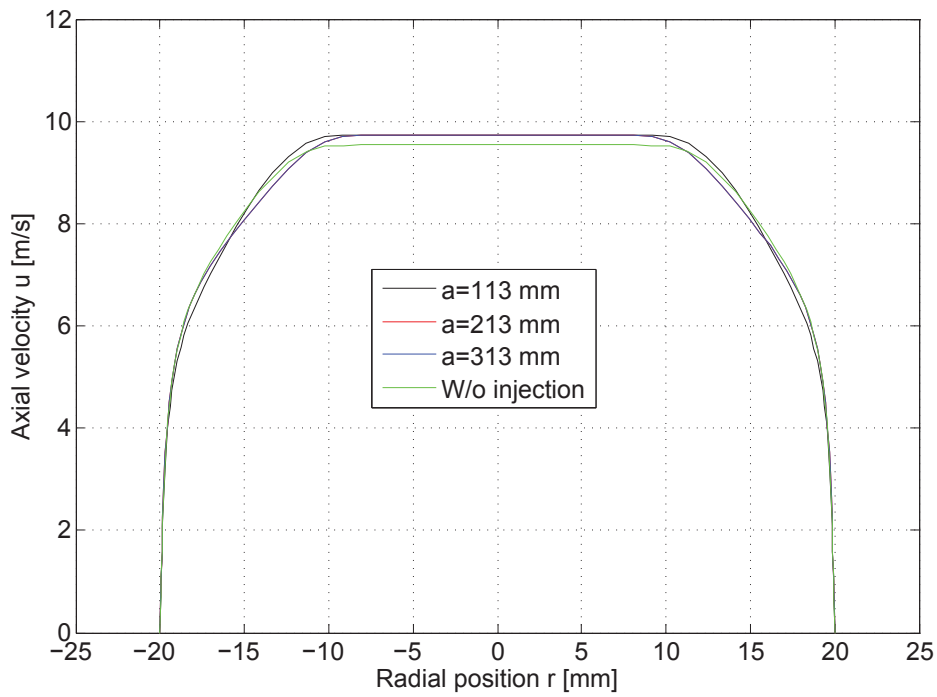


Figure 6.25: Velocity profile at tube outlet for radial injection

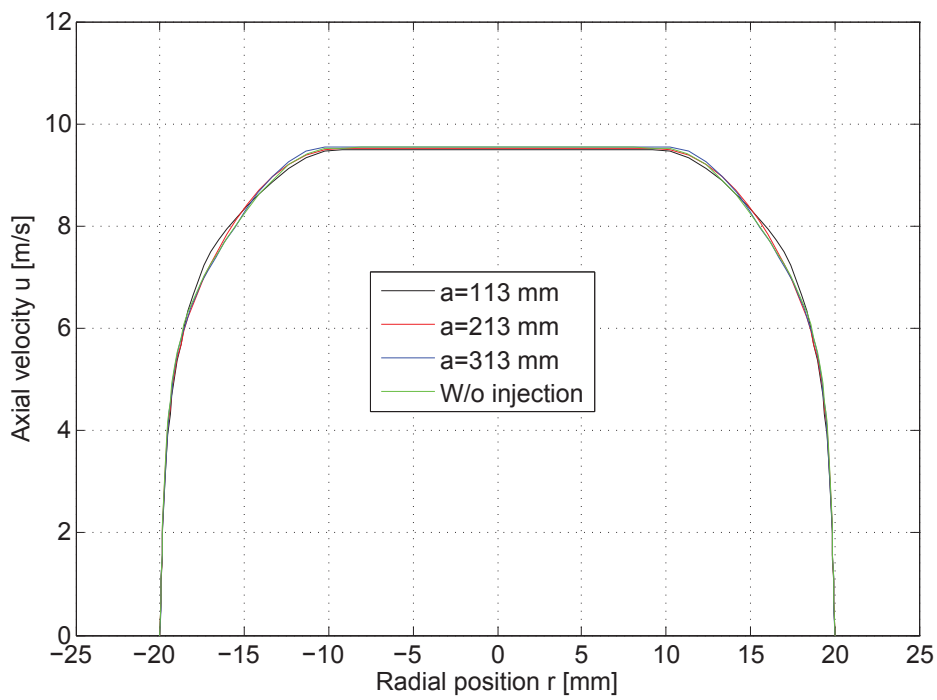


Figure 6.26: Velocity profile at tube outlet for 45° injection

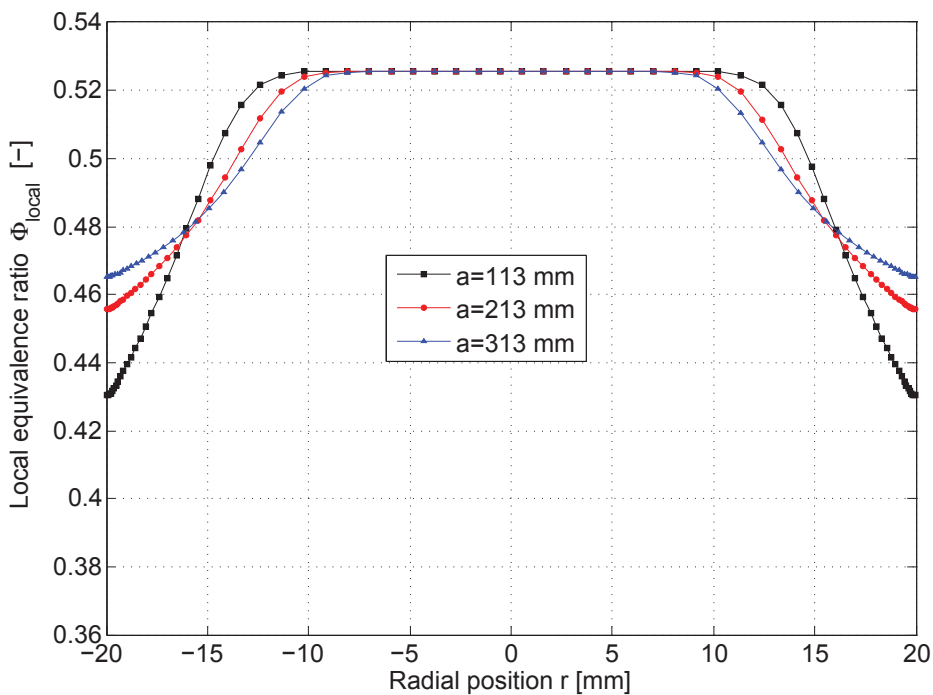


Figure 6.27: Distribution of local equivalence ratio at the tube outlet for radial injection

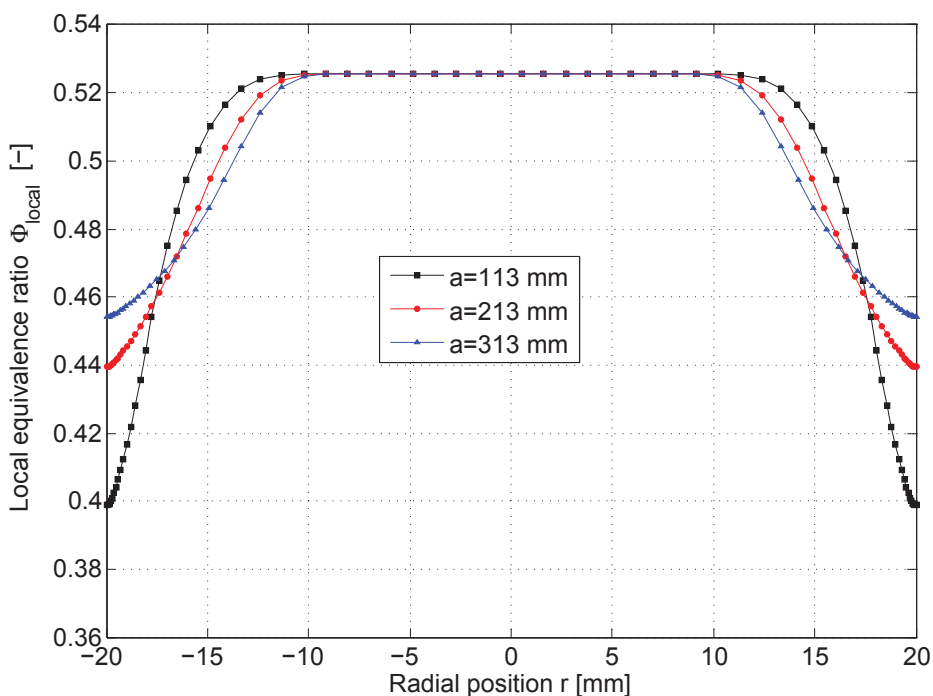


Figure 6.28: Distribution of local equivalence ratio at the tube outlet for 45° injection

Flame Propagation:

An interesting observation that applies to almost all experiments in this investigation is that the flame was not stopped before or at the injection location once it had entered the tube. Only for very lean mixtures ($\Phi < 0.4$), flashback was not a sudden event but the flame was flickering back and forth for a few seconds in the tube before it eventually flashed back all the way down to the plenum. This can be explained by the entirely different flashback behavior of confined and unconfined flames. It was shown in Sec. 5.2 (Fig. 5.5) that confined H_2 -air flames require substantially higher wall velocity gradients in the approaching flow to prevent boundary layer flashback than unconfined flames (see also [29, 31]). Moreover, the deviation between the critical velocity gradients increases with increasing equivalence ratio, reaching approximately one order of magnitude for stoichiometric mixtures. Translated into the observations for boundary layer injection, the following conclusions can be drawn:

- For very lean mixtures ($\Phi < 0.4$), the flame is able to remain inside the tube for a short time, because the flashback propensity of the confined flame is not much higher than the one of the initially unconfined flame stabilized at the tube exit. This leads to subsequent heating of the tube walls, which drives the further upstream propagation (cf. Sec. 5.3).
- For richer flames ($\Phi > 0.4$), the bigger difference in critical velocity gradients between the unconfined and the confined situation leads to immediate flashback.

Thus, the boundary layer fluid injection is to some degree capable of preventing the flame from entering the tube, however, it cannot stop the flashback process once it has started and the flame is confined inside the tube.

6.3.2.2 Boundary Layer Injection: a=213 mm and a=313 mm

The flashback limits with the injection devices located at a=213 mm and a=313 mm upstream of the stable flame are shown in Figs. 6.29-6.34. Again, curves for both the critical bulk flow velocities and the critical velocity gradients are presented. The total number of tests was reduced because the positive influence of the air injection was found to be far smaller than in the previous setup (a=113 mm). Nonetheless, it can be seen that the radial injection

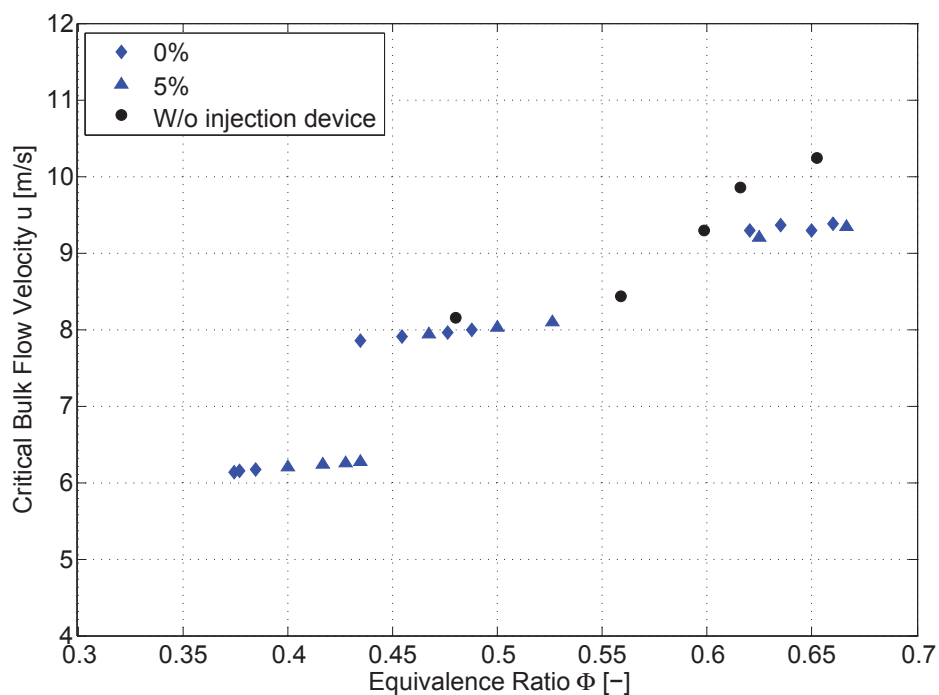


Figure 6.29: Critical bulk flow velocities, 45° injection, a=213 mm

performs slightly better than the 45°-injection. Furthermore, injecting air at a=213 mm is slightly more effective than at a=313 mm, both of which are less effective than injecting at a=113 mm. The CFD simulations of the isothermal flow (Figs. 6.25-6.28) demonstrate the reasons for this behavior. The shorter the mixing length is, the less uniform the distribution of the local equivalence ratio at the tube exit is, with lower Φ_{local} in the near-wall region. Thus, boundary layer flashback is prevented more effectively when the injection takes place closer to the tube exit. The influence of the wall velocity gradients, however, was found to be negligible. The flame shape prior to flashback and the upstream flame propagation were similar for all three injection locations.

6.3.3 Summary and Conclusions

The influence of boundary layer air injection on the turbulent flashback limits of fully premixed hydrogen-air flames was investigated using the TUM burner. The injection devices were located at three different streamwise locations upstream of the stable flame and two different injection angles were considered - either injection in radial direction or at an angle of 45° to the main flow. Small

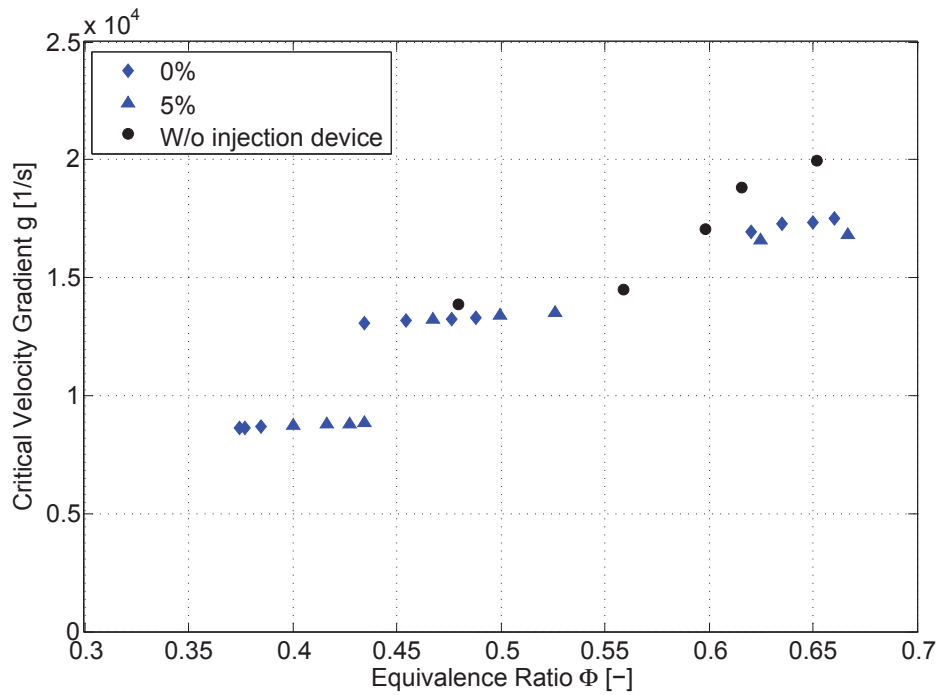


Figure 6.30: Critical velocity gradients, 45° injection, a=213 mm

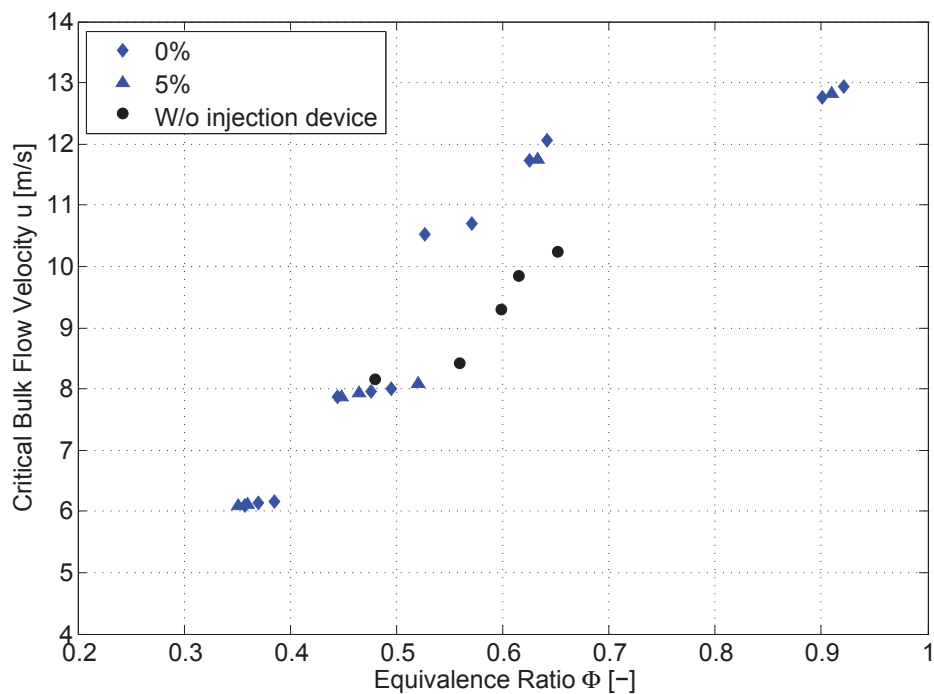


Figure 6.31: Critical bulk flow velocities, 45° injection, a=313 mm

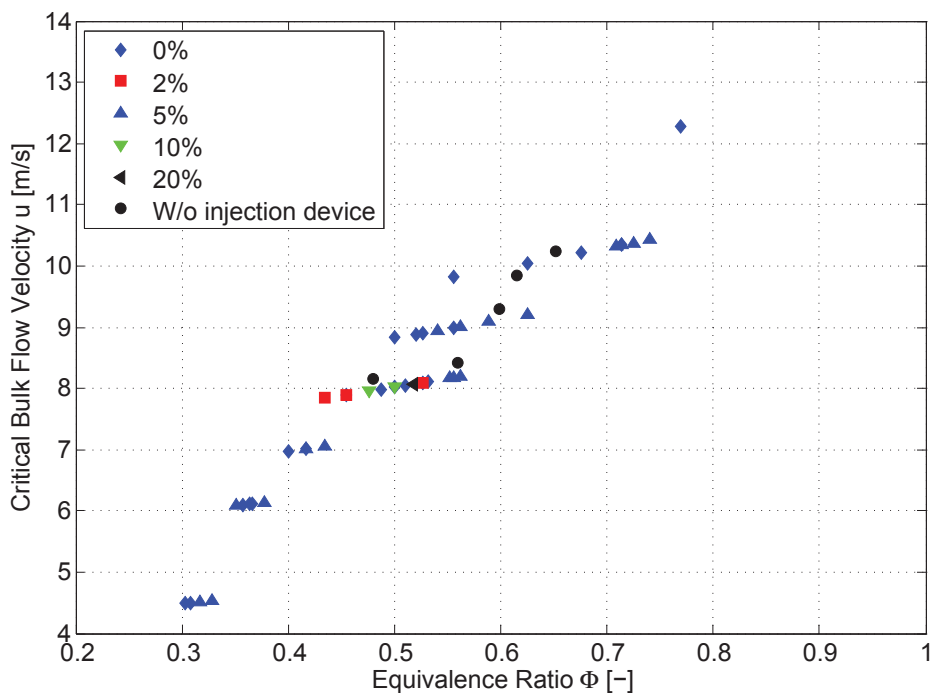


Figure 6.32: Critical bulk flow velocities, radial injection, a=313 mm

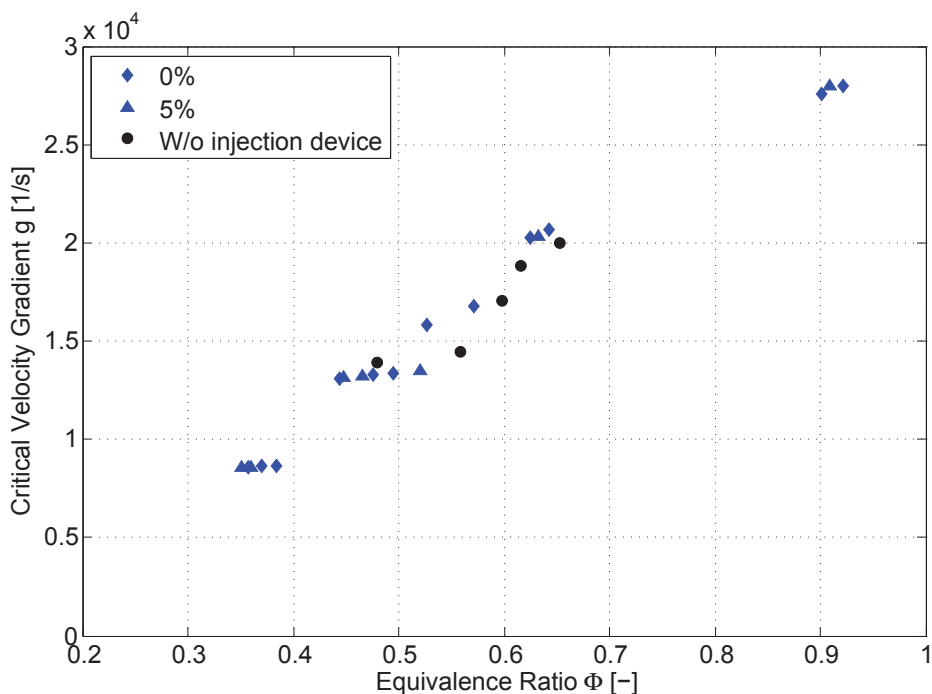


Figure 6.33: Critical velocity gradients, 45° injection, a=313 mm

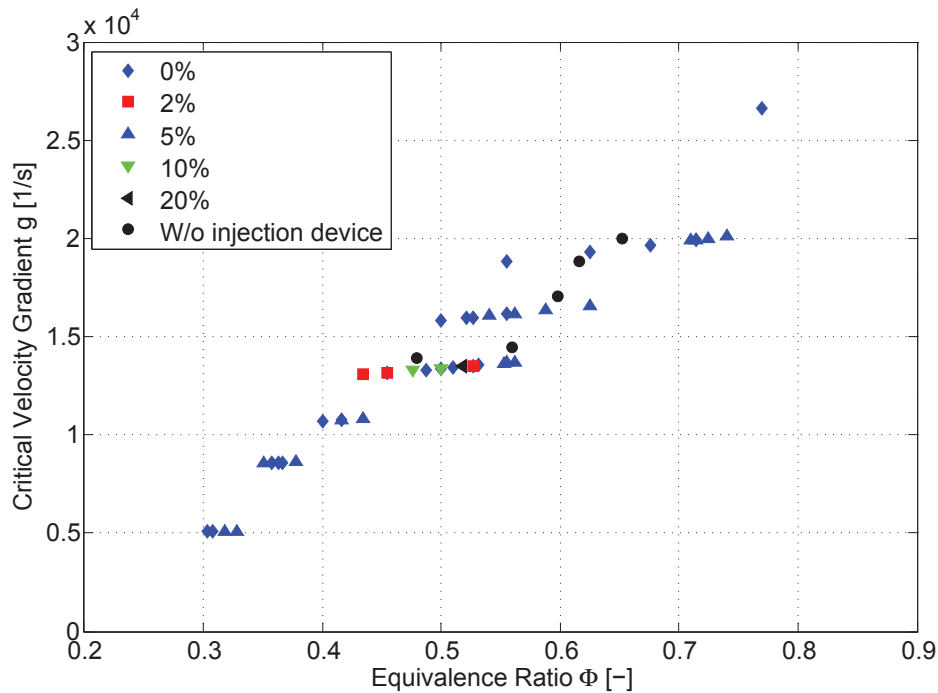


Figure 6.34: Critical velocity gradients, radial injection, $a=313$ mm

amounts of air were injected into the wall boundary layer, ranging up to 20 vol.-% of the total air mass flow. The following conclusions can be drawn from the obtained results:

- For both injection angles the flashback propensity in terms of critical velocity gradients is considerably decreased over the investigated range of equivalence ratios when the air injector is located at $a=113$ mm upstream of the tube exit. This is accompanied by lower critical bulk flow velocities and, thus, reduced total mass flow rates that are necessary to avoid flame flashback. The effect is stronger for higher air injection amounts, however, there is an upper limit. Above approximately 10% of the total air mass flow, no further improvement is observed because of a change in flame shape and flashback mechanism. Flashback images for these high injection rates revealed that the flame no longer flashes back along the wall but propagates upstream in the richer zones toward the center of the tube. In addition, increased momentum-induced mixing of the injected air with the main flow may contribute to this saturation effect.
- The positive effect on flashback propensity diminishes quickly with in-

creasing distance between injection location and tube exit ($a=213$ mm and $a=313$ mm). CFD simulations have shown that this is mainly due to improved mixing of injected air and main flow. Although the CFD results indicate some degree of equivalence ratio gradient for $a \geq 213$ mm, the observed positive effect on flashback propensity was only marginal, even for high injection rates (10, 20%).

- The CFD simulations have also revealed that the decrease in flashback propensity is primarily caused by the dilution of the near-wall mixture, whereas the additional momentum resulting from the injection plays a negligible role. This is corroborated by the marginal differences between radial and 45° -injection.
- The air injection is not capable of stopping the upstream propagating flame once it has entered the burner duct. A physical explanation for this behavior has been provided, which is based on the strong increase in flashback propensity after the change from unconfined to confined flame situation.

In a parallel research effort at the Lehrstuhl für Thermodynamik Mayer [90] investigated the influence of boundary layer injection on H_2 -air flashback in a conical swirl burner. He injected 2-5 % air either through one or through two annular slots close to the burner exit at an angle of 20° to the main flow and found that the flashback stability considerably increased. This corroborates the conclusion that flashback is primarily prevented by the near-wall dilution with air, whereas the injection angle only plays a negligible role.

In summary, boundary layer air injection constitutes a cheap, easy to implement, and effective method to improve the safety margin against flame flashback in burners operating with highly-reactive premixed fuels. It allows for partial adjustment of the local mixture equivalence ratio at the burner exit in order to get closer to the theoretical optimum. The latter is achieved when the distribution of the flame speed matches the distribution of the flow velocity over the whole burner cross section. Since an upstream propagating flame cannot be stopped by air injection once it has entered the burner duct, the boundary layer air should be injected close to the burner exit for maximum effectiveness. However, it is important to design the fluid injection properly in order to avoid flow disturbances and negative impacts on flow stratification

that could spoil the positive effects on flashback propensity. Furthermore, the positive effects of boundary layer injection need to be verified also for gas-turbine like conditions. It is also apparent that the problem of increased flashback propensity for confined flames could not be mitigated. To address this issue, a combination of the flashback prevention approach presented here with other means, such as fast-responding active control mechanisms, should be considered.

7 Microscopic Investigation of the Onset of Flashback

In this chapter, the transition from stable flame to flashback, i.e. the onset of the flashback process, will be discussed [7]. The channel burner setup was used for these investigations, because it offers improved optical access and the location of flashback onset is better predictable than in tube burners (cf. Sec. 3.2).

Results from Particle Image Velocimetry (PIV) and Planar Laser-Induced Fluorescence (PLIF) measurements will be analyzed to gain insight into the initial upstream propagation of the flame, which occurred along the wall boundary layer. In order to characterize the interaction of the flame with the flow in detail, both measurement techniques were applied to very small fields of view using (UV) long-distance microscopes in some of the experiments. The repetition rates were 20 kHz for PLIF and 3 kHz for PIV, respectively, in order to capture the highly transient phenomena during flashback. To obtain information about the lateral position of the flame during flashback, both measurement techniques were combined with simultaneous OH* chemiluminescence recordings from the top (cf. Secs. 3.4.3.2 and 3.4.4.2).

All flashback experiments presented in this chapter were conducted with hydrogen-air mixtures at atmospheric pressure and ambient temperature. The only parameter that has been varied was the equivalence ratio ($0.4 < \Phi < 0.9$). In the following sections, the flow fields at the channel burner exit in the isothermal case and for stable combustion as well as for a flame at flashback will be exemplarily presented for an equivalence ratio of $\Phi \approx 0.5$. All the effects observed were qualitatively the same within the above-mentioned range of equivalence ratios.

7.1 Velocity Field for Isothermal Flow and Stable Combustion

In Fig 7.1, Mie-scattering images for isothermal and reactive flow, respectively, are shown. The images were taken with the micro-PIV setup with a field of view of $4.15 \times 4.15 \text{ mm}^2$. In both cases the flow conditions were identical ($\bar{u}=7 \text{ m/s}$, $\Phi=0.5$, $T=293 \text{ K}$) with the only difference being that a stable flame was established in Fig. 7.1(b). The following statements can be made:

- The light reflections at the downstream end of the lower channel wall are slightly stronger in the reactive case. It has been found that the flame's chemiluminescence contributes to this effect in spite of using a bandpass filter (cf. Sec. 3.4.3.2). Nevertheless, the reflections are confined to a layer of less than 0.2 mm in both images.
- In the reacting case, the quality of the seeding images in the bottom left has slightly deteriorated, because the light scattered in the laser sheet is distorted by the stable flame on its way to the PIV camera.
- The position of the stable flame in Fig. 7.1(b) is discernible as a relatively sharp transition from high seeding density to low seeding density (unsharp region between the two dashed lines). This is due to the thermal expansion of the flow across the flame front and the associated acceleration of the particles. Moreover, the opening angle of the flame is vaguely perceptible as a second transition from low seeding density to no seeding particles at all.

The corresponding axial velocity fields (u-component) are depicted in Fig 7.2. In both cases the mean vector field resulting from 100 double images was taken to obtain a representative stationary velocity field. According to the definition of the coordinate system in Fig. 3.4, all velocities are negative (flow direction from right to left). Streamlines are superimposed to illustrate the flow path of the particles. For the sake of clarity, the density of velocity vectors shown in the plots is reduced by 50%. Valid vectors are shown in black, whereas interpolated ones are shown in orange. The latter are mainly found in the wake region and in the immediate vicinity of the channel walls.

It is apparent that the streamlines of the reacting flow are somewhat deflected downwards over the entire channel height. This is caused by flow displace-

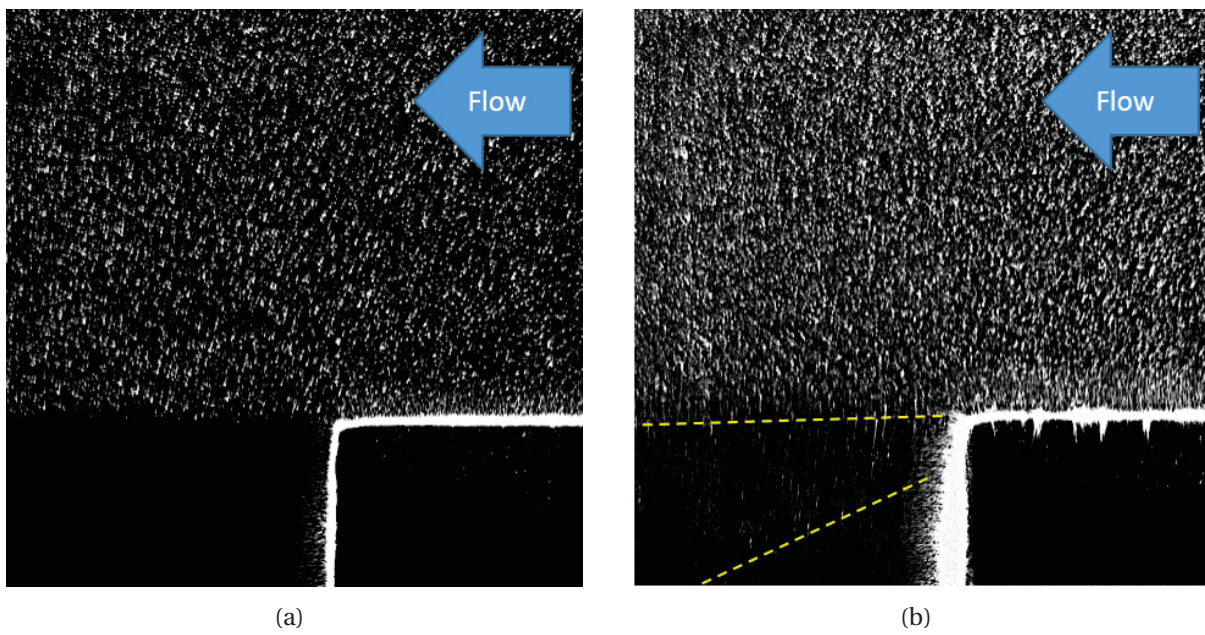


Figure 7.1: Seeding image for isothermal flow (a) and stable combustion (b) ($\bar{u}=7$ m/s, $\Phi=0.5$, $T=293$ K)

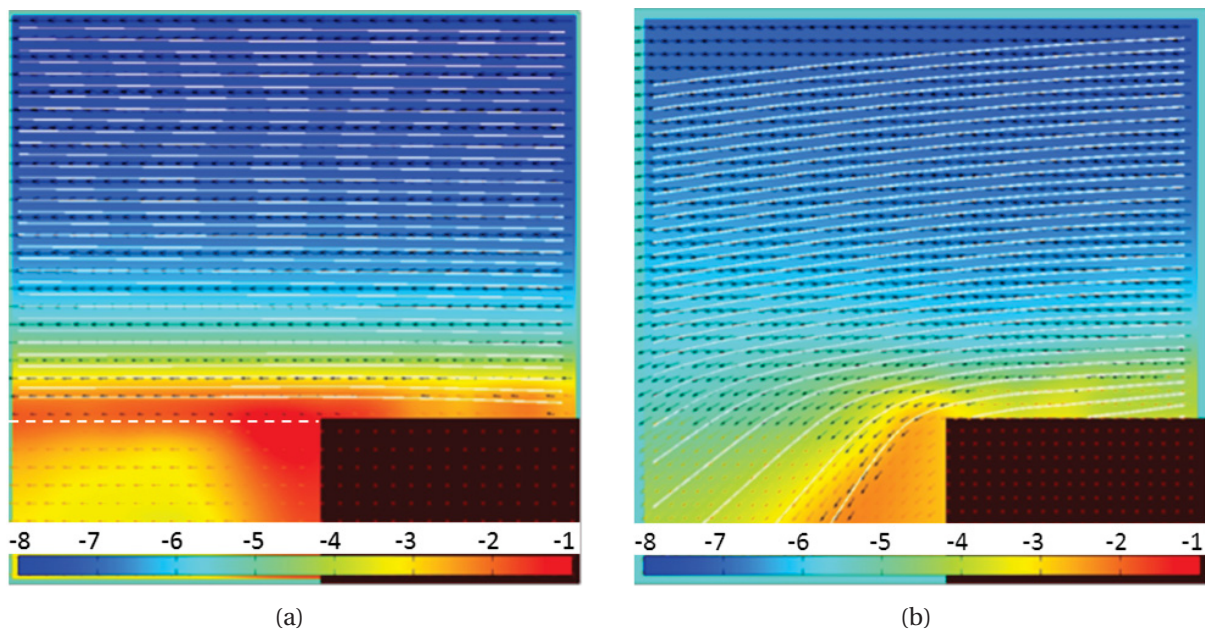


Figure 7.2: Axial velocity field u [m/s] for isothermal flow (a) and stable combustion (b) ($\bar{u}=7$ m/s, $\Phi=0.5$, $T=293$ K)

ment effects due to the presence of the upper flame sheet, which is anchored 7 mm upstream of the lower flame (see Fig. 3.4). In addition, further strong downward deflection is taking place downstream of the lower wall, because the flow is accelerated across the stable flame. Apart from these differences, the flow fields are very similar with respect to velocity magnitude and boundary layer development perpendicular to the wall (y-direction). Thus, contrary to what Eichler et al. [32] found for confined flames, there is no distinct interaction of the stable, unconfined flame with the approaching (boundary layer) flow. Please note that the velocity vectors in the bottom left of Fig. 7.2(a) (below the dashed white line) are not physically meaningful, because there are no seeding particles in this area (cf. Fig. 7.1(a)).

To gain better insight into the shape of the stable flame, macroscopic PLIF measurements with a field of view of $46.5 \times 28.5 \text{ mm}^2$ and a repetition rate of 20 kHz were conducted under identical flow conditions ($\bar{u}=7 \text{ m/s}$, $\Phi=0.5$, $T=293 \text{ K}$). Figure 7.3 shows an instantaneous PLIF image as well as an image representing the time-average of 100 single images. It can be seen that the flame sheets downstream of both the upper and the lower channel wall are first deflected outwards (angle β) before they adopt the wrinkled cone shape (angle α), which is characteristic for turbulent flames. This initial outward deflection, which is obstructed in a confined setup, inhibits interaction of the stable flame with the approaching flow. It is interesting to note that the Mie scattering image shown in Fig. 7.1(b) also indicates a slight outward inclination of the stable flame. As mentioned earlier, the fuel-air equivalence ratio was varied between $\Phi=0.4$ and $\Phi=0.9$ and the effects described above could be observed for the whole range of equivalence ratios.

7.2 Velocity Field during Flame Flashback

Fig. 7.4 presents a top view on a flame at flashback under similar flow conditions ($\bar{u}=6.9 \text{ m/s}$, $\Phi=0.53$, $T=293 \text{ K}$). Since the flashback process started at the lower channel wall, the stable flame that was anchored at the upper wall hampered the view. To mitigate this problem, the high-speed camera was focused upon the lower wall. This had the effect that the chemiluminescence coming from the lower flame appeared brighter in the recorded images than that coming from the upper flame. Additionally, details in the resulting im-

ages were enhanced through application of postprocessing techniques, such as linear contrast stretch, some degree of unsharp masking and specification of appropriate intensity thresholds. In this way, it was possible to verify that the leading flame tip propagated in the PIV laser sheet during this flashback experiment, which is shown in the temporal evolution in Fig. 7.5

In Fig. 7.6 an instantaneous seeding image and the corresponding velocity field are shown for the flame at flashback ($\bar{u}=6.9$ m/s, $\Phi=0.53$, $T=293$ K). Here, the shape of the flame can be identified considerably better than in the sta-

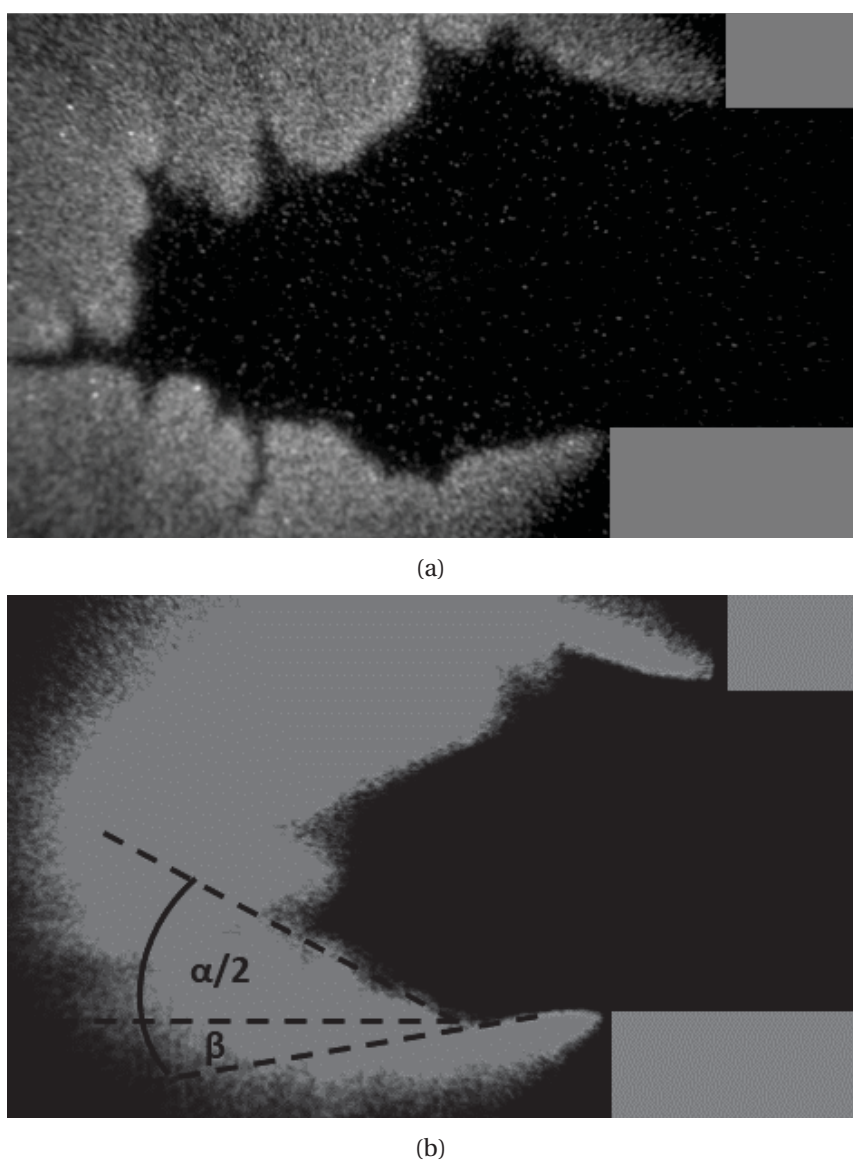


Figure 7.3: Instantaneous (a) and time-averaged (b) macroscopic PLIF image of stable flame ($\bar{u}=7$ m/s, $\Phi=0.5$, $T=293$ K)

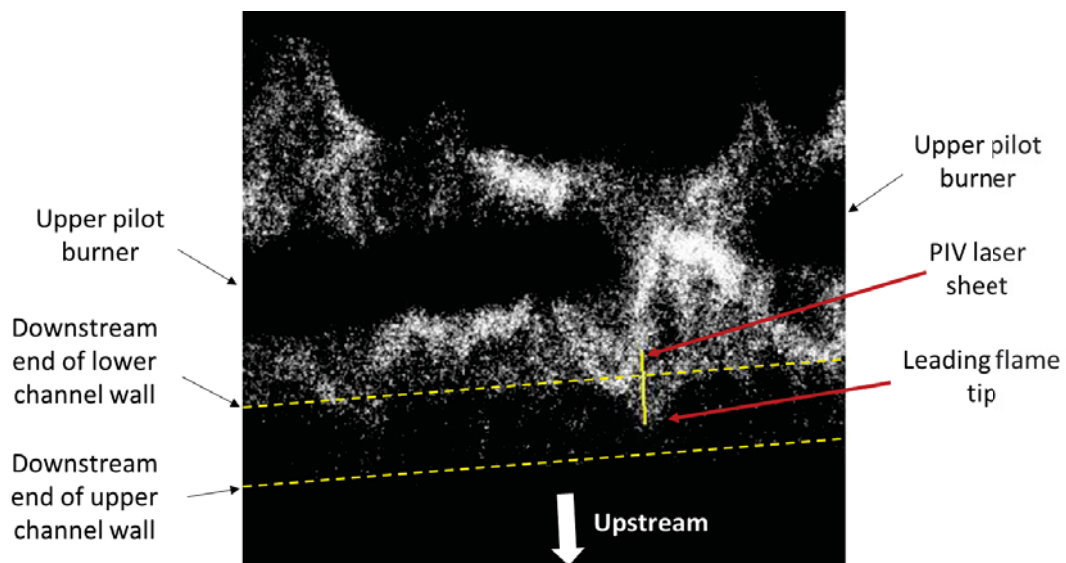


Figure 7.4: Instantaneous OH* chemiluminescence image of flame at flashback from the top

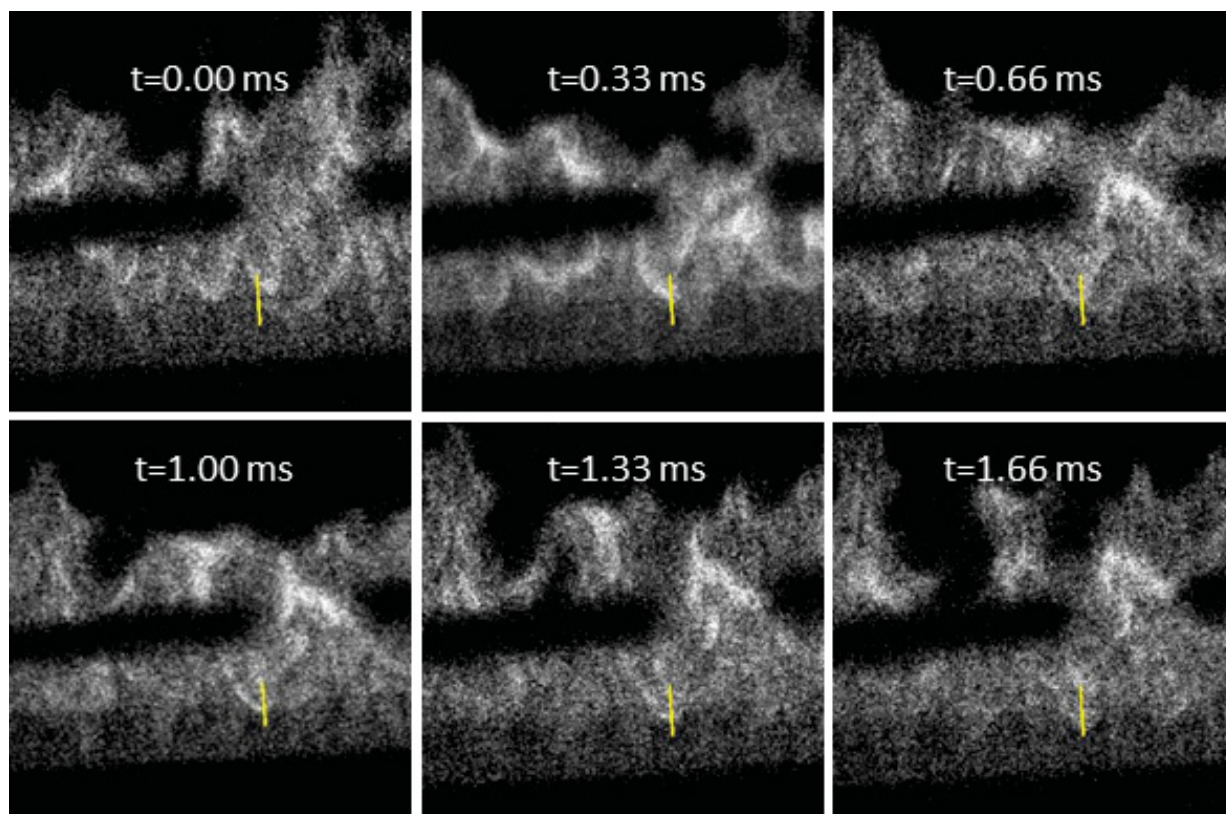


Figure 7.5: Upstream flame propagation during flashback with leading flame tip inside PIV measurement plane, $\Delta t=0.33$ ms

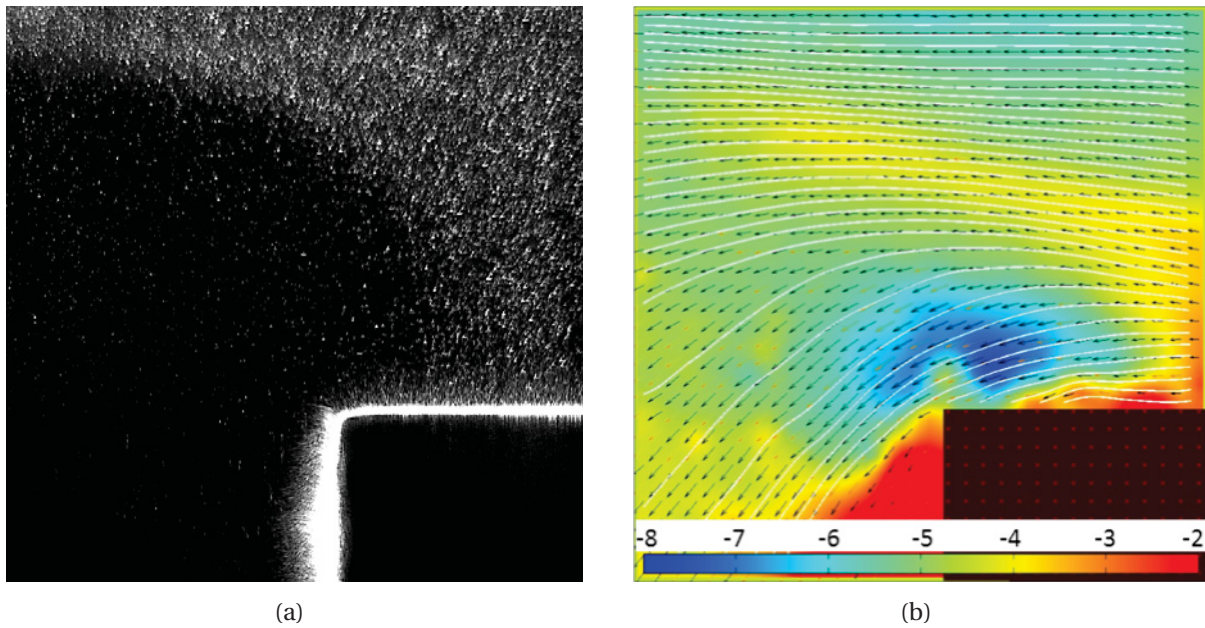


Figure 7.6: Seeding distribution (a) and axial velocity field u [m/s] (b) for flame at flashback ($\bar{u}=6.9$ m/s, $\Phi=0.53$, $T=293$ K)

ble case (cf. Fig. 7.1(b)), because the light scattered by this leading part of the flame is no longer distorted by the stable flame on its way to the PIV camera in lateral direction.

Regarding the axial velocity field, the following observations and statements can be made:

- The approaching flow is retarded directly upstream of the flame. Additionally, it is deflected around the flame, both upwards and downwards as shown in Fig. 7.6. It is reasonable to conclude that flow deflection takes place in lateral direction (perpendicular to the measurement plane) accordingly.
- Although the percentage of interpolated vectors is higher in the reaction zone due to low seeding density, it can be clearly seen that the flow is accelerated across the flame front.

The temporal evolution of the axial velocity field during upstream flame propagation - starting from a stable flame - is displayed in Fig. 7.7. The time between two images is $\Delta t=0.33$ ms. Once again, it can be clearly seen that the flow upstream of the flame becomes increasingly retarded the further the

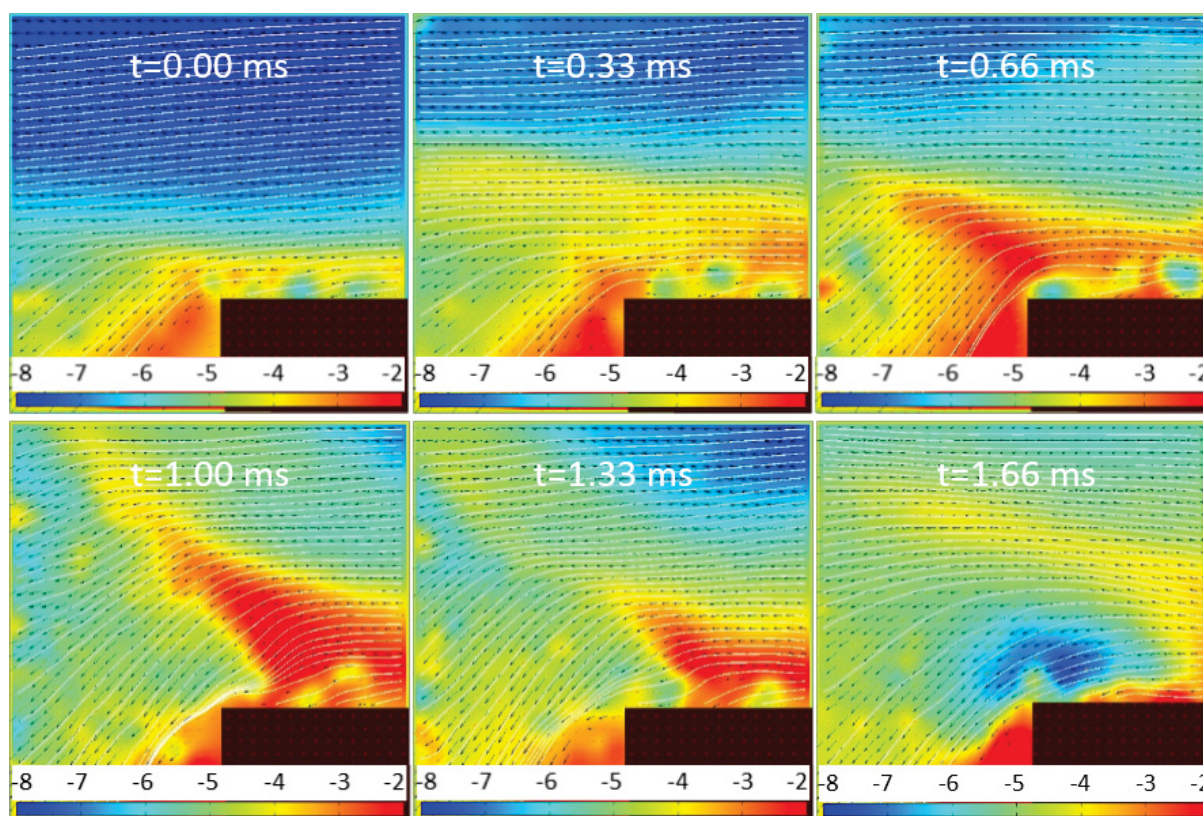


Figure 7.7: Temporal evolution of axial velocity field u [m/s] during upstream flame propagation with leading flame tip inside PIV measurement plane (μ -PIV), $\Delta t=0.33$ ms

flame proceeds upstream. In addition, the image sequence indicates that the flame does not "jump" into the flow duct directly along the lower channel wall, but starts to travel upstream from some distance downstream of the rim. This means that the propagating flame tip enters into the measuring field in the very left of the second image ($t=0.33$ ms). This observation will be further discussed later. It is worth noting that the brindled zones in Figs. 7.6 and 7.7 are no measurement errors but large-scale vortex structures that are typical for turbulent flow.

The distinct flame-flow interaction can be traced back to the flame backpressure, which is caused by the thermal expansion and the associated acceleration of the flow across the flame front (cf. Sec. 2.2.4). Nevertheless, in contrast to confined flames [32], no backflow region, i.e. boundary layer separation, was detected. It is very likely that the upward deflection of flow is hampered for an entirely confined flame due to the presence of the opposite wall, which enhances the retardation effect of the flame backpressure and leads to a backflow region. Since the upper wall in the present channel setup was 7 mm

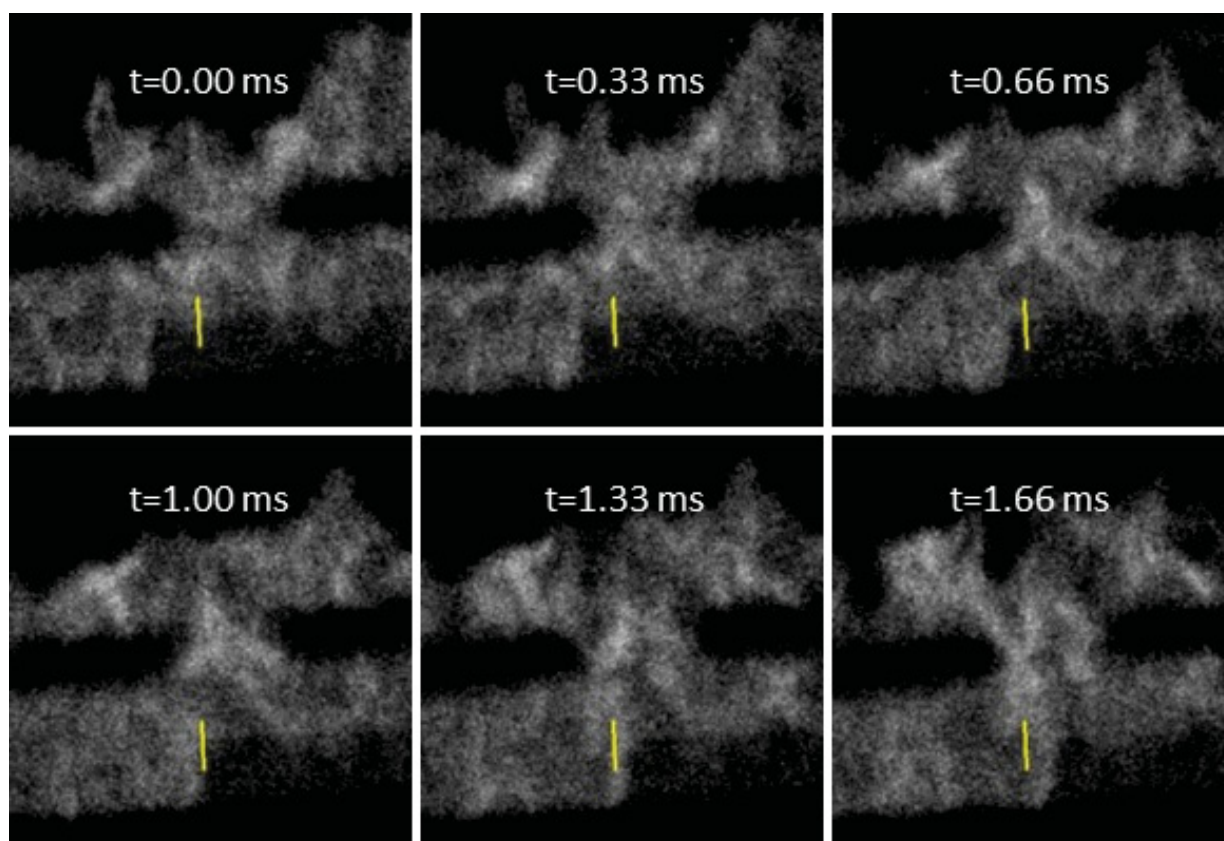


Figure 7.8: Upstream flame propagation during flashback with leading flame tip outside PIV measurement plane, $\Delta t=0.33$ ms ($\bar{u}=6.8$ m/s, $\Phi=0.52$, $T=293$ K)

shorter than the lower wall, the flame was not entirely confined during the initial phase of upstream propagation.

It is important to note that the retardation and deflection of the approaching flow during flashback only applies to the flow regions directly upstream of the leading flame tip. This is concluded from measurements where the leading flame tip had some lateral displacement from the PIV measurement plane, such that the flame tail passed through the laser sheet mainly in lateral direction (cf. Fig. 7.8). In these cases the seeding density suddenly decreased in the whole field of view and the axial velocity abruptly increased as is demonstrated in Fig. 7.9. This can again be attributed to the adverse pressure gradient generated by the flame backpressure, which is always perpendicular to the flame surface.

For further characterization of the reaction zone during flame flashback, OH-PLIF measurements at a repetition rate of 20 kHz have been conducted on a microscopic scale. The field of view was 10.3×6.25 mm² at a camera resolu-

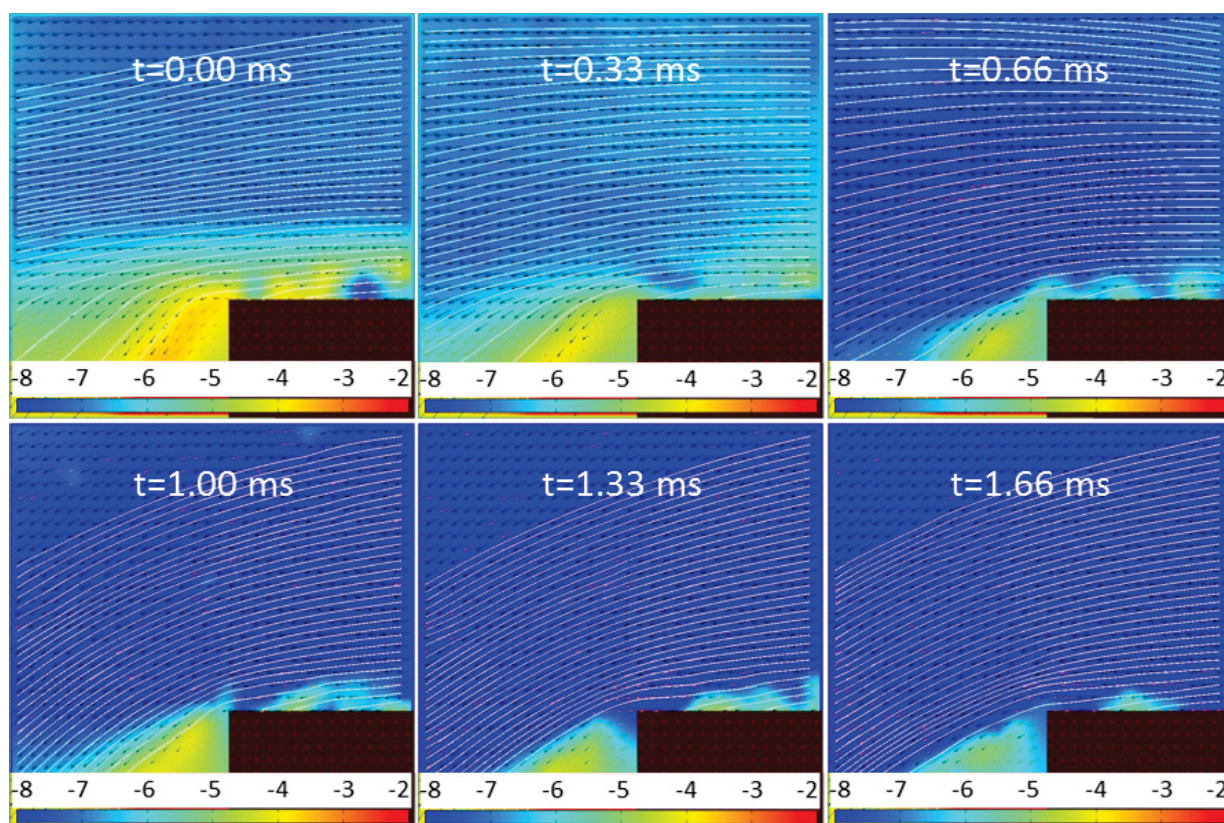


Figure 7.9: Temporal evolution of axial velocity field u [m/s] during upstream flame propagation with leading flame tip outside PIV measurement plane, $\Delta t=0.33$ ms ($\bar{u}=6.8$ m/s, $\Phi=0.52$, $T=293$ K)

tion of 1024x632 pixels. Fig. 7.10 displays an instantaneous view of the flame at flashback under nearly the same conditions as in Figs. 7.4-7.7 ($\bar{u}=7.2$ m/s, $\Phi=0.51$, $T=293$ K). To facilitate comparison with the PIV images (Figs. 7.6 and 7.7), the PLIF image is cropped so that the vertical dimension is identical ($h=4.15$ mm). Compared to the macroscopic PLIF images (Fig. 7.3), the signal-to-noise ratio has considerably deteriorated, because the light transmission of the UV long-distance microscope is much lower than that of standard UV lenses. Therefore, the image intensifier had to be operated at its maximum level. Nonetheless, the results demonstrate the following:

- Compared to Fig. 7.6(a) the shape of the leading flame section is a little flatter, yet the corresponding velocity field in Fig. 7.6(b) indicates a similarly flat shape of the flame. Taking into account that the flashback conditions are not exactly identical and that the flame has not advanced the same distance in upstream direction, the agreement is good.

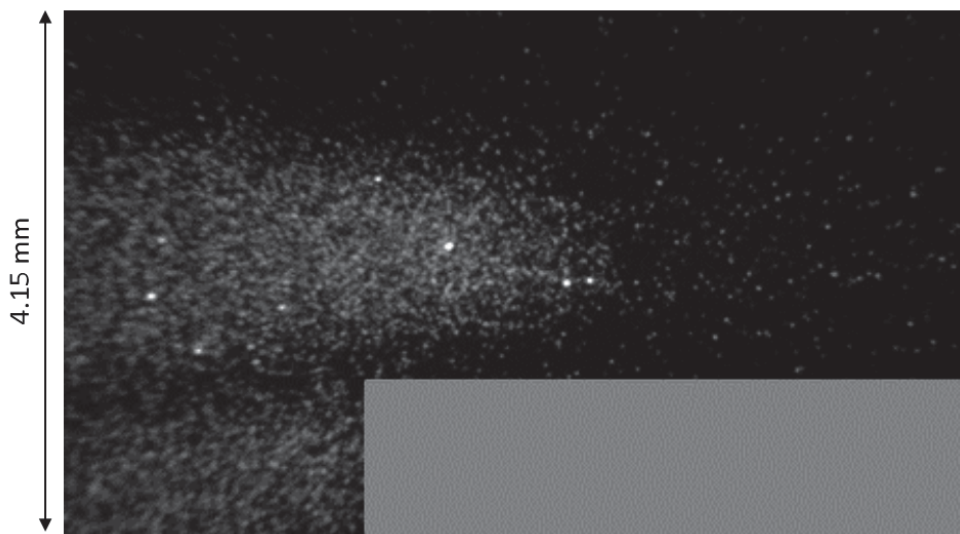


Figure 7.10: Instantaneous microscopic PLIF image of flame at flashback

- The leading flame tip propagates against the main flow with a vertical displacement of approximately 1 mm from the wall. This gives rise to the so-called leakage flow between flame and wall, which was postulated in [31, 32] (cf. Ch. 8). The latter is strongly deflected downwards at the burner exit, such that it is released almost in negative y-direction.
- Similar to the observation in Fig. 7.7, monitoring of the flame over time ($f=20$ kHz) revealed that the upstream flame propagation does not directly start at the downstream end of the lower channel wall. Instead, the lower flame bends upwards already further downstream and forms the leading flame tip that propagates against the main flow into the channel duct. This manifests itself in the dark region downstream of the lower wall in Fig. 7.10. At the same time, the flame portion anchored in the wake region directly downstream of the lower wall remains relatively unchanged (the angle β remains approximately constant during the initial phase of flashback). This is further confirmed by macroscopic PLIF measurements ($46.5 \times 28.5 \text{ mm}^2$) of flashback events, where it was discovered that the leading flame tip is formed approx. 3 mm downstream of the burner rim (see temporal evolution ($\Delta t=0.25$ ms) of the flame front in Fig. 7.11). It is concluded that the above-mentioned leakage flow prevents the flame from entering the flow duct directly along the channel wall.

The detailed evolution of the flame front during the onset of flashback will be further discussed in Sec. 8.2.

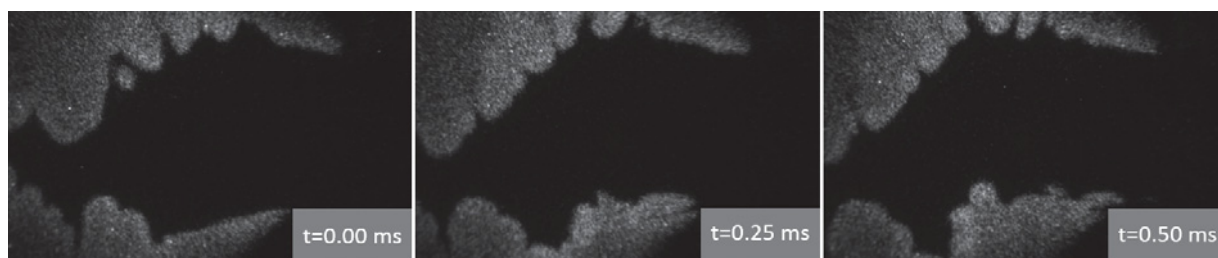


Figure 7.11: Temporal evolution of reaction zone during upstream flame propagation with leading flame tip inside PLIF measurement plane, $\Delta t=0.25$ ms ($\bar{u}=7.2$ m/s, $\Phi=0.51$, $T=293$ K)

8 Theoretical Analysis of the Flashback Process

In this chapter, the flashback behavior of confined flames will be theoretically analyzed and the differences between unconfined and confined flames will be highlighted. Thereafter, the onset of the flashback process of an (initially) unconfined flame will be examined. The experimentally observed phenomena will be analyzed and an improved theoretical flashback model for unconfined flames will be proposed.

8.1 Theoretical Analysis of Confined Flame Flashback

According to [29] the flashback process of confined flames is dominated by the interaction of the (stable) flame with the approaching flow as a result of the flame backpressure Δp_f . This hypothesis will now be examined both *qualitatively* and *quantitatively*.

8.1.1 Qualitative Analysis

As a first step, the backpressure was calculated for lean H₂-air flames according to Eq. (2.46) in order to obtain a qualitative understanding of the influence of the backpressure on the flashback limits. As can be seen from Fig. 8.1, the backpressure almost vanishes below $\Phi=0.3$, but steeply increases with increasing equivalence ratio. This is plausible with regard to the flashback limits of confined flames in Fig. 5.5. In the very lean range the backpressure seems to be too low to appreciably influence the upstream flow and thus the flashback limits for unconfined and for confined flames are almost the same. This low backpressure also explains why flashback is not a sudden event for very lean mixtures, as was described in Sec. 3.3.1. For $\Phi < 0.35$, the flame flickers back and forth for a while during the onset of flashback, because the situ-

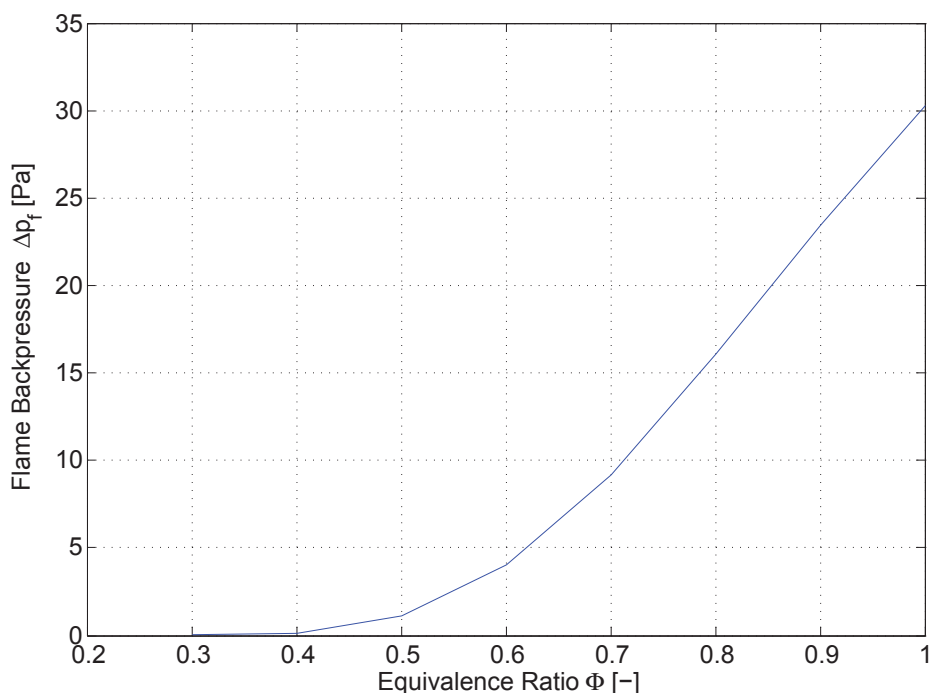


Figure 8.1: One-dimensional flame backpressure for laminar H₂-air flames

ation slightly upstream of the burner exit is not substantially different from that directly at the exit. With increasing equivalence ratio the backpressure steeply increases and is therefore able to retard and finally reverse the approaching boundary layer flow. This explains the continuously growing deviation in flashback propensity between unconfined and confined flames with increasing equivalence ratio (cf. Fig. 5.5). It is important to note that the laminar unstretched flame speed S_l was used for calculating the flame backpressure in Eq. (2.46), whereas turbulent structures affect the flame speed of a confined flame burning in the turbulent flow near a wall. The effect of turbulence on the backpressure will be taken into account in the following analysis, because the turbulent flame speed depends on the specific flow conditions, e.g. the velocity fluctuations (cf. Sec. 2.2.2).

As a second step, the Stratford criterion [115] for turbulent boundary layer flow (cf. Eq. (2.34)) will now be applied to find out whether flow separation due to the backpressure can be expected under the critical flashback conditions measured for the confined tube burner flames in Fig. 5.5, i.e. the occurrence of flow separation will be regarded as an indicator/prerequisite for the occurrence of flashback in the following analysis.

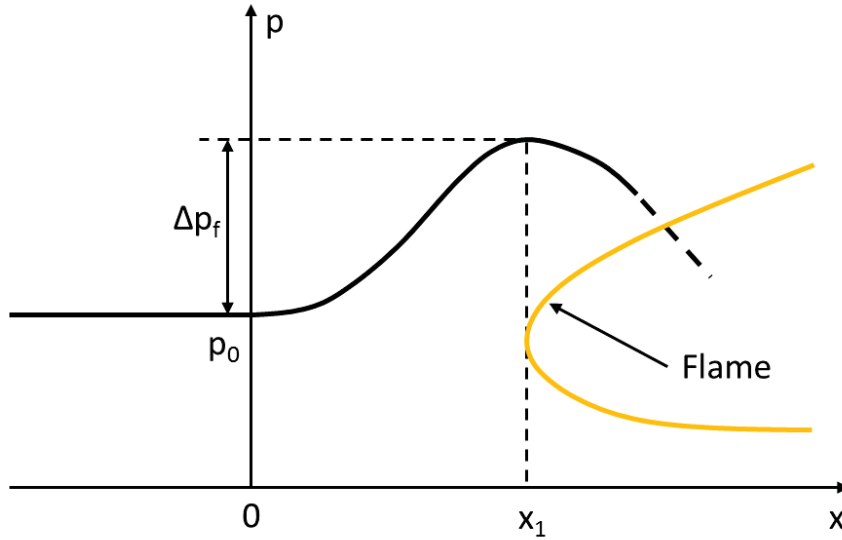


Figure 8.2: Qualitative illustration of Stratford model during presence of a flame

For $Re \leq 10^6$ and $\frac{d^2 p}{dx^2} \geq 0$, the constants in Eq. (2.34) are $\beta = 0.73$ and $n = 6$. Eichler [29] performed Direct Numerical Simulations (DNS) of laminar flame flashbacks in flat plate boundary layers. The simulations for $\Phi = 0.55$ demonstrated that the main proportion of the pressure rise takes place within a distance of approx. $x_1 = 10$ mm upstream of the flame tip, i.e. the influence of the flame backpressure vanishes after the distance x_1 in upstream direction. On the basis of the DNS simulations the pressure development right upstream of the flame can be approximated by means of the following quadratic equation, where $x = x_1$ denotes the position of the flame tip and $x = 0$ is the start of the pressure rise, i.e. $0 \leq x \leq x_1$ (cf. Fig. 8.2):

$$p(x) = \frac{\Delta p_f}{x_1^2} x^2 + p_0 \quad (8.1)$$

Due to the lack of information about the corresponding pressure development in the turbulent case, Eq. (8.1) is used here as an approximation. Inserting Eq. (8.1) into Eq. (2.35) yields:

$$C_p(x) = \frac{p(x) - p_0}{\frac{1}{2} \rho U_\infty^2} = \frac{2 \Delta p_f x^2}{\rho U_\infty^2 x_1^2}, \quad Re(x) = \frac{U_\infty x}{\nu} \quad (8.2)$$

Inserting Eq. (8.2) into Eq. (2.34) gives:

$$2 \frac{2 \Delta p_f x^2}{\rho U_\infty^2 x_1^2} \sqrt{\frac{4 \Delta p_f x^2}{\rho U_\infty^2 x_1^2}} = 1.06 \cdot 0.73 \left(10^{-6} \frac{U_\infty x}{\nu} \right)^{0.1} \quad (8.3)$$

Solving Eq. (8.3) for x yields the separation position x_{sep} :

$$x_{sep} = \left(\frac{0.387 \left(10^{-6} \frac{U_\infty}{\nu} \right)^{0.1}}{4 \left(\frac{\Delta p}{\rho U_\infty^2 x_1^2} \right)^{1.5}} \right)^{10/29} \propto \Delta p^{-\frac{15}{29}} x_1^{\frac{30}{29}} \quad (8.4)$$

Equation (8.4) will first be interpreted in a *qualitative* manner. As indicated in Eq. (8.4), the separation position x_{sep} is approx. inversely proportional to the square root of the backpressure. Thus, for a given length x_1 , the occurrence of separation is also approx. inversely proportional to the square root of the backpressure, because separation only occurs for $x_{sep}/x_1 \leq 1$. It is worth noting that the length x_1 in Eq. (8.4) is approx. directly proportional to x_{sep} , i.e. increasing or decreasing x_1 by a certain factor will increase/decrease x_{sep} by approx. the same factor. Therefore, a variation (or uncertainty) of x_1 does not appreciably alter the flow separation propensity (cf. quantitative sensitivity analysis in Tab. 8.1).

8.1.2 Quantitative Analysis

Below, an attempt to obtain quantitative information from the Stratford criterion is made. First, Eq. (8.4) will be applied to a number of experimental flashback points measured with the confined TUM burner (cf. Fig. 5.5) in order to check whether the criterion predicts separation under these conditions. Thereafter, Eq. (8.4) will be rearranged in order to predict the critical bulk flow velocities for confined flames and to compare them with the experimental flashback results.

Regarding the first point, the variables ρ and ν in Eq. (8.4) are taken from the experimentally determined flashback points, and U_∞ are the measured critical bulk velocities \bar{u} at flashback (cf. Tab. 8.1). In order to account for the influence of turbulence in Eq. (8.4), the flame backpressure Δp_f is calculated using a turbulent flame speed. The latter is obtained from the correlation proposed by Damköhler [22], which relates the turbulent flame speed S_t to the laminar

Φ [-]	0.40	0.50	0.55	0.60	0.68	0.80	0.85
\bar{u}_{crit} [m/s]	12.40	16.85	20.41	21.62	25.62	31.89	32.43
x_{sep}/x_1 [-] ($x_1=1$ mm)	1.64	1.35	1.26	1.14	1.05	0.98	0.93
x_{sep}/x_1 [-] ($x_1=10$ mm)	1.78	1.46	1.37	1.24	1.13	1.06	1.01
x_{sep}/x_1 [-] ($x_1=100$ mm)	1.92	1.58	1.48	1.34	1.23	1.15	1.09

Table 8.1: Separation positions for confined flames according to the Stratford criterion [115]

flame speed S_l and the root mean square of the turbulent velocity fluctuations u'_{rms} :

$$S_t(d_f) \approx S_l + u'_{rms}(d_f) \approx S_l + (b \cdot \bar{u}) Tu(d_f) \quad (8.5)$$

The root mean square of the turbulent velocity fluctuations u'_{rms} in Eq. (8.5) is estimated by Eq. (2.8). In the present analysis a turbulence intensity of $Tu(d_f)=15\%$ is used, which is based on the experimentally determined distribution of Tu in channel flow with an unconfined flame (cf. values of Tu in the near-wall region in Fig. 8.6). The choice of this value will be further discussed at the end of this section. The velocity coefficient b in Eq. (8.5) takes into account that the leading flame tip during flashback propagates upstream at a wall-normal distance of $d_f \approx 0.53\text{--}0.96$ mm [29], i.e. the turbulent flame speed must be calculated at the position d_f inside the wall boundary layer. The microscopic PIV measurements in Ch. 7 have shown that the axial velocity u at the position d_f amounts to approximately 60-70% of the bulk flow velocity \bar{u} in the channel. Therefore, an average value of $b=0.65$ is assumed. Table 8.1 shows the resulting ratios x_{sep}/x_1 for a range of equivalence ratios and three different values of x_1 .

The following conclusions can be drawn:

- A variation of x_1 over two orders of magnitude does not change the results significantly.
- x_{sep} is in the same order of magnitude as x_1 , which indicates that the backpressure of the flame is generally in the right order of magnitude to cause boundary layer separation.

- In particular for very lean mixtures, the ratio x_{sep}/x_1 is greater than unity. This implies that separation should not take place under these conditions, whereas flashback occurred in the experiments. However, the following two arguments must be taken into account: On the hand, complete flow separation is no necessary condition for flashback. The latter can already occur when the flow is sufficiently retarded such that the flame speed exceeds the flow velocity, as was shown for an unconfined flame in Ch. 7. On the other hand, the estimations made for the calculation of the turbulent flame speed S_t in Eq. (8.5) are likely to contribute to the observed deviations, because the flame backpressure Δp_f in Eq. (8.4) scales with the square of S_t .

In spite of the approximations made, it could be shown that the separation points calculated by Eq. (8.4) match relatively well with the measured flashback limits.

In a final step, the Stratford criterion will be used to predict the flashback limits of confined flames. For this purpose, the separation point x_{sep} in Eq. (8.4) is set equal to the distance x_1 , i.e. $x_{sep}/x_1=1$. This is the critical condition for the onset of flow separation. Rearranging of Eq. (8.4) yields the critical bulk velocity at the separation point \bar{u}_{sep} :

$$\bar{u}_{sep} = \left(\frac{4}{0.387} \frac{\left(\frac{\Delta p_f}{\rho}\right)^{1.5}}{\left(10^{-6} \frac{x_1}{v}\right)^{0.1}} \right)^{10/31} \quad (8.6)$$

Since the flame backpressure Δp_f must be calculated from the turbulent flame speed, \bar{u}_{sep} also appears on the right side of Eq. (8.6):

$$\bar{u}_{sep} = \left(\frac{4}{0.387} \frac{\left[(S_l + (b \cdot \bar{u}_{sep}) Tu)^2 \left(\frac{T_{ad}}{T_1} - 1 \right) \right]^{1.5}}{\left(10^{-6} \frac{x_1}{v}\right)^{0.1}} \right)^{10/31} \quad (8.7)$$

Equation (8.7) can now be solved iteratively with the software MATLAB using a Newton solver with an appropriate initial estimate of the solution. The resulting critical bulk velocities are compared to the ones measured with the confined TUM Burner in Fig. 8.3. For reference, the flashback limits measured

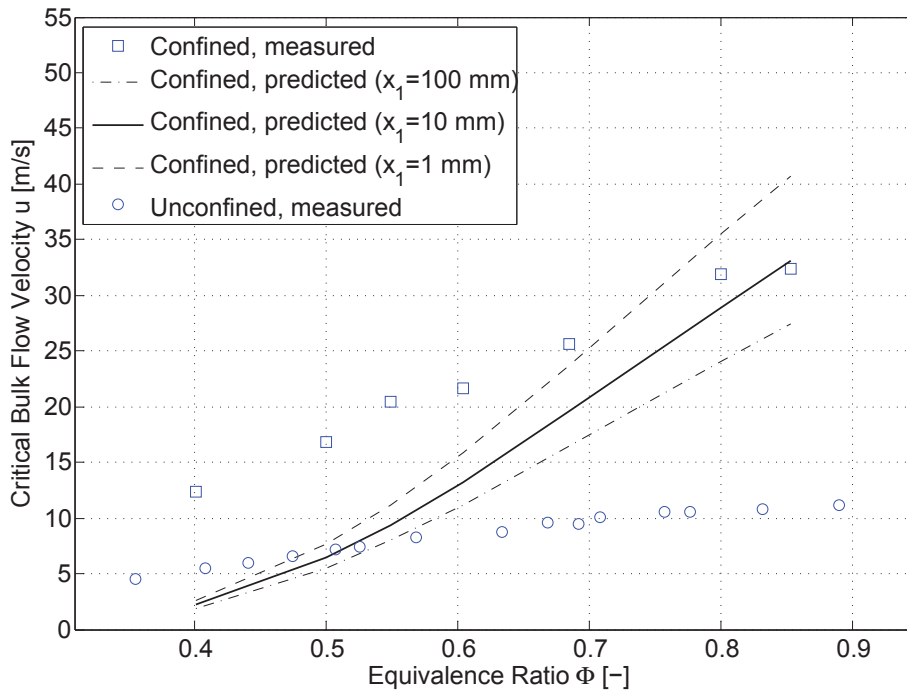


Figure 8.3: Predicted vs. measured critical bulk flow velocities for confined H_2 -air flames (TUM Burner, $d=40$ mm)

for unconfined flames with the TUM Burner are also plotted. The distance x_1 was again varied within two orders of magnitude ($x_1=1$ – 100 mm).

Figure 8.3 shows that the flashback propensity of confined flames is considerably underpredicted for $\Phi < 0.6$, with the critical bulk velocities for $\Phi < 0.5$ even being below those for unconfined flames. With increasing Φ the predicted limits quickly approach the measured limits until an almost perfect match is reached for $\Phi \approx 0.82$. The two dashed lines in Fig. 8.3 illustrate the influence of varying x_1 . It is likely that x_1 varies with varying backpressure, because a higher total pressure rise in front of the flame is probably accompanied by an increase in area of influence, and vice versa. However, even the extensive variation of x_1 in Fig. 8.3 only leads to a relatively small variation of the critical bulk velocity, which reaches a value of $\Delta \bar{u} \approx \pm 5$ m/s for $\Phi \approx 0.8$.

From these results it can be concluded that the calculated flame backpressure for very lean mixtures ($\Phi < 0.5$) is too low to cause flow separation. Therefore, in contrast to richer mixtures, it is likely that the backpressure is not the main reason for the occurrence of flashback for $\Phi < 0.5$. In this lean region, flashback is probably driven by a combination of the (moderate) influence of the back-

pressure and the flame speed being in the same order of magnitude as the (almost unaltered) flow velocity. It is emphasized again that complete flow separation is no necessary condition for the occurrence of flashback. Taking this into account, the predictive capability of the Stratford model is satisfactory for a rough quantitative estimation of the flashback propensity of confined flames.

It is mentioned that the requirement $C_p(x) \leq 4/7$ was fulfilled for all points in the analysis above (cf. Sec. 2.1.2).

In summary, it is concluded that the Stratford criterion for turbulent flow is helpful with regard to the qualitative description of the flashback propensity of confined flames. In addition, the quantitative analysis has shown that the flame backpressure is generally in the right order of magnitude to cause flow separation, in particular for relatively rich flames ($\Phi > 0.5$). If the pressure field upstream of the confined flame and the turbulent flame speed are sufficiently well known, the Stratford criterion can be used for a rough quantitative estimation of the flashback limits. For a confined flame at a given operating point, a conservative approximation of the flashback propensity based on the results shown in Tab. 8.1 would be that flashback is unlikely to occur if $x_{sep}/x_1 > 2$.

The limitations and shortcomings of the model are:

- The turbulent flame speed S_t is generally difficult to obtain, but has a decisive influence on the model predictions. Therefore, the turbulence intensity Tu in the model must be chosen with great care. This value serves as an adjustment factor in the model and must therefore be adjusted according to the flow conditions. Alternatively, the predictive capability of the model will probably improve by accurately determining the turbulent flame speed or by replacing Eq. (8.5) by a more sophisticated correlation for the determination of the turbulent flame speed.
- Based on laminar DNS simulations the pressure field upstream of the flame was approximated by a quadratic equation (cf. Eq. (8.1)), which may not be generally valid. Deviations from this quadratic expression will have an impact on Eqs. (8.4) and (8.7). This may turn the distance x_1 into a more decisive variable for the prediction of flashback.

8.2 Theoretical Analysis of Unconfined Flame Flashback

8.2.1 Transition from Stable Unconfined Flame to Flashback

Based on the findings in Ch. 7 the flashback process of an initially unconfined flame can be described as follows: In stable mode the flame exhibits a short outward bent section downstream of the burner exit (angle β). Further downstream it adopts the cone angle α until the upper and the lower flame sheet merge (cf. Fig. 7.3). On approaching flashback conditions, the angle α increases, while the angle β remains approximately constant. The flashback process starts at $s_f \approx 3$ mm downstream of the burner rim, i.e. in a region where low-velocity mixture from the wall boundary layer is consumed by the flame (cf. Figs. 8.4 and 8.5). At this position the local flame speed is equal to the local flow velocity. It is important to note that the axial flow velocity is not yet altered by the presence of the flame at this instant of time, because the flame front is almost aligned with the axial direction. Upon exceeding the flashback limit, a flame tip is formed locally which moves in upstream direction. At the same time, the adverse pressure gradient created by the flame backpressure in front of this flame tip becomes aligned with the (axial) approaching flow. This leads to the experimentally observed effect of flow deflection and retardation, which accelerates the upstream flame propagation. The deeper the flame propagates into the flow duct, the more the deflection of flow is hampered by the surrounding duct walls. Supposedly, this leads to stronger retardation of the approaching flow until backflow regions are generated when the whole flame is entirely confined in the burner duct, as was demonstrated in [32]. The latter is accompanied by an increase in flashback speed.

In the initial phase of flashback the leading flame tip propagates upstream at $d_f \approx 1$ mm away from the wall. The measurements revealed that this distance is relatively independent of the equivalence ratio. However, there is evidence that this distance slightly decreases the further the flame moves upstream. This is consistent with observations for confined flames in [29], where it was concluded that the leading flame tip propagates upstream inside a wall-bound backflow region, whose maximum penetration depth into the flow was between 0.53 and 0.96 mm. It can be concluded that the maximum upstream propagation speed (flashback speed) is reached at the wall distance d_f due to the combined effect of flow retardation and the increase of the flame speed

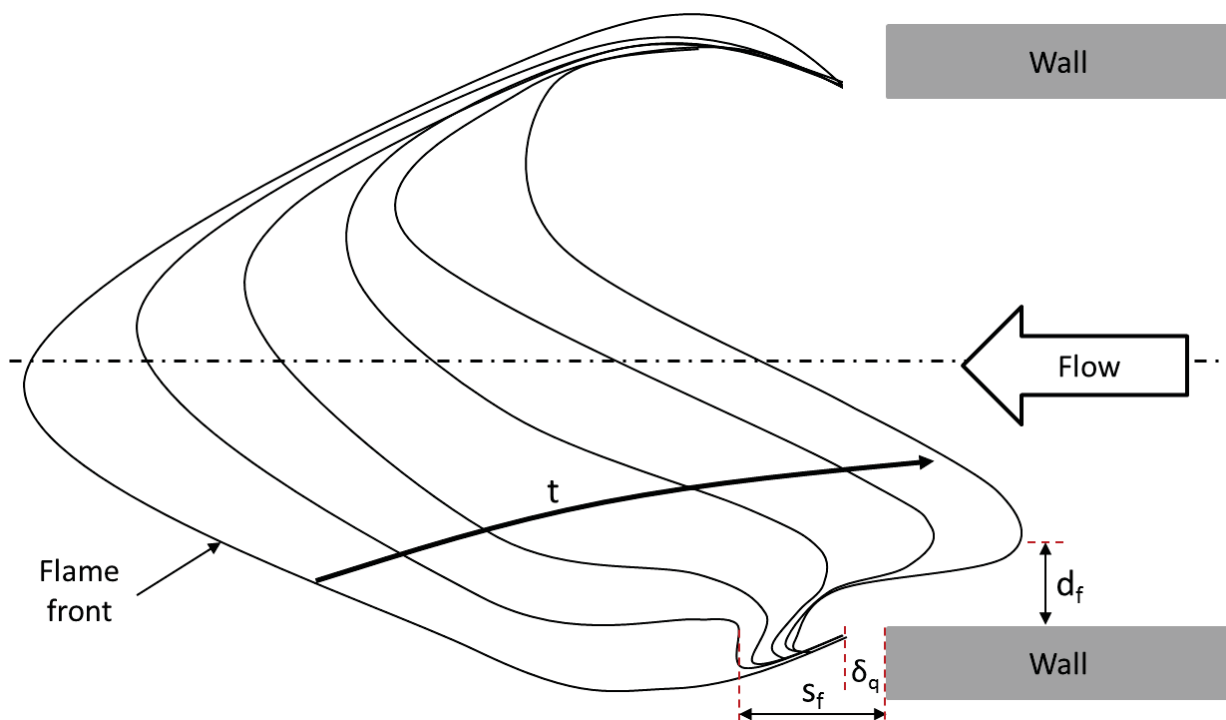


Figure 8.4: Schematic illustration of the transition from stable flame to flashback

normal to the wall.

In summary, it was discovered that there is no appreciable interaction of the stable, unconfined flame with the flow inside the burner duct until the flashback limit is reached. Nevertheless, as was the case for confined flames, the critical gradient model developed by Lewis and von Elbe [84] does not adequately represent the physical reality during the onset of flashback. Neither does it correctly reflect the position and the shape of the stable flame nor does it consider the influence of leakage flow between flame and burner wall. Therefore, an improved model will be presented in the following section, which accounts for the experimentally observed phenomena described above.

8.2.2 Improved Flashback Model for Unconfined Flames

The stable, unconfined flame close to the flashback limit is schematically depicted in Fig. 8.5 along with the path of the leading flame tip during flashback. On the right-hand side of the figure the axial velocity profile $u(y)$ in the burner duct is sketched along with some streamlines. On the left-hand side the sta-

ble, unconfined flame is shown including a qualitative representation of the flame backpressure distribution. The shape and the dimensions of the flame were determined on the basis of the PLIF images presented in Ch. 7. The flow direction is from right to left. The essential aspects of the schematic in Fig. 8.5 can be summarized as follows:

- Downstream of the burner exit the stable flame is first bent outward (angle β) before it adopts the cone angle α after the distance a . The reason for this initial outward deflection is that the reactive mixture is also deflected outwards at the burner exit, because it experiences the backpressure of the downstream (converging) part of the flame. This pressure field with the comparatively lower ambient pressure p_∞ in the outward direction forces the flow outwards. After a certain distance a the flame can no longer burn further outwards because there is no reactive mixture left. Therefore, it adopts the angle α and consumes the mixture flow coming from the central parts of the burner duct.
- As a result of heat losses to the wall and radical recombination processes there is a relatively large head-on quenching gap δ_q downstream of the burner exit between flame and wall. The fresh gas flow in the immediate vicinity of the wall is accelerated through this gap because the ambient pressure p_∞ is lower than the pressure inside the burner duct. This leakage flow mixes with entrained ambient air and is consumed by the flame further downstream. On its way, the leakage flow convectively transports heat (\dot{q}) generated at the flame base in outward direction and at the same time convectively cools the burner rim.
- The axial velocity distribution near the burner wall is only little affected by the backpressure of the stable flame because of the outward bent flame section downstream of the burner exit and the fact that the adverse pressure gradient generated by the flame is perpendicular to the flame surface. Nevertheless, the flow in the immediate vicinity of the wall, i.e. the leakage flow, is slightly accelerated on approaching the head-on quenching gap δ_q . Such a flow acceleration does not take place in the isothermal case, because due to the lacking flame backpressure the pressure level inside the burner duct is generally lower than in the reactive case (cf. flow fields with and without flame in Fig. 7.2).

downstream direction). Thus, the critical condition for the onset of flashback can be expressed in terms of a balance between the axial velocity u and the flame speed S_f according to the following equation:

$$S_f(s_f) = u(s_f) \propto u(y_f) \quad (8.8)$$

As can be seen, the expression in Eq. (8.8) is similar to the flashback condition in the critical gradient model (cf. Fig. 1.1). However, the flame-flow configuration sketched in Fig. 8.5 represents the physical reality better, because it explains why the flow in the burner is not affected by the flame backpressure until the flashback limit is reached. The new model demonstrates that the flashback tendency of an unconfined flame can be correlated by the undisturbed velocity profile of the approaching flow. This is an important finding as it explains why the existing critical gradient concept is capable of correlating flashback tendencies. However, the wall distance y_f estimated from the μ -PIV measurements was between 0.6 and 0.7 mm, with y_f being almost independent of the equivalence ratio. According to the turbulent boundary layer regions introduced in Sec. 2.1.1, the velocity profile at this distance from the wall is no longer linear (the non-dimensional wall coordinates range between $y_f^+ = 13$ and $y_f^+ = 21$). Nevertheless, the velocity at the position y_f is to a large degree determined by the velocity gradient at the wall.

It is important to note that all quantities in Eq. (8.8) are interdependent (cf. comments at the end of this section) and fluctuate over time due to the highly turbulent nature of the flow. Therefore, the onset of flashback is most probable when at a certain instant of time the turbulent flame speed is maximal and the flow velocity is minimal. Thus, the critical flashback condition in Eq. (8.8) can be rewritten as follows:

$$S_{f,max}(s_f) \approx u_{min}(y_f) \quad (8.9)$$

If this "worst-case" scenario remains for a sufficiently long time, a flame tip is formed that propagates into the burner. The subsequent upstream propagation of the flame is facilitated by the local generation of an adverse pressure gradient upstream of the flame tip as a result of the flame backpressure.

Quantitative Plausibility Check:

Equation (8.9) will now be subjected to a quantitative plausibility check. The equation will be used to determine the approximate flame speed S_f at the position s_f in the channel burner experiments that were presented in Ch. 7. For this purpose, the instantaneous minimum velocity u_{min} at the position y_f is estimated using the following statistical approach:

$$\begin{aligned} u_{min}(y_f) &= \langle u \rangle (y_f) - u'_{max}(y_f) \approx \langle u \rangle (y_f) - (u'_{rms}(y_f) \cdot k) \\ &= \langle u \rangle (y_f) - (Tu \cdot \langle u \rangle (y_f) \cdot k) = \langle u \rangle (y_f)(1 - Tu \cdot k) \end{aligned} \quad (8.10)$$

In Eq. (8.10) $\langle u \rangle$ is the time-mean velocity and k is a coefficient. Assuming a Gaussian distribution of the velocity, k represents a multiple of the standard deviation σ , with $\sigma = u'_{rms}$. For instance, according to the standardized normal distribution $k=2.58$ implies that 99 % of the velocity values lie within the velocity interval $\langle u \rangle \pm k \cdot u'_{rms}$.

Both the time-mean velocities $\langle u \rangle (y_f)$ and the time-mean velocity fluctuations u'_{rms} are extracted from the μ -PIV measurements, where a stable flame was burning near the flashback limit (cf. Ch. 7). The corresponding distribution of the turbulence intensity Tu in the flow field is exemplarily shown for an equivalence ratio of $\Phi=0.5$ in Fig. 8.6 (average of 250 instantaneous velocity fields).

While Tu is between 5 and 10 % toward the center of the channel, it is between 15 and 20 % very close to the wall and in the shear layer downstream of the burner exit (i.e. where the stable flame is anchored).¹ This distribution of Tu compares well (both qualitatively and quantitatively) with the findings of Moser et al. [93], who performed DNS simulations of fully developed turbulent channel flow. Based on Fig. 8.6 a turbulence intensity of $Tu=15$ % is chosen for the following analysis. Along with using $k=2.58$ the velocity $u_{min}(y_f)$ can be calculated.² The results for $u_{min}(y_f)$ are displayed for different equivalence ratios in Fig. 8.7, where they are compared with the laminar flame speed S_l as well as with a turbulent flame speed calculated according to Eq. (8.5) using u'_{max} (cf. Eq. (8.10)).

¹ Note that Tu is particularly high within a layer of approx. 0.2 mm normal to the wall, which is caused by measurement errors due to laser light reflections (cf. Ch. 7).

² The choice $k=2.58$ implies that statistically only 0.5 % of the velocity values are below the calculated $u_{min}(y_f)$, which seems a reasonable choice for the lower limit of $u(y_f)$.

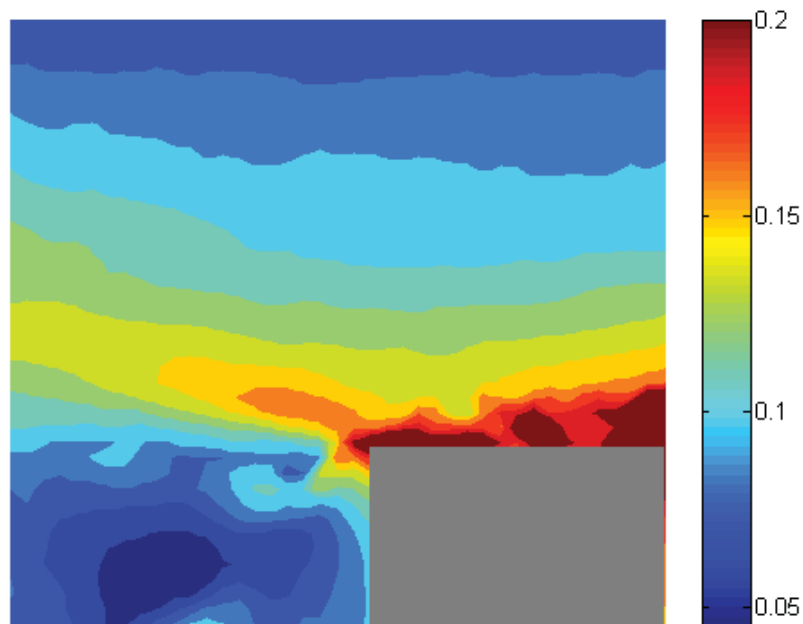


Figure 8.6: Distribution of the turbulence intensity Tu in the channel flow field with stable flame ($\bar{u}=7$ m/s, $\Phi=0.5$, $T=293$ K)

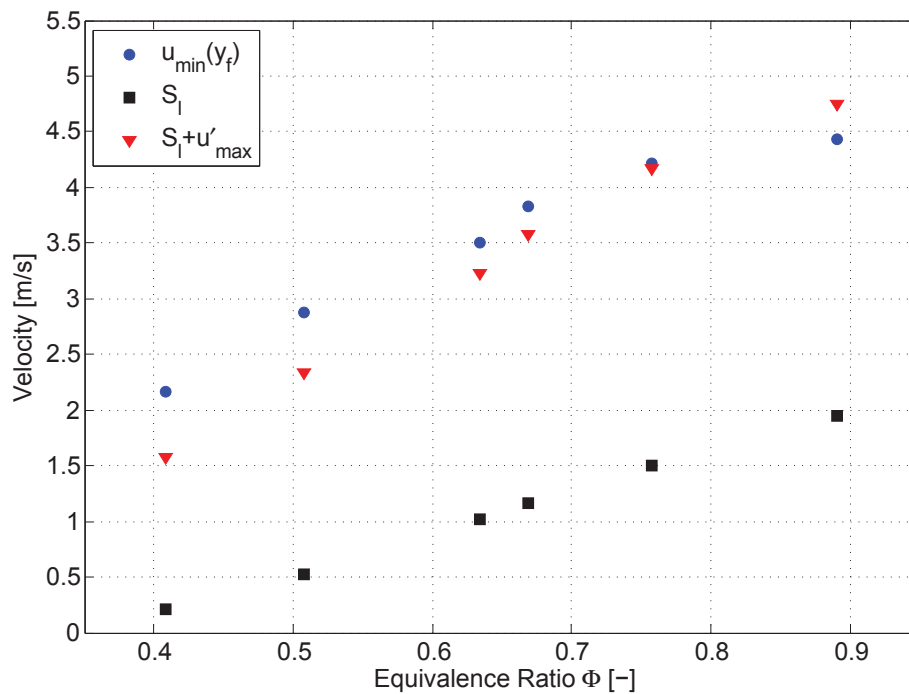


Figure 8.7: Comparison of estimated minimum flow velocities at the position y_f with the laminar flame speed and a turbulent flame speed

The plot demonstrates that the laminar flame speed is far below the estimated values of u_{min} , which confirms that the flames were stabilized under turbulent conditions in the experiments. Interestingly, adding u'_{max} to the laminar flame speed yields a turbulent flame speed that compares fairly well with the estimated u_{min} . In other words, estimating the turbulent flame speed as the sum of the laminar flame speed and the maximum velocity fluctuations according to Eq. (8.10) leads to a satisfactory prediction of $u_{min}(y_f)$.

Following up on this finding, Eq. (8.9) is now used to predict the flashback limits of the unconfined channel flames that were investigated in Ch. 7. By combining Eqs. (8.9) and (8.10) and applying $S_f = S_l + u'_{max}$ the time-mean velocity $\langle u \rangle(y_f)$ at the wall distance y_f can be determined:

$$\langle u \rangle_{pred}(y_f) = \frac{S_l}{1 - 2 Tu \cdot k} \quad (8.11)$$

The experiments in Ch. 7 have shown that $\langle u \rangle(y_f)$ corresponds to approx. 60–70% of the bulk flow velocity \bar{u} in the channel. Using an average value of $b = \langle u \rangle(y_f) / \bar{u} = 0.65$ yields the critical bulk velocities shown in Fig. 8.8. The graph also demonstrates the influence of a variation of the coefficient k and the turbulence intensity Tu , i.e. the impact of a variation of the maximum velocity fluctuation u'_{max} .

While the predictions for $k=2.58$ and $Tu=0.15$ are acceptable for a rough quantitative estimation of the flashback limits, even slight variations or uncertainties in k and Tu lead to a substantial shift of the predicted limits. Therefore, it can be concluded that Eqs. (8.9) and (8.11) are only of limited suitability for the quantitative prediction of the flashback limits of unconfined flames, because they require accurate knowledge of the reacting flow field and the flame speed at the burner exit. Nevertheless, the predictions can be considered satisfactory if the parameters in the correlations are adjusted according to the burner configuration used, for instance by measuring them for a single flashback point. In this way, Eq. (8.11) could potentially be used even for preheated mixtures. Assuming direct proportionality between $\langle u \rangle(y_f)$ and the velocity gradient g at the wall and keeping the parameters Tu and k constant, Eq. (8.11) would predict an increase of the critical velocity gradients with the preheating temperature T according to the power exponent $n \approx 1.4-1.7$, because $S_l \propto T^{1.4-1.7}$ (cf. Eq. (6.1)). This compares well with the experimentally deter-

mined value of $n=1.3-1.5$ (cf. Sec. 6.1).

In summary, the quantitative analysis above has shown that Eqs. (8.9)-(8.11) deliver plausible flashback limits, if the parameters Tu and k are adequately determined/adjusted.

Returning to the critical condition for the onset of flashback in Eq. (8.8), it must be generally taken into account that the distances s_f , y_f and d_f as well as the flame speed S_f depend on a number of different parameters, such as mixture reactivity, preheating temperature, operating pressure, heat transfer to and from the burner walls, quenching distances, turbulence level, and boundary layer development (cf. Sec. 8.2.3). Moreover, these variables are interdependent and not straightforward to be determined in an analytical/theoretical manner. Thus, it is from a practical point of view reasonable to correlate the flashback limits of unconfined flames with (experimentally determined) critical velocity gradients and to use appropriate scaling rules for different operating conditions (cf. Sec. 6.1).

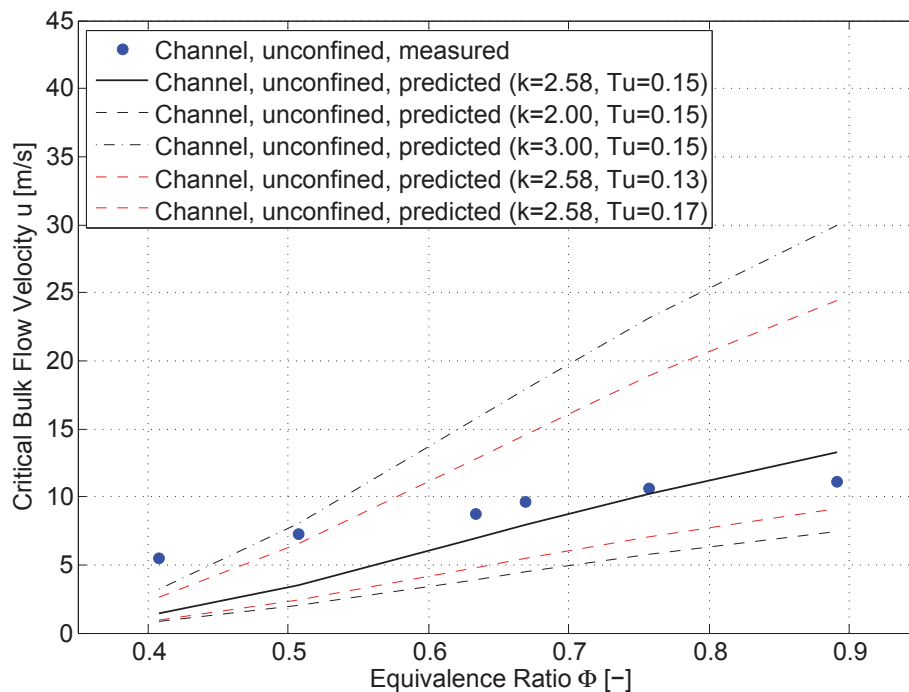


Figure 8.8: Measured vs. predicted critical bulk flow velocities for unconfined channel flames

8.2.3 Implications of the Improved Model for the Flashback Behavior of Unconfined Flames

The flashback model of Fig. 8.5 is now used for a qualitative explanation of the flashback tendencies observed for the different burner configurations in Ch. 5, which are summarized in Fig. 5.12.

Except for the design of the burner exit (cf. Fig. 5.1) the upstream passages of all test setups were identical. Therefore, the velocity profile $u(y)$ in the approaching flow at the burner exit can also be considered identical. Since the distance d_f is not relevant for the onset of flashback, it is also neglected in the following discussion.

Regarding the critical condition for flashback in Eq. (8.8) the following interdependent variables are of particular interest: S_f , s_f and y_f . It is clear that both s_f and $S_f(s_f)$ near the burner rim are to a large extent governed by the heat transfer \dot{q} between the flame and the leakage flow as well as between the leakage flow and the burner rim. If only little heat is extracted by the burner rim, the flame can burn closer to the burner rim, i.e. δ_q decreases, which in turn reduces the heat convection through the leakage flow. Additionally, s_f and the corresponding y_f are decreased as a result of the steeper increase of the flame speed normal to the wall (toward its freestream value). This implies that the burner tip temperature T_{tip} also plays a decisive role for the onset of flashback, because \dot{q} is a result of the temperature difference between flame and burner rim.

In light of these considerations the reasons for the variation in flashback tendency for the different burner configurations in Fig. 5.12 can be summarized as follows (cf. Sec. 5.4):

- A large-diameter flame enclosure substantially increases T_{tip} because on the one hand it decreases heat removal from the reaction zone, on the other hand it prevents entrainment of cold ambient air.
- Cooling of the burner rim reduces T_{tip} and therefore leads to a reduction in flashback propensity.
- The burner material affects the heat fluxes \dot{q} by its thermal conductivity λ , which determines the tip temperature for a given heat load.

- Since the burner diameter neither influences S_f nor s_f , it has negligible influence on the flashback limits, which corroborates the validity of the new flashback model. It is important to note that this diameter insensitivity only applies to conditions within either the laminar or the turbulent flow regime. In case of a regime change the magnitude of the flame speed considerably changes, leading to a shift in flashback limits (cf. [33, 84]).

In summary, the flashback propensity of unconfined flames is mainly driven by the flame speed and the heat fluxes between flame base, leakage flow and burner rim and is therefore closely linked with the burner tip temperature. As can be seen in Fig. 5.12, the flashback propensity of an uncooled quartz burner with flame enclosure is of the same order of magnitude as the one for confined flames. Most likely the low thermal conductivity of quartz in combination with the flame enclosure causes very high tip temperatures and flame speeds. For a quantitative assessment of the influence of T_{tip} and \dot{q} on the flashback propensity a detailed study should be carried out in the future, which accounts for a wide range of tip temperatures, i.e. active heating and cooling of the burner rim is required. At the same time the tip temperature should be measured at accurately defined positions for the sake of comparability. Similarly to what has been done for preheated mixtures in Sec. 6.1, it may be possible to introduce a correction term in the critical gradient correlation that accounts for the influence of the tip temperature. Finally, it is important to note that the model of Fig. 8.5 is not applicable to tightly enclosed/confined flames, where the interaction of the stable flame with the approaching flow is no longer negligible (cf. Sec. 8.1).

9 Summary and Conclusions

The potential occurrence of flame flashback is a critical safety hazard in pre-mixed combustion systems as it can lead to severe hardware damage. This applies in particular to highly reactive fuels, such as hydrogen-rich synthesis gases or pure hydrogen, and to low-velocity flow regions, such as wall boundary layers. In this thesis, flame flashback was investigated both on a macroscopic and on a microscopic scale for pure hydrogen-air mixtures at atmospheric pressure and turbulent flow conditions. In a recent study it was found that the existing critical gradient model for flashback correlation is not applicable to confined flames. In the light of this finding, advanced optical measurement techniques were employed to check the applicability of the critical gradient model to unconfined flames.

The macroscopic flashback studies involved a number of different burner exit configurations and operating conditions, which closely mimic the conditions in technical burner applications. Regarding the burner exit configurations the results demonstrated that burner material and narrow flame confinement have a strong effect on the flashback propensity, whereas the effects of burner diameter and large flame enclosures are relatively weak. Within the configurations tested, the lower and upper limits of flashback propensity for atmospheric hydrogen-air flames were observed for a cooled, unconfined brass burner and an uncooled, confined quartz burner, respectively. Differences in thermal conductivity and the associated response of the burner tip temperature were identified as the reason for the change in flashback propensity for different materials. The negative effect of flame confinement on flashback resistance could be shown to be independent of the burner geometry (circular vs. rectangular cross-section). Flashback is thus primarily driven by the interaction of the confined flame with the flow as a result of the flame backpressure.

Regarding different operating conditions, mixture preheating was found to deteriorate the flashback propensity of unconfined flames, with the increase

in flame speed most likely being the primary cause. Imposing a certain degree of swirl upon the burner flow proved to be beneficial with respect to boundary layer flashback as the resulting centrifugal forces lead to higher axial flow velocities near the wall. It was also shown that for a given swirl intensity - which was below all critical swirl numbers given in the literature due to the specific burner configuration tested - CIVB-initiated boundary layer flashback can occur when a certain equivalence ratio, i.e. mixture reactivity, is exceeded. In other words, CIVB leads to initial upstream propagation of the flame along the burner axis until the flame tail gets in touch with the burner wall. As the latter resembles a confined flame situation with regard to boundary layer flashback, the consecutive flame propagation is along the wall boundary layer. In an attempt to extend the safe operating range of premixed hydrogen burners, small amounts of pure air were injected into the wall boundary layer. This resulted in a considerable increase in flashback stability, which was mainly caused by dilution of the near-wall flow, whereas the injection angle played a negligible role.

The transition from stable flame to flashback was investigated for unconfined flames with high spatial and temporal resolution by means of simultaneous application of μ -PIV and OH* chemiluminescence as well as simultaneous application of μ -PLIF and OH*-chemiluminescence. It turned out that the stable unconfined flame adopts such a shape that there is no appreciable interaction with the approaching flow. In other words, contrary to confined flames, the flame backpressure does not alter the flow profile inside the premixing duct until the flashback limit is reached. Flashback is initiated when the flame speed exceeds the flow velocity at a certain distance downstream of the burner exit. A local flame tip is formed which propagates toward the premixing duct. The adverse pressure gradient generated upstream of this flame tip as a result of the flame backpressure retards and deflects the fresh gas flow, which in turn facilitates the upstream flame propagation. The initially unconfined flame becomes more and more confined the further it propagates into the burner duct. As a result, the deflection of flow is more and more hampered by the duct walls and it was concluded that backflow regions are eventually induced upstream of the flame, similarly to what has been observed for confined flames in a recent study.

The microscopic studies revealed that the critical gradient model of Lewis and von Elbe does not adequately represent the physical reality during flash-

back of unconfined flames. Therefore, an improved flashback model was proposed that accounts for the real position and shape of the stable unconfined flame and that includes the physical boundary conditions that are relevant for the onset of flashback. The model implies that the thermal conditions at the burner rim, e.g. heat convection and heat conduction, have a decisive influence on the flashback propensity. If the reactive flow field at the burner exit is accurately known, the model allows for a rough quantitative prediction of the flashback limits of unconfined flames by using a statistical approach for the velocity and flame speed fluctuations. Moreover, the negligible interaction of the stable flame with the burner flow demonstrated that - in spite of the shortcomings of the critical gradient model - it is a meaningful and practicable approach to correlate the flashback limits of unconfined flames by means of the critical velocity gradient. Regarding confined flames, the flame backpressure must be taken into account. It could be shown that Stratford's separation criterion for turbulent boundary layers provides both qualitative and quantitative information about the influence of the backpressure on the flashback propensity.

In summary, the outcome of the flashback studies highlights some design rules for increasing the flashback safety of technical burners, for instance in gas turbines. While modification of mixture temperature and flow rate is usually not possible, implementation of the following measures should be considered:

- Avoiding a tight confinement of the flame.
- Providing for active cooling of the burner rim to decrease the tip temperature.
- Using burner materials or coatings with high thermal conductivity close to the burner rim to enhance heat transport.
- Using burner materials or coatings with low thermal conductivity further upstream in order to decrease the flashback speed. In combination with fast-responding detection devices, which activate countermeasures, severe hardware damage can potentially be avoided.
- Decreasing the swirl intensity to the minimum level necessary for flame stabilization. This implies that the swirl intensity should be adjusted according to the reactivity of the fuel.

- Implementing boundary layer injection devices close to the burner exit such that fluid injection can be enabled when the burner is operated near its flashback limits.
- Avoiding (boundary layer) flow perturbations, in particular close to the burner exit.

Future work on boundary layer flashback may be dedicated to the following open issues:

- The influence of the burner tip temperature on flashback propensity should be further quantified in experiments that allow for higher peak temperatures. In this way it may be possible to introduce appropriate correction factors in the gradient model or scaling rules similar to that for mixture preheating.
- The material influence on flashback should be further investigated, for instance, by studying catalytic surfaces.
- A systematic study of the influence of flame enclosure/confinement sizes should be carried out in order to learn about the flashback behavior as a function of the diameter ratio between burner and enclosure/confinement.
- The role of elevated pressure on flashback propensity is still unclear.
- A detailed investigation of the influence of acoustic excitations on boundary layer flashback is missing.
- The flame disengagement/wash-out behavior is an important criterion for practical devices and should therefore be examined.

A Isothermal Flow Field in the Plenum of the TUM Burner

Figure A.1 shows the development of the flow in the plenum of the TUM burner. It is obvious that recirculation zones are created close to the inlet at the centre of the plenum and next to the cylinder wall. Nevertheless, their impact decays in streamwise direction until they are no longer discernible shortly upstream of the tube nozzle, as is illustrated by the axial velocity profile in the marked plane.

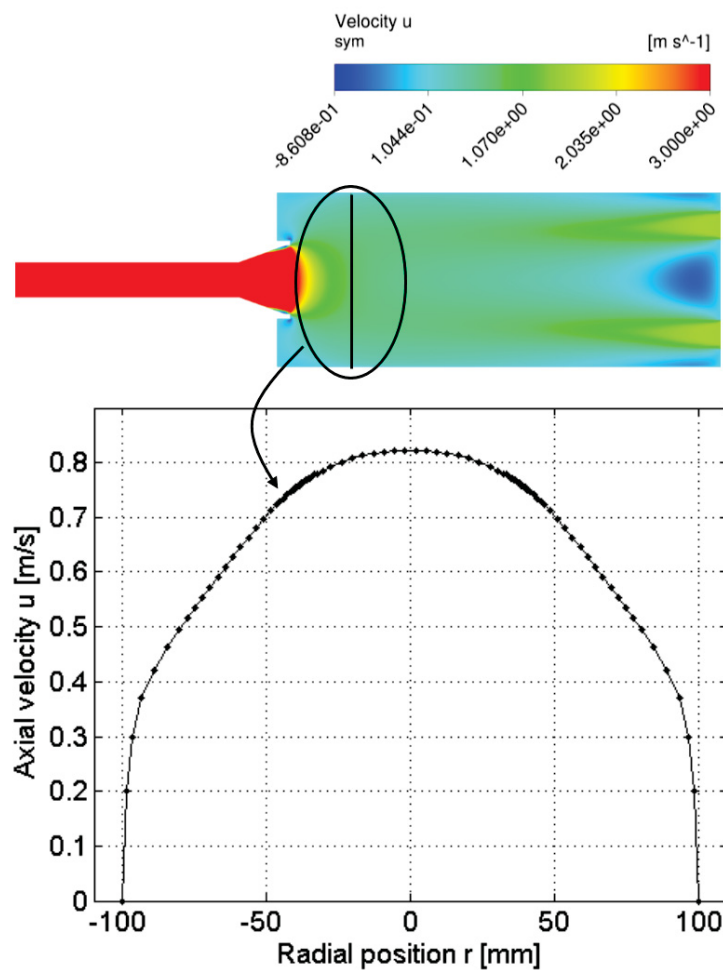


Figure A.1: Isothermal flow development in TUM burner test rig

B Long-Distance Microscopes

B.1 Micro-PIV Measurements

For the μ -PIV measurements in this work, the long-distance microscope Infinity K2/S with CF-3 lens (Edmund Optics) was used. Its specifications are given in Tab. B.1, including the field of view based on a 1/2" camera sensor.

Working distance	Numerical Aperture	Depth of field	Field of view
[mm]	[-]	[μ m]	[mm]
92	0.200	≈ 20	2.1
125	0.156	≈ 20	3.1

Table B.1: Specifications of the K2 Infinity long distance microscope (field of view based on 1/2" sensor)

B.2 Micro-PLIF Measurements

For the μ -PLIF measurements in this work, the long-distance microscope Questar QM1 UV (LaVision) was used, which is transmissible for UV light. Its specifications are shown in Tab. B.2. The horizontal field of view (based on a 2/3" camera sensor) as a function of the working distance is shown in Fig. B.1, depending on the exact assembly.

Working distance [mm]	Numerical Aperture [-]	Depth of field [μm]
560	0.06	155
1020	0.04	408
1270	0.03	595
1676	0.02	1152

Table B.2: Specifications of the Questar QM1 UV long distance microscope

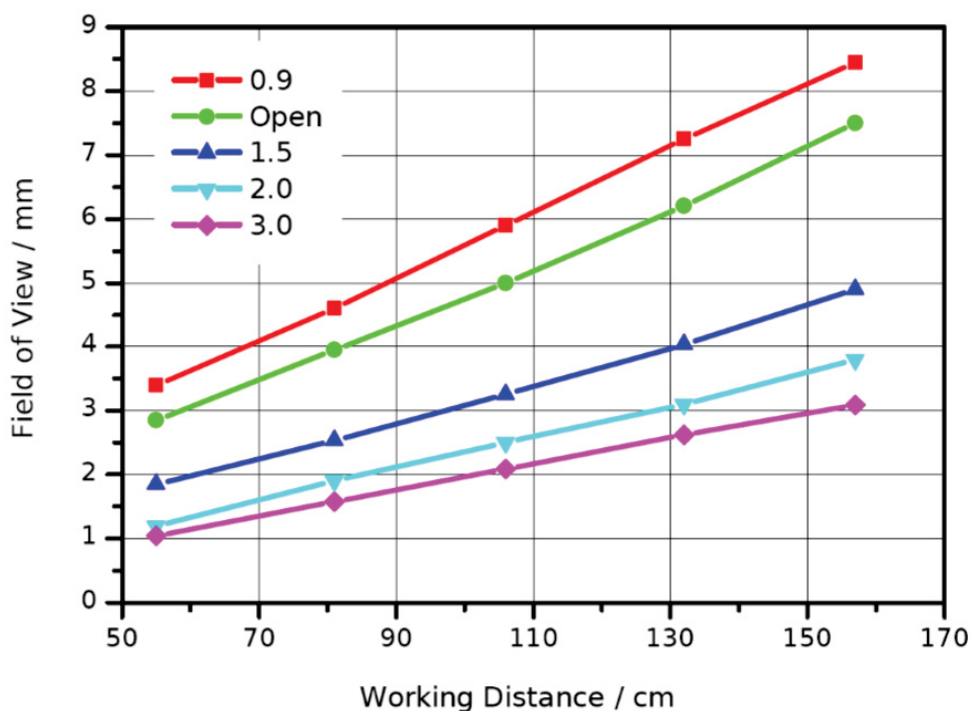


Figure B.1: Horizontal field of view (based on a 2/3" sensor) for the QM1 as a function of the working distance

List of Figures

1.1	Critical velocity gradient model for laminar boundary layer flashback [29,84]	4
1.2	Critical velocity gradients for unconfined laminar and turbulent hydrogen-air flames, [64]*, [35]**, [33]***	7
1.3	Boundary layer flashback model for confined flames [29]	9
2.1	Boundary layer flow over a solid wall	20
2.2	Boundary layer separation due to an adverse pressure gradient	22
2.3	Influence of an adverse pressure gradient on boundary layer flow according to Stratford [115]	23
2.4	Schematic of the qualitative pressure distribution assumed in the Stratford model	24
2.5	Baroclinic torque on a fluid element according to [17] with pressure and density gradient parallel (a) and perpendicular (b)	26
2.6	Structure of a premixed flame front according to [99]	28
2.7	Turbulent combustion regimes according to Peters [99]	30
3.1	Basic design of the TUM tube burner test rig	35
3.2	Details of pilot burner	36
3.3	Channel burner test rig	37
3.4	Schematic of the channel burner test section	39

3.5	Detailed view of the channel burner exit	40
3.6	Setup for simultaneous PIV/PLIF and chemiluminescence . . .	48
3.7	Synchronization scheme for simultaneous application of PIV and chemiluminescence	50
3.8	Simplified scheme of laser-induced fluorescence and relaxation processes in a multi-level system [55]	51
3.9	Synchronization scheme for simultaneous application of PLIF and chemiluminescence (not true to scale)	54
4.1	Isothermal velocity profiles at tube burner outlet	57
4.2	Comparison of wall shear stress from μ -PIV with theoretical cor- relation [29]	60
5.1	Terminology for burner configurations (cf. [26]); thermocouples in red	62
5.2	Comparison of tube burner flashback data with literature data [64]*	63
5.3	Pilot burner with flame confinement [31]	65
5.4	Superposition of unconfined and confined flame in stable mode (a) and flame at flashback (b). The white lines mark the edges of the ceramic block.	66
5.5	Flashback limits for confined flames, [64]*, [29]**, [111]***	67
5.6	Flashback process in the channel burner: Instantaneous OH* images from the side (a) and from the top (b). In (a) the white lines mark the upper and the lower wall, respectively; in (b) they mark the lateral boundaries of the inspection window; flow di- rection from right to left	68
5.7	Flashback limits for open tube and channel flames	68
5.8	Effect of enclosure on flashback limits, [111]*	70
5.9	Effect of enclosure on burner tip temperature	70

5.10 Influence of burner material on critical velocity gradients (derived from [26])	72
5.11 Influence of burner material on tip temperature (derived from [26])	72
5.12 Overview of flashback limits for atmospheric H ₂ -air flames, [64]*, [111]**	75
6.1 Flashback limits for preheated H ₂ -air flames (TUM burner) . . .	79
6.2 Flashback limits for preheated H ₂ -air flames (BaCaTeC burner) .	80
6.3 Flashback limits for preheated, confined H ₂ -air channel flames (derived from [29])	81
6.4 Flashback test rig with optional swirl generator	84
6.5 Details of the swirl generator	85
6.6 Isothermal velocity profiles for non-swirling and swirling flow at tube exit ($\bar{u}=12$ m/s)	86
6.7 Schematic of the high-speed Mie scattering setup	88
6.8 Schematic of the high-speed camera setup	89
6.9 Critical bulk flow velocities for non-swirling and swirling H ₂ -air flames	90
6.10 Critical velocity gradients for non-swirling and swirling H ₂ -air flames	91
6.11 Time series of Mie scattering images for a non-swirling flame at flashback: $\Phi=0.53$, $\Delta t=2$ ms	92
6.12 Time series of Mie scattering images for a swirling flame at flashback; $\Phi=0.49$, $\Delta t=2$ ms	93
6.13 Time series of simultaneous OH*-chemiluminescence images for a swirling flame at flashback; $\Phi=0.77$, $\Delta t=2$ ms: t=0-18 ms . .	95
6.14 Time series of simultaneous OH*-chemiluminescence images for a swirling flame at flashback; $\Phi=0.77$, $\Delta t=2$ ms: t=20-38 ms . .	96

6.15 TUM tube burner with injection devices	100
6.16 Boundary layer injection device: 45°	101
6.17 Boundary layer injection device: Radial	101
6.18 Isothermal velocity profiles at tube burner outlet with and with- out injection ($\bar{u}=10$ m/s)	102
6.19 Stable flame and flame at flashback: No air injected	104
6.20 Critical bulk flow velocities, radial injection, a=113 mm	106
6.21 Critical bulk flow velocities, 45° injection, a=113 mm	106
6.22 Critical velocity gradients, radial injection, a=113 mm	107
6.23 Critical velocity gradients, 45° injection, a=113 mm	107
6.24 Stable flame and flame at flashback: 15% air injected	109
6.25 Velocity profile at tube outlet for radial injection	111
6.26 Velocity profile at tube outlet for 45° injection	111
6.27 Distribution of local equivalence ratio at the tube outlet for ra- dial injection	112
6.28 Distribution of local equivalence ratio at the tube outlet for 45° injection	112
6.29 Critical bulk flow velocities, 45° injection, a=213 mm	114
6.30 Critical velocity gradients, 45° injection, a=213 mm	115
6.31 Critical bulk flow velocities, 45° injection, a=313 mm	115
6.32 Critical bulk flow velocities, radial injection, a=313 mm	116
6.33 Critical velocity gradients, 45° injection, a=313 mm	116
6.34 Critical velocity gradients, radial injection, a=313 mm	117
7.1 Seeding image for isothermal flow (a) and stable combustion (b) ($\bar{u}=7$ m/s, $\Phi=0.5$, T=293 K)	123

7.2	Axial velocity field u [m/s] for isothermal flow (a) and stable combustion (b) ($\bar{u}=7$ m/s, $\Phi=0.5$, $T=293$ K)	123
7.3	Instantaneous (a) and time-averaged (b) macroscopic PLIF image of stable flame ($\bar{u}=7$ m/s, $\Phi=0.5$, $T=293$ K)	125
7.4	Instantaneous OH* chemiluminescence image of flame at flashback from the top	126
7.5	Upstream flame propagation during flashback with leading flame tip inside PIV measurement plane, $\Delta t=0.33$ ms	126
7.6	Seeding distribution (a) and axial velocity field u [m/s] (b) for flame at flashback ($\bar{u}=6.9$ m/s, $\Phi=0.53$, $T=293$ K)	127
7.7	Temporal evolution of axial velocity field u [m/s] during upstream flame propagation with leading flame tip inside PIV measurement plane (μ -PIV), $\Delta t=0.33$ ms	128
7.8	Upstream flame propagation during flashback with leading flame tip outside PIV measurement plane, $\Delta t=0.33$ ms ($\bar{u}=6.8$ m/s, $\Phi=0.52$, $T=293$ K)	129
7.9	Temporal evolution of axial velocity field u [m/s] during upstream flame propagation with leading flame tip outside PIV measurement plane, $\Delta t=0.33$ ms ($\bar{u}=6.8$ m/s, $\Phi=0.52$, $T=293$ K)	130
7.10	Instantaneous microscopic PLIF image of flame at flashback	131
7.11	Temporal evolution of reaction zone during upstream flame propagation with leading flame tip inside PLIF measurement plane, $\Delta t=0.25$ ms ($\bar{u}=7.2$ m/s, $\Phi=0.51$, $T=293$ K)	132
8.1	One-dimensional flame backpressure for laminar H ₂ -air flames	134
8.2	Qualitative illustration of Stratford model during presence of a flame	135
8.3	Predicted vs. measured critical bulk flow velocities for confined H ₂ -air flames (TUM Burner, $d=40$ mm)	139

8.4	Schematic illustration of the transition from stable flame to flashback	142
8.5	Schematic of the stable, unconfined flame close to the flashback limit (dimensions are not true to scale). Streamlines are shown in red and the bold dashed line illustrates the propagation path of the leading flame tip during flashback	144
8.6	Distribution of the turbulence intensity Tu in the channel flow field with stable flame ($\bar{u}=7$ m/s, $\Phi=0.5$, $T=293$ K)	147
8.7	Comparison of estimated minimum flow velocities at the position y_f with the laminar flame speed and a turbulent flame speed	147
8.8	Measured vs. predicted critical bulk flow velocities for unconfined channel flames	149
A.1	Isothermal flow development in TUM burner test rig	157
B.1	Horizontal field of view (based on a 2/3" sensor) for the QM1 as a function of the working distance	160

List of Tables

3.1	Overview of vibrational transitions of the OH-radical [73]	52
4.1	Constants for the calculation of the dynamic viscosity	58
5.1	Thermophysical properties of quartz, brass and alloy	74
8.1	Separation positions for confined flames according to the Stratford criterion [115]	137
B.1	Specifications of the K2 Infinity long distance microscope (field of view based on 1/2" sensor	159
B.2	Specifications of the Questar QM1 UV long distance microscope	160
B.3	List of supervised theses	170

Supervised Theses

Im Rahmen dieser Dissertation entstanden am Lehrstuhl für Thermodynamik in den Jahren von 2010 bis 2013 unter wesentlicher wissenschaftlicher, fachlicher und inhaltlicher Anleitung des Autors die im Folgenden aufgeführten studentischen Arbeiten. Ergebnisse aus diesen Arbeiten können in Teilen in das vorliegende Dokument eingeflossen sein. Der Autor dankt hiermit nochmals explizit allen ehemals betreuten Studenten für ihr Engagement bei der Unterstützung dieser wissenschaftlichen Arbeit.

Associated with this Ph.D. thesis are a number of student theses (Semesterarbeiten, Diplomarbeiten) that were supervised by the author of the present work. These theses were prepared at the Lehrstuhl für Thermodynamik in the years 2010 through 2013 under the close supervision of the present author. Parts of these supervised theses may have been incorporated into the present thesis. The author would like to express his sincere gratitude to all formerly supervised students for their commitment supporting this research project.

Student	Title
Felix Rasp	Numerische Simulation der Grenzschichtströmung in einem wasser-stoffbetriebenen Modellbrenner mit Ansys CFX; Semesterarbeit, submitted in March 2011
Albert Roger Figuerola	Proprietats de l'aire humit (Moist Air Properties); Semesterarbeit, submitted in May 2012
Jan Krick	Experimentelle Untersuchung des Einflusses einer Grenzschichteindüsung auf die Flammenrückschlagsneigung in einem Wasserstoffbrenner; Semesterarbeit, submitted in June 2012
Matthias Danzer	Gegenüberstellung turbulenter Verbrennungsmodelle und numerische Simulation der turbulenten Strömung am Beispiel eines wasserstoffbetriebenen Modellbrenners; Semesterarbeit, submitted in December 2012
Tobias Hummel	Simulation of Premixed Hydrogen-Air Flow Subjected to Lateral Boundary Layer Injection via Computational Fluid Dynamics (CFD); Semesterarbeit, submitted in December 2012
Jan Ollo Olthoff	Geschwindigkeitsmessung in einem wasserstoffbetriebenen Kanalbrenner mittels Particle Image Velocimetry (PIV); Semesterarbeit, submitted in January 2013
Hae-Bong Yim	Numerische Simulation der Strömung in einem wasserstoffbetriebenen Kanal- und Diffusorbrenner unter besonderer Berücksichtigung der Wandgrenzschicht; Semesterarbeit, submitted in June 2013
Tobias Hummel	3D Conjugate Heat Transfer Analysis of Engine Cylinder Heads; Diplomarbeit, submitted in July 2013

Table B.3: List of supervised theses

Bibliography

- [1] Abdulsada, M., Syred, N., Griffiths, A., Bowen, P., and Morris, S.: Effect of Swirl Number and Fuel Type upon the Combustion Limits in Swirl Combustors. *ASME Turbo Expo, GT2011-45544*, 2011.
- [2] Adrian, R. J., Duraó, D. F. G., Durst, F., Heitor, M. V., Maeda, M., and Whitelaw, J. H.: *Laser Techniques Applied to Fluid Mechanics*. Springer, 2000.
- [3] Ball, D. A., Putnam, A. A., Radhakrishnan, E., and Levy, A.: Relation of Burning Velocity, Quenching Distance, and Flashback Velocity Gradient for Low and Intermediate BTU Gases. Battelle Columbus Laboratories, 1978.
- [4] Baumgartner, G.: Experimental Investigation on Transverse Injection of Fuel into the Supersonic Flow in a Model Combustor. Diploma thesis, Technische Universität München, 2010.
- [5] Baumgartner, G., and Sattelmayer, T.: Experimental Investigation of the Flashback Limits and Flame Propagation Mechanisms for Premixed Hydrogen-Air Flames in Non-Swirling and Swirling Flow. *ASME Turbo Expo, GT2013-94258*, 2013.
- [6] Baumgartner, G., and Sattelmayer, T.: Experimental Investigation on the Effect of Boundary Layer Fluid Injection on the Flashback Propensity of Premixed Hydrogen-Air Flames. *ASME Turbo Expo, GT2013-94266*, 2013.
- [7] Baumgartner, G., Boeck, L. R., and Sattelmayer, T.: Investigation of the Flame-Flow Interaction during Flame Flashback in a Generic Premixed Combustion System by Means of High-Speed Micro-PIV and Micro-

- PLIF. *16th International Symposium on Flow Visualization, ISFV16-1135*, 2014.
- [8] Baumgartner, G., Boeck, L. R., and Sattelmayer, T.: Experimental Investigation of the Transition Mechanism from Stable Flame to Flashback in a Generic Premixed Combustion System with High-Speed μ -PIV and μ -PLIF Combined with Chemiluminescence Imaging; submitted to *ASME Turbo Expo, GT2015-42605*, 2015.
- [9] Berlad, A. L., and Potter, A. E.: Relation of Boundary Velocity Gradient for Flash-back to Burning Velocity and Quenching Distance. *Combustion and Flame*, 1:127-128, 1957.
- [10] Blasius, H.: Grenzschichten in Flüssigkeiten mit kleiner Reibung. *Zeitschrift für angewandte Mathematik und Physik*, 56:1-37, 1908.
- [11] Boeck, L. R., Primbs, A., Hasslberger, J., and Sattelmayer T.: Investigation of Flame Acceleration in a Duct Using the OH PLIF Technique at High Repetition Rate. *Fachtagung Lasermethoden in der Stroemungsmesstechnik, Paper no. 40*, 2013.
- [12] Bohren, C. F., and Huffmann, D. R.: Absorption and Scattering of Light by Small Particles. Wiley-Interscience, 2010.
- [13] Bollinger, L. E.: Studies on Burner Flames of Hydrogen-Oxygen Mixtures at High Pressures. WADC Technical Report, 52-59, Wright Air Development Center, 1952.
- [14] Bollinger, L. E., and Edse, R.: Effect of Burner-Tip Temperature on Flash Back of Turbulent Hydrogen-Oxygen Flames. *Industrial & Engineering Chemistry*, 48:802-807, 1956.
- [15] Boyce, M. P.: Gas Turbine Engineering Handbook. Butterworth-Heinemann, 2012.
- [16] Brown, G. L., and Lopez, J. M.: Axisymmetric Vortex Breakdown Part II Physical Mechanics. *Journal of Fluid Mechanics*, 221:553-576, 1990.
- [17] Burmberger, S.: Optimierung der aerodynamischen Flammenstabilisierung für brennstoffflexible, vorgemischte Gasturbinenbrenner. Ph.D. thesis, Technische Universität München, 2009.

- [18] Caffo, E., and Padovani, C.: Flashback in Premixed Air Flames. *Combustion and Flame*, 7:331-337, 1963.
- [19] Cebeci, T., and Smith A. M. O.: A Finite-Difference Method for Calculating Compressible Laminar and Turbulent Boundary Layers. *Journal of Basic Engineering*, 92:523-535, 1970.
- [20] Cebeci, T., Mosinskis, G. J., and Smith A. M. O.: Calculation of Separation Points in Incompressible Turbulent Flows. *Journal of Aircraft*, 9:618-624, 1972.
- [21] Dahoe, A. E.: Laminar Burning Velocities of Hydrogen-Air Mixtures from Closed Vessel Gas Explosions. *Journal of Loss Prevention in the Process Industries*, 18:152-166, 2005.
- [22] Damköhler, G.: Der Einfluss der Turbulenz auf die Flammgeschwindigkeit in Gasgemischen. *Zeitschrift für Elektrochemie und angewandte Chemie*, 46:601-626, 1940.
- [23] Daniele, S., Jansohn, P., and Boulouchos, K.: Flashback Propensity of Syngas Flames at High Pressure: Diagnostic and Control. *ASME Turbo Expo, GT2010-23456*, 2010.
- [24] Dantec Dynamics A/S: FlowManager software and Introduction to PIV Instrumentation. Software User's Guide, publication no.: 9040U3625, Denmark, 2002.
- [25] Davu, D., Franko, R., and Choudhuri, A.: Investigation on Flashback Propensity of Syngas Premixed Flames. *41st AIAA/ASME/SAE/ASEE Joint Propulsion Conference & Exhibit, AIAA 2005-3585*, 2005.
- [26] Duan, Z., Shaffer, B., McDonell, V., Baumgartner, G., and Sattelmayer, T.: Influence of Burner Material, Tip Temperature and Geometrical Flame Configuration on Flashback Propensity of H₂-Air Jet Flames. *ASME Turbo Expo, GT2013-94823*, 2013.
- [27] Duan, Z., Shaffer, B., and McDonell, V.: Study of Burner Material and Tip Temperature Effects on Flashback of Confined Jet Flame. *ASME Turbo Expo, GT2013-94822*, 2013.
- [28] Dugger, G. L.: Flame Stability of Preheated Propane-Air Mixtures. *Industrial & Engineering Chemistry*, 47:109-114, 1995.

- [29] Eichler, C.: Flame Flashback in Wall Boundary Layers of Premixed Combustion Systems. Ph.D. thesis, Technische Universität München, 2011.
- [30] Eichler, C., and Sattelmayer, T.: Experiments on Flame Flashback in a Quasi-2D Turbulent Wall Boundary Layer for Premixed Methane-Hydrogen-Air Mixtures. *Journal of Engineering for Gas Turbines and Power*, 133:011503, 2011.
- [31] Eichler, C., Baumgartner, G., and Sattelmayer, T.: Experimental Investigation of Turbulent Boundary Layer Flashback Limits for Premixed Hydrogen-Air Flames Confined in Ducts. *Journal of Engineering for Gas Turbines and Power*, 134:1-8, 2012.
- [32] Eichler, C., and Sattelmayer, T.: Premixed Flame Flashback in Wall Boundary Layers Studied by Long-Distance Micro-PIV. *Experiments in fluids*, 1-14, 2012.
- [33] Elbe, G. von, and Mentser, M.: Further Studies of the Structure and Stability of Burner Flames. *Journal of Chemical Physics*, 13:89-100, 1945.
- [34] Fine, B.: Stability Limits and Burning Velocities for Some Laminar and Turbulent Propane and Hydrogen Flames at Reduced Pressure. NACA - Technical Note, No. 4031, p.49, 1957.
- [35] Fine, B.: The Flashback of Laminar and Turbulent Burner Flames at Reduced Pressure. *Combustion & Flame*, 2:253-266, 1958.
- [36] Fine, B.: Effect of Initial Temperature on Flash Back of Laminar and Turbulent Burner Flames. *Industrial & Engineering Chemistry Research*, 51:564-566, 1959.
- [37] Fox, J. S., and Bhargava, A.: Flame Speed and Flashback Gradient for Simulated Biomass Gasification Products. *Intersociety Energy Conversion Engineering Conference*, 2, 1984.
- [38] France, D. H.: Flashback of Laminar Monoport Burner Flames. *Journal of the Institute of Fuel*, 50:147-152, 1977.
- [39] Fritz, J.: Flammenrueckschlaege durch verbrennungsinduziertes Wirbelaufplatzen. Ph.D. thesis, Technische Universitaet Muenchen, 2003.

- [40] Ghoniem, A. F., Park, S., Wachsman, A., Annaswamy, A., Wee, D., and Altay, H. M.: Mechanism of Combustion Dynamics in a Backward-Facing Step Stabilized Premixed Flame. *Proceedings of the Combustion Institute*, 30:1783-1790, 2005.
- [41] Goldschmied, F. R.: An Approach to Turbulent Incompressible Separation under Adverse Pressure Gradients. *Journal of Aircraft*, 2:108-115, 1965.
- [42] Greitzer, E., Tan, C., and Graf, M.: Internal Flow - Concepts and Applications. Cambridge University Press, 2004.
- [43] Goulard, R.: Combustion Measurements - Modern Techniques and Instrumentation. Hemisphere Publishing Corporation, 1976.
- [44] Gruber, A., Chen, J. H., Valiev, D., and Law, C. K.: Direct Numerical Simulation of Premixed Flame Boundary Layer Flashback in Turbulent Channel Flow. *Journal of Fluid Mechanics*, 709:516-542, 2012.
- [45] Grumer, J.: Predicting Burner Performance with Interchanged Fuel Gases. *Industrial & Engineering Chemistry*, 41:2756-2761, 1949.
- [46] Grumer, J., and Harris, M. E.: Flame-Stability Limits of Methane, Hydrogen, and Carbon Monoxide Mixtures. *Industrial & Engineering Chemistry*, 44:1547-1553, 1952.
- [47] Grumer, J., Harris, M. E., and Schultz, H.: Predicting Interchangeability of Fuel Gases - Interchangeability of Oil Gases or Propane-Air Fuels with Natural Gases. *Industrial & Engineering Chemistry*, 44:1554-1559, 1952.
- [48] Grumer, J., and Harris, M. E.: Temperature Dependence of Stability Limits of Burner Flames. *Industrial & Engineering Chemistry*, 46:2424-2430, 1954.
- [49] Grumer, J., Harris, M. E., and Schultz, H.: Flame- Stability Limits of Ethylene, Propane, Methane, Hydrogen, and Nitrogen Mixtures. *Industrial & Engineering Chemistry*, 47:1760-1767, 1955.
- [50] Grumer, J., Harris, M. E., and Rowe, V.: Fundamental Flashback, Blow off, and Yellow-Tip Limits of Fuel Gas-Air Mixtures. United States Department of the Interior, Bureau of Mines, 1956.

- [51] Grumer, J.: Flashback and Blowoff Limits of Unpiloted Turbulent Flames. *Jet Propulsion*, 28:756-759, 1958.
- [52] He, G., Guo, Z., and Hsu, A.: The Effect of Schmidt Number on Turbulent Scalar Mixing in a Jet-in-Crossflow. *International Journal of Heat and Mass Transfer*, 42:3727-3738, 1999.
- [53] Hellat, J.: Turbulente Stroemung und Mischung in Erdgas-Diffusionsflammen mit Luftdrall. Ph.D. thesis, Universität Fridericiana Karlsruhe, 1979.
- [54] Head, M. R.: Entrainment in the Turbulent Boundary Layer. *Aeronautical Research Council*, Technical Report No. 3152, 1960.
- [55] Höinig, R.: Konzentrations- und Temperaturbestimmung in Brennkammern luftatmender Antriebe mit Hilfe laserspektroskopischer Messverfahren. Ph.D. thesis, Technische Universität München, 1995.
- [56] Ivanova, E., Noll, B., and Eigner, M.: Computational Modelling of Turbulent Mixing of a Transverse Jet. *ASME Turbo Expo, GT2010-22764*, 2010.
- [57] Jakirlic, S.: Reynolds-Spannungs-Modellierung komplexer turbulenter Stroemungen. Herbert Utz Verlag Wissenschaft, 1997.
- [58] Kähler, C. J., McKenna, R., and Scholz, U.: Wall-Shear-Stress Measurements at Moderate Re-Numbers with Single Pixel Resolution Long Distance Micro-PIV - an Accuracy Assessment. *6th International Symposium on Particle Image Velocimetry*, 2005.
- [59] Kähler, C. J., Scholz, U., and Ortmanns, J.: Wall-Shear-Stress and Near-Wall Turbulence Measurements up to Single Pixel Resolution by Means of Long-Distance Micro-PIV. *Experiments in fluids*, 41:327-341, 2006.
- [60] Karim, G. A., Kibrya, G., and Wierzba, I.: Flashback and Flame Propagation Limits through Streams of Premixed Fuel and Air. *7th International Symposium on Air Breathing Engines*, 783-786, 1985.
- [61] Karim, G. A., and Lapuch, R.: Flame Flashback for Low Reynolds Number Flows. *Progress in Astronautics and Aeronautics*, 113:367-383, 1988.
- [62] Kathrotia, T., Fikri, M., Bozkurt, M., Hartmann, M., Riedel, U., and Schulz, C.: Study of the H+O+M Reaction Forming OH*: Kinetics of

- OH* Chemiluminescence in Hydrogen Combustion Systems. *Combustion and Flame*, 157:1261-1273, 2010.
- [63] Keller, J. O., Vaneveld, L., Korschelt, D., Ghonium, A. F., Daily, J. W., and Oppenheim, A. K.: Mechanisms of Instabilities in Turbulent Combustion Leading to Flashback. *AIAA 19th Aerospace Sciences Meeting*, 1981.
- [64] Khittrin, L., Moin, P., Smirnov, D., and Shevchuk, V.: Peculiarities of Laminar- and Turbulent-Flame Flashbacks. *10th Symposium (International) on Combustion*, 1285-1291, 1965.
- [65] Kieseewetter, F.: Modellierung des verbrennungsinduzierten Wirbelaufplatzens in Vormischbrennern. Ph.D. thesis, Technische Universität München, 2005.
- [66] Kieseewetter, F., Konle, M., and Sattelmayer, T.: Analysis of Combustion Induced Vortex Breakdown Driven Flame Flashback in a Premix Burner with Cylindrical Mixing Zone. *Journal of Engineering for Gas Turbines and Power*, 129:929-936, 2007.
- [67] Konle, M.: Simultane PIV-LIF-Messungen zur Bestimmung der Flammenstreckungsrate. Diploma thesis, Technische Universität - Lehrstuhl für Thermodynamik, 2005.
- [68] Konle, M., Kieseewetter, F., and Sattelmayer, T.: Simultaneous High Repetition Rate PIV-LIF Measurements of CIVB Driven Flashback. *Experiments in Fluids*, 44:529-538, 2008.
- [69] Konle, M.: Verbrennungsinduziertes Wirbelaufplatzen in moderat turbulenten Drallströmungen. Ph.D. thesis, Technische Universität München, 2010.
- [70] Krevelen, van D. W., and Chermin, H. A. G.: Generalized Flame Stability Diagram for the Prediction of Interchangeability of Gases. *Symposium (International) on Combustion*, 7:358-368, 1958.
- [71] Kröner, M.: Einfluss lokaler Löschvorgänge auf den Flammenrückschlag durch verbrennungsinduziertes Wirbelaufplatzen. Ph.D. thesis, Technische Universität München, 2003.

- [72] Kröner, M., Sattelmayer, T., Fritz, J., Kiesewetter, F., and Hirsch, C.: Flame Propagation in Swirling Flows - Effect of Local Extinction on the Combustion Induced Vortex Breakdown". *Combustion Science and Technology*, 179:1385-1416, 2007.
- [73] Kuhn, D.: Messung von Temperatur- und Konzentrationsprofilen mittels Laserinduzierter Fluoreszenz (LIF). Ph.D. thesis, Universität Karlsruhe, 2000.
- [74] Kurdyumov, V.N., Fernández, E., and Liñán, A.: Flame Flashback and Propagation of Premixed Flames near a Wall. *Proceedings of the Combustion Institute*, 28:1883-1889, 2000.
- [75] Kurdyumov, V., Fernández-Tarrazo, E., Truffaut, J. M., Quinard, J., Wangher, A., and Searby, G.: Experimental and Numerical Study of Premixed Flame Flashback. *Proceedings of the Combustion Institute*, 31:1275-1282, 2007.
- [76] Kurdyumov, V.N., Truffaut, J. M., Quinard, J., Wangher, A., and Searby, G.: Oscillations of Premixed Flames in Tubes Near the Flashback Conditions. *Combustion Science and Technology*, 180:731-742, 2008.
- [77] Lakowicz, J. R.: Principles of Fluorescence Spectroscopy. Springer, 2006.
- [78] Law, C. K.: Combustion Physics. Cambridge University Press, 2006.
- [79] Law, C. K., and Sung, C. J.: Structure, Aerodynamics, and Geometry of Premixed Flamelets. *Progress in Energy and Combustion Science*, 26:459-505, 2000.
- [80] Lee, S. T., and Tien, J. S.: A Numerical-Analysis of Flame Flashback in a Premixed Laminar System. *Combustion and Flame*, 48:273-285, 1982.
- [81] Lechner, C., and Seume, J.: Stationäre Gasturbinen. Springer, 2003.
- [82] Leon, A.: Hydrogen Technology. Springer, 2008.
- [83] Lewis, B., and Elbe, G. von: Combustion, Flames and Explosions of Gases. Academic Press Inc., 1987.
- [84] Lewis, B., and Elbe, G. von: Stability and Structure of Burner Flames. *Journal of Chemical Physics*, 11:75-97, 1943.

- [85] Lieuwen, T., McDonell, V., Santavica, D., and Sattelmayer, T.: Burner Development and Operability Issues Associated with Steady Flowing Syn-gas Fired Combustors. *Combustion Science and Technology*, 180:1167-1190, 2008.
- [86] Lieuwen, T., McDonell, V., Petersen, E., and Santavicca, D.: Fuel Flexibility Influences on Premixed Combustor Blowout, Flashback, Autoignition, and Stability. *Journal of Engineering for Gas Turbines and Power*, 130, 2008.
- [87] Lieuwen, T., Yang, V., and Yetter, R.: Synthesis Gas Combustion - Fundamentals and Application. CRC Press, 2010.
- [88] Lin, Y.-C., Daniele, S., Jansohn, P., and Boulouchos, K.: Turbulent Flame Speed as an Indicator for Flashback Propensity of Hydrogen-Rich Fuel Gases. *Journal of Engineering for Gas Turbines and Power*, 135:111503, 2013.
- [89] Mathur, S., and Saxena, S. C.: Viscosity of Polar Gas Mixtures: Wilke's Method. *Applied Scientific Research*, 15:404-410, 1965.
- [90] Mayer, C.: Konzept zur vorgemischten Verbrennung wasserstoffhaltiger Brennstoffe in Gasturbinen. Ph.D. thesis, Technische Universität München, 2012.
- [91] Melling, A.: Tracer Particles and Seeding for Particle Image Velocimetry. *Measurement Science and Technology*, 8:1406-1416, 1997.
- [92] Moin, F. B., and Shevchuk, V. U.: Flame "Blow-Back" in the Combustion of Premixed Gases in Flow-through Systems. *Combustion, Explosion, and Shock Waves*, 4:121-123, 1968.
- [93] Moser, R. D., Kim, J., and Mansour, N. N.: Direct Numerical Simulation of Turbulent Channel Flow up to $Re_\tau=590$. *Physics of Fluids*, 11:943-945, 1999.
- [94] Munson, B. R., Young, D. F., and Okiishi, T. H.: Fundamentals of Fluid Mechanics. John Wiley & Sons, 2006.
- [95] Nauert, A., Petersson, P., Linne, M., and Dreizler, A.: Experimental Analysis of Flashback in Lean Premixed Swirling Flames: Conditions Close to Flashback. *Experiments in Fluids*, 43:89-100, 2007.

- [96] Nitsche, W., and Brunn, A.: Strömungsmesstechnik. Springer, 2006.
- [97] O’Connaire, M., Curran, H. J., Simmie, J. M., Pitz W. J., and Westbrook, C. K.: A Comprehensive Modeling Study of Hydrogen Oxidation. *International Journal of Chemical Kinetics*, 36:603-622, 2004.
- [98] Payrhuber, K., Moliere, M., Scholz, M., and Jones, R. M.: Future Energy Challenges in a Carbon Constrained Environment - Fuel Flexibility is a Growing Need. *VGB Power Tech*, 10:23-27, 2007.
- [99] Peters, N.: Turbulent Combustion. Cambridge University Press, 2006.
- [100] Poruba, C.: Turbulente Flammenausbreitung in Wasserstoff-Luft-Gemischen. Ph.D. thesis, Technische Universität München, 2003.
- [101] Prandtl, L.: Über Flüssigkeitsbewegung bei sehr kleiner Reibung. III. Internationaler Mathematiker-Kongress, 484-491, 1904.
- [102] Putnam, A. A., and Jensen, R. A.: Application of Dimensionless Numbers to Flash-back and Other Combustion Phenomena. *Symposium on Combustion and Flame, and Explosion Phenomena*, 3:89-98, 1949.
- [103] Putnam, A. A., Ball, D. A., and Levy, A.: Effect of Fuel Composition on Relation of Burning Velocity to Product of Quenching Distance and Flash-back Velocity Gradient. *Combustion and Flame*, 37:193-196, 1980.
- [104] Raffel, M., Willert, C., Wereley, S., and Kompenhans, J.: Particle Image Velocimetry - A Practical Guide. Springer, 2007.
- [105] Robinson, S. K.: Coherent Motions in the Turbulent Boundary Layer. *Annual Review of Fluid Mechanics*, 23:601-639, 1991.
- [106] Robinson, S. K.: The Kinematics of Turbulent Boundary Layer Structure. Technical Memorandum 103859, National Aeronautics and Space Administration (NASA), 1991.
- [107] Salim, M. S., and Cheah, S. C.: Wall y^+ Strategy for Dealing with Wall-Bounded Turbulent Flows. *Proceedings of the International MultiConference of Engineers and Computer Scientists*, 2, 2009.
- [108] Sangl, J.: Erhöhung der Brennstoffflexibilität von Vormischbrennern durch Beeinflussung der Wirbeldynamik. Ph.D. thesis, Technische Universität München, 2011.

- [109] Schäfer, O., Koch, R., and Wittig, S.: Flashback in Lean Prevaporized Premixed Combustion: Non-Swirling Turbulent Pipe Flow Study. *ASME Turbo Expo, GT2001-0053*, 2001.
- [110] Schlichting, H.: *Grenzschicht-Theorie*. Springer, 2006.
- [111] Shaffer, B., Duan, Z., and McDonell, V.: Study of Fuel Composition Effects on Flashback Using a Confined Jet Flame Burner. *Journal of Engineering for Gas Turbines and Power*, 135:011502-9, 2013.
- [112] Simpson, R. L.: Aspects of Turbulent Boundary-Layer Separation. *Progress in Aerospace Sciences*, 32:457-521, 1996.
- [113] Smith, C. R., and Metzler, S. P.: The Characteristics of Low-Speed Streaks in the Near-Wall Region of a Turbulent Boundary Layer. *Journal of Fluid Mechanics*, 129:27-54, 1983.
- [114] Sogo, S., and Yuasa, S.: Flame Stretch Rate of Laminar Flame Base just before Flashback at Different Burner Temperatures. *20th International Colloquium on the Dynamics of Explosions and Reactive Systems*, 2005.
- [115] Stratford, B. S.: The Prediction of Separation of the Turbulent Boundary Layer. *Journal of Fluid Mechanics*, 5:1-16, 1959.
- [116] Tanimura, S., Komiyama, M., Takeishi, K., Iwasaki, Y., and Nakayama, K.: Visualization of Flashback in a Premixed Burner with Swirling Flow. *Science China Technological Sciences*, 53:40-45, 2010.
- [117] Thibaut, D., and Candel, S.: Numerical Study of Unsteady Turbulent Premixed Combustion: Application to Flashback Simulation. *Combustion and Flame*, 113:53-65, 1998.
- [118] Thielicke, W., and Stamhuis, E. J.: PIVlab - Time-Resolved Digital Particle Image Velocimetry Tool for MATLAB (version: 1.35). Mathworks, 2014.
- [119] Turns, S. R.: *An Introduction to Combustion - Concepts and Applications*. McGraw-Hill, 2000.
- [120] Umemura, A., and Tomita, K.: Rapid Flame Propagation in a Vortex Tube in Perspective of Vortex Breakdown Phenomenon. *Combustion and Flame*, 125:820-838, 2001.
- [121] Verein Deutscher Ingenieure: *VDI-Wärmeatlas*. Springer, 2006.

- [122] Versailles, P., Chishty, W. A., and Vo, H. D.: Application of Dielectric Barrier Discharge to Improve the Flashback Limit of a Lean Premixed Dump Combustor. *Journal of Engineering for Gas Turbines and Power*, 134:1-8, 2012.
- [123] Versailles, P., Chishty, W. A., and Vo, H. D.: Plasma Actuation Control of Boundary Layer Flashback in Lean Premixed Combustor. *ASME Turbo Expo, GT2012-68224*, 2012.
- [124] Wäsle, J. G.: Vorhersage der Lärmemission turbulenter Vormischflammen. Ph.D. thesis, Technische Universität München, 2007.
- [125] Warnatz, J.: Das komplexe Problem der Verbrennung. *Ruperto Carola*, 1, 1999.
- [126] Wang, S., and Rusak, Z.: The Dynamics of a Swirling Flow in a Pipe and Transition to Axisymmetric Vortex Breakdown. *Journal of Fluid Mechanics*, 340:177-223, 1997.
- [127] White, F. M.: *Viscous Fluid Flow*. McGraw-Hill, 2005.
- [128] White, F. M.: *Fluid Mechanics*. McGraw-Hill, 2011.
- [129] Wierzba, I., and Kar, K.: Flame Flashback within Turbulent Streams of Lean Homogeneous Fuel Mixtures and Air. *Journal of Energy Resources Technology*, 114:142-145, 1992.
- [130] Wierzba, I., Oladipo, A. B., and Karim, G. A.: The Limits for Flame Flashback Within Streams of Lean Homogeneous Fuel-Diluent-Air Mixtures Involving Hydrogen. *International Journal of Hydrogen Energy*, 18:223-226, 1993.
- [131] Wilcox, D. C.: *Turbulence Modeling for CFD*. Birmingham Press Inc., 2006.
- [132] Wohl, K.: Quenching, Flash-back, Blow-off-Theory and Experiment. *Symposium (International) on Combustion*, 4:68-89, 1953.